# Space variant manipulation of vector beams in ultrafast laser direct writing chirality

Jiafeng Lu

THESE DE DOCTORAT

NNT : 2023UPASF074

# Space variant manipulation of vector beams in ultrafast laser direct writing chirality

*Manipulation de faisceaux vectoriels afin d'imprimer une chiralité optique par laser femtoseconde dans les verres*

**Thèse de doctorat de l'université Paris-Saclay et Shanghai University**

École doctorale n° 571 Sciences chimiques : molécules, matériaux, instrumentation et biosystèmes (2MIB)
Spécialité de doctorat : Physique
Graduate School : Chimie. Référent : Faculté des sciences d'Orsay

Thèse préparée dans l'unité de recherche **Institut de chimie moléculaire et des matériaux d'Orsay** (Université Paris-Saclay, CNRS), sous la direction de **Matthieu LANCRY**, Professeur des Universités, et la co-direction de **Xianglong ZENG,** Professeur des Universités

**Thèse soutenue à Shanghai, le 12 Novembre 2023, par**

**Jiafeng LU**

## Composition du Jury

Membres du jury avec voix délibérative

| | |
|---|---|
| **Xianfeng CHEN**<br>Professeur des Universités,<br>Shanghai Jiao Tong University | Président |
| **Quanzhong ZHAO**<br>Professeur des Universités,<br>University of Chinese Academy of Science | Rapporteur & Examinateur |
| **Junsong PENG**<br>Professeur des Universités,<br>East China Normal University | Rapporteur & Examinateur |
| **Ye DAI**<br>Professeur des Universités,<br>Shanghai University | Examinateur |
| **Vincent JI**<br>Professeur des Universités,<br>Université Paris-Saclay | Examinateur |

université PARIS-SACLAY

ÉCOLE DOCTORALE
Sciences Chimiques : Molécules, Matériaux, Instrumentation et Biosystèmes (2MIB)

**Titre:** Manipulation de faisceaux vectoriels afin d'imprimer une chiralité optique par laser femtoseconde dans les verres

**Mots clés:** laser ultra-rapide; faisceaux vectoriels; la chiralité; variante spatiale; polarisation; silice; fibre optique

**Résumé:** La chiralité, ou l'incapacité à coïncider l'objet et son image par translation et rotation, existe largement dans la nature, comme les molécules d'ADN duplex qui contiennent des informations génétiques, les acides aminés ou les galaxies spirales dans l'univers. L'essence de la chiralité est la rupture de symétrie, qui présente des réponses différentes lors de l'interaction avec d'autres objets chiraux.

La lumière peut aussi être chirale. Par exemple, les faisceaux lumineux à polarisation circulaire gauche/droite et les faisceaux de vortex porteurs de moments angulaires orbitaux sont des énantiomères chiraux. Par conséquent, les champs lumineux chiraux sont souvent utilisés pour la détection de substances chirales, comme la technique de spectroscopie basée sur le dichroïsme circulaire. En raison des caractéristiques des distributions topologiques spatiales, la génération, la manipulation et l'application de champs de lumière vortex chiraux sont des sujets essentiels en optique et en nanophotonique.

L'interaction chirale entre la lumière et la matière enrichit non seulement les fondamentaux, mais favorise également le développement de matériaux photoniques aux propriétés chirales. La chiralité peut ainsi être transférée entre la lumière et la matière, c.-à-d., la matière peut induire et manipuler la chiralité du champ lumineux, tandis que le champ lumineux peut également induire et manipuler la chiralité de la matière. L'exploration du mécanisme d'interaction chirale entre la lumière et la matière amène une pierre à l'édifice et favorise par ce biais notre compréhension de l'origine de la chiralité de la vie. De plus, il nous aidera à clarifier le mécanisme de manipulation des matériaux fonctionnels chiraux ainsi que les propriétés optiques chirales sous-jacentes.

En partant des principes de manipulation des champs lumineux chiraux, cette thèse étudie la génération de champs lumineux structurés chiraux et cela au travers des interactions acousto-optiques et du contrôle de la polarisation ainsi que de sa distribution en 3D.

Par exemple, nous démontrons une commutation vortex entre différentes charges topologiques de "+1" et "-1" avec une vitesse de commutation pouvant atteindre 4 kHz. Grâce à la technique de la transformée de Fourier dispersive, la dynamique de commutation dans un laser à fibre est modélisée et observée. D'autre part, nous montrons que le mécanisme de la chiralité induite par laser femtoseconde dans les verres est bien une chiralité optique (mais une chiralité extrinsèque), qui est due à un effet joint de la biréfringence de forme et de la biréfringence induite par contrainte avec des axes neutres non parallèles et non perpendiculaires. En tirant profit d'un modèle à deux couches linéaires, de fortes propriétés optiques circulaires ont été réalisées dans la silice par une stratégie multicouche ou encore avec un faisceau Bessel chiral dont l'orientation de polarisation linéaire tourne le long de la propagation. En outre, des assemblages de nanoréseaux sont étudiés pour former des polariseurs intégrés dans une fibre optique et des dispositifs optiques potentiellement chiraux.

Ainsi l'étude de la manipulation du champ lumineux chiral et de son interaction avec les matériaux joue un rôle important dans les domaines du tri des particules, de la communication optique à grande capacité, des puces photoniques, de l'imagerie à super-résolution et du traitement micro-nano laser ultra-rapide.

université PARIS-SACLAY

ÉCOLE DOCTORALE
Sciences Chimiques : Molécules, Matériaux, Instrumentation et Biosystèmes (2MIB)

**Title:** Space variant manipulation of vector beams in ultrafast laser direct writing chirality

**Keywords:** ultrafast laser; vector beams; chirality; space variant; polarization; silica; optical fiber.

**Abstract:** Chirality, the inability of objects to coincide with their mirror images by translation and rotation, exists widely in nature, such as duplex DNA molecules that contain genetic information, amino acids that constitute biological proteins, and spiral galaxies in the universe. The essence of chirality is symmetry breaking, which exhibits different responses when interacting with other chiral objects.

Light can also be chiral. For example, left- and right-handed circularly polarized light beams and vortex light beams carrying positive and negative orbital angular momentums (OAMs) are chiral enantiomers, respectively. Therefore, chiral light fields are often used for the detection of chiral substances, such as circular dichroism spectrum technique. Due to the characteristics of spatial topological distributions, the generation, manipulation, and application of chiral vortex light fields are essential topics in optics and nano-photonics.

The chiral interaction between light and matter not only enriches the nonlinear fundamentals, but also promotes the development of chiral photonics materials. Chirality can be transferred between light and matter, i.e., matter can induce and manipulate the chirality of light field through chiral interaction, while light field can also induce and manipulate the chirality of matter through chiral interaction. Exploring the mechanism of chiral interaction between light and matter will promote our understanding of the origin of chirality and life. In addition, it will help us clarify the mechanism of manipulating chiral functional materials as well as chiral optical properties.

By starting from the manipulation principles of chiral light fields, this thesis studies on the generation of chiral structured light fields through acousto-optic interactions and polarization controls.

Specifically, we obtain a vortex switching between different topological charges of "+1" and "-1" with a switching speed up to 4.3 kHz. Benefit from the time-stretched dispersive Fourier transform technique, the switching dynamics in a mode-locked fiber laser is observed.

On the other hand, by investigating the polarization dependence, we reveal that the internal mechanism of femtosecond laser induced chirality is indeed an optical chirality (extrinsic chirality), which is due to a joint effect of form birefringence and stress induced birefringence with non-parallel and non-perpendicular neutral axes. By taking profit from the proposed two-layers model, strong circular optical properties have been realized in silica glasses by a multilayer strategy and a chiral Bessel beam with linear polarization orientation rotating along the beam propagation. In addition, fiber nanograting arrays are investigated to form in-line polarizers and potentially chiral optical devices.

Since chirality is an important physical and chemical property, the study on the manipulation of chiral light field and its interaction with materials plays an important role in the fields of particle sorting, high-capacity optical communication, photonic chips, super-resolution imaging and ultrafast laser micro-nano processing.

# CONTENU

## ACKNOWLEDGMENT

*"Life is a box of chocolates; you never know what you are gonna get"*. We are ordinary like sand in a desert, someone owns oceans of stars in his/her eyes. Just like a simple volume in the glass, one day the femtosecond light brightens everything in a flash and the evolution lasts forever. All kinds of persistence, come from this little spark. Despite scientific research is never easy, we enjoy exploring the unknown.

On my way to pursue PhD degrees, I was so lucky to meet a lot of kind people, who make me strong enough to fight my way through. The most important people are my two supervisors, Prof. Matthieu Lancry and Prof. Xianglong Zeng. Prof. Xianglong Zeng, as the first guide of my scientific career, provides a wonderful environment for my beginning. The first step is always the hardest. Because of your thoughtful protection, I can learn to move forward smoothly. Your rigorous attitude and flexible thinking also inspired me a lot. Prof. Matthieu Lancry, as my supervisor in France, has opened a new world to me. Your passion for both life and research infects me so much, and teaches me a new way of research, indeed with efficiency and joys. You are really a best friend with expert knowledge and wonderful thinking and help me in all matters whether important or trivial. I would like to give my huge appreciation to you two since your friendly help makes my journey without a hitch!

Along the way, I have also met friendly colleagues who help me a lot with both research and daily life. Prof. Bertrand Poumellec, the big father of our MAP team, has inspired me with his vast amount of knowledge. Prof. Tingyun Wang, the leader of SFOAN, has provided a wonderful condition for us to carry out our research. Prof. François Courvoisier, the expert in Bessel beams, has taught me a lot of knowledge. Prof. Ye Dai always considers everything about me and helps me with all efforts. In my heart, you are already my third supervisor. Enrique Garcia-Caurel, who helps me in Mueller experiments, has infected me a lot with his optimistic smile. Dr. Fan Shi, teaches me in experiment operations according to his experience.

I would never forget our interesting time. Qiong Xie, one of my best friends with strong determination and hardworking. It is your support and help that save me through the tough times and make the journey less lonely. Ruyue Que, who has an endless capacity of conversation with me, provides a deep friendship to me and makes me stronger. Yitao Wang, a cool guy with independent thinking and his own lifestyle, has provided kind helps and accompany with me. And Maxime, Julien, Jing Tian, Jun Zou, Jing Kong, Elisa, Benjamin, Nadezhda, Imane, Timothée, Ismail, Selma, Chaoyan Yin, Yi Jiang, Ning Chen, Yifei Sun, Dayi Liu, Shanyu Tang, Tianyue Wei, Xiaodan Yu, Bocheng Chen, Chanjuan Zhang, Liangjian Hu, etc., thanks for your kind helps during my life abroad.

I would like to thank the colleagues in China as well including teachers: Fufei Pang, Xiaobei Zhang, Chengbo Mou, Jianxiang Wen, Chunhua Wang, Yunqi Liu, Hairun Guo, Zhenyi Chen, Liang Zhang, Hemin Wei, Yana Shang, Na Chen, Ziwen Zhao, Xiaolan Sun, Nian Fang, Qiang Guo, Yi Huang, Yanhua Dong, Yan Na etc. and students: Xuekun Bai, Shaofei Wang, Yunhe Zhao, Yang He, Feng Wang, Teng Wang, Ao Yang, Jinqiu Zheng, Yiping Huang, Ke Liu, Linghao Meng, Linping Teng, Longkun Zhang, Jiangtao Xu, Gongyang Li, Ming Jia, etc.

I am also grateful for the support from Chinese Scholarship Council, University Paris-Saclay and Shanghai University.

Furthermore, I would give my sincere thanks to my parents due to their unconditional love and support. I am growing to be a person who others could rely on, but I know I can always be a child under your protection.

Finally, I would like to say something to myself:

*To go beyond light,*

*Until summer coming back.*

*To go being real,*

*With time flowing to the end.*

*Every child cries for a yard,*

*Every adult trapped in a doubt.*

*Flower, lover.*

*Remember, member.*

*To seek what behind,*

*To stop for a stand.*

*If joy holds a counter,*

*Only love tells forever.*

No matter how the future will be, these years in PhD study construct a beautiful painting and become a precious treasure in my life. Stay passionate and go for seeking the stars!

Thanks all and may my work bring some values to the world!

Jiafeng LU

Shanghai, China

18 July 2023

# GENERAL INTRODUCTION

What is the limitation existing in mastering the advanced functional light-matter interactions by laser manufacturing? It lies on the high-dimensional manipulation of spatial-temporal properties of light. Time domain has been advanced from continuous wave to ultrafast duration, however, one of the current challenges now emerges to the "vectorial" control of ultrafast light.

"*Music is the arithmetic of sounds as optics is the geometry of light*," the famous saying from a famous French musician, Achilles-Claude Debussy describes the intense connection between the physical fundamentals of acoustics and optics [1]. At that time, optics was mainly deemed as geometric optics, however, wave optics soon appeared to be another essential part of optics, which is more fundamentally analogue to acoustic waves for music arts. Music, that is played by an instrument, is a temporal train of acoustic signals similar to optical pulsed beams. The composers use staves to write/spread their music, which is a kind of employment of frequency domain similar to Fourier analysis in optics. Furthermore, a fully complex ancient classical music requires the grand ensemble by utilizing spatially distributed instruments. Parallelly, modern optics has moved the research community into new degree of light manipulation, i.e., spatiotemporal sculpture of light. This novel prospect provides new possibilities in light manufacturing since it innovates the fabrication style and enriches the light-matter interaction fundamentals.

Early light manufacturing stood on the excimer lasers operated at ultraviolet (UV) spectral range for light lithography in 1980s [2]. Subsequently, continuous wave (CW) lasers (or nanosecond lasers) appeared tremendous attentions from chemistry because photosensitivity was a controllable function of not only the chemical composition of the material (e.g., glass) but also the surrounding physicochemical environment it experienced (memorial thermal history and physicochemical conditions). By means of laser irradiation, the subsequently induced physicochemical properties of the

materials rely tightly with the mechanism of photochemical dynamics. However, the utilized CW lasers and nanosecond lasers only allow linear energy absorption or low-efficient two-photon nonlinear absorption. Although it is somewhat intense and sufficient for simple structural modifications inside materials, it in turn restricts the strategy only in point defects, as an initial level to deposit photon energy into the glass network.

The breakthrough of mode-locking, i.e., fixing the temporal phase of longitudinal optical modes in the laser oscillation cavity emerged to be disruptive in the laser industry and directly transformed light manufacturing technology. Subsequently, ultrafast pulsed laser was perceived as a potential tool for functionalizing materials via photosensitivity. Shorter light pulses brought high-power density up to the order of $10^{9}$ W/cm$^{2}$ (picosecond laser) or extremely high-power density up to the order of $10^{12\text{-}14}$ W/cm$^{2}$ (femtosecond laser) after focusing, which leaded the laser manufacturing science into nonlinear optics. In fact, femtosecond laser provides the possibility of delivering optical energy precisely into each specific volume with electrons excitation across the bandgap of the glass material. This means the energy deposition has transferred from linear absorption or two-photon absorption to multiphoton absorptions (typically six-photon ionization by 800 nm femtosecond laser irradiation or eight-photon ionization by 1030 nm femtosecond laser irradiation). These innovative nonlinear excitations allow complex photoinduced structural modifications and thus the caused physicochemical properties. Various material modifications are catalogued into physicochemical reactions: intrinsic material ordering enabled by fictive temperature change; phase change such as phase separation and re-crystallization; chemical migration. This endows permanent changes of physical properties to the materials such as second-order nonlinear optical properties (electro-optical effect and frequency doubling), dielectric tensors, which bring novel strategies in precise material processing in 3D degree of freedom of localized “voxels” at a cubic micrometric scale.

Due to the new effects and the unique ability of 3D micro-nano structuring of linear or nonlinear physicochemical properties inside transparent materials, femtosecond laser direct writing (FLDW)

emerges to be a low-cost and super precise tool for optical devices fabrication. In general case, the FLDW can be highly controlled by a set of laser parameters including light wave vector $\vec{k}(r,t)$, electric field $\vec{E}(r,t)$ and intensity profile $\vec{I}(r,t)$. To control the light by a spatial prospect, structured light allows on-demand engineering of light parameters, encountered in transformation optics [3]. For instance, conventional structuring of 2D control unlocks functionalities such as Laguerre-Gaussian (LG) beams that carry orbital angular momentum (OAM) [4], Bessel beams that possess non-diffracting nature over long distances [5]. Although still emerging, 3D controls, such as z-dependent polarization shaping, topological charge management [6,7] or arbitrary trajectory design in space [8], receive considerable interest. Recent advances in spatial-temporal control have opened a new exciting prospect of 4D structured light, such as "optical cyclons" where the wave packet possesses a transverse OAM, that is, a spiral phase in *x*-*t* plane [9]. The concepts above have not (or very initially) been implemented in fs-laser writing configuration, despite the spatial manipulation of light is essential in FLDW.

In this context, temporal control of lasers has innovated the light-matter interaction from linear effects to nonlinear mechanisms. From now on, spatial manipulation of the ultrafast lasers is expected to become a new standpoint of enriching the mechanism of multi-dimensional interactions between ultrashort light and materials. One objective of this PhD thesis is to develop the space variant control of ultrashort lasers and the subsequent material transformations through it.

Understanding the inner fundamentals of interaction between matter and spatially manipulated femtosecond laser pulses will definitely pave the way for advanced physics research and industrial potential evaluation. Structures make the things topologically different and so do the manners of light-matter interaction. Some of the mechanisms are quite new and unveiled. In general, the underlying principles of normal femtosecond laser pulses interacted with materials lie on the core of electrons plasma behavior. At first, the electrons are excited due to the multiphoton ionization effect that transitioned through

the gap of the transparent insulator after the irradiation of the femtosecond laser pulses. The plasma emerges and coexist with the solid at a fraction of picosecond. Here, the light and material itself play important roles in structural organization of the plasma density. When the pulse withdraws, all the electrons are trapped in the solid and thus the structure of the plasma density is "memorized" to be an original source for the subsequent pulse. In addition, the solid remains below the vaporization threshold and still non-destroyed. Instead, it is restructured by the laser-induced force field. Here, the optical field of the laser pulse is quite essential since it strongly interact with the material and co-determine each state of the plasma density distribution and its evolution. Undoubtedly, the force field is highly determined by the laser parameter of the femtosecond laser pulses including their intensity, polarization, phase, and likely topological singularity. This is a new physics. But it is also a new chemistry since it is evolved with highly excited states, which exhibits large effects of off equilibrium at many prospects. We can therefore imagine, in a simple case, normal interaction of matter with an unstructured femtosecond laser is a punch that can make a simple effect on the material. However, the highly manipulated femtosecond laser becomes a hand with fingers which is more accurate and creative. It is therefore necessary to innovate from the state-of-the-art of FLDW that only stay in simple patterning to new precise and novel creation. Their control leads to the new era of a science of material modification via light, and it is also the key objective that this PhD thesis wants to achieve. In particular, three discoveries construct the basis of this PhD thesis.

The first milestone is from our colleagues namely P. Kazansky and Y. Shimotsuma at Southampton University and Kyoto University that they discovered, for the first time, the self-organized nanogratings in $SiO_2$ glass [10]. In fact, this was the smallest structure ever imprinted by light, i.e., 200-400 nm periodicity with 20-30 nm thin fringes. Simultaneously, they proposed that the created nanogratings are likely originated from the modulation of chemical composition, i.e., the oxygen element restructuring. This would be interpreted as the stationary density waves in the plasma induced by the coupling of irradiated light waves and the bulk plasma waves. In 2011, our group

reported that the nanogratings are consist of nanoporous layers that mainly caused by oxygen decomposition [11,12]: $SiO_2 = SiO_{2(1-x)} + x \cdot O_2$. It is likely caused by a tensile stress assisted nanocavitation mechanism [13]. The nanogratings are also called Type II structures, which are different from Type I (isotropic average index variation) and Type III (micro/nano voids caused by localized micro-explosions), due to their outstanding anisotropic subwavelength structures yielding strong birefringence response (up to $-10^{-2}$), anisotropic light scattering, polarized luminescence, and extraordinary high thermal stability (stable for few 10's hours at 1000 ℃). These experimental observations raised a lot of open questions that should be addressed to figure out the formation mechanism and future potential applications of nanogratings.

The second breakthrough is our recent progress that a photoinduced chirality can be created in an achiral material (center-symmetric glasses) by an achiral femtosecond laser beam (being linearly polarized and with normal incidence, neglecting tilt effects) [14]. This phenomenon asks an important question that what is the origin of "parity violation" created by femtosecond laser irradiation? The experimental proof of obtained circular di-attenuation and how it was obtained remain thoroughly debated as an interesting topic. At first, the symmetry breaking was assumed to originate from a volume torque caused by the combined action of a stress field and a direct current. It is affected by the pulse front tilt, the focusing conditions and importantly the laser polarization. Although the quenched glass network records evidence of some parts of the molecular activities during the ultrashort light-matter interaction, there is still not enough information to support that the observed chirality and the caused circular optical properties originate from a photon-induced molecular optical activity just like sucrose or α-quartz with their chiral lattice arrangement i.e., a so-called intrinsic chirality.

Another pioneered work was from B. Y. Kim at KAIST that discovered the acousto-optic interaction for converting the light modes propagating in fibers between core modes and cladding modes [15]. The acoustic waves can propagate along the fiber to form a travelling grating with periodic modulations of refractive index according to the

acoustic vibration modes. This is a kind of long period fiber gratings, but the induced fiber grating is dynamically controlled by the acoustic waves. Let us recall that the fiber remains non-destroyed in the acousto-optic interaction region, which means that as soon as the acoustic wave is gone, the fiber in turn goes back to the original state without any structural change. Whereas a traditional long period fiber grating is fixed by applying permanent index change on the fiber. Thus, acousto-optic interaction allows a dynamic modulation of different periodicity of the induced fiber gratings or simply switching on/off them by manually or automatically altering the acoustic signal. The manipulation of the mode conversion through an acousto-optic fiber grating lies on the phase matching condition from the photon-phonon transfer. From a quantum mechanical view, the photon-phonon scattering consists of the energy and momentum conservation, which leads to the light scattering and carries a frequency shift from the acoustic wave. Such a frequency shift-based acousto-optic interaction plays a crucial role in photon-phonon interaction mechanisms, tunable filters, vector mode converters, interferometers, heterodyne detections, and potentially frequency shift feedback mode-locking fundamentals [16–20]. However, how to master the dynamic control of acousto-optic interaction and thus the light propagation mode manipulation?

The challenge of this PhD thesis is to pave the way of space variant manipulation of the light field in ultrafast lasers and build a new paradigm in understanding the interaction between matter and structured ultrashort lasers, towards controlling all the imprinted anisotropic optical properties including induced chirality (orientation, amplitude and sign). It will unlock a low-cost, sustainable and ideally environment-friendly technology for light manufacturing industries. The experimental observations raise a lot of questions to be addressed, therefore, the heart of this PhD thesis work lies on:

(1) Dynamic switching of fiber scalar modes and vector modes in the ultrafast lasers to unlock and understand the phonon-photon interaction mechanisms and the advanced strategy to dynamically manipulate the light modes in the ultrafast laser cavity. Observation of the transient switching dynamics in the ultrafast laser evolution between different scalar and vector modes to

obtain the effects caused by the mode altering.

(2) Master the photosensitivity during the light-matter interaction to allow us to properly understand the inner physics and chemistry of light induced chirality by employing different designs of the material structuration and also the structured light. Characterize and control the laser-induced transformation in silica-based glasses and optical fibers to underpin the root of the light manufacturing. Unlock the on-demand engineering of targeted linear and circular optical properties through well-designed configurations of both the light field and writing geometry.

At first, the aim of **chapter I** is to provide a general context necessary to fully understand this PhD thesis. We will highlight the ultrafast lasers, which is the core platform throughout the whole thesis. Additionally, silica glasses and optical fibers are introduced as the fundamental materials constituting our samples. Then, it is necessary to introduce the ultrashort laser pulse propagation in glass-based materials. We shall summarize and identify the mechanisms of light-matter interactions and the types of induced permanent structural changes in glass materials. Subsequently, we will focus on the space variant vector fields of the optical light, associated with the generation and manipulation methods. In the last part of this chapter, we will concentrate on the optical chirality and anisotropic optical properties (linear/circular birefringence and dichroism) induced by light.

Then the **chapter II** describes in depth the experimental details and theoretical methods necessary to carry out all of our research works throughout this PhD thesis. At first, we shall introduce the acousto-optic interaction mechanism, which is the predominant way that we used to carry out the dynamic manipulation of scalar modes and vector modes in optical fibers. Subsequently time-stretched dispersive Fourier transformation technique is described, which paves the way for visualizing the transient dynamics of ultrafast evolutions in the ultrafast laser oscillators. It will definitely observe the detailed evolution process of dynamic switching among different modes in the ultrafast lasers. Afterwards, we will describe the specific platform of the FLDW systems utilized in this PhD thesis work which are available both in ICMMO at University Paris Saclay in France and in

College of Science at Shanghai University in China. We also post the information of adopted samples in our experiments. Quantitative measurements of birefringence and more generally, anisotropic optical properties are deemed as very outstanding nondestructive ways for characterizing nanogratings. This in turn provides detailed information of different laser writing configurations as well as the induced optical properties. Therefore, we will describe the physical fundamentals of light polarization, theory of Stokes optics and more generally the Mueller formalism. The latter is supposed to be a complete mathematical description to deliver all the polarimetric optical properties of the light modified materials. Thus, we will present the characteristics of the light irradiated samples with different types of structural modifications by crossed polarized microscopy and more precisely, quantitative measurements of retardance enabled by a polarimetric microscope equipped with a "de Sénarmont" compensator. At last, a spectroscopic Mueller polarimeter is introduced specifically because it provides the possibilities to carry out the key physical quantities of femtosecond laser induced structures with sufficient accuracy to produce meaningful conclusions throughout all the experiments designed in this PhD thesis.

The **chapter III** is dedicated to the dynamic switching of vector beams via acousto-optic interactions. The mechanism of acousto-optic interactions along the optical fiber is not fully understood especially in few-mode fibers. Traditional acousto-optic interactions are usually adopted in single-mode fibers to construct a tunable filter that in fact, converts the fiber core mode to the cladding modes, which exponentially elapse during the propagation. New theory in acousto-optic interactions in few-mode fibers allows the mode conversion between fundamental core mode and high-order core modes to obtain the generation and manipulation of high-order scalar modes or even vortex modes. The first part of this chapter is related to a paper published in ***Optics Letters*** in 2018, which proposes a new strategy of dynamic switching between different high-order scalar modes and the related vortex modes with different topological charges. The creative mechanism is to figure out the dual-resonant fundamentals and master this interesting property of

acousto-optic device to unlock the vortex switching via altering the driven frequency of the electric signal. The second part of this chapter follows a published paper in ***IEEE Photonics Journal*** in 2020, which corresponds to a work of agile mode manipulations in high-power lasers. Traditional mode converters such as long-period fiber gratings are fabricated by laser written periodic refractive index modulation, which are not stable in high temperature environments. However, acousto-optic interaction is a predominant approach that converts the phonons' energy and momentum to the photons travelling inside the fiber, which relates low connections of thermal effects of photons and shows a significant compatibility in high-power lasers.

**Chapter IV** is dedicated to the investigation of switching dynamics enabled inside an ultrafast laser cavity through time-stretched dispersive Fourier transformation technique, which is published in ***Photonics Research*** in 2020. Acousto-optic manipulation, as a positive modulation strategy, can somewhat provide a perturbation into the ultrafast laser to break the stable mode-locking state and then reconstruct another mode-locking state at another spatial mode. The behaviors of the lasing mode, pulse decomposition, separation and re-formation are quite interesting, while traditional mode-locking dynamics only focuses on one single process of build-up or collapse phenomena. Additionally, the vortex mode switching between different topological charges of OAMs in ultrafast fiber lasers unlocks the functionality of dynamic vortex manipulation applications itself. We can imagine the potentials in optical communications with dynamic coding and decoding in vortex mode division multiplexing and particle manipulation with dynamic requirements. The second part is dedicated to a demonstration of dynamic pulse-width switching between picosecond laser pulses and femtosecond laser pulses via an acousto-optic interaction based dynamic attenuation control in one single laser cavity. Electronic circuit has alternative switches to adjust the electrical current very conveniently, however, current state-of-the-art of optical circuit lacks this kind of simple switches to manipulate the optical path. Acousto-optic interaction owns the unique advantages of external control of the light propagating inside optical fibers, which is a predominant

nondestructive approach to dynamically control the behavior of the light. This method allows the dynamic manipulation between different operation modes (different mode-locking states) without changing any optical device in the laser cavity. Specifically, both narrow-band and broadband reflections are demonstrated in the laser cavity which are controlled by the acousto-optic interaction assisted attenuation adjustment. Besides, the mode-locking dynamics of pulse width switching process is also recorded by time-stretched dispersive Fourier transform technique. This work will tentatively bring new prospects to the nondestructive optical switches and enrich the physical fundamentals of mode-locking dynamics.

**Chapter V** focuses on the femtosecond laser direct writing nanogratings in silica fibers. Silica fibers, as the most widely used media for optical communication, possess cylindrical structures including high refractive index cores and low refractive index claddings that allow restricting the light propagating inside fiber cores with low loss. Embedding nanogratings inside silica fibers paves the way for new advanced functional fiber devices towards simple control of light propagation. This is technologically new, which provides new degree of freedom in fiber design. The first part of this chapter depicts a published paper in ***Nanoscale*** in 2019 about fiber nanogratings induced by femtosecond laser direct writing for in-line polarizers. Nanogratings show good performances about anisotropic dichroism, which can be utilized for selecting the targeted orientation of linearly polarized light by attenuating the other orthogonal one. We creatively imprint several nanogratings around the fiber core to form a polarizing array for manipulating the light propagating in the fiber core through evanescent fields. The results show good broadband polarizing phenomena. This strategy is fundamentally novel because it requires simple fabrication process and very low cost for constructing an in-line polarizer. We can imagine and easily extend this idea to produce other potential in-line devices profit from the prominent anisotropic properties and especially chiral optical properties of fiber nanogratings. The second part of this chapter is related to a paper submitted to ***Applied Surface Science*** in 2023. Since the anisotropic properties of fiber nanogratings are quite essential, the orientation control of the nanogratings appears to the

research community towards more possibilities in fiber nanogratings based functional devices or even new paradigm for lab-in-fiber and lab-on-fiber fields. We thus propose a strategy of synchronous control of laser polarization during the laser writing process to unlock complex designs of fiber nanogratings patterns. Besides, we also demonstrate the chiral optical properties imprinted in the optical fibers, which is potential in constructing in-line linear polarization rotators, in-line isolators and likely in-line circular polarizers.

In **Chapter VI**, we discuss the femtosecond laser direct writing optical chirality in silica glass, associated with both mechanisms and strategies. The first part of this chapter is dedicated to a published paper in ***Light: Science & Applications*** in 2023. Here we creatively investigate the polarization dependences of laser induced form birefringence and stress-related birefringence and tentatively disentangle the contribution of these two origins of birefringence. We therefore reveal the inner physical principle that the femtosecond laser written optical chirality attributes to two contributions, i.e., the form-related birefringence and stress-related birefringence with non-parallel non-perpendicular neutral axes. This, in turn, unlocks the potential of precisely controlling the light induced chirality (sign, amplitude, orientation) and thus the related circular optical properties and optical rotation. The second part of the chapter is related to a published paper in ***Optics Letters*** in 2023, which is a subsequent work according to the first part. As we confirmed that the laser induced optical chirality is attributable to the two linear contributions, which is called an extrinsic chirality, but not an intrinsic chirality that related to chiral molecular arrangements. We can imagine constructing several layers of linear properties to achieve tunable circular ones. Thus, we utilized a multilayer strategy with different slow axis orientations in each layer to build a highly chiral structure for obtaining very strong circular optical properties. This multilayer based chiral waveplates show good performances with at least 5 times improved circular birefringence and 3 times suppressed linear birefringence when compared to a single layer configuration. Finally, the third part of this chapter is summarized in a paper published in ***APL Photonics*** in 2023, which reports a novel work about 3D polarization structuring of a Bessel beam and its application

to imprint chirality in silica. This work is innovative because, the method of generating a polarization evolution along the optical path, namely here in a Bessel beam, for writing chirality in silica is definitely new. Traditional structuring of the femtosecond laser only focuses on the transverse section of the beam, namely cross section. However, this work arises insights on the z axis, i.e., along the optical propagation direction to create a so-called z-variable-polarized Bessel beam shaped by a laser written space variant birefringent waveplate. This demonstrated laser beam possesses a "helical polarization" and can thus imprint "twisted nanogratings" without any scanning. Note that an arbitrary polarization distribution could be achieved by precisely designing the retardance and slow axis distribution of the space variant birefringent waveplate.

The PhD thesis structure is organized and summarized in **Fig. 0-1**.

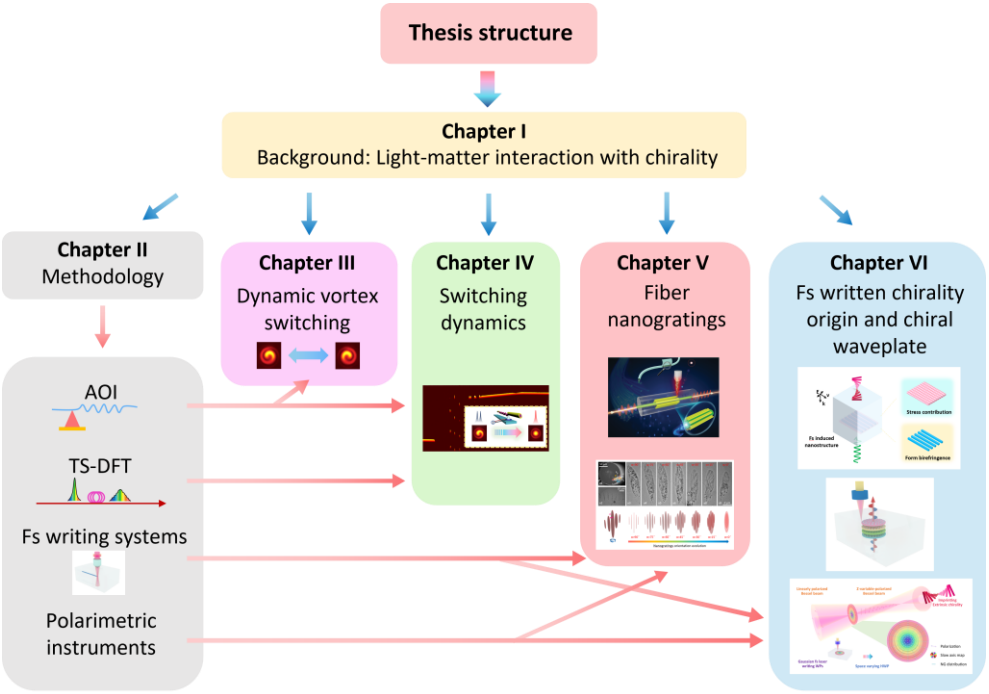


*Fig.0-1 Schematics of the PhD thesis structure. Insets are reproduced from the publications related to this PhD thesis* [21–25].

# Chapter.I STATE-OF-THE-ART OF LIGHT-MATTER INTERACTION WITH CHIRALITY IN ULTRAFAST LASERS

## I.1 INTRODUCTION

This section intends to provide the basic notions for a fully understanding of this PhD thesis. First, we will introduce the basic principles of ultrafast lasers. Then, the main aspects of silica glasses and optical fibers are described. Subsequently, ultrafast light-matter interactions with glass materials will be introduced. The associated permanent modifications by ultrafast lasers are summarized, especially for the nanograting structure since it is the main topic in this PhD thesis.

Finally, the last part is dedicated to the introduction of chirality. This section contains the basic properties of chirality and the chirality in lights. The states-of-the-art of manipulation of chiral optical field as well as light producing chirality in matters are summarized.

## I.2 GENERAL INTRODUCTION OF ULTRAFAST LASERS

### I.2.1 Laser principles

A laser refers to light amplification by stimulated emission of radiation, which is firstly mentioned by G. Gould in 1957. Jokily, it was deemed as “a solution looking for a problem”. But in fact, it has revolutionized the development of civilization and redefined the light science.

Laser is praised as “the fastest knife", "the most accurate ruler" and "the brightest light”. It possesses a lot of fantastic properties such as high coherence, high monochromaticity, high degree of collimation, wide tuning wavelength range, and small spot size, which in turn lead to a huge number of applications ranging from nonlinear optics, material processing, optical communication, medical surgery, particle trapping, optical displays and beyond.

Einstein proposed the stimulated emission principles forming the

basic theory of laser. Stimulated emission is a process by which an incident photon with certain energy (i.e., $h\nu = E_1 - E_0$), can thus stimulate an excited electron (i.e., at $E_1$ state) to a lower state (i.e., at $E_0$ state) and create a new photon, as depicted in **Fig. 1-1(a)**. Different from spontaneous emission, the new created photon by stimulated emission will have the same performance as the incident photon, i.e., same frequency, direction, phase, and polarization. Specifically, a laser consists of at least three key components, namely a pump for population inversion, a laser cavity for light oscillation and a gain media for ensuring the energy accumulation during the oscillation process, as shown in **Fig. 1-1(b)**.

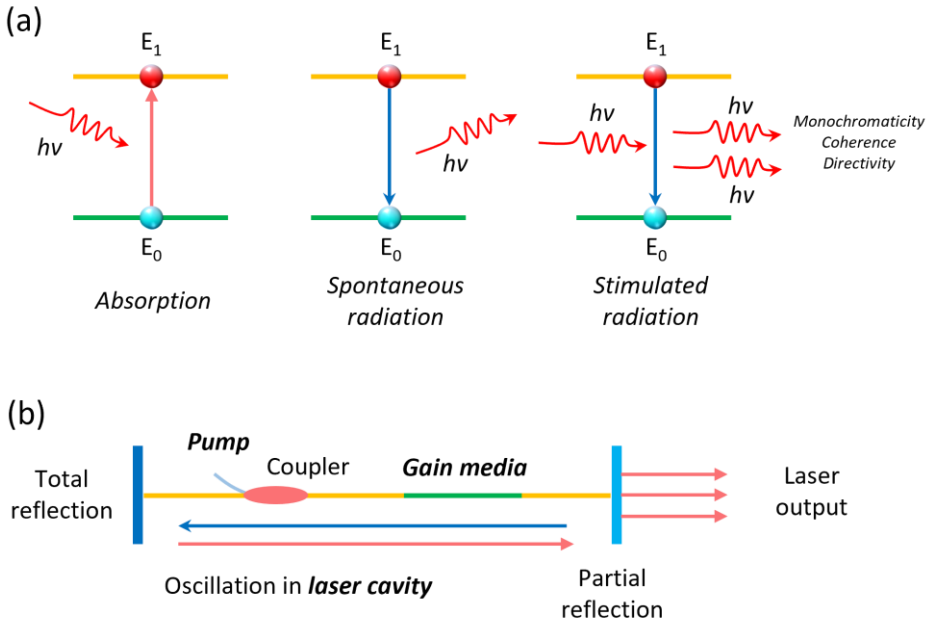


*Fig.1-1 Schematics of stimulated emission and laser structures. (a) Principles of absorption, spontaneous radiation and stimulated radiation. $E_0$: ground state; $E_0$: excited state; h: Planck constant; v: frequency of the photon; here, $h\nu = E_1 - E_0$. (b) Schematics of a basic laser structure with three key components: pump, gain media and laser cavity.*

Pump source is an external energy supply to produce the population inversion e.g., an electric current, a laser diode or even a chemical reaction. Laser cavity, also known as an optical resonator, in general consists of two parallel mirrors. One is total reflection while another exhibits partial reflection to output some laser lights. Besides, in fiber

lasers there are also ring cavity for light circulating in the cavity that can generate laser light and output from a coupler. Gain medium is dedicated to an active medium to amplifying the oscillating light. Nd-doped glass is usually used as a gain medium in solid lasers while Er/Yb-doped fibers are commonly used gain media in fiber lasers.

### I.2.2 Ultrafast lasers

Since T. H. Maiman reported the first laser, namely a ruby crystal pumped by a Xenon flash lamp, in 1960, laser science and industry develop very fast, especially in ultrafast lasers, as depicted in **Fig. 1-2**. Compared to continuous wave (CW) lasers, ultrafast lasers deliver optical pulses at picosecond (ps, $10^{-12}$ s) and femtosecond (fs, $10^{-15}$ s) scales, which own unique features such as ultrashort durations, ultrahigh peak powers that lead to various novel nonlinear effects.

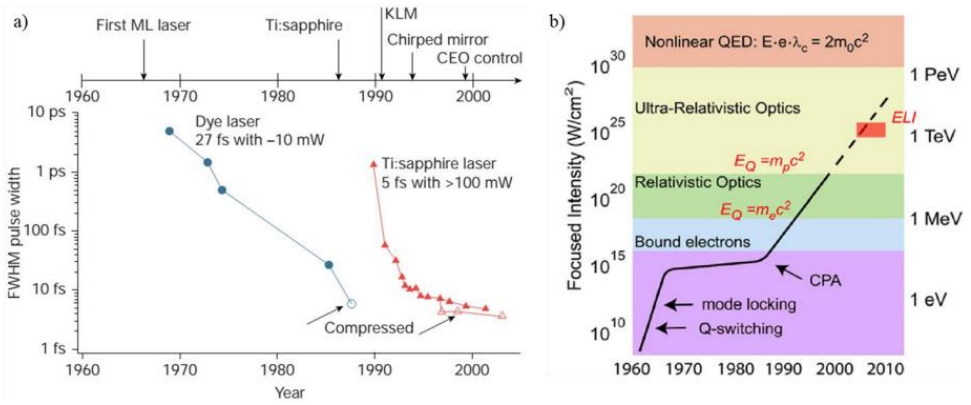


*Fig. 1-2 Development of (a) ultra-short pulse generation and (b) laser intensity of the laser industry. CPA: chirped pulse amplification, ELI: extreme light infrastructure (cited from [26,27])*

In 1970s and 1980s, sub-ps laser pulses are demonstrated in passively mode-locked dye lasers. Subsequently, a solid-state laser material, namely Ti: Sapphire is discovered to be a possible material for supporting broadband gain spectra to achieve narrow fs duration pulses. The development of the laser pulse generation is depicted in **Fig. 1-2(a)**. Intensity is a key parameter for a laser because ultrahigh peak power can allow "adiabatic ablation", i.e., to process the material with nonlinear effects instead of thermal effects. This technique contributes to higher quality/resolution than any CW or nanosecond

laser can achieve. There are two milestones that breakthrough the laser intensity improvement: one is Q-switching and mode locking mechanism to create ultrashort laser pulses and the other is chirped pulse amplification (CPA) to enable the amplification of ultrashort pulses (even few fs) to very high energy levels (>$10^{20}$ W/$cm^2$) [28], as shown in **Fig. 1-2(b)**.

### I.2.3 Mode-locking mechanisms

Mode-locking refers to the locking of the phase relationship between multiple longitudinal modes in the laser cavity. The locking of this phase relationship makes the laser output periodically stable with time, and the round-trip time correlates to the light circulating time of one cycle in the resonator. If enough longitudinal modes are locked at the same time, the laser spectrum will be wideband and thus the pulse could be an ultrashort one.

The passive mode-locking technique is one of the main ways to realize ultrashort pulse generations. Compared with the active mode-locking method, the saturated absorber can generate shorter pulses due to its ultrashort recovery time (can achieve fs level). Generally, in a passive mode-locking resonator there exists a saturable absorber mode-locking device that absorbs light energy by a nonlinear relationship with the light intensity. Specifically, its function is to rarely absorb the middle part of the pulse (namely the high-intensity part of the pulse). However, the low-intensity light on the two wings of the pulse is strongly absorbed and thus attenuated. As a result, the pulse is continuously narrowed, and finally a short pulse of stable oscillation is formed in the cavity. To some extent, passive mode-locking can be understood as self-driven mode-locking, and the phase disorder of each longitudinal mode in the initial connection segment cannot form an effective coherent superposition. At a certain moment, the intensity of one of the pulses in the cavity is strong enough to reduce the loss of the mode-locking device in the cavity, which supports the continuous cyclic amplification in the cavity. Finally, stable pulse trains are established from the chaotic noise. The main passive mode-locking methods are nonlinear polarization rotation (NPR) mode-locking [29,30], nonlinear amplifying loop mirror (NALM) mode-locking [31–34], semiconductor

saturable absorber mirror (SESAM) mode-locking [35,36] and novel nanomaterial saturable absorber mode-locking [37–40]. Here we mainly introduce the principles and typical resonator structures based on SESAM and NPR mode-locking techniques related to this PhD thesis work.

#### *I.2.3.1 SESAM mode-locking*

A saturable absorber is a general term for a type of device that achieves laser mode-locking by nonlinear absorption, namely absorbing low-intensity part of light and almost passing the high-intensity part of light. In fact, it performs that as the incident light intensity gradually increases, the transmittance of the saturable absorber will increase and eventually reach the saturation threshold. This allows strong light to pass through and weak light to be attenuated, which leads to the ultimate pulse narrowing. Although the mode locking schemes based on new materials attract more interests, i.e., various material based saturable absorbers, such as graphene, carbon nanotubes, topological insulator, which have been successively confirmed in the mode locking lasers, semiconductor saturable absorbers are still the most widely used mode locking devices in commercial ultrashort lasers due to their reliable stability. In practical use, semiconductor saturable absorbers are encapsulated as cavity mirrors, i.e., a SESAM [41], which is composed of semiconductor wafers such as gallium arsenide (GaAs) and distributed Bragg reflectors (DBRs) grown on the wafers, as well as a large number of quantum wells layers covering on the Bragg reflectors. DBR plays the reflective role while multi-layer quantum well structures provide an amplitude modulation in intensity dependent absorption. Besides, indium gallium arsenide (InGaAs) quantum wells are usually used as saturable absorber materials. When light is incident on a semiconductor material, electrons in the valence band are excited to the conduction band, creating electron hole pairs. As the number of photons continues to increase, more electrons are excited, but only a limited number of electron hole pairs can be generated, resulting in the depletion of the ground state electrons and thus the saturation of photons. After a period of in-band thermal equilibrium and inter-band relaxation, photons can be absorbed again. In-band thermal equilibrium and inter-band

relaxation time possess a great impact on the mode locking state. The shorter the recovery time is, the easier it is to obtain sub-picosecond pulses. The longer the recovery time is, the more conducive to the self-starting of the mode locking state in the lasers [42–44]. The relaxation time of a typical SESAM is 500 fs to 30 ps, while the spontaneous emission time of a semiconductor material is about 1 ns. Therefore, low temperature molecular-beam epitaxy technique and ion implantation technique are usually used to introduce lattice defects in the absorption layer to achieve fast relaxation of carriers.

In the case of using SESAM to achieve mode-locking, a large modulation depth is conducive to achieve stable mode-locking states. In general, SESAMs with resonance modes have a higher modulation depth but a narrower response bandwidth when compared to non-resonant SESAMs. Mode-locked lasers enabled by SESAMs are generally linear cavity structures, as shown in **Fig. 1-3**. One end of the resonator is a broadband mirror composed of SESAM, and the other end is an optic fiber ring mirror. The signal light in the cavity is usually focused onto the SESAM by a set of coupled lenses, and the size of the focused spot can be controlled by adjusting the position of the lens, thus controlling the saturation flux on the SESAM. The optical fiber ring mirror is made of a "2×2" coupler, whose reflection can be adjusted by controlling the beam splitting ratio of the coupler. Based on the above typical structures, mode-locked fiber lasers of various wavelengths have been realized successively. In addition, fiber ring mirrors can also be replaced by fiber Bragg gratings (FBGs) or chirped fiber Bragg gratings (CFBGs) to form narrowband filtering or dispersion compensation. For example, I. A. Litago et al. demonstrated the selection of mode-locking wavelength by using FBG as a mirror, and then applied axial stress to the FBG in the resonator to achieve wavelength tuning ranging from 1558 nm to 1567 nm [45]. H. Wang et al. used a CFBG to provide negative dispersion compensation in the 1-micron band and adjusted the net dispersion value in the cavity to make the laser work with self-similar sub-pulse mechanism, and finally obtained an ultra-short pulse output of 83 fs [46].

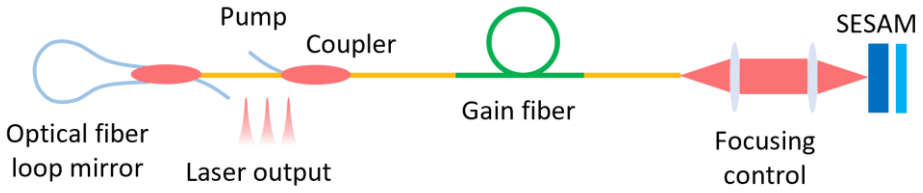


*Fig. 1-3 Schematics of a typical linear cavity of a SESAM based mode locked fiber laser.*

### *I.2.3.2 NPR mode-locking*

NPR mode-locking technology is to use the birefringence effect of optical fiber and polarization related devices to achieve artificial saturable absorption effect and thus the created ultrashort pulses. **Fig. 1-4** shows a typical ring-cavity laser based on NPR mode-locking.

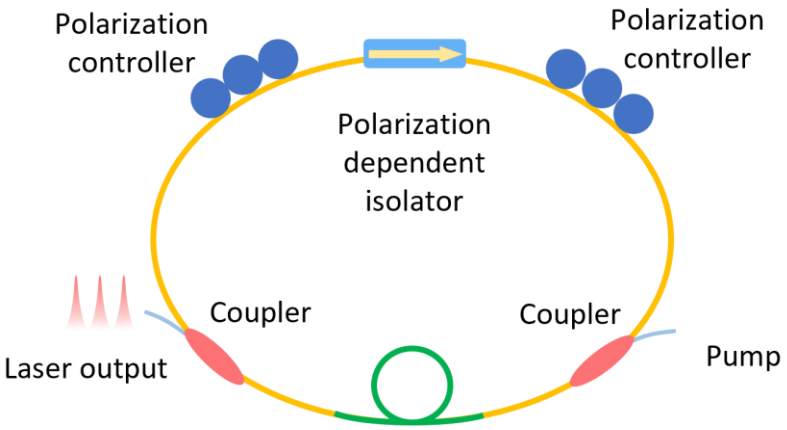


*Fig. 1-4 Schematics of a typical ring cavity of an NPR based mode locked fiber laser.*

A polarization dependent isolator (PDI) and polarization controllers (PCs) in the optical fiber ring cavity form the artificial saturable absorber. The linear polarized light that passes through the PDI is split into two orthogonal directions perpendicular and parallel to the optical axis due to the existence of inherent birefringence of the gain fiber and the ordinary single-mode fiber. The polarized lights with two orthogonal directions are affected by self-phase modulation (SPM), which produces different nonlinear phase shifts and finally makes the polarization rotation of the resultant vector polarization state. When the pulse passes through the PDI again, the saturable

absorption effect of polarization dependent self-amplitude modulation occurs due to the polarization states of the different parts of the pulse. Finally, the saturable absorption is obtained, and ultrashort pulses can be achieved.

### I.2.4 Chirped pulse amplification (CPA)

Direct amplification in ultrafast lasers will destroy the laser components in the cavity due to the ultrahigh energy level. However, CPA was developed to amplify the ultrashort pulses in a smart way by preventing the nonlinear effects from destroying the crystals. This novel amplification strategy contains three steps, i.e., pulse stretching, amplification and pulse compression, as depicted in **Fig. 1-5**. By extending the pulse duration through typically $10^4$-$10^8$ times larger, the pulses can be amplified without approaching the damage threshold of the crystal materials. Thus, the fluence remains the same but the power measured at any one frequency is quite low [47]. Finally, the amplified pulses are compressed back to ultrashort pulses for subsequent uses. G. Mourou and D. Strickland have won the Nobel prize in Physics in 2018 due to CPA.

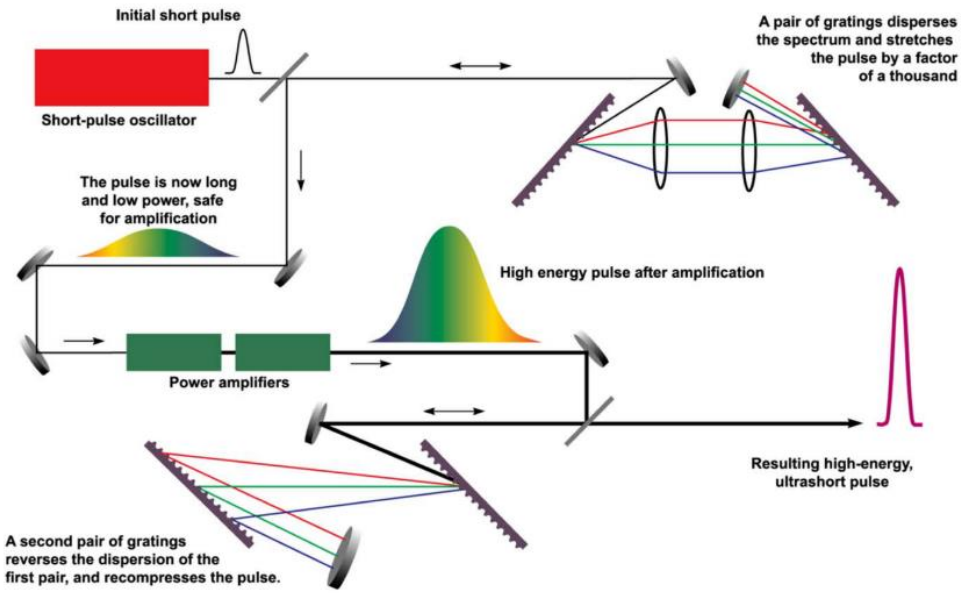


*Fig. 1-5 Schematics of CPA with beam stretching, amplification and compressing system (cited from* [47]*).*

## I.3 SILICA GLASS

### I.3.1 Silica structures

Silica glass, as an extensively studied material, has been discovered to own obvious photosensitivity to UV radiation at the end of 1970s [48]. In 1960s, the effects of electron bombardment on glasses were reported and studied by means of high-energy sources at MeV levels [49]. Subsequently, researchers began to use lower energy level electron beams (KeV scale) to unveil the induced volume changes and optical modifications in 1990s [50,51]. Irrespective of the irradiation types, these modifications and volume changes are deemed as originated from irradiation induced structural changes inside silica glass networks. This is why the structures of silica glass is such important for the light-matter interaction mechanism and we shall introduce it in this section.

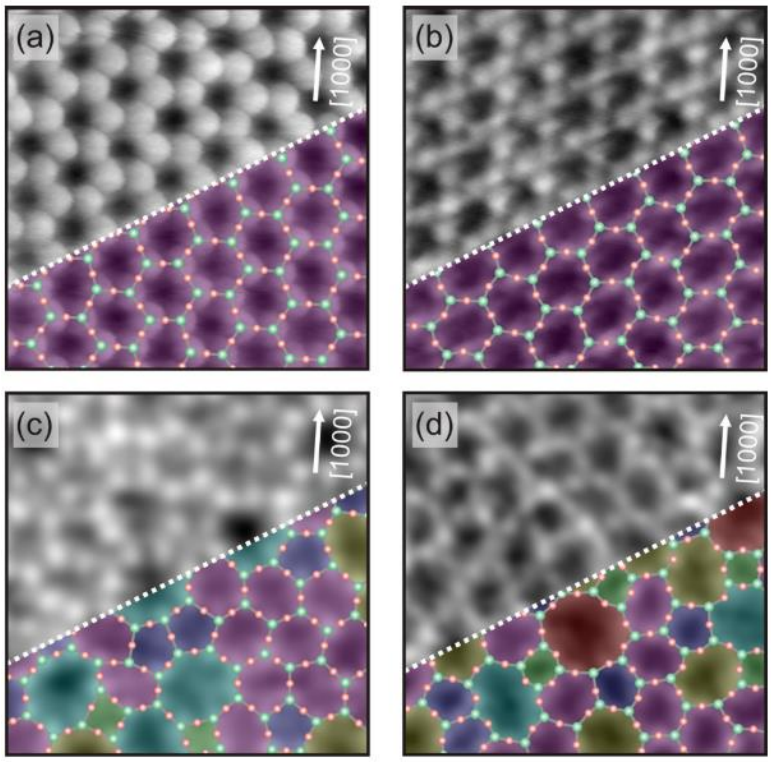


*Fig. 1-6: Scanning tunneling microscopy (STM) images with atomic resolution of silica bilayers: (a) Si atoms and (b) O atoms arrangements of the crystal structures of α-quartz; (c) Si atoms and (d) O atoms arrangements of the disordered $SiO_2$ glass; Cited from* [52].

Most commercial glasses are silicates. In fact, they contain a lot of constituents included in a $SiO_2$ based matrix. Pure silica glass, as the glass with simplest composition owns its difficulty for achieving high purity via technical development. Basically, it exhibits an irregular 3D network consisting of disordered tetrahedral $SiO_4$ units, as depicted in **Fig. 1-6** obtained by atomic resolution scanning tunneling microscopy (STM) of silica bilayers [52]. The silica glass adopted in this PhD thesis are mostly Type III- silica glasses. They are synthetic vitreous silica produced by hydrolysis of $SiCl_4$ with spraying into an oxygen-hydrogen flame. Practically, due to the Cl starting materials, most synthetic pure silica materials are free (<ppb level) from metallic impurities. However, it may contain a high amount of OH (typically, in the order of 1000 ppm for Suprasil CG glasses, Heraeus, Germany).

In fact, various assembling $SiO_4$ tetrahedra in 3D with each other are possible however, the most stable established configuration is approaching the longest Si-Si distance, which is achieved in an assembly by the vertices. Therefore, this mode of assembly can be easily found in all forms of crystalline silica such as quartz, cristobalite, tridymite and coesite. The average angle of the intermediate bond of the Si-O-Si group is 145° [53], which leads to a certain dispersion, corresponding to an Si-Si distance of approximately 3.12 Å. The Si-O distance varies between 1.62 Å and 1.77 Å while the O-O distance varies between 2.50 Å and 2.65 Å. The complete assembly of all the tetrahedra in silica glass can therefore form a three-dimensional glass network constructing a short-range order. However, we shall recall that it exhibits no order at a long distance. This construction of the glass group represents the definition of the disordered or random network from the literatures.

At a short distance, the order is governed by the coordination of silicon, i.e., a silicon atom is surrounded by 4 oxygen atoms, which forms a tetrahedron. Additionally, each oxygen is shared by 2 tetrahedra, from the prospect of $SiO_2$ stoichiometry. Silica glass is a special case of disordered systems due to its medium range order, which corresponds to its molecular connectivity. Specifically, there are always four tetrahedra surround a given tetrahedron however, it has no Euclidean translational symmetry. In fact, the free space in the

structure allows tetrahedra to rotate. In this case, the correlation length (defined as the number of successive ordered tetrahedra) or the degree of polymerization would somewhat change corresponding to the method of preparation, the cooling rate and more generally the thermal history. The cooled glass structure is frozen from a so-called fictive temperature ($T_f$) as described in detail from Ref. [54]. Silica has the same medium-range order as the crystalline form of tridymite and cristobalite. When silica is suffered under high pressures [55], its specific volume will be lower and thus adopt a denser structure. This new configuration approaches that of quartz or coesite.

### I.3.2 Point defects in silica glasses

The structures of a glass can be subjected to a lot of treatments, e.g., high pressure, heating, ionizing or non-ionizing irradiations and their combination. By means of these treatments, point defects can locally be modified. The definition of a defect in the glass is different from that in a crystal. In fact, any exception in translational symmetry is considered as a defect in a crystal. However, in a glass, this symmetry of translation does not exist, and thus this definition cannot apply. Then the notion of default is from the notion of chemical order. Generally, the perfect network of silica glass is a sequence of $SiO_4$ tetrahedra interconnected by common oxygen atoms. Thus, each silicon atom is connected to four oxygen atoms and each oxygen atom must have two Si as nearest neighbors. Any exception in this sequence "≡Si-O-Si≡" can be considered as a defect. Each variant of point defect would have its unique structure and properties (absorption, magnetism, fluorescence, etc...). Therefore, the key point of view to understand and subsequently manipulate the point defect properties of the glass is to clearly know the atomic structure. This can be obtained by a combination of experimental results from spectroscopy and theoretical calculations of quantum chemistry. Electronic Paramagnetic Resonance (EPR) has proved to be the most suitable experimental technique for developing and confirming defect models. Although the EPR is a priori only applicable to paramagnetic defects, the absence of EPR signal representing a diamagnetic defect could be an important support for the models. Thus, rigorously applied, the EPR enables the detections of orbital

composition of the single electron spin functions, together with size, chemical nature, and steric environment of the atoms. Therefore, each defect could have its own EPR signature. If one can somehow figure out the correlation between an optical absorption band and the EPR signal, the inner mechanical origin can thus be studied and therefore a number of absorption bands could be identified. Though started several decades ago, the point defects studies remain many things to be unveiled. For example, the absorption bands associated with some point defects, or the mechanisms of their appearance or disappearance, are still under discussion.

## I.4 OPTICAL FIBERS

Optical fibers, as the mostly used medium in optical communications, have brought revolutionary development to the industry ranging in information science, optical sensing, and medical detection. Due to the ultralow loss in communication band and the constituent material, namely silica glass, optical fibers own unique advantages of low cost and environmental stability.

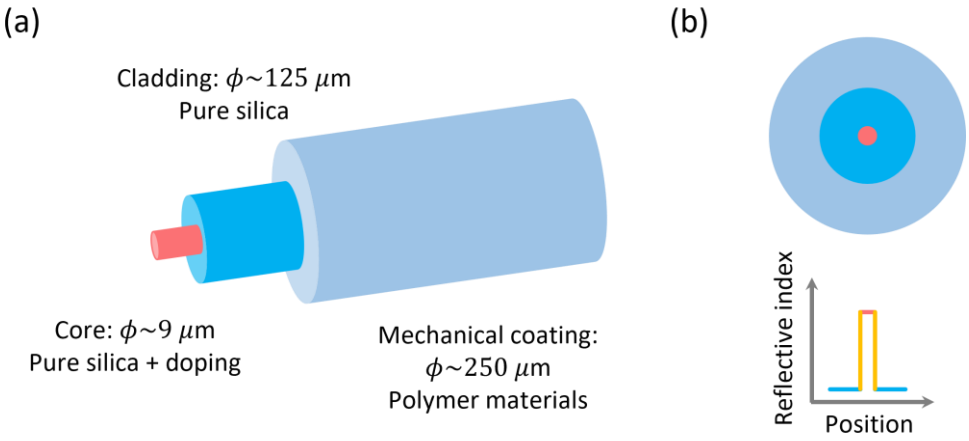


*Fig. 1-7: Schematics of simplified optical fiber structure: (a) fiber cylindrical structure; (b) fiber cross section and its index profile (exemplification of a normal step index fiber).*

In general, an optical fiber is deemed as a long flexible glass wire made of vitreous silica materials, in which light can propagate over long distances (typically several thousand kilometers) with low loss. More rigorously, an optical fiber is, in fact, an optical "waveguide"

with cylindrical geometry and several regions with different refractive indices, for example, fiber core and fiber cladding. This allows to maintain the light restricted inside the fiber core with certain propagation mode for long distance transmission. Specifically, the central region (generally the center of the cylinder), namely fiber core, owns a higher refractive index than the region around it (outer layer of the cylinder, i.e., fiber cladding). Different index profiles can be designed and demonstrated in the fiber fabrication process for different intended applications, such as gradient index profile, step index profile and even more complex designs (e.g., hollow core fibers, photonic crystal fibers and anti-resonant fibers). Simplified fiber structure is depicted in **Fig. 1-7**. Usually, the high refractive index in the fiber core is realized typically by Germanium (Ge) doping.

## I.5 ULTRAFAST LIGHT-MATTER INTERACTIONS IN GLASS MATERIALS

### I.5.1 Ionization and relaxation in intense fields

Ultrafast light-matter interaction exhibits diverse linear and nonlinear effects and contributes to a large number of physicochemical properties endowed in the materials. Light-matter interaction occurring during femtosecond time scale is mainly determined by the effects caused by the intense and ultrafast electromagnetic field, as summarized shortly in **Fig. 1-8**.

The time scale of the interaction principle can be divided into three steps: (1) electron excitation [56]; (2) thermalization; (3) different relaxation mechanisms and permanent modifications. In the process of light-matter interaction, within approximately 10 picoseconds: laser energy is absorbed by electrons and transferred to the network of silica materials (i.e., photon-phonon transfer). Subsequently, the shock wave is generated within few nanoseconds. On the time scale from nanoseconds to microseconds: heat propagates around the focal area. Within a few microseconds: if the rate of heat propagation is low enough to prevent heat accumulation [57,58], the material will recover to ambient temperature. At sufficiently high energy, these processes can also lead to non-thermal ionic motion and cause permanent structural changes, such as inelastic deformation

(densification or expansion, depending on irradiation conditions and material composition), elastic response (stress) in and around the irradiation area [59–63], and the formation of point defects that absorb UV and vacuum ultraviolet (VUV) lights[64].

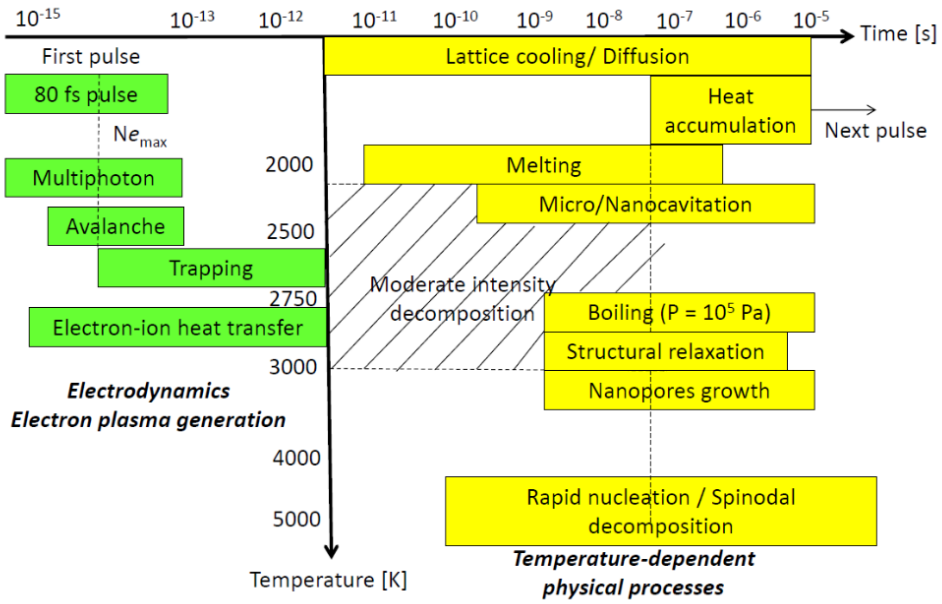


*Fig. 1-8: Schematics of main physical processes involved in the ultrashort laser interaction with silica glass materials (according to temperature dependence). Cited from* [65].

In general, the solids studied in this PhD thesis, i.e., silica materials, are essential dielectric materials, which possess wide bandgaps. In a transparent silica glass, the energy of a single photon (typically, for a Ti-Sa laser is 1.5 eV at 800 nm or 1.2 eV at 1030 nm) is not sufficient for electron excitation from valence band to conduction band. However, the ultrahigh peak power of the focused femtosecond laser pulses is enough to excite nonlinear absorption effects, e.g., multi-photon absorption. In this case, the electrons can absorb the energy of several photons at one time and can be excited from valence band to conduction band. This multi-photon ionization process can only occur at high laser field amplitude. In fact, this phenomenon can be deemed as an "electron heating" since the electrons continue to absorb many photons after they crossed the forbidden band.

The multi-photon absorption relies strongly to the intensity of the

laser pulses:

$$\eta_{MPA} = \sigma_m I^m \qquad \text{(Eq. 1-1)}$$

Here, m refers to the number of absorbed photons, $\sigma_m$ is the absorption coefficient and $I$ stands for the intensity of the laser.

Apart from multi-photon ionization, another possible process could happen in the photoionization process is tunnel ionization. When the electric field of femtosecond laser is strong enough, the coulomb field of valence electrons could be suppressed by the laser electric field. Thus, the valence electrons become free electrons through the tunnelling effect. While the frequency of the laser field is low, the tunnel ionization can dominate the photoionization process. It can be determined by the Keldysh parameter:

$$\gamma_{Kel} = \frac{\omega}{e}\sqrt{\frac{m_e c n_0 \varepsilon_0 E_g}{I}} \qquad \text{(Eq. 1-2)}$$

Where $\omega$ is the laser frequency, $e$ and $m_e$ represent the effective charge and mass of the electron. $n_0$ and $\varepsilon_0$ are the refractive index and permittivity in the vacuum. $c$ is the velocity of light in the vacuum. $E_g$ is the bandgap of the glass.

From our previous work and the collaboration with Stéphane Guizard (LSI, CEA Saclay), the multi-photon absorption is mainly identified to be six-photon absorption in silica glass and five-photon absorption in Germanium doped glass at our experimental conditions with numerical aperture (NA) of 0.5 and $I = 30\ TW/cm^2$. The experimental results show that neither tunnel effect or avalanche ionization is detected for the short pulse duration below 200 fs [56,66]. Recently, it has been proved that it is possible to observe an increase of carrier impact ionization under specific conditions [67]. For a new point of view, the avalanche ionization process that was previously employed to interpret the laser breakdown is now proved to be not dominant in short pulse duration conditions. The importance of this phenomenon is under intense discussion and now is widely accepted according to experimental parameters: pulse duration, illumination as well as the bandgap of the material [68,69].

### I.5.2 Relaxation mechanisms

The process after electronic excitation, which occurs during the excitatory pulse, exhibits that the photo-excited charge carriers "lose equilibrium". Thus, excited charges thermalize with the solid material through different mechanisms according to their kinetic energy. Indeed, the inelastic collisions between electrons of the conduction band and the valence band, or the impact ionization, can occur at attosecond scale as if the energy of the electrons is greater than the forbidden band, depicted as step 1 in **Fig. 1-9**.

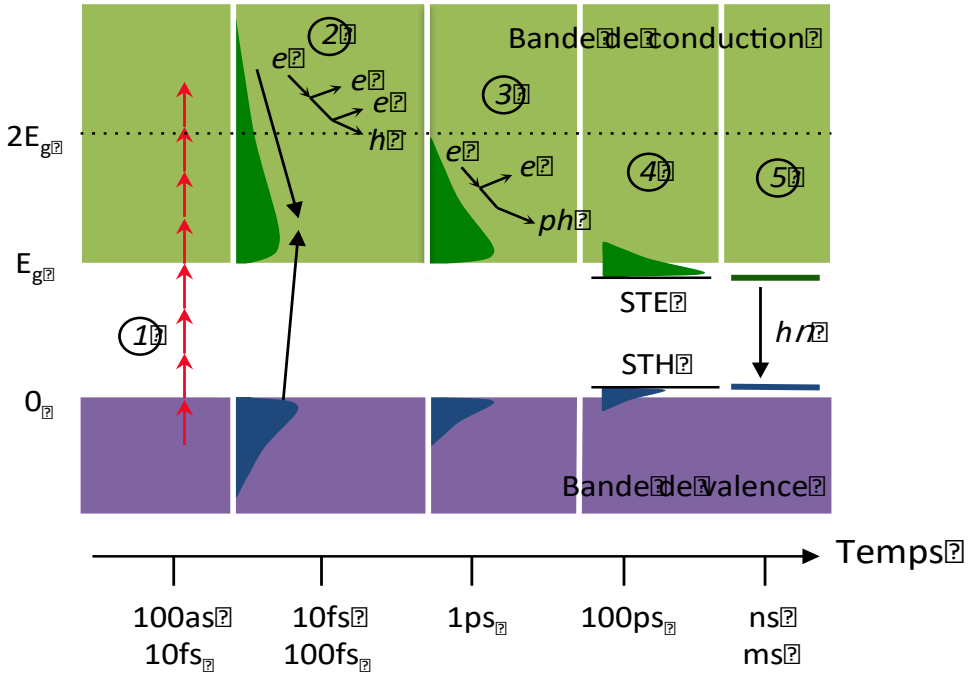


*Fig. 1-9: Diagram showing the different elementary mechanisms involved during and after the interaction between a short pulse and a dielectric sample. 1: electronic excitation: either multiphoton (hv<Eg) or one photon (hv>Eg); 2: electronic relaxation: process of inelastic electron-electron collisions or impact ionization; 3: thermalization via collisions with the network; 4: trapping and location of charges (self-trapped excitons); 5: radiative recombination of excitons. Cited from* [70].

In this case, a significant energy of the electron, at least equal to the forbidden band, will be consumed. Thus, it will leave two electrons of lower energy at the bottom of the conduction band. At step 2 with a time scale from femtosecond to picosecond, the electrons with lower energy could transfer their energy to the lattice mainly through collisions, i.e., by acoustic or optical phonon emission leading to heat

effects. This can lead permanent changes to the solid such as phase transition, photochemistry, etc. In some materials, local polarization and lattice deformation can be induced by the electron-hole or excitons pairs, as depicted in step 3. In fact, this kind of deformation or atomic displacement, strongly depends on the appearance of electronic levels in the forbidden band, which provides the location of the charge carriers, as shown in step 4. It is normally about not only trapped excitons (or self-trapped excitons, STEs), but also self-trapped holes (STHs). In this mechanism, it has a very short lifetime and occurs only for a small percentage of charge carriers. Wide study of STEs has been carried out in all alkali halides [71]. Recently, it has been studied in silica and doped silica glass. Additionally, STEs are deemed to constitute the intermediate step between electronic excitation and point defects, also known as "color centers". Besides, the non-trapped electrons will finally recombine with a hole in the valence band as shown in step 5.

### I.5.3 Material changes induced by fs laser irradiations with different damage thresholds

Structural modifications by fs laser irradiation of glass materials rely strongly on the efficiency of the energy transfer during the light-matter interaction. As mentioned above, due to the ultrashort duration time, the very high peak power of fs pulses makes multi-photon ionization statistically possible and thus leads to the generation of “quasi-free” electrons plasma. The subsequent relaxation mechanisms such as point defects, STEs and network heating contribute to the permanent structural changes in the silica materials, which can be generally identified into three categories: (1) isotropic modifications of refractive index (Type I); (2) anisotropic subwavelength nanogratings with strong birefringence (Type II); (3) nano/micro voids due to micro-explosions (Type III).

The different types of structural modifications own different damage thresholds, which correlates tightly with the laser parameters: laser pulse energy, repetition rate, pulse duration, NA, scanning velocity, etc. It is summarized into four regimes with three damage thresholds in silica glass with fs laser irradiation, as we reviewed these laser parameters as depicted in **Fig. 1-10** [72]:

Regime I (no damage): Below the first threshold of T1 (e.g., 0.085±0.015 μJ/pulse in pure silica, 800 nm, 160 fs, 0.5 NA, 100 kHz, 100 μm/s), there will be an increase of refractive index according to third-order kinetics. The process contains a two-photon absorption when the absorption band exists at the relevant final energy. However, the index modification will decay within a few seconds. That is, under these writing conditions, permanent structural modifications are not enabled.

Regime II (isotropic index change): Between the thresholds of T1 and T2, there exists a regime related to a permanent refractive index change, which is nearly isotropic. The thermal stability of this modification is moderately higher than UV-induced structural changes. To date, a maximum value of positive index change of 3-6×$10^{-3}$ induced in fused silica material (negative in many other silicate glasses) can be obtained [73]. This result is quite large when compared to index change induced by UV-laser induced structures which is restricted to only 3×$10^{-4}$ as reported by using 157 nm or 193 nm excimer lasers [74].

Regime III (anisotropic index change): Above threshold T2 (e.g., 0.31±0.05 μJ/pulse in pure silica, 800 nm, 160 fs, 0.5 NA, 100 kHz), the case is quite different. The refractive index change can be negative as large as a few -$10^{-2}$. Furthermore, the index modification exhibits strong thermal stability that can survive several hours under 1000 ℃ [75,76]. Another striking feature of this index change is anisotropy [77,78]. This property is fundamentally interesting because the orientation can be manipulated by the laser polarization [10]. This is attributed to the self-organization of nanogratings consisting of nanoporous silica [12].

Regime IV (Voids): When the damage is above threshold T3 (e.g., 4 μJ/pulse in pure silica, 800 nm, 160 fs, 0.5 NA, 100 kHz), voids can be observed, which is mainly attributed to the micro-explosion [76,79].

These regimes can be easily distinguished by manipulating the laser writing parameters with shorter pulse duration (<200 fs). But for longer pulse durations, the regime II narrows a lot, and it is quite difficult to obtain in multi-pulses conditions.

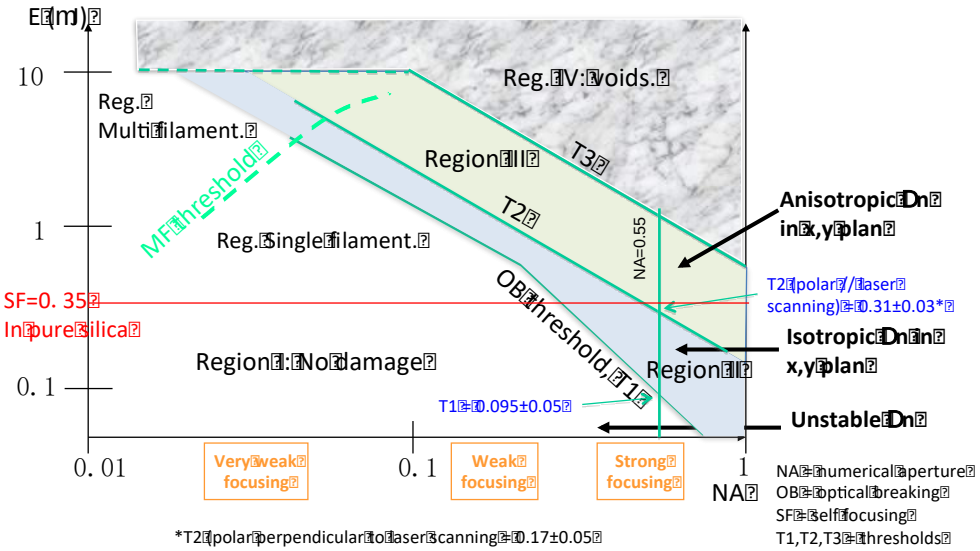


*Fig. 1-10: Summary of different modifications induced by fs laser irradiations according to the laser energy and focusing condition. MF: multi-filamentation; AF: self-focusing; T1, T2 and T3: thresholds of the different types of structural modifications. Laser writing parameters: 800 nm; 250 fs; 100 kHz; NA 0.03-1, 100 μm/ s; parallel configuration; $SiO_2$. Cited from [72].*

### *I.5.3.1 Type I: Isotropic modifications of refractive index*

For diffraction-limited focusing and weak self-focusing effect, the energy threshold to achieve the breakdown intensity is strongly related to the NA [69]:

$$E_{th} = \frac{I_{th}\tau\lambda^2}{\pi(NA)^2 + \frac{I_{th}\lambda^2}{P_{cr}}} \qquad \text{(Eq. 1-3)}$$

Here, $I_{th}$ is the intensity. $\tau$ and $\lambda$ refer to the pulse duration and wavelength, respectively. $P_{cr} = 3.77\lambda^2/8\pi n_0 n_2$ is the critical power, in which $n_0$ is the linear refractive index and $n_2$ is the nonlinear refractive index due to the Kerr effect (the refractive index is given by $n = n_0 + n_2 I$).

With a low energy laser irradiation, a positive refractive index change of from $10^{-4}$ to $5\times10^{-3}$ can be obtained, which can be mainly interpreted to a permanent densification subsequent to a rapid cooling of the ultra-hot focal volume caused by laser irradiation [80,81]. Defect centers (color centers) could be a contribution of a

portion of this refractive index modification through the Kramers-Kronig relationship (K-K connection), i.e., the absorption change causes the change of refractive index because these quantities are conjugate complexes of the dielectric constant [82]. However, no strong connection between color centers and refractive index changes was observed in experimental proofs. Another plausible explanation is the observation that photo-induced absorption peaks at both 213 nm and 260 nm are found in the fs laser written waveguide structures. Indeed, these two absorption peaks are related to the respective center defects E′ and non-bridging Oxygen hole center (NBOHC) [83]. However, these two defects can be completely erased at 400 ℃ with the guiding properties remained up to 900 ℃, which indicates that the color center is not the main contribution of the refractive index change. Recently, it has been certified that the contribution of color center is about 20% [73]. Thus, the authors conceived that the dominate part of the refractive index change is defect-assisted densification.

Let's go to a simple view of the free electron plasma relaxation. The energy transfer from free electron plasma to the glass network will indeed lead to an ultrahigh local temperature, e.g., up to few thousand degrees at the focal point region restricted by the thermal conduction (or likely high pressures) [58,84]. This local temperature can reach the local melting of the glass and thus the densification or expansion according to the function of the relationship between density and cooling rate, i.e., glass fictive temperature [85]. This result contributes to a lower average Si-O-Si angle and thus some changes in some infrared bands (e.g., antisymmetric elongation vibration at 1120 $cm^{-1}$). There are some changes in the $D_1$ and $D_2$ bands (associated to the vibrations of cycles of 4 and 3 tetrahedra, respectively) observed by Raman spectroscopy [85,86]. This structural modification in silica glass can contribute to the refractive index change of few $10^{-3}$, which is plausible for the experimental results.

The hypothesis of local densification of glass as a contribution of index change has been evaluated from atomic force microscopy to phase shift interferometer observations of the surface morphology with few 10s of nanometers [82,87–91]. But what is the origin of this

observation of Type I modification?

A decade ago, our team at ICMMO proposed a physicochemical model to interpret this question. In fact, the first threshold (named T1) is based on the fictive temperature of the glass ($T_f$) when the interaction duration with light pulse heating is larger than the glass relaxation time, i.e., $\eta(T)/G(T)$. $\eta(T)$ and $G(T)$ are the viscosity and shear modulus of the material, respectively. Accordingly, we know that the lower the viscosity, the smaller the relaxation time. Additionally, the larger the temperature, the smaller the relaxation time. What determines the first threshold T1 is the timing that the temperature is increasing to be high enough to transform the glass material. The Fourier equation is taken into account for calculating the heat capacity variations of thermal diffusion, viscosity and shear modulus with different cases of doping and temperatures. It shows that the glass fictive temperature increases to several hundred degrees higher than the original temperature and then remains the same [84].

#### *I.5.3.2 Type II: Anisotropic nanograting structures*

As the pulse energy approaches the second threshold T2, the permanent structural modification is quite different from traditional densification, instead, it exhibits very interesting properties such as anisotropic light scattering, negative refractive index change, and more importantly a strong birefringence.

This self-organized nanograting structure was firstly observed by Shimotsuma and Kazansky et al. in 2003 [10]. From a chemical perspective, such a subwavelength nanograting was observed to have a periodic modulation of oxygen-deficient region [10]. This periodic structuration of the glass shows strong anisotropy, which can be controlled by the laser parameter, especially laser polarization. A decade ago, Bricchi et al. reported that this self-organized nanograting structure behaves as a negative uniaxial birefringent material, of which the slow axis is perpendicular to the laser polarization orientation [78]. This property originates from a form birefringence, which is different from an intrinsic birefringence. In general, an intrinsic birefringence is the anisotropy of oriented

molecules or atomic arrangement in uniaxial or biaxial crystals. However, a form birefringence is due to the structural arrangement of submicroscopic rodlets or platelets [78,92]. As the structure of a nanograting depicted in **Fig. 1-11**, a probe light that parallel to the interfaces of the nanograting will definitely suffer a larger refractive index than the perpendicular light, thus a phase difference can be achieved. In fact, the form birefringence of the nanograting can be determined by the filling factor and the chemical composition of the material (or we could say the inherent refractive index of the materials).

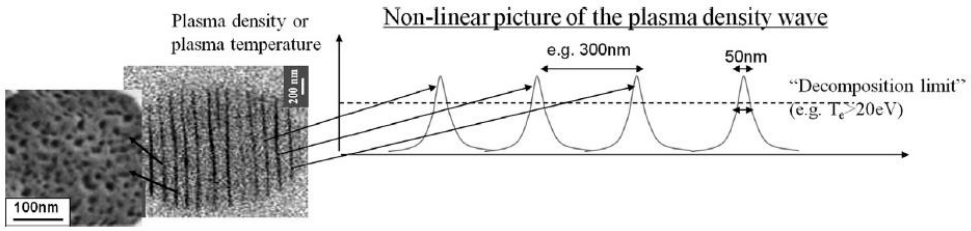


*Fig. 1-11: Images of the nanogratings made by nanoporous layers with nonlinear picture of the plasma density wave. Cited from* [12].

Actually, the nanograting is consists of nanoporous silica as depicted in **Fig. 1-12**, which has been revealed by our group [11]. The form birefringence is strongly related to the porosity filling factor $ff_{porous}$ of the nanolayers [93]. Thus, to manipulate the form birefringence can be converted to the question of controlling the filling factor of porosity, which is derived to pulse energy control associated with pulse overlapping rate (pulse number per micrometer) [93] and the chemical composition of the material [94,95].

In strongly Ge-doped $SiO_2$ glass, we have found that the region surrounding the nanopore shows a significantly negative refractive index change of $\Delta n$, which is likely derived from a fictive temperature increase (related to an increased $\Delta n$ in $SiO_2$). Another plausible interpretation could be a significant amount of Frenkel oxygen defects: $O_0^x \rightarrow V_0^{\cdot\cdot} + O_I$, i.e., a vacancy and an interstitial oxygen [93].

In-between the nanolayers, there exhibit increases of Young's modulus [96]. Thus, the refractive index indicates a plausible densification as suggested by Raman micro-spectroscopy. This

signature is quite similar to a Type I modification [59,89,97]. Lancry et al. reported a plasma density profile showing that in the non-porous region, the thermo-mechanical conditions of a Type I modification are achieved while in the porous region, a decomposition threshold of $SiO_2$ molecules could be exceeded [12]. Alternatively, some authors estimated an increased $\Delta n$ response going from $2x10^{-2}$ to $5x10^{-2}$ [78]. Note, this kind of refractive index increase is much higher than a Type I modification (only few $10^{-3}$). Here, the formation of color centers should be noted as it could somewhat decline the glass Young's modulus since it lowers the connectivity of the 3D network of glass materials. Thus, it is more likely that the origin of the considerable $\Delta n$ increase is attributed to the occurrence of fast compressive stress accompanied by thermal quenching resulting in a strong densification between the nanolayers somehow similar to what happen to silica glass under hot compression.

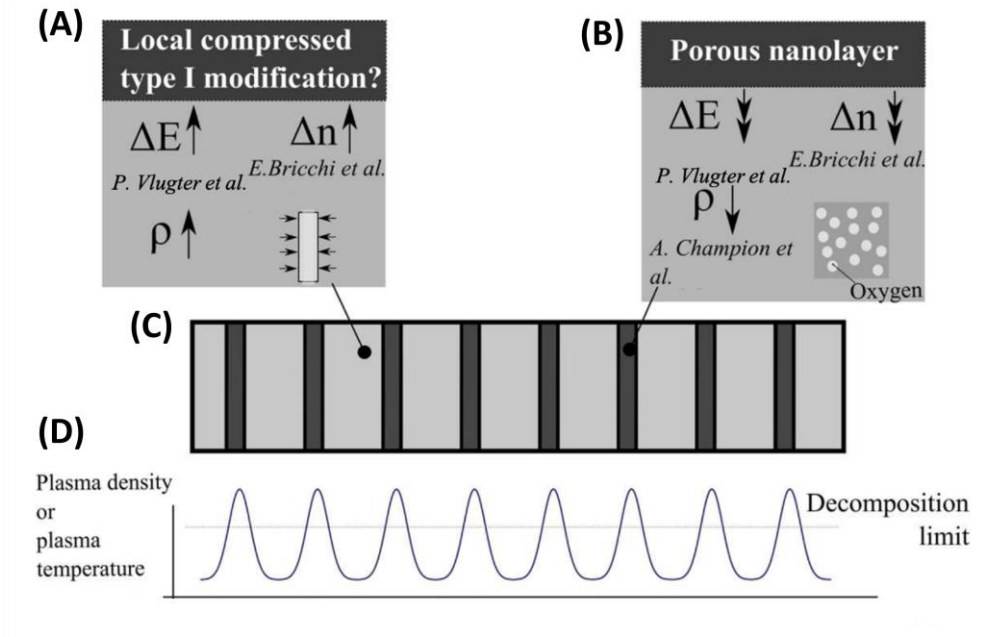


*Fig. 1-12: Illustrative summary of the nanograting. (A) Illustration of an increase of refractive index* [76] *and an increase of the elastic modulus* [96]*; (B) Illustration of the predicted material properties and chemical composition signature of a porous layer: refractive index change estimated by* [76]*, oxygen filled pores* [12] *and elastic modulus* [96]*; (C) Schematic image of a nanograting; (D) Spatial distribution of plasma density, with peaks exceeding the decomposition limit. Schemes are adapted from Ref.* [12].

#### I.5.3.2.1 Form birefringence of nanogratings

One of the very important optical properties of Type II nanogratings is form birefringence, which endows the possibility of manipulating the light by nanograting-based devices. From a classical perspective, assuming the medium being two dimensions, the light propagating in the medium could be decomposed to two orthogonal directions. In the case of nanograting structures, the light with its electrical field oscillating parallel to the nanolayers, is considered as TE mode (also called ordinary light). The other one with its electrical field oscillating perpendicular to the nanolayers, is considered as TM mode (also called extraordinary light).

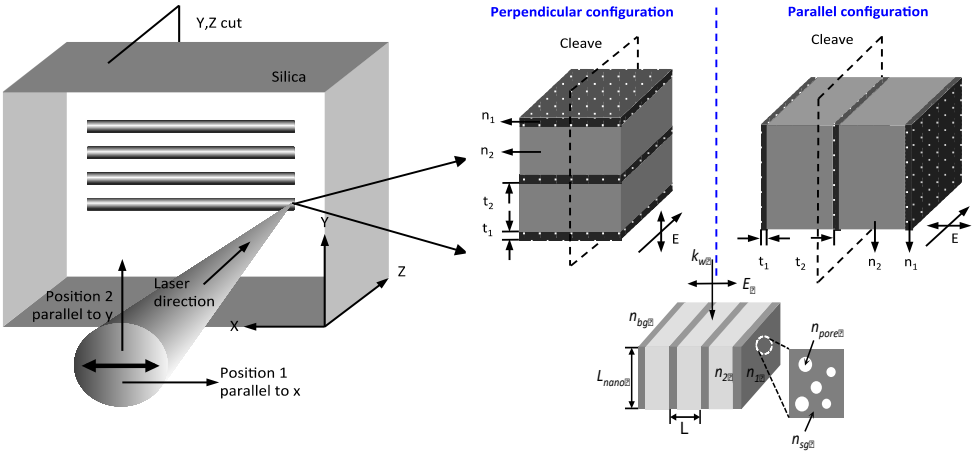


*Fig. 1-13: Illustrative of sub-wavelength periodic structure formed in cross-section of the irradiated region. $n_1$ and $n_2$ are local refractive indices of the nanolayers and the region between adjacent nanolayers, respectively; $t_1$ and $t_2$ are the thicknesses of the nanolayers and the region between adjacent nanolayers, respectively. Right bottom: Schematic of sub-wavelength nanograting structure formed in cross-section of the irradiated region. $n_{pore}=1$ is the local refractive index of the nanopore region and $n_{sg}$ is the local refractive index for surrounding oxygen defect regions, respectively; $\Lambda=t_1+t_2$: period of nanogratings and $n_{bg}$: refractive index of the surrounding material, $L_{nano}$: thickness of nanogratings. Cited from* [93,98].

The uniaxial birefringence of the nanograting can be described as a refractive index difference $(n_e - n_0)$ between these two orthogonal directions [93]:

$$\Delta n = n_e - n_0 = \frac{n_1 n_2}{\sqrt{f_\perp n_2^2 + (1-f_\perp) n_1^2}} - \sqrt{f_\perp n_1^2 + (1-f_\perp) n_2^2} \quad \text{(Eq. 1-4)}$$

Here, $f_{\perp} = t_1/(t_1 + t_2) = t_1/\Lambda$ refers to the filling factor of the Type II nanograting. As shown in **Fig. 1-13**, $\Lambda = t_1 + t_2$ is the period of a nanograting, where $t_1$ and $t_2$ refer to the thickness of nanolayers and the thickness of the region in-between adjacent nanolayers, respectively. $n_{1/2}$ is the refractive index of nanolayer region and the region in-between, respectively.

#### I.5.3.2.2 Stress related birefringence of nanogratings

Stress-induced birefringence widely exists in the nature, originating from process-induced temperature gradients, applied external pressures, manufacturing processes (e.g., in fiber drawing process due to the mismatching of thermal expansion coefficients). However, laser writing has been proved also to be a possibility for creating stress-induced birefringence. The main principle could be a permanent volume change $\varepsilon^p$ leading to an elastic response $\varepsilon^e$. As the departure of the laser pulse, the stress field $\sigma$ can be left. This will result in an anisotropic arrangement of the refractive index in the glass material and thus cause the stress related birefringence through photoelastic effects. In this case, the electromagnetic waves with different polarization orientations (parallel and perpendicular to the slow axis of the stress related birefringence) propagating in the stress related region will have different responses of speed, which can be expressed as:

$$n_{\parallel} = n_0 + \Delta n_{\parallel} \qquad \text{(Eq. 1-5)}$$

$$n_{\perp} = n_0 + \Delta n_{\perp} \qquad \text{(Eq. 1-6)}$$

Here, $n_0$ is the original refractive index of the material, which is considered as isotropic. $\Delta n_{\parallel}$ and $\Delta n_{\perp}$ refer to the proportional refractive index change of the parallel and perpendicular to the small mechanical stress field $\sigma$, respectively.

Similarly, as normal birefringence definition, stress related birefringence also has the retardance proportional to the stress induced birefringence and the thickness of the layer. For a simple view due to a single axis stress state, the retardance can be simplified as:

$$R = (n_{\parallel} - n_{\perp}) \cdot d \qquad \text{(Eq. 1-7)}$$

The orientation and amplitude of the birefringence are determined by the stress applied on the region through the photoelastic tensor.

Fs laser writing in a silica glass can cause diverse structural modifications within or around the focal region. The structural modifications are likely accompanied by a creation of stress field, however by different principles. Among all kind of modifications, Type I and Type II regimes are more interesting interacting with stress fields.

In general, Type I modifications are deemed as a homogeneous refractive index increase in silica glasses which are mainly due to an isotropic densification (although being found to be negative in some other glasses). However, inside Type I regime, there are also a tensile stress field and a minor contribution to point defect (typically, 25% of the measurable index changes), which are found to be responsible for the final $\Delta n$.

Type II modification shows a more complex phenomenon due to its nanopore structures [12]. Due to the decomposition of $SiO_2$, a large number of nanopores or nanocavities are generated in the hot plasma nanolayers, which contribute to significant net volume expansion in the glass [59,99]. This is an important process in the formation of nanogratings, but also, an essential origin for the birth of stress fields. In fact, the specific volume expansion inside the irradiated region leads to a permanent strain $\varepsilon_{II}^{p} > 0$ (here we define the expansion direction as the positive strain and the contraction direction as the negative strain). As a response, there will be an elastic strain $\varepsilon_{II}^{e} < 0$ against the expansion strain in the medium. Therefore, a compressive stress $\sigma$ is generated within and around the laser track. Due to the photoelastic effect, there will be a linear birefringence caused by the compressive stress. As Champion et al. have reported a laser-written pattern, the stressed region can be enlarged. They have also proposed a model to describe the stress fields accordingly [99]. The results show that the amount of the stress surrounding the irradiated regions is dependent on the orientation of the nanolayers, which is determined by the laser polarization. It provides

the possibility to control the amplitude of the laser induced stress field [59] and thus the related birefringence, which has been achieved from $10^{-5}$ to $10^{-3}$ [100–102].

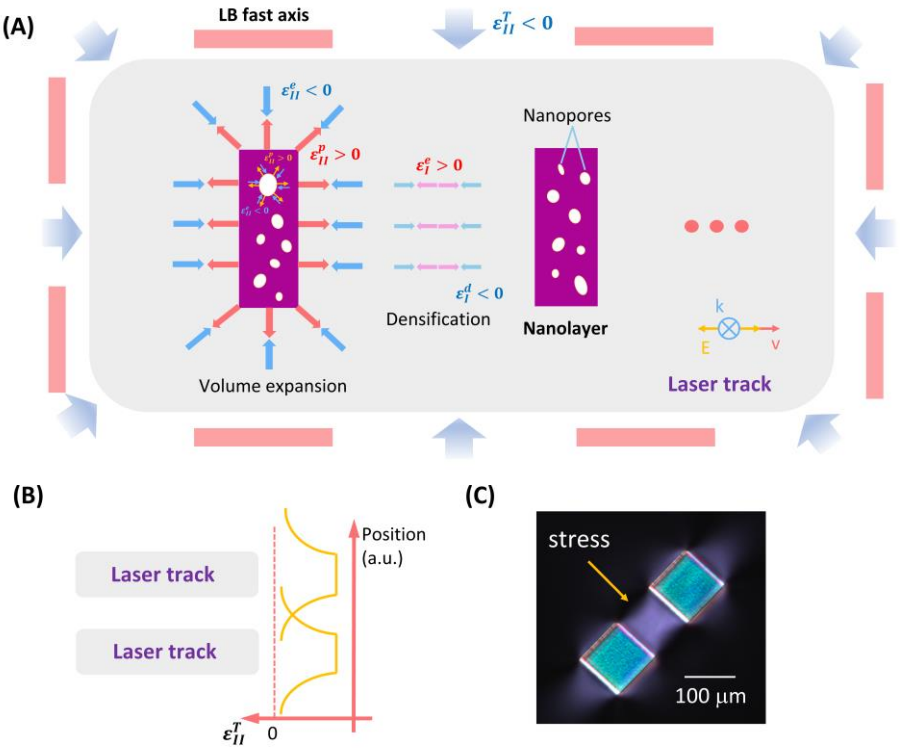


*Fig. 1-14: Illustrative of the stress related birefringence. (A) The schematic image of the stress fields in and around a line scanning of Type II regime. k: light propagation direction; E: laser polarization direction; v: laser scanning direction. (B) The total stress field distribution of two line-shaped laser tracks. (C) The experimental observation of stress field under a crossed polarized microscopy. Figure (C) is cited from* [23].

However, another important characteristic of the stress related birefringence is slow axis, i.e., the orientation. Here, we tentatively illustrate a model for discussing the stress field, as depicted in **Fig. 1-14**. We apply fs laser writing at a horizontal scanning "*v*" with a horizontal polarization direction "*E*". The light propagation direction is illustrated as "*k*". This laser polarization is responsible for a vertical arrangement of the lamellas made of nanoporous $SiO_2$. The formation of the nanopores contributes to the volume expansion which leads to the expansion strain $\varepsilon_{II}^{p} > 0$ and the material response $\varepsilon_{II}^{e} < 0$ around the nanopores. In-between the adjacent nanolayers,

there exists the densification region corresponding to a negative strain of $\varepsilon_I^d < 0$ and it will also result in a response elastic strain of $\varepsilon_I^e > 0$. This is similar to a Type I regime. However, these two strain fields are quite small when compared to the strains originated from net volume expansion. When the laser pulse left, the structural modification was embedded permanently in the irradiated region and the expansion strain disappeared. However, the total stress field caused by the elastic strains remained to be $\varepsilon_{II}^T = \varepsilon_{II}^e + \varepsilon_I^e < 0$. Since the $\varepsilon_{II}^e$ is the dominant part of the stress field, the total stress field exhibits a negative property. Here, we set a line trajectory as the scanning geometry, the total stress field distribution is depicted in **Fig. 1-14(A)**. Thus, the stress related birefringence has a fast axis perpendicular to the total stress field. That is, the fast axis of the stress related birefringence is parallel to the scanning line direction (with radial shape at the edges of the line geometry), which indicates that the stress field orientation is strongly dependent on the writing geometry but not associated with laser parameters including polarization. However, the amplitude remains dependent on the laser parameters as discussed above [60].

What's next is about a scanning of squares or rectangles enabled by the combination of a set of lines. The distribution of the elastic stress field is strongly connected to the position corresponding to the volume expansion. That is, it is quite strong at the place of volume expansion and decays fast with the distance increases, as shown in **Fig. 1-14(B)**. Therefore, the composite stress field can be considered as the superposition of lines (as a first approximation) and so as the stress related birefringence, as depicted in **Fig. 1-14(C)**.

#### *I.5.3.3 Type III: Voids*

If the peak intensity of the laser pulses approaches the third threshold T3, i.e., greater than $10^{14}$ W/cm$^2$, voids (holes in volume) can be obtained. In fact, it is mainly attributed to the micro-explosion mechanism. Fleischer et al. reported the first model [103] and later it was confirmed and developed in laser induced structures by Schaffer et al. [104]. Initially, the micro-explosion mechanism is suggested as a Coulomb explosion. Specifically, the density of the excitons at the irradiated point is large enough to make the Coulombic force

between ions overcome the binding energy. In this situation, the ions move to the interstitial positions around the point. However, it is unlikely to happen in the situation of laser irradiation. Thus, the mechanism of voids formation is revisited by a new development. A small volume that absorbs a large amount of energy will produce a high pressure, which subsequently generates a shock wave and stress exceeding the Young's modulus of the material. Later, the spherical shock wave starts to propagate outside the symmetric center of the compressed material. Simultaneously, a rarefaction wave that propagates to the symmetric center of the energy absorbed region decreases the density of the energy deposition. The shock wave will stop when the pressure is behind the wave front of the shock wave. Thus, the voids can be imprinted.

#### *I.5.3.4 Type X: Low-loss modifications*

Recently, a Type X modification is discovered by Kazansky et al., which is close to the energy threshold of avalanche ionization [105]. Type X modification correlates to randomly distributed nanopores elongated perpendicular to the laser polarization. Indeed, it can be considered as an early birth of the nanogratings. As we all know, the nanogratings own non-negligible scattering loss in the visible band, typically a 74% transmission at 550 nm [23]. However, Type X modifications exhibit ultralow-loss properties [106].

The formation of these polarization controlled oblate nanopores from a Type X modification is suggested as two essential processes. The first step is the formation of randomly distributed nanopores originated from the oxygen molecules construction. However, there exists a critical value of the pulse duration (typically should be larger than 220 fs) for the nanopores related to a Type X modification, which is mainly attributed to the excitation of sufficient interstitial oxygen atoms to form oxygen molecules and thus the nanopores.

Another essential process, namely elongation of nanopores perpendicular to the laser polarization is mainly attributed to the near-field enhancement around the nanopores [107]. On the one hand, the enhanced field enables more local ionizations; on the other hand, the enhancing of the near filed is strongly dependent on the

laser polarization and thus leads to an anisotropic stress field. This anisotropic stress field then contributes to elongation of the nanopores.

Type X modifications own their advantages in high transmission efficiency (for example, 99% at 550 nm with a 38 nm retardance), which provides great potentials in data storage and low-loss geometric optics [105]. While Type II nanogratings can create higher retardance than Type X modifications. For the future, the different structural modifications can be utilized in their proper applications and may coordinate with each other.

### I.5.4 Heat accumulation

The diffusion time, according to the dissipation of the deposit energy out of the fs laser irradiated volume can be calculated by [108]:

$$t_D = \frac{\omega_0^2}{2D} \qquad \text{(Eq. 1-8)}$$

Here, $\omega_0$ is the focal radius while $D$ refers to the diffusivity, which can be obtained by:

$$D = \frac{\kappa}{\rho} \cdot C_p \qquad \text{(Eq. 1-9)}$$

$\kappa$ refers to the conductivity while $C_p$ is the specific heat. $\rho$ stands for the material density. Considering a focusing lens with a NA around 0.5, the modification width in the fused silica material by a single pulse could be about 1 μm. Thus, the diffusion time is about 1 μs. One can imagine that if the successive pulse comes before the heat diffusion, i.e., the interval time between two pulses is shorter than the diffusion time, the temperature of the focal volume region will increase stepwise as the accumulation of the pulses. Therefore, it forms a heat accumulation process [57,58,69].

As shown in **Fig. 1-15**, the calculated fictive temperature increases when the repetition rate increases at a fixed pulse energy of 150 nJ, a duration of 450 fs and a NA of 0.5. In the center of the focal volume (around 70 μm), the temperature increases very fast when the pulse interval time becomes shorter. This model uses Fourier equation on a

Gaussian heat source. It considers a radial axis and a Lorentzian distribution along the propagation direction of the beam.

In general, a laser irradiation with a large number of laser pulses but a low repetition rate (typically, <200 kHz in silica) will lead the irradiated region cool to room temperature since the interval time between two adjacent pulses are too large. In $SiO_2$, the deposited energy from one pulse could be "removed" by the thermal diffusion within a microsecond in the mass of the material. This will lead to an independent modification by single pulses in the volume with no heat accumulation mechanism.

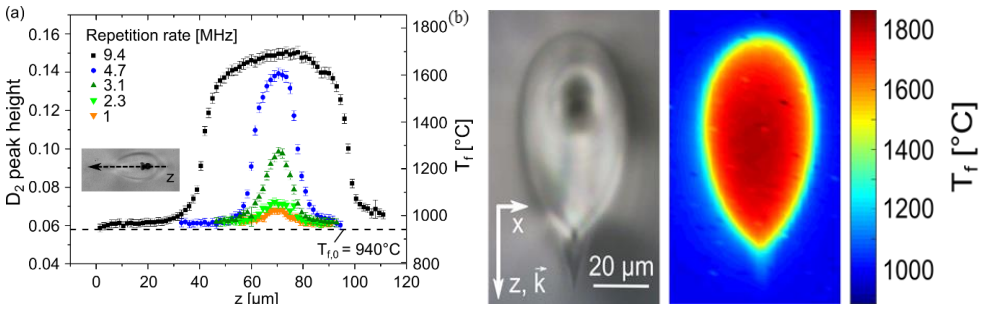


*Fig. 1-15: Raman measurements. (a) $D_2$ peak height and fictive temperature evolutions at the longitudinal position moving. Inset is the illustration of the longitudinal position direction. (b) Microscopic optical image and the corresponding fictive temperature map of the laser irradiated region. The modification is written by 150 nJ, 9.4 MHz, 1000 pulses per laser spot. Cited from* [109].

For the case of high repetition rate irradiation (typically >0.5 MHz in $SiO_2$), the interval time is now shorter than the thermal diffusion time out of the irradiated volume. Thus, the pulse train can heat the irradiated zone gradually, which leads to a thermal accumulation and thus a permanent modification with an area much larger than the focal region. Besides, the heat-affected zone is dependent on the number of the pulses since the thermal diffusion is isotropic. It can be attributed to a local melting with the theoretical simulation correspondingly [57]. After the absence of laser pulse irradiation, the material will resolidify via possible densification mechanisms of silica. Importantly, silica becomes denser at a high fictive temperature due to its "anomaly" between density and fictive temperature when compared to other vitreous glasses.

## I.6 CHIRALITY

### I.6.1 Chirality in nature

Chirality, as a very important concept in chemistry, describes that an object cannot overlap by its mirror image through simple rotation and transition. This word is originated from a Greek vocabulary "cheir", which means hand. Because our hands are the most representative chiral objects in the nature, as shown in **Fig. 1-16**.

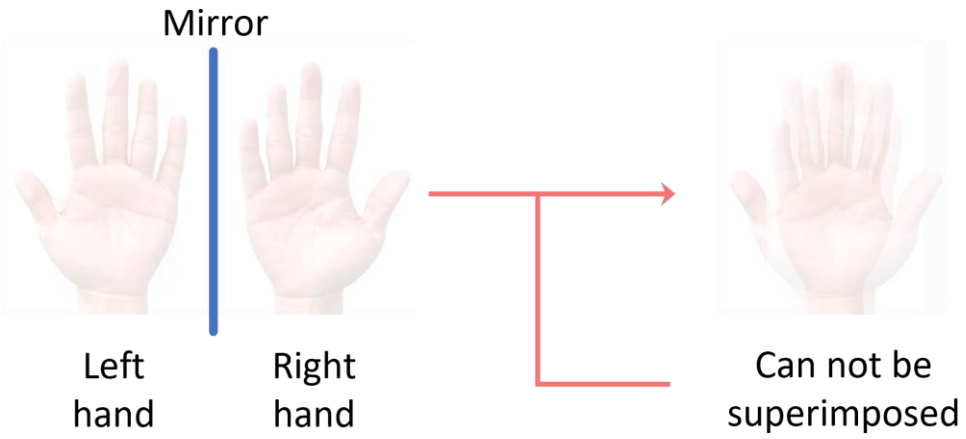


*Fig. 1-16: Schematics of chirality of hands. Left and right hands can be considered as mirror images (from geometric view of point with ignoring the detail difference). They cannot be superimposed by each other due to their chiral property.*

Generally, in chemistry disciplines, chirality is always deemed as the molecular geometry of a binary left or right shape that owns different optical responses to left-handed and right-handed circularly polarized lights. Chiral molecules usually come in pairs of left-handedness and right-handedness, called chiral isomers or enantiomers [110], divided into S-enantiomers and R-enantiomers. These enantiomers have the same chemical formula and molecular composition with only difference in structural spin. However, they own different chemical properties, biological properties, and pharmaceutical effects. Thus, it is essential to distinguish the enantiomers both in chemistry, biology, and pharmacy [111]. The enantiomers only exhibit chirality when interacting with chiral objects, but nothing to do with their physical properties. Thus, light with

chirality emerges to be a useful probe to detect and distinguish the enantiomers with simple interactions, e.g., a circular dichroism spectroscopy technique [112].

In fact, the origin of chirality is symmetry breaking. Chirality is a common phenomenon existing in the nature, such as double helix-based DNA molecules, amino acids, shells, spiral vines and snails, spiral galaxies, etc. However, the chiral objects in nature seem to prefer only one chirality for their own. For example, DNA molecules are right-handed; almost all the amino acids that naturally form proteins are left-handed; almost all spiral shells are right-handed.

The chiral effects that originate from a number of natural phenomena lead to great essentials both in fundamental science and industrial practice, ranging in analytical chemistry [113], optical switches [114], broadband circular polarizers [115], optical recording [116] and quantum materials [117].

It is worth noting that chirality owns two categories due to its origin: intrinsic chirality and extrinsic chirality. An intrinsic chirality is mainly attributed to a chiral arrangement of molecules or lattice, such as sucrose or α-quartz [118]. This chirality is based on the scale of molecular activity and can exhibit a small amount of circular optical properties, e.g., optical activity and related optical rotation. An extrinsic chirality is based on a chiral arrangement of optical objects/structures at a larger scale, typically at micrometer scale or larger. This chirality can, somewhat be deemed as an optical chirality that originates from several internal linear optical properties such as linear birefringence and linear dichroism with non-parallel and non-perpendicular neutral axes [119,120].

### I.6.2 Chirality in light

Light, as an electromagnetic wave, can also possess chirality when it carries angular momentums. Since the advance that circularly polarized lights can carry SAM was founded by Poynting in 1909 [121], light is widely used in chiral molecular analysis. This is a local property in which the electric and magnetic field vectors form a spiral pattern when light propagates. Vortex light that carries OAMs is

another typical source of chiral light. The chirality of a vortex beam originates from its helical phase front, which shows left-handedness or right-handedness according to its topological charge number and sign.

Chiral light field, as a new physics, is appealing more attentions in the research community, thus the manipulation, transmission and application of chiral light fields are mainstreams in the field of optics and nano-photonics. Indeed, chiral light field provides a rich spatial topological distribution of light. From now on, the degree of freedom of manipulating light fields mainly contains amplitude, time, waveform, frequency, phase, and polarization. Generally, it can be divided into two aspects: temporal manipulation and spatial manipulation. The time domain control mainly takes the frequency and time waveform of the light field as parameters. The flexible control in time domain correspondingly drives the development of light science in ultrafast optics. Spatial manipulation mainly takes the spatial arrangements of amplitude, polarization, and phase of light fields. With the development of optics, spatial control of light fields has become more mature in the research, which lies on the heart of chiral manipulation of light fields. In this PhD thesis, we focus on the spatial manipulation of light (vector modes and vortex modes) and their interaction with materials. Thus, the introduction of vector modes manipulation is necessary here.

Vector modes, in fact, are defined as the light modes that possess different polarization states at each point in the beam. This kind of "different" can be different polarization types such as linear, circular and elliptical polarizations, or different orientations, etc. In general, vector beams can be easily obtained by local/overall polarization conversion to achieve the different polarization at each point. Vortex modes are the essential part of the vector modes due to their unique helical phases and OAMs. The manipulation of the vortex beams attracts tremendous interest in the field. Generally, it can be divided into two strategies: one in free space and another in fibers.

#### *I.6.2.1 Vortex modes generation in free space*

For the case of free space, the key point is to apply a helical phase

term on the light beam. Perhaps the simplest way to create a beam with helical phase is to make a plane wave pass through an optical component that possesses a helical surface. Spiral phase plate emerged to be a good choice due to its simple structure, as shown in **Fig. 1-17** [122]. Although it seems as a very simple way, it requires highly precise thickness of each "step" and only serves to one single wavelength.

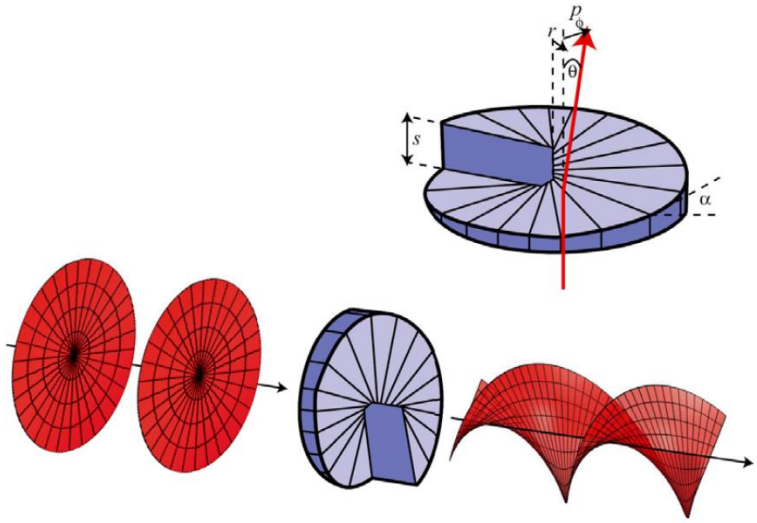

*Fig. 1-17: Schematics of a spiral phase plate and its application to convert a Gaussian beam to a vortex beam. Cited from* [123].

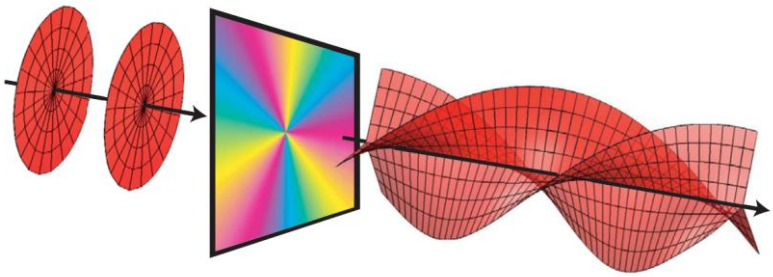

*Fig. 1-18: Schematics of a helical profile to convert a Gaussian beam to a vortex beam using hologram technique. Cited from* [123].

Another approach to realize a helical phase beam is to apply diffractive optical elements. In practice, it is designed as a hologram component and is always referred to the "computer generated holograms", as depicted in **Fig. 1-18**. Specifically, to demonstrate the

helical beams, the holograms can be designed as a forked diffraction grating [124] or a spiral Fresnel lens [125]. What makes this approach widely used is the birth of spatial light modulator (SLM). SLMs are pixelated liquid crystal devices that can be easily programmed by computer to generate any pattern of holograms [126].

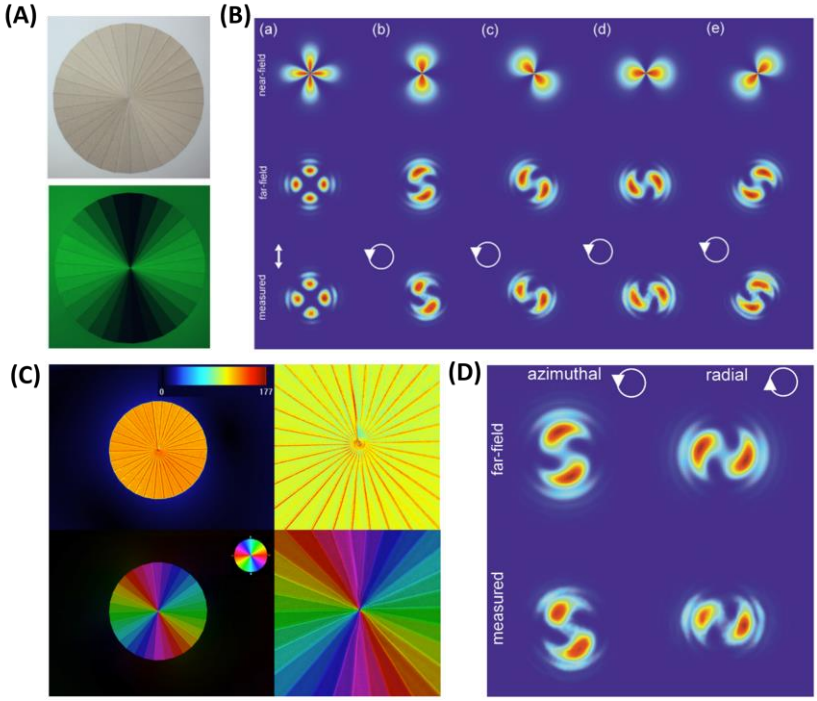


*Fig. 1-19: Illustration of polarization vortex converter. (A) Microscopic images of the polarization converter under bright field (top) and crossed polarizers (bottom). (B) Modeled near-field (top), far-field (middle) and measured far-field (bottom) intensity distributions recorded after passing through the polarization converter from the incident light of linearly polarized (a) and left-handed circularly polarized at different angles of a polarizer 0°(b), 45° (c), 90° (d), 135° (e). (C) Birefringence characterization of the polarization converter measured by Abrio system. Retardance distribution (top) and slow axis map (bottom) of the polarization converter with 5× (left) and 20× (right) magnification, respectively. (D) Modeled and measured far-field intensity profiles of the recorded optical vortex light after the polarization converter with right-handed circularly polarized light and left-handed circularly polarized light at 532 nm under a horizontal linear analyzer. Cited from* [127].

Additionally, q-plate device is another alternative to achieve SAM-OAM coupling. Q-plate device consists of an anisotropic/non-uniform medium (such as polymer, liquid crystal, or subwavelength grating), whose optical axis changes spirally along the center azimuth.

In 2006, Marrucci et al. proposed a q-plate to convert a Gaussian beam to be a left-handed/right-handed vortex light with an OAM of " $\pm 2$" [128].

In 2011, Beresna et al. proposed a polarization vortex converter based on femtosecond laser direct writing self-organized birefringent nanogratings, as depicted in **Fig. 1-19**. This converter can generate optical vortices with radial and azimuthal polarization, which is controlled by the handedness of the incident circularly polarized light. The space variant polarization vortex converter is enabled by a space variant design of form birefringence in the waveplate, which can be precisely manipulated by the femtosecond laser parameters, especially the polarization azimuth [127].

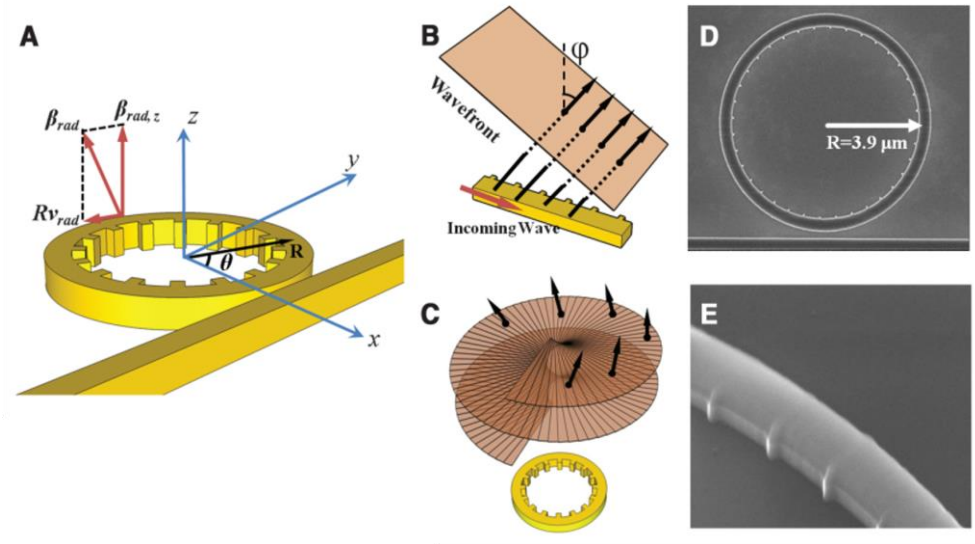


*Fig. 1-20: Illustration of a silicon-integrated vortex generator. (A) The schematic of the micro-ring generator with angular gratings patterned along the inner wall. (B) Schematic of a linear waveguide with gratings and its effect leading to the tilted wavefront of light. (C) Schematic of a micro-ring generator and a helical beam with its wavefront. (D) SEM image of the fabricated micro-ring generator. (E) The detailed SEM image of the fabricated micro-ring generator. Cited from* [129].

Miniaturized vortex light generator has been proved as an effective way to generate vortex light at a small scale on the integrated photonics. In 2012, Yu et al. [129] demonstrated a silicon-based micro-ring generator with inner wall patterned by angular gratings, as shown in **Fig. 1-20**. This generator is capable of vortex light

extraction confined in whispering gallery modes (WGMs) under precise control of OAM amount. The principle is coupling the light into the cavity and generating the vortex light with helical wavefront by utilizing the diffraction of the angular gratings. The topological charge of the vortex light is determined by both the optical period of the cavity and the period of the angular gratings. Subsequently, an electrically controlled thermo-optical effect is utilized to dynamically tuning the different OAM modes with a response time of 10~20 μs [130]. This vortex emitter only has a radius of 3.9 μm that provides the potential in integrations of vortex generator and is compatible to silicon nano-photonics. In 2016, Feng et al. reported an OAM micro-laser enabled by ring cavity made by InGaAsP/InP semiconductor materials patterned with angular gratings [131], as depicted in **Fig. 1-21**. It can directly generate vortex laser light excited by pump light and the polarization of the vortex light can be manipulated.

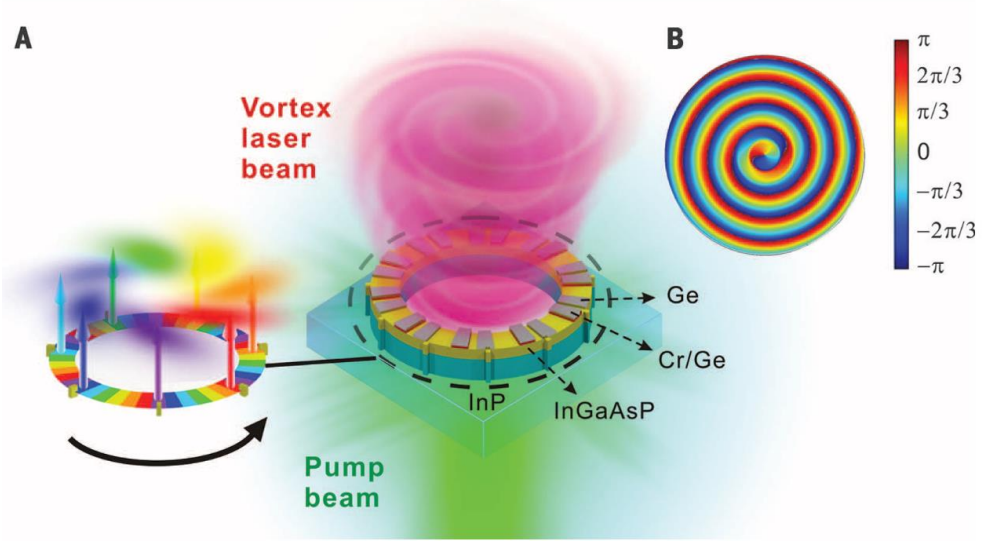


*Fig. 1-21: Illustration of a semiconductor OAM micro-laser. (A) Schematic of the OAM micro-laser on an InP substrate. (B) Simulated phase distribution of light emission. Cited from* [131].

Recently, Qiao et al. utilized a symmetry-broken microcavity to demonstrate high OAM lasing with degree of chirality tunability [132], as depicted in **Fig. 1-22**. This OAM micro-laser is made by a Fabry-Perot microcavity with two distributed Bragg mirrors, which can excite vortex lasing with a quantum number ranging from "-352" to

"+352". More surprisingly, the micro-laser can support multiple vortex modes with different chirality oscillating simultaneously in the microcavity, which leads to a superposition of OAM states. The degree of chirality can be adjusted by pumping at different positions on the microcavity. This work provides new perspective in controlling the chirality of the excited OAM modes by introducing a symmetry broken strategy.

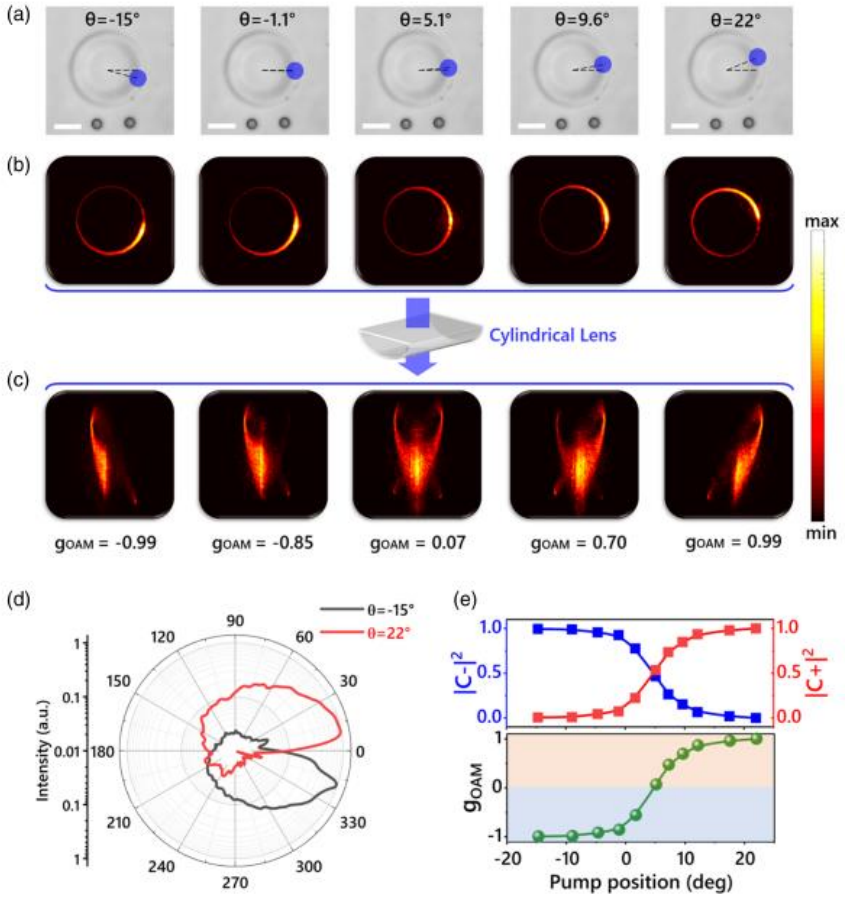


*Fig. 1-22: Illustration of an OAM micro-laser with degree of chirality tunability. (A) Bright-field images of the microcavity. (B) Far-field images of the lasing mode patterns. (C) Lasing mode patterns after a cylindrical lens. (D) OAM mode intensity distributions along the microcavity with different pump positions. (E) Purity and dissymmetry factor evolutions at different pump positions. Cited from* [132].

Since the rapid development of micro-nano fabrication technique, metasurface emerges to be a novel strategy to precisely control the light field, especially at integrated optics due to its ultra-compact size.

Metasurfaces are subwavelength metamaterials made of planar electromagnetic structures designed to have specific electromagnetic responses and thus the related functions of manipulating electromagnetic waves, especially lights [133]. According to Maxwell's equations, the permittivity and permeability of a media determine the propagation conditions of an electromagnetic wave. Thus, to design these parameters of the media is an effective way to manipulate the behavior of the electromagnetic wave propagating inside the media. In 2011, Capasso et al. reported a two-dimensional array of optical resonators with space variant phase responses to achieve an abrupt phase change at the scale of wavelength and thus the manipulation of the light beams [134]. Specifically, the array consists of V-shape antennas to adjust the phase of the scattered light. Each antenna is analogous to the pixel of a hologram, thus, a space variant phase modulation can be designed to approach the generation of vortex light, as depicted in **Fig. 1-23**.

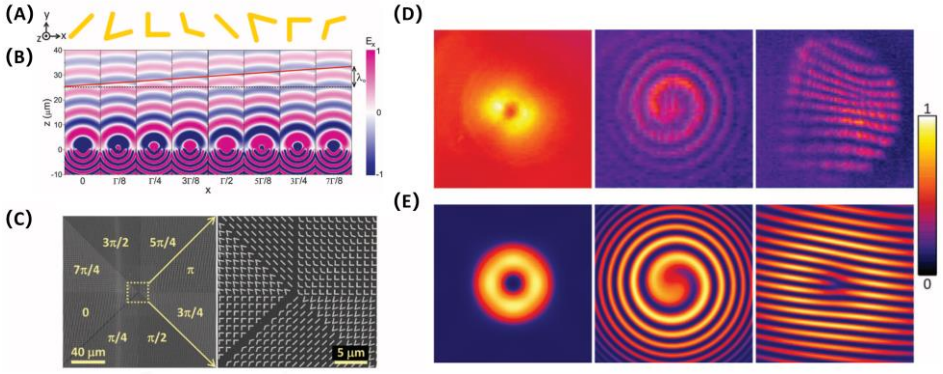


*Fig. 1-23: Illustration of a V-shape antenna based metasurface vortex generator. (A) Schematic of the meta-atom, i.e., the unit cell of the plasmonic interface. (B) Simulation results of the scattered electric fields of the antennas presented in (A), respectively. (C) SEM images of the fabricated metasurface. (D) The measured intensity profile, spherical wave interference, and planar wave interference of the generated vortex light beam. (E) The simulated intensity profile, spherical wave interference, and planar wave interference of the vortex light beam. Cited from* [134].

In 2014, Karimi et al. presented a plasmonic metasurface for generating optical vortex at visible band [135]. This metasurface allows the coupling of SAM-OAM during the light-matter interaction, i.e., can convert a left-handed circularly polarized light to be right-

handed circular polarized vortex light carrying an OAM of "2", as shown in **Fig. 1-24**.

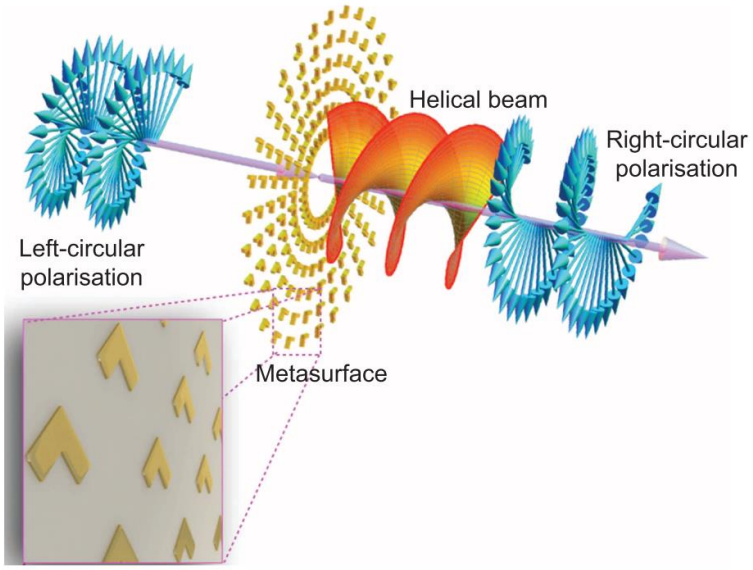


*Fig. 1-24: Illustration of a plasmonic metasurface converting a left-handed circularly polarized light to be right-handed circular polarized vortex light carrying OAM of "2". Cited from* [135].

Nowadays, metasurface is a new branch of optics and appealing more and more research interest in the community.

### *I.6.2.2 Vortex modes generation in fibers*

The cylindrical refractive index distribution of a silica fiber does well support the optical field distribution of vector modes. Therefore, optical fibers are good waveguides for vector modes and are benefit from their advantages in high conversion efficiency, low energy loss and high system compatibility. However, vortex mode generation in all-fiber devices is quite different from that in free space. The principle of generating vortex modes in optical fibers lies on the heart of phase-matching based mode coupling [136]. The general strategy is to convert the fundamental mode to high-order modes (HOMs, including high-order eigen vector modes or scalar LP modes) and achieve the subsequent vortex modes by applying a "$\frac{\pi}{2}$" phase difference.

The simplest way is then dedicated to off-set splicing technique to generate the HOMs. For example, Pang et al. proposed a method for generating first-order OAM light beams by off-set splicing a single-mode fiber and a single-mode ring fiber at the communication band [137]. These obtained first-order OAM modes are attributed to the combination of two eigen modes, i.e., $HE_{21}^{odd}$ mode and $HE_{21}^{even}$ mode with a "$\frac{\pi}{2}$" phase difference, which is adjusted by the polarization controller.

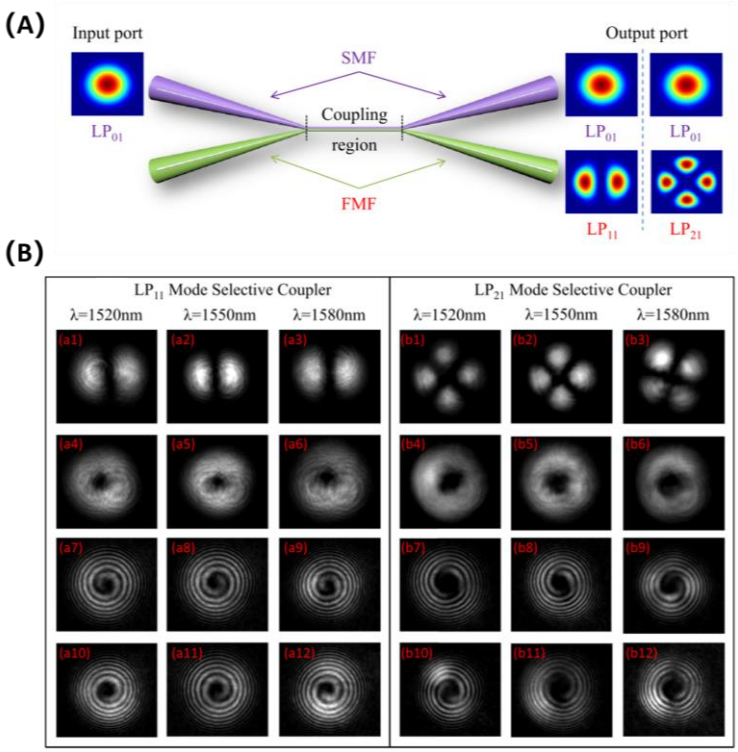


*Fig. 1-25: Illustration of a mode selective coupler based optical vortex converter. (A) The schematic of a mode selective coupler. (B) The experimental results of mode conversions of both $LP_{11}$ mode and $LP_{21}$ mode and the related vortex modes at different wavelengths, respectively. Cited from* [138].

Off-set splicing technique requires easy processes. However, it is difficult to control the mode conversion efficiency and it induces non-negligible splicing loss. Mode selective couplers emerge to be a reliable method to generate HOMs and OAMs. In 2017, Wang et al. demonstrated the femtosecond optical vortex beams generation by using mode selective couplers [138]. A mode selective coupler is

fabricated by twisting, stretching, and fusing two parallel optical fibers under an oxyhydrogen flame. Therefore, the fiber cores of these two parallel fibers are very close to form a coupling region with the condition of phase-matching, as depicted in **Fig. 1-25(A)**. By setting the appropriate parameters of the fused mode selective coupler, especially the diameters of the two parallel optical fibers, different phase-matching conditions can be achieved to convert the fundamental mode ($LP_{01}$ mode) to $LP_{11}$ mode and $LP_{21}$ mode. Thus, the optical vortex modes can be obtained by applying the "$\frac{\pi}{2}$" phase difference, as depicted in **Fig. 1-25(B)**. Mode selective couplers exhibit wide conversion band, high conversion efficiency and stable mode conversion.

Long-period fiber grating is another solution to generate HOMs in optical fibers. Long-period fiber grating is a fiber structure with a periodic modulation of alternative high and low refractive index along the optical fiber axis. This periodic modulation of refractive index, i.e., a grating, will introduce a micro-perturbation to the propagating light in the fiber core. If the micro-perturbation satisfies the phase-matching conditions of the propagation constants of two guided modes, the mode conversion can be achieved. Generally, long-period fiber grating is fabricated in single-mode fibers to generate the fiber core mode to cladding modes and thus can form a band-rejection filter or a sensing component since the cladding modes cannot stably propagate in the fiber. Recently, long-period fiber gratings in few-mode fibers are appealing to the research community due to their mode conversions between fiber core modes. This allows the generation of fiber core modes (instead of the evanescent cladding modes), which can stably propagate in the fiber core. For example, Zhao et al. demonstrated both the uniform and tilted long-period fiber gratings to achieve the mode conversion from fundamental mode ($LP_{01}$ mode) to HOM ($LP_{11}$ mode) with a high conversion efficiency over 99% in two-mode fibers [139]. Subsequently, the vector eigen modes ($HE_{21}^{odd}$ mode and $HE_{21}^{even}$ mode) and the OAM modes are also obtained. Long-period fiber gratings can be easily fabricated by $CO_2$ laser writing. As an in-line device, it can be easily integrated in the fiber systems, e.g., fiber communication systems and fiber laser cavities.

Fiber Bragg gratings (FBGs) can also be a mode selective device since FBGs in few-mode fibers operate several resonances for the high-order reflective modes. This property provides the possibility of selecting HOMs and thus creating the OAM modes. However, few-mode FBGs are not capable of HOM creation by themselves. Therefore, a method for generating HOMs is required before the reflection of the few-mode FBGs, typically it could be off-set technique due to its simplicity. In 2014, Dong et al. reported a mode-locked fiber laser incorporating a two-mode FBG for transverse mode selection [140]. High-order LP modes are obtained in the mode-locked fiber laser. Then, Sun et al. utilized cascade FBGs to achieve cylindrical vector modes with mode-locked rectangle pulses output in 2015 [141]. Besides, Wang et al. have reported FBGs written on OAM fibers for reflecting OAM modes with a charge inversion [142].

Passive devices such as long-period fiber gratings and mode selective couplers, sharing a common restriction of flexibility. That is, the function of the device is totally determined once it is fabricated. However, there is an active solution for all-fiber HOM generations, which employs the dynamic acousto-optic interactions in fibers, i.e., acousto-optic mode converters. In 1986, Kim et al. firstly proposed a frequency shifter based on acousto-optic interaction in an optical fiber [15]. Afterwards, this device was proved to enable the mode conversion in few-mode fibers. In 2006, Lee et al. demonstrated an orthogonally cascaded piezoelectric transducers to achieve two orthogonal eigen vector modes [143]. By applying a phase difference between two acoustic waves, the OAM modes can be generated directly. In this PhD thesis, acousto-optic interactions in optical fibers are chosen as a dynamic vector mode manipulation strategy. We will introduce more detailed information and the related mechanisms in **Chapter II**.

### I.6.3 Chirality induced by light

From an extremely simple view, the light can induce chiral structures inside or on the surface of the material to form the structural chirality (or we could say to form a chiral object). Typically, the chiral structures can be helical stairs, helical strings, or helical needles. In 2009, Gansel et al. reported a three-dimensional gold helix enabled

by direct laser writing photoresist with subsequent electrochemical deposition of gold. This structure can effectively block the circularly polarized lights with same handedness as the helices, which provides new possibilities for compact broadband circular polarizers [115]. Giessen et al. proposed a novel method of lithography for fabricating 3D chiral plasmonic structures by hole masks and tilted angle evaporation strategies [144]. This large-area chiral structures exhibit significant circular dichroism within 3000 nm range as shown in **Fig. 1-26**. However, this degree of utilizing light only remains an initial stage by fabricating a "template" or just using simple lithography, despite of 3D structures with strong chiral responses they can make.

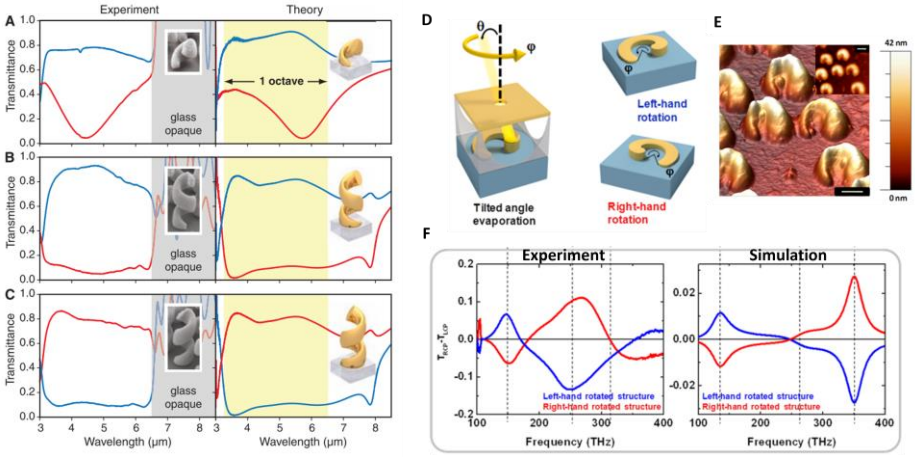


*Fig. 1-26: Laser induced gold helices and their responses to left- and right-handed circularly polarized lights. Experimental and theoretical results of a left-handed helix with slightly less than one pitch (A), a left-handed helix with two pitches (B) and a right-handed helix with two pitches (C). Cited from* [115]. *Laser induced large-area chiral plasmonic structures and their responses to left- and right-handed circularly polarized lights. (D) The schematics of the laser writing chiral plasmonic structures by colloidal nanohole lithography. (E) The AFM image of the constructed 3D chiral plasmonic structures. (F) Experimental and simulated results of different responses to left- and right-handed circularly polarized lights for the 3D chiral plasmonic structures. Cited from* [144].

Actually, the chirality belongs to a light beam can be transferred to the matter by light-matter interaction. The idea for converting the chirality from light to matter is somehow to realize an asymmetric writing or excitation to break the inherent symmetry of the original material. Vortex light has a strong chirality. Theoretically, the OAMs carried by vortex lights possess infinite states of chirality while SAMs

in circularly polarized lights only have two states of chirality. However, how can we transfer the chirality of OAMs to the matter?

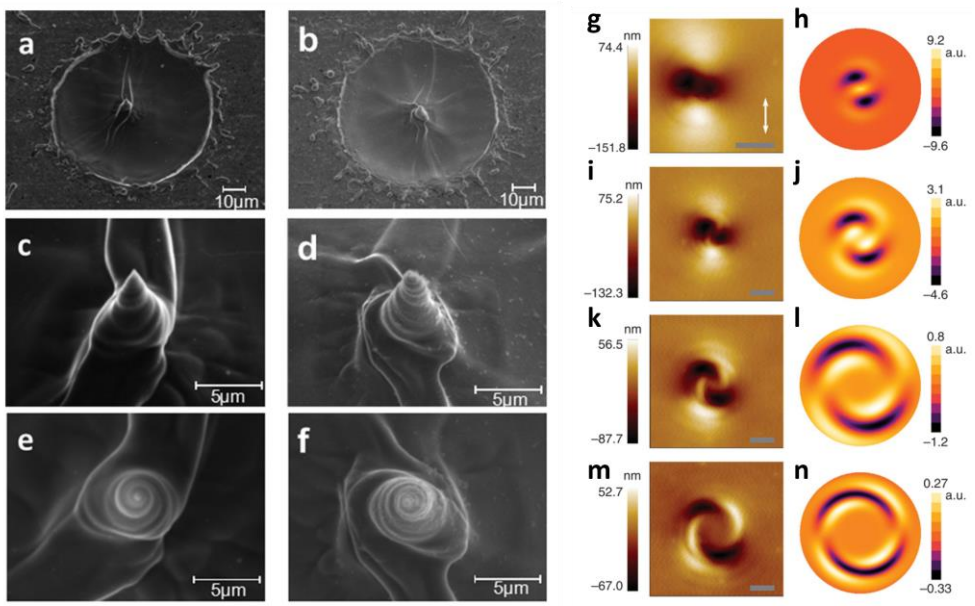


*Fig. 1-27: Vortex light written nanoneedles. The SEM images of a nanoneedle written by a vortex nanosecond laser with a topological charge of "-2" with overview (a), 25° view (c) and top view (e). The SEM images of a nanoneedle written by a vortex nanosecond laser with a topological charge of "2" with overview (b), 25° view (d) and top view (f). Cited from* [145]. *Vortex laser induced spiral relief pattern on azobenzene-containing polymer films. Topographical AFM map of the relief patterns induced by a vortex beam with topological charge of "1" with experimental result (g) and modeling result (h). Topographical AFM map of the relief patterns induced by a vortex beam with topological charge of "2" with experimental result (i) and modeling result (j). Topographical AFM map of the relief patterns induced by a vortex beam with topological charge of "5" with experimental result (k) and modeling result (l). Topographical AFM map of the relief patterns induced by a vortex beam with topological charge of "10" with experimental result (m) and modeling result (n). Cited from* [146].

In 2012, Omatsu et al. from Chiba University reported a chiral nanoneedle structure demonstrated by vortex nanosecond laser (with topological charge of "2" and "-2", generated by a spiral phase plate) irradiation on a ~1-mm-thick Tantalum plate, as depicted in **Fig. 1-27**. The experimental proof indicates that the helicity of the nanoneedle structures can be directly controlled by the sign of the vortex nanosecond laser [145]. In another word, the chirality of the nanosecond light can be converted to the metal plate for creating

corresponding chiral structures. This is mainly attributed to the metal twist caused by the OAM of the light after laser ablation of the metal surface. Importantly, the singularity in the center of the laser beam (with zero intensity) thus leads to the formation of the nanoneedle structure, of which the tip is extremely small (<40 nm).

Ambrosio et al. utilized Laguerre–Gaussian beams to induce spiral-shaped relief patterns on azobenzene-containing polymer films [146,147]. It is mainly originated from the surface-mediated interference of the longitudinal and transverse components of the light field. Specifically, since the azobenzene-containing polymer material has anisotropic polarization dependence, the interference of the transverse and longitudinal components of the vortex light field can lead to the spiral mass transport.

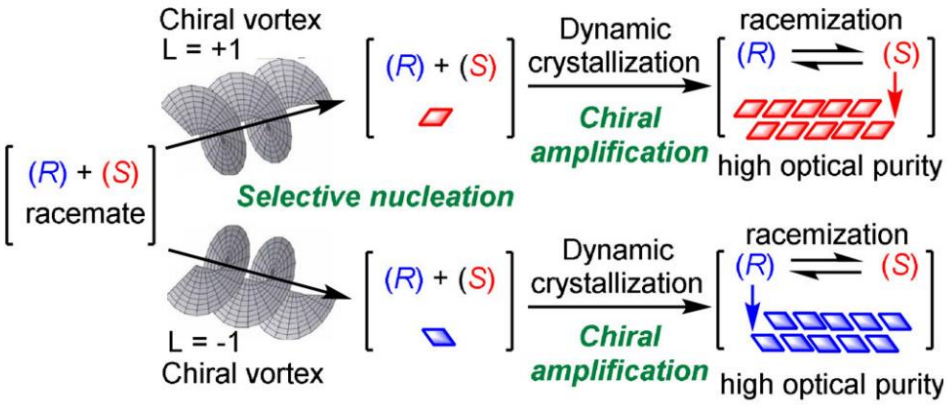


*Fig. 1-28: The schematic of chirality transfer from vortex light to molecules by enantioselective crystal nucleation with dynamic crystallization. Cited from* [148].

In 2021, Sakamoto et al. proposed a novel method for chiral symmetry breaking from a racemate via a vortex light beam. The authors utilized a 532 nm CW vortex beam to determine the seed of the enantioselective crystal nucleation with controlled handedness according to the helicity of the vortex light. Subsequently, the chirality of the molecules of the isoindolinone is thus amplified by the dynamic crystallization, as shown in **Fig. 1-28** [148]. This new strategy provides new possibilities in molecular chirality control through the vortex light, which is potential in the photochemical regulation and paves the way for transferring light chirality to the chemical reaction

process at a molecular scale.

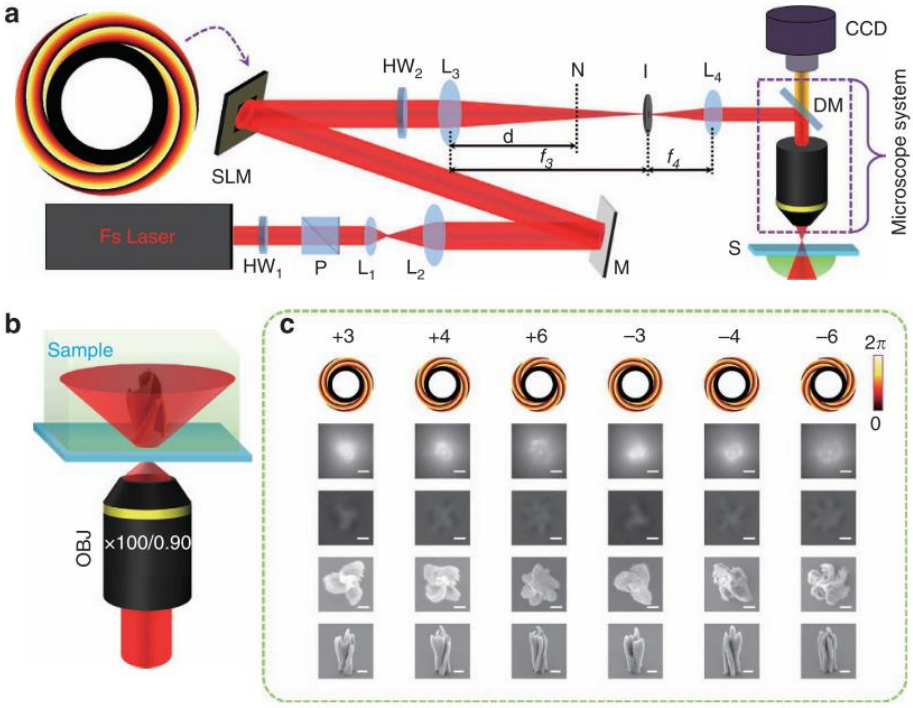


*Fig. 1-29: Structured vortex light writing 3D chiral structures in isotropic materials. (a) The schematics of the fs laser writing system. HW: half-wave plate; P: polarizer; L: lens; M: mirror; SLM: spatial light modulator; I: iris; DM: dichroic mirror; S: sample: CCD: charge coupled device. (b) The schematic of a focus diffracted beam for inducing chiral structures via an objective with a NA of 0.9. (c) The designed holograms (first row), the intensity patterns (second row) and the optical micrographs (third row) of the polymer, the top view (fourth row) and the side view (fifth row) of the 3D chiral structures according to different topological charges are depicted, respectively. Cited from* [149].

Two-photon-polymerization, as an effective method for laser writing complex 3D microstructures such as microchips [150], photonic crystals [151], has also been proved to be an excellent platform for micro-manufacturing chiral objects. In 2013, Gu et al. reported a diffraction-limited non-Airy multifocal arrays fabricated by a spatially shifted vortex beam. Specifically, they shift the spatial position of the vortex beam phase to manipulate the intensity distribution and thus to create the split-ring patterns. This split-ring microstructure array can be obtained by a single exposure of the fs vortex light with predicted phase modulation, which is of great potential in chiral

metamaterials [152]. In 2017, Ni and Wu et al. proposed a 3D chiral microstructure manufacturing strategy in isotropic materials by utilizing a structured vortex fs laser beam [149]. Normally, microstructures fabricated in isotropic materials by two-photon-polymerization are usually non-chiral cylindrical shapes due to the donut intensity profile of the vortex beams. However, the authors developed a coaxial interference technique of a vortex beam and a plane wave for generating a 3D spiral vector field, enabled by applying contrivable hologram patterns consisting of an azimuthal phase on the spatial light modulator. Thus, the 3D chiral structures are demonstrated by the chirality transfer from the 3D structured vortex beams, as depicted in **Fig. 1-29**.

Recent years, symmetry breaking has been found in ultrafast direct writing in inorganic glass materials [153]. Several new innovative discoveries have been reported, for example, Type II nanograting with strong polarization dependence [77], "Quill" writing with writing orientation dependence [154], silica decomposition [12], shear stress induced field [61,155] and efficient anisotropic defects generations [156]. According to the Pierre Curie principle stipulating that the symmetry of the effects is always higher than the symmetry of the causes [157], the nonlinear interaction with infrared light develops the nonlinear optics. A famous example is the spontaneous appearance of the second harmonic creation during the infrared light interaction with matter [158], however, it can be hardly observed in center-symmetric materials. Besides, it is conceivable that chiral light can transfer the chirality to an achiral material. However, without spatial structuration of the chiral light or an amplification process, the chiral modification is of low effectiveness and is hardly to be seen [159].

It has been proved that fs laser can shear the matter in a proper manner in the previous work from our group in 2003 (as subsequently confirmed in 2008) [63,155]. This effect can "cut" the material for moving different sides of the material to opposite directions, which is similar to a scissor. Indeed, by controlling the laser scanning direction and laser polarization, the behavior of shearing matters can be well manipulated, as depicted in **Fig. 1-30**. This discovery is innovative because it is very amazing for an achiral

light beam (axially symmetric intensity profile with linear polarization) to create a chiral strain in an achiral material (pure silica glass) with an achiral interaction manner (namely a normal orthogonal incidence). This observation is more like a torsion leading to strain field in the matter, but it is not the case for creating circular optical properties.

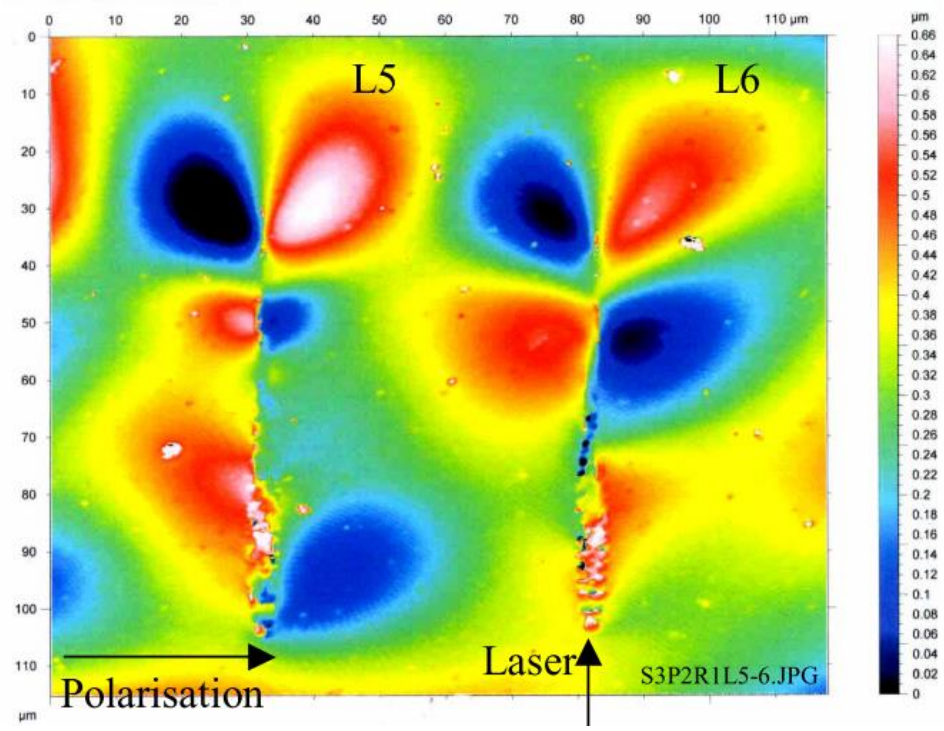


*Fig. 1-30: Topography under an x40 objective. The laser writing configuration: polarization perpendicular to X axis. L5 and L6 with opposite scanning directions. Cited from* [63].

Taylor et al. reported that a circularly polarized light that carries SAMs can somewhat give rise to a permanent patterning of helicity in fs laser direct writing in glass in 2008 [160]. This structural modification consists of highly ordered sub-micrometric structures with chiral shape that records the handedness of the circularly polarized light, as shown in **Fig. 1-31**. However, there are some disordered modifications surrounding the recorded helicity, or we could say that this kind of chiral structures are arising from chaos under a complex multi-pulse ordering mechanism. However, this process is sensitive to a delicate balance between dominant central modification of the

initial circular polarization and proper depolarization for the curled strands.

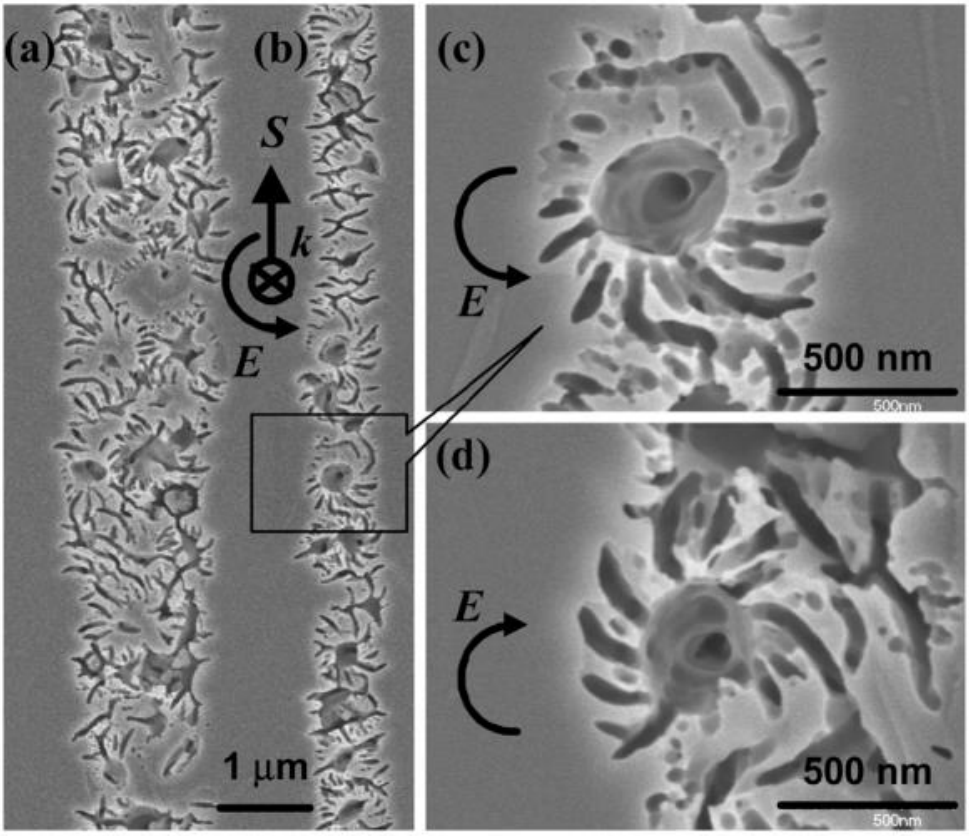


*Fig. 1-31: SEM images of the chiral patterning induced by circularly polarized fs laser writing in silica glass. (a) ~4 μm below the top of the structure, written by 350-nJ pulses. (b) ~2 μm below the top of the structure, written by 200-nJ pulses. (c) Detailed image of one chiral section with right-handedness. (d) Detailed image of one chiral section with left-handedness. Cited from* [160].

Subsequently in 2016, Poumellec et al. revealed that an achiral fs laser beam is capable of chiral optical property (e.g., circular diattenuation) induced in the achiral silica glass [14]. This result is surprising because in general, neither silica nor pure quartz owns circular dichroism in the ultraviolet-visible band. However, the laser writing can imprint a circular dichroism in the silica glass with a high magnitude, as depicted in **Fig. 1-32**. The authors suggested that this chiral optical property is attributed to a volume torque induced by the misalignment of a direct current field and the polarization field of the material. This volume torque thus leads to the chiral behavior of

the molecules, which contributes to the circular optical properties. However, no obvious evidence is observed to confirm that a molecular activity forms the intrinsic chirality, despite of the recorded network of the irradiated glass volume. Therefore, the origin of this fs laser imprinted chirality in achiral material (namely silica glass) remains to be unveiled, and thus being an important topic in this PhD thesis.

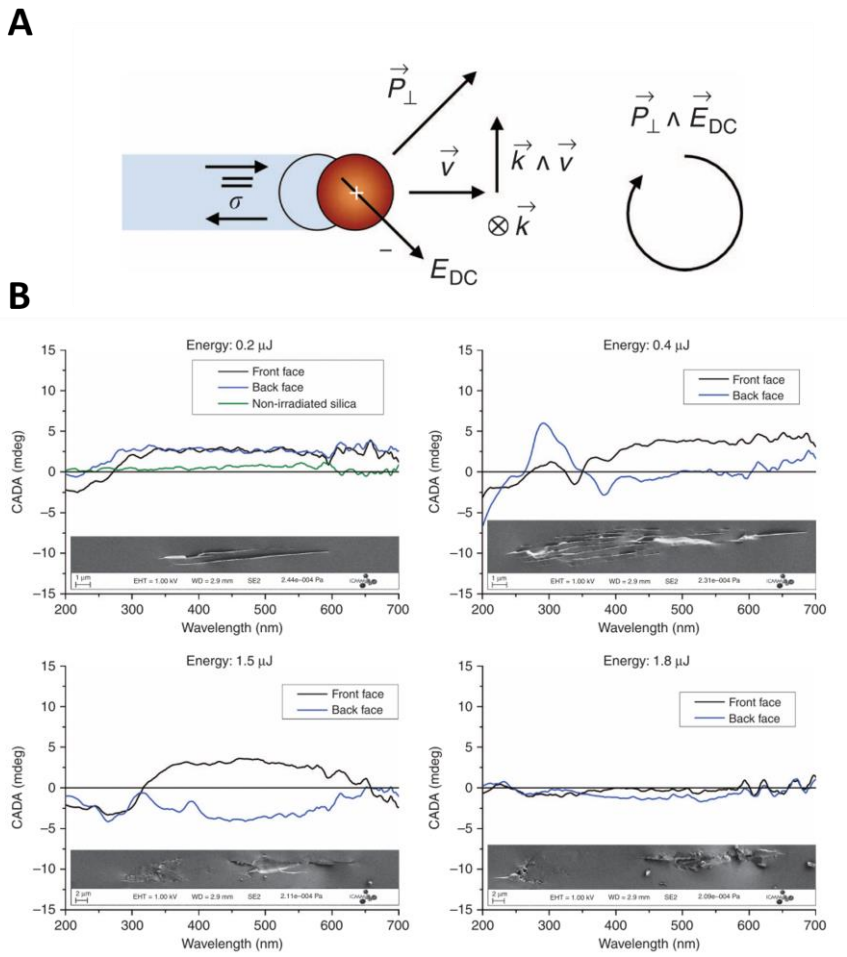


*Fig. 1-32: Fs laser writing chiral optical property in achiral silica glass. (A) Schematics of the combined action of a direct current and stress field contributing to a volume torque. (B) Spectra of circular polarization degrees of attenuation (CADA) and SEM images of the written structures with different pulse energies. Laser parameters: 1030 nm, 300 fs duration, 500 kHz, 0.6 NA, 0.5 mm/s scanning speed, focal depth of 192 µm below the surface of the silica glass, scanning direction and laser polarization are all along the X axis. Cited from* [14].

## I.7 CONCLUSION

The main strategy of the chirality construction is based on symmetry breaking in 3D. However, how to induce the symmetry broken? Or we could ask how to tailor the degree of light-matter interactions with chirality? These questions are essential since the full control of chirality is the key point for unlocking the light manipulation and its photonics manufacturing. The answer should arise from the chirality transfer from matter to light and from light to matter.

Towards controlling the chiral light fields, the chirality should be applied to the matter and subsequently transferred to the light or directly introduce a chiral manner to the matter-light interaction. From the summary of previous research works on the chiral optical fields (especially the optical vortex fields), generation of vector beams are mainly involved by introducing the helical phase or non-symmetric polarization shaping. Another way in fibers is quite same by utilizing micro perturbation to break the equilibrium state of the guiding mode to make the mode coupling take place. But many methods stay only in the creation of vector fields, few work focuses on the altering or dynamic switching of the chiral optical fields.

For the case of light induced chirality in matters, generally it employs two strategies on the light-matter interactions with chirality. One is shaping the light to be a chiral light. Then by using this chiral light to irradiate the matter can make it chiral. Another approach is introducing a chiral structure organized in the light manufacturing process. However, these two processes contain either chiral light or chiral matters. For a case of achiral fs laser written chirality in achiral materials, it still needs to be clarified. What is the clear original mechanism of fs laser direct writing chirality in silica glasses and how to tailor the chiral optical properties remains a fundamental question to be solved in this field.

# Chapter.II EXPERIMENTAL DETAILS AND METHODS

## II.1 INTRODUCTION

This chapter describes the methodology and experimental details that are adopted in this PhD thesis work. Since the PhD thesis work are related to two main parts: chiral optical field manipulation via acousto-optic interactions and fs laser imprinting chirality inside silica materials, the mechanisms of acousto-optic device, fs laser writing system and polarimetric instruments are mainly described.

In Section II.2, we will firstly introduce the acousto-optic interactions in fibers, which contains the basic mechanism of the acousto-optic interaction with different types of acoustic modes. This section provides the information of the acousto-optic device fabrication and the related characteristics. Subsequently in Section II.3, in order to achieve the observation of the transient dynamics of the chiral vortex modes switching process, the time stretched dispersive Fourier transform technique is described. Later in Section II.4, we will introduce the fs laser writing systems that are utilized in this PhD thesis. Two fs laser writing systems are used since I stay both in China and France for carrying out the thesis works during my PhD study. Then, the fundamentals of polarizations in light are introduced including Jones vectors, Stokes vectors and related Mueller matrix methodology in Section II.5. In order to achieve the anisotropic optical properties, a decomposition strategy is necessary to be described. Finally in Section II.6, for experimentally demonstrating and tailoring the fs laser writing anisotropic properties including circular optical properties, polarimetric instruments should be summarized. In this PhD thesis work, we use polarimeters equipped with a "de Sénarmont" compensator and full-wave plate technique. Besides, the experimental identifications of different types of structural modifications are illustrated. Finally, a Mueller spectro-polarimeter (Vis-Near IR polarimeter with 16 elements) with broadband measurement range is introduced.

## II.2 ACOUSTO-OPTIC INTERACTIONS IN FIBERS

Acousto-optic interactions employ the acoustic wave propagation on the optical fiber to manipulate the inner light wave behavior by the acoustically induced dynamic refractive index modulation. As an external manipulation tool, it exhibits diverse unique advantages such as non-destruction, dynamic tunability, switching capability. The pioneered work carried out by B. Y. Kim et al. in 1986 has promoted the acousto-optic interactions in fibers to a new paradigm. With unremitting research of about two decades by the community, acousto-optic interaction has been proved to show great impact in diverse fields ranging from fundamental devices such as tunable filters, super lattice modulators, and heterodyne vibration detectors to functional applications in fiber lasers, e.g., tunable lasers, Q-switch lasers, and polarization control. Recently, acousto-optic interaction in few-mode fibers for HOMs or even vortex modes manipulation has appealed large interests owing to its dynamic tunability. The development of the acousto-optic interactions in fibers is summarized in **Fig. 2-1**.

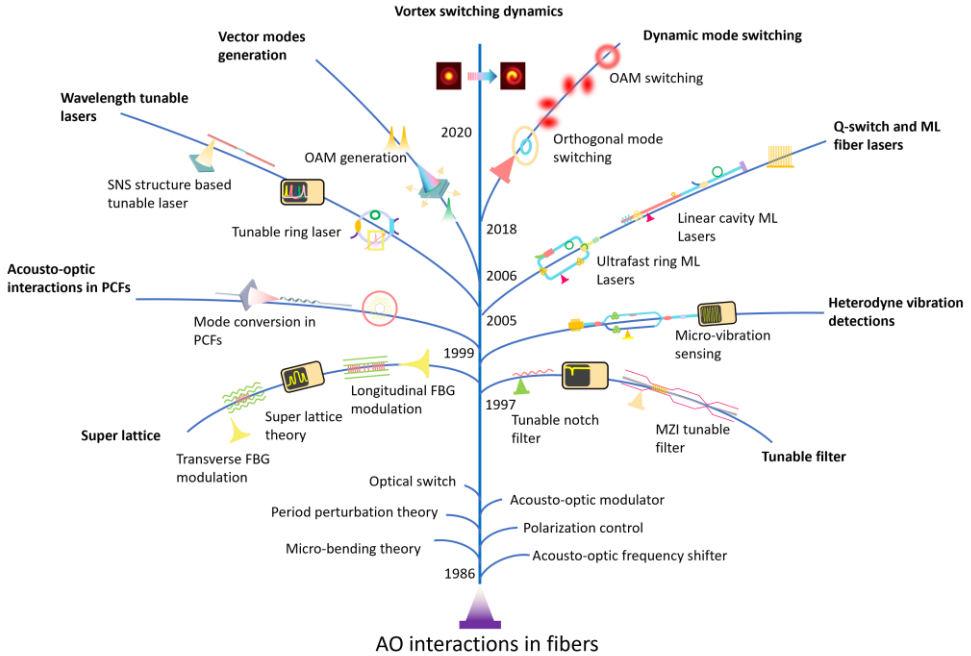


*Fig. 2-1: Summary of the development of acousto-optic interactions in fibers. Cited from* [161].

It is the advanced discovery from Brillouin in 1922 that acoustic waves can interact with light waves that leads to the appreciable frontiers of acousto-optic physics. The acousto-optic interaction in an optical fiber is mainly related to the light diffraction from a travelling periodic modulation of the refractive index along the fiber. To think about this case in a quantum mechanical perspective, the photon-phonon interaction can be considered as the conservations of both energy and momentum due to photon-phonon scattering:

$$\omega' = \omega_0 + \omega_a;\ k' = k_0 + k_a \qquad \text{(Eq. 2-1)}$$

Here, $(\omega', k')$, $(\omega_0, k_0)$, and $(\omega_a, k_a)$ correspond to the frequencies and wavenumbers of diffracted light wave, incident light wave and acoustic wave, respectively. Indeed, in acousto-optic interactions, the periodic refractive index modulation is strongly dependent on the acoustic vibration modes, which can be categorized into three main vibration modes: (1) flexural acoustic vibration [15,162], (2) longitudinal acoustic vibration [163–166], and (3) torsional acoustic vibration [167–172], as shown in **Fig. 2-2**.

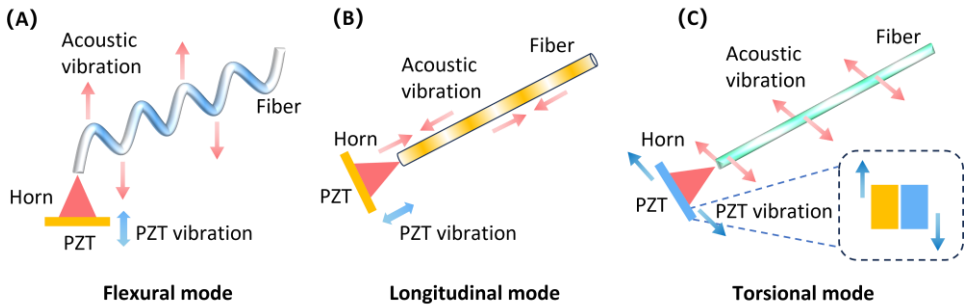


*Fig. 2-2: Illustration of three types of acoustic vibration modes travelling on the optical fibers. (A) Flexural mode. (B) Longitudinal mode. (C) Torsional mode.*

Here, the acousto-optic interactions are mainly excited by applying the acoustic waves on the fibers via an acoustic transducer consisting of a piezoceramic transducer (PZT), a horn and an external radio-frequency electric signal. The frequency of the acoustic wave is determined by the radio-frequency signal. The PZT is the heart component for transferring the electric signal to an acoustic vibration due to the piezoelectric effect. The horn is utilized for amplifying the acoustic wave and guiding the acoustic wave to the fiber media by

adherence using an epoxy gum. Importantly, the material of the horn is mainly silica glass or aluminum to satisfy the impedance matching. The epoxy gum ensures a good connection between the top of the horn and the optical fiber, which leads to a low loss guiding of the acoustic waves. On the other side, a clamp is used for absorbing the acoustic waves to control the length of the region of acousto-optic interactions.

Longitudinal acoustic mode is indeed acoustic pulses that induce an alternation of the medium density. This density modulation thus contributes to the refractive index change. This mode of acousto-optic interaction is mostly utilized in generating superlattice in FBGs. Specifically, it can modulate the side band of the spectroscopic response of the FBGs. The setups and applications are summarized in **Table. 2-1**.

*Table. 2-1 Summary of the devices and applications of longitudinal acoustic mode.*

| Fiber | Frequency (MHz) | $\lambda$ (nm) | Length (cm) | Modes | Applica-tion | Ref. |
|---|---|---|---|---|---|---|
| SM-FBG | 8.02 | 1526.5 | 0.3 | Reflection | Super lattice | [163] |
| SM-FBG | 10/10.7 | 1528 | 0.3 | Reflection | Reflector | [164] |
| SM-FBG | 2.1/2.4/5.6/10 | 1550 | 1 | Reflection | Super lattice | [165] |
| SM-FBG | 1/2.66/5.5 | 1543.2 | 5 | Reflection | Laser | [166] |

SM-FBG: single-mode FBG

*Table. 2-2 Summary of the devices and applications of torsional acoustic mode.*

| Fiber | Frequency (MHz) | $\lambda$ (nm) | Length (cm) | Modes | Applica-tion | Ref. |
|---|---|---|---|---|---|---|
| HBSMF | 1.337 | 1550 | 60 | Polarization | Filter | [168] |
| E-TMF | 3.24/3.4 | 1300 | 25.5 | $LP_{11}$ | Sensing | [169] |
| HBSMF | 2.638-2.788 | 1575 | 82 | Polarization | Filter | [170] |
| HBSMF | 1.189 | 1320 | 49.8 | Polarization | Filter | [172] |

HBSMF: high birefringence SMF; E-TMF: elliptical two-mode fiber

The torsional acoustic mode is demonstrated by using an acoustic transducer with two PZTs oscillating at opposite directions at the same time, which leads to a shear vibration mode of the overall

transducer, as depicted in **Fig. 2-2(C)**. The horn will have a twist force that exhibits an alternative clockwise and anticlockwise orientation. This mode with acoustic perturbation shows high polarization dependence of mode conversion. Therefore, it is widely used in polarization mode conversion or filtering, as summarized in **Table. 2-2**.

*Table. 2-3 Summary of the devices and applications of flexural acoustic mode.*

| Fiber | Frequency (MHz) | Wavelength (nm) | Length (cm) | Modes | Application | Ref. |
|---|---|---|---|---|---|---|
| TMF | 8 | 488 | 7.5 | $LP_{11}$ | Shifter | [15] |
| TMF | 2.51 | 1550 | 4.5 | $LP_{11}$ | Filter | [173] |
| SMF | 1-1.5 | 1532-1550 | 10 | Cladding | Filter | [174] |
| SMF | 1.95-2.45 | 1550 | 8.3 | Cladding | Filter | [162] |
| SMF | 0.90-1.07 | 1490-1610 | 10 | Cladding | Coupler | [175] |
| SMF | 2.384 | 1527.7 | 70 | Cladding | Filter | [176] |
| SMF | 1.3 | 1541.5 | 1.7 | Cladding | Reflector | [177] |
| SMF | 0.9 | 1550 | 4 | Cladding | Sensing | [178] |
| PCF | 7.4 | 633 | 48 | $LP_{11}$ | Sensing | [179] |
| SMF | 0.91-0.99 | 1562-1569 | 6 | Cladding | Laser | [180] |
| EDF | 1.2 | 1550 | 8 | Cladding | Laser | [181] |
| SMF | 1.23 | 1530-1533 | 23.7 | Cladding | Laser | [182] |
| SMF | 1.04-1.07 | 1539-1571 | 13.5 | Cladding | Converter | [183] |
| TMDCF | 0.6-0.9 | 1520-1570 | 30 | OAM | Converter | [143] |
| FMF | 0.82-0.83 | 633 | 4 | OAM | Converter | [184] |
| TMF | 2.687/2.749 | 1040.8 | 50 | CVB | Converter | [185] |

TMF: two-mode fiber; PCF: photonic crystal fiber; TMDCF: two-mode dispersion compensation fiber CVB: cylindrical vector beam.

Besides, the flexural acoustic mode can excite the highest conversion efficiency among all the three acoustic vibration modes. This acoustic mode allows a mode conversion between two co-propagating light modes in the optical fibers. Previously, the flexural mode is utilized for converting fundamental core mode to cladding modes decaying exponentially in the evanescent field for constructing band-rejection

filters [162,186–188]. However, recent studies focus on the light mode conversion between two core propagating modes by applying this flexural acoustic wave on few-mode fibers [20,143,184,185,189]. This strategy provides new possibilities of HOMs generation (or even OAMs) with a dynamic tunability. The setups and applications of flexural acoustic mode are summarized in **Table. 2-3**.

It is commonly believed that the basic principle of the mode conversion caused in an acousto-optic mode converter is micro-bending theory. There is a micro-bending on the fiber medium induced by an asymmetric vibration from the flexural acoustic wave (FAW). The FAW is produced by the radio-frequency signal controlled PZT device and contributes to the mode conversion from fundamental core mode ($LP_{0,n}$ mode) to high-order core modes ($LP_{1,n'}$ modes). In fact, it is the lowest FAW mode ($F_{11}$ mode) travelling on the unjacketed silica fibers that gives rise to the periodic density change. This density modulation is asymmetric respected to the acoustic vibration orientation. The mechanism is related to an acoustically induced displacement vector (AIDV) of $\tilde{u}$. Consequently, the micro-bending induced by the AIDV thus contributes to a permittivity modification $\Delta\varepsilon$. Indeed, the permittivity modification is composed of two terms corresponding to a geometric perturbation term of $\Delta\varepsilon_g$ and an elastic effect term of $\Delta\varepsilon_e$, which can be expressed as [21,161,190]:

$$\Delta\varepsilon(x,y,z,t) = \Delta\varepsilon_g(x,y,z,t) + \Delta\varepsilon_e(z,t) \qquad \text{(Eq. 2-2)}$$

Here, the AIDV caused geometric deformation of the permittivity modifications could be expressed according to the standard framework in the micro-bending principle [21,161,190]:

$$\Delta\varepsilon_g = n_{co} \cdot {k_a}^2 \cdot u \cdot x \qquad \text{(Eq. 2-3)}$$

In the equation, $n_{co}$ refers to the refractive index of the fiber core material. $k_a$ is the wave vector. $x$ represents the x axis. Therefore, the value of the AIDV can be simplified to be $u$, which can be calculated as:

$$u = u_0 \cos(k_a z - 2\pi f_a t) \cdot e^{i\frac{2\pi}{\Lambda}} \qquad \text{(Eq. 2-4)}$$

Here, $u_0$ and $f_a$ are the amplitude and the frequency of the AIDV. Additionally, $\Lambda$ is the period of the acoustically induced fiber grating. Indeed, the periodic modulation of the refractive index based on the acousto-optic interactions in fiber is analogous to a long-period fiber grating however, with unique dynamic tunability. The period can be therefore expressed as:

$$\Lambda = \sqrt{\frac{\pi C_a R_{cl}}{f_a}} \qquad \text{(Eq. 2-5)}$$

Besides, $C_a = 5760\, m/s$ is the velocity of the acoustic wave propagating on the silica materials (i.e., fibers). $R_{cl}$ stands for the radius of the fiber cladding (typically, 125 μm for an un-etched fiber). Importantly, the period of the acoustically induced fiber grating can be controlled easily by the external applied signal, which delivers the original mechanism of dynamic tunability.

The photo-elastic term can be determined by [21,161,190]:

$$\Delta\varepsilon_e = \varepsilon_{co}^2 p k_a u_0 \begin{pmatrix} 0 & 0 & 1 \\ 0 & 0 & 0 \\ 1 & 0 & 0 \end{pmatrix} sin(k_a z - 2\pi f_a t) \qquad \text{(Eq. 2-6)}$$

Here, $\varepsilon_{co}$ refers to the permittivity of the fiber core material. $p$ is the photo-elastic coefficient.

Subsequently, it is necessary to satisfy the phase matching condition for the mode conversion:

$$L_B = \lambda_c \cdot (n_{01} - n_{p,q})^{-1} = \Lambda \qquad \text{(Eq. 2-7)}$$

Here, $L_B$ stands for the beat-length between fundamental core mode and high-order core modes while $\lambda_c$ corresponds to the resonant wavelength. The refractive indices of the fundamental mode and the high-order modes are expressed as $n_{0,n}$ and $n_{p,q}$ $(p, q = 0,1,2,3 \ldots)$, respectively.

The mode conversion efficiency can be calculated according to the incorporation of the identified electric field distributions of the targeted modes, namely $E_{0,1}(x, y)$ and $E_{p,q}(x, y)$:

$$\kappa \propto \frac{\pi}{\lambda_c}\sqrt{\frac{\varepsilon_0}{\mu_0}}n_{co}\int E_{0,1}^{*}(x,y)\cdot\Delta\varepsilon\cdot E_{p,q}(x,y)dxdy \qquad \text{(Eq. 2-8)}$$

$\varepsilon_0$ and $\mu_0$ are the permittivity and permeability in the vacuum, respectively.

The dynamic tunability is the essential, or we could say the unique advantage of a mode converter based on acousto-optic interactions in fibers. Specifically, the dynamic tunability of an acousto-optic mode converter can be identified into three aspects: (1) on/off dynamic switching, (2) resonant wavelength tunability, (3) mode conversion efficiency control. A summary of typical acousto-optic mode conversion is depicted in **Fig. 2-3**.

The first ability enables the switching of the acousto-optic interaction on the fiber. This means, in fact, that the acousto-optic modulation is non-destructive respect to the fiber. The acousto-optic interaction is activated only if the external radio-frequency signal is applied on the PZT, which is quite friendly in some practical situations with requirement of non-destruction of the fiber.

Besides, it is possible to utilize this approach to generate a modulated light signal with coding of different spatial modes, easy obtained by coding on the applied acoustic signal. It in turn provides a strategy of transferring information from electric signals to optical signals propagating inside fibers.

The second tunability of the acousto-optic mode converter is related to the resonant wavelength tunability, which indicates great potentials in wavelength tuning/scanning applications. Since acousto-optic interactions can be utilized to make filters, the tunability is a key property of these novel components, whatever it is a band-rejection filter or a band-pass filter. Besides, a wavelength tunable HOMs and OAM modes are essential laser sources in optical communications system or stimulated emission depletion (STED) microscopy [191]. Typical results of dynamic tunability of resonant wavelength is shown in **Figs. 2-3(E)** and **2-3(F)**.

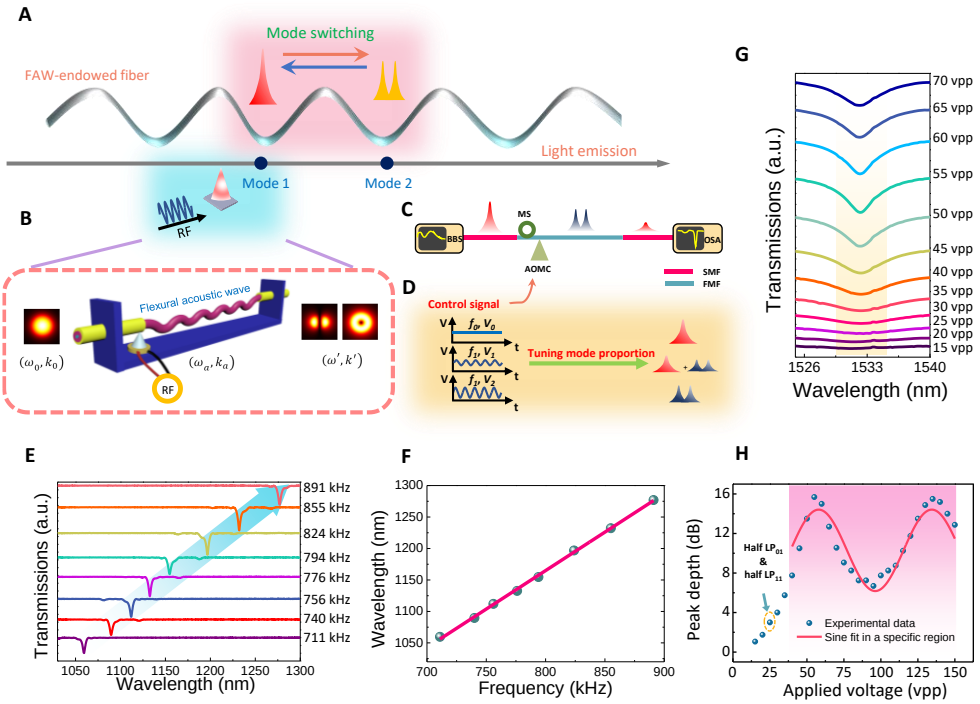


*Fig. 2-3: Illustration of a typical acousto-optic mode converter. (A) Schematic of mode switching by acousto-optic interactions. (B) Illustration of an acousto-optic mode converter device. (C) Schematic of the detecting system of mode switching by an acousto-optic mode converter. (D) Schematic of mode controlling by applying radio-frequency signals. (E) Transmission spectra obtained by applying different frequencies. (F) Experimental result of resonant wavelength evolution at the function of applied frequencies. (G) Transmission spectra obtained by applying different voltages. (H) Experimental result of resident fundamental mode power evolution at the function of applied voltages. Cited from* [161].

The third dynamic manipulation is related to the mode conversion efficiency. In general, the mode conversion efficiency is expected to be ultrahigh, which decides a total energy transfer from one mode to the other. Normally, an acousto-optic mode converter can achieve a mode conversion of >97% (corresponding to a -15 dB resonant peak depth) in a wide tunable wavelength range. With optimized, it can approach a conversion efficiency higher than 99% (respected to -20 dB) at an expense of tunability of wavelength. On the other hand, the acousto-optic mode converter can dynamically adjust the mode conversion from 0% (off state) to the highest efficiency (let's take 97% for example) with simply adjusting the applied voltage, as depicted in **Fig. 2-3(G) and 2-3(H)**. One should notice that the relationship

between the applied voltage and the mode conversion efficiency is not a simple linear connection because of a $\sin^2(\kappa L_{ao})$ term in the transmission calculation [162]. Here, $L_{ao}$ refers to the length of the acousto-optic interaction region.

## II.3 TIME-STRETCHED DISPERSIVE FOURIER TRANSFORM

The dynamic manipulation enabled by the acousto-optic mode converter, especially in ultrafast laser cavities, yielding new physical fundamentals in ultrafast optics. However, to study the complex of this issue, it requires an effective method to observe the dynamics caused by the acousto-optic interactions in the laser cavity.

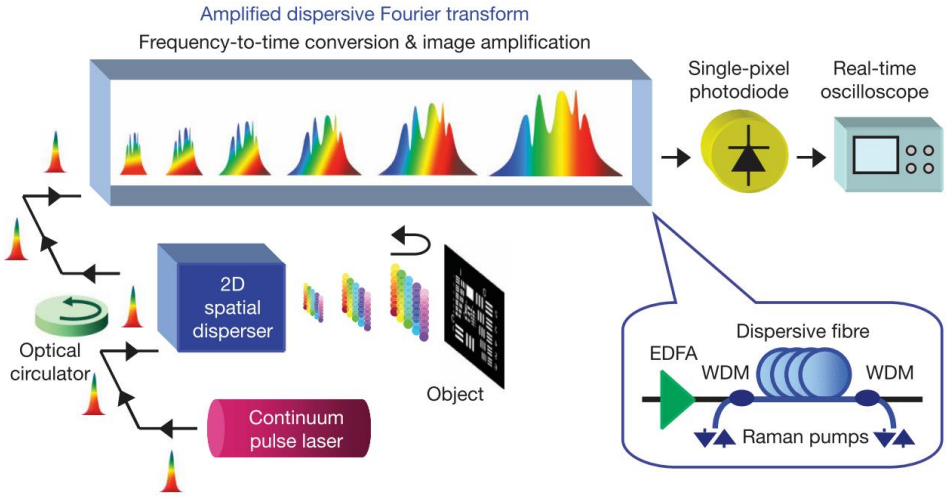


*Fig. 2-4: Illustration of a serial time-encoded amplified microscopy (STEAM) camera system. The STEAM camera contains a dispersive Fourier transformation and amplification process. Cited from* [192].

Transient dynamic process in an ultrafast laser cavity delivers the landscape of the ultrafast pulse behavior and reflects the inner mechanism of the laser pulse activities. However, these behaviors take place within an ultrashort transient time scale, which traditional photoelectric detectors (PDs) are not capable of observation. It is due to the limitations of conventional PDs: (1) narrow electric band widths, (2) limited reading speed from the sensor array, (3) inherent compromise between sensitivity and frame rate [192]. Surprisingly, a time-stretched dispersive Fourier transform technique emerges to be

a great platform for observing the transient dynamic processes.

The time-stretched dispersive Fourier transformation technique provides an elegant way for recording the ultrafast dynamics. The fundamental principle of this technique lies in the heart of dispersive Fourier transform. That is, the pulses in time domain are transferred to frequency domain by a dispersion compensation enabled by a dispersive compensation fiber (DCF) or very long single-mode fibers. Specifically, by means of the high group-velocity dispersion (or we could say temporal dispersion), the DCF can validate a Fourier transform operation, which provides a mapping from spectral information to the time domain [192,193]. Therefore, the spectrum evolutions can be recorded in the sequence of the pulse train, as shown in **Fig. 2-4**. The dynamic evolution can be obtained by enumerating the "spectroscopic pulses" one by one. For this case, the "pulse" duration is not that short for the PDs. That is, one can elegantly receive the "spectroscopic pulses" with a typical data collection speed.

*Table. 2-4 The dynamics observations in mode locking (ML) fiber lasers via dispersive Fourier transformation (DFT) method. DS: dispersive soliton.*

| Laser type | Dynamics | Ref. |
|---|---|---|
| ML fiber laser | Rogue wave formation | [194] |
| Soliton fiber laser | Q-switch and ML build-up | [195] |
| DS fiber laser | DS Molecules build-up | [196] |
| DS fiber laser | DS break-up and collisions | [197] |
| Soliton fiber laser | Soliton explosions | [198] |
| Soliton fiber laser | Soliton triplets vibrating | [199] |
| Bidirectional soliton laser | Bidirectional soliton build-up | [200] |

Previously, the time-stretched dispersive Fourier transform technique is used for real-time imaging (e.g., microfluidic flow observation and

phase-explosion effects detection) [192]. However, it is now appealing a lot of researchers for studying the transient dynamics in diverse ultrafast lasers (especially a large amount of mode-locked fiber lasers). Since the mode-locked lasers could experience a number of instabilities before approaching the ultimate stable mode locking state, the energy oscillation that is strongly dependent on the light wave interactions through nonlinearity, intracavity gain and loss, dispersion can contribute and determine the final mode locking states [201]. The transient dynamics observed by time-stretched dispersive Fourier transform technique are build-up dynamics, rogue wave formation, dispersive soliton formation and break-up, soliton explosions etc., some examples are listed in **Table. 2-4**.

In this PhD thesis, we study on the dynamic control of the light wave oscillating in the laser intracavity (especially in a mode-locked fiber laser cavity). The dynamic switching between different spatial modes will definitely introduce perturbations into the laser cavity, which is very likely to break the initially stable mode locking state due to the "off equilibrium" situation. The spatial mode transformation could lead the mode locked fiber laser back to the initial quantum state and may create new dominant pulses and a subsequent mode locking state of the targeted mode. This process is transient with a total duration time lasting for few milliseconds. However, if one wants to get the whole information of the pulse behaviors, of which each takes place within only few tens of microseconds, conventional PDs cannot achieve. Therefore, we applied the time-stretched dispersive Fourier transform technique.

Experimentally, a DCF with a dispersion ($D$) of $-648\ ps \cdot nm^{-1} \cdot km^{-1}$ and a length ($L_{DCF}$) of ~5 km is utilized and the mapping relationship can be calculated as [21]:

$$\delta t = |D| \cdot L_{DCF} \cdot \delta\lambda = 3.24\ ns \cdot nm^{-1} \cdot \delta\lambda \qquad \text{(Eq. 2-9)}$$

Accordingly, one can easily map the spectrum evolution to the real-time pulses recorded by the real-time oscilloscope. Thus, the full process of the switching dynamics can be observed clearly.

## II.4 FEMTOSECOND LASER DIRECT WRITING SYSTEMS

For carrying out the experiments dedicated to the studies in this PhD thesis, two femtosecond laser writing systems are utilized according to the labs I stayed. One FLDW system is in the group of advanced photonic materials (MAP) at Institut de Chimie Moléculaire et des Matériaux d'Orsay (ICMMO) during my stay in France. Another FLDW system is in Department of Physics in Shanghai University during my stay in China.

### II.4.1 FLDW system in MAP, ICMMO, Université Paris Saclay

This FLDW system is based on a directly diode pumped fiber laser with Ytterbium (Yb) doped gain media (Satsuma HP from Amplitude Systèmes). The laser system delivers a pulsed beam at a central wavelength of 1030 nm with adjustable repetition rates from 200 kHz to 2 MHz. A pulse picker (enabled by an acousto-optic modulator) is utilized to modulate the repetition rate of the laser output, which can reduce the repetition rate to be one single pulse irradiation if required. The average power can achieve 10 W and is always fixed. This power allows an output of 25 μJ/pulse with a repetition rate of 400 kHz or 10 μJ/pulse with a repetition rate of 1 MHz. The detailed information of the parameters is summarized in **Fig. 2-5**.

| | Laser Parameters | | Unit | Target | | *Measurement* | |
|---|---|---|---|---|---|---|---|
| | | | | 400 kHz | 2000 kHz | 400 kHz | 2000 kHz |
| IR | Energy per pulse | | *μJ* | ≥ 25 | ≥ 5 | 26.5 | 27 |
| | Average power | | *W* | ≥ 10 | ≥ 10 | 11.1 | 11.3 |
| | Center wavelength | | nm | 1030 +/- 5 | | 1032.1 | 1032.2 |
| | Bandwidth FWHM | | | ≤ 10 | | 8.6 | 8.9 |
| | Pulse duration | | *fs* | < 500 | | 220 | 240 |
| | Pulse energy over 12h | *Average* | *μJ* | > 25 | > 5 | 27.8 | - |
| | | *RMS* | *%* | < 2 | | 0.08 | |
| | Polarization ratio | | - | > 100:1 | | 625:1 | |
| | $M^2$ | $M^2x$ | - | < 1.30 | | 1.10 | |
| | | $M^2y$ | | | | 1.07 | |
| | Beam diameter | $W_{ox}$ | *mm* | 2 +/- 0.5 | | 1.53 | |
| | | $W_{oy}$ | | | | 1.50 | |
| | Beam ellipticity | | *%* | < 13% | | 1.9 | |
| | Astigmatism | | | < 50% | | 27.8 | |
| | Waist ellipticity | | | < 13% | | 0.1 | |

*Fig. 2-5: Certificate of the Conformance (CoC) of the Satsuma HP laser from Amplitude Systèmes with detailed information of parameters. Cited from* [70].

The pulse width is typically 250 fs of full width half maximum (FWHM)

after amplification and compression. The chirped gratings are utilized and the intra-cavity distance between them is dynamically tunable via a motorized translation stage, which provides the possibility of optimizing the pulse compression correlated to the repetition rate of the laser. The pulse width is once measured by the autocorrelator with an autocorrelation function performed on the typical output from the 1030 nm fs laser. The experimental result is fitted to a Lorentzian function, which shows a pulse FWHM of 341 fs, as depicted in **Fig. 2-6**. This value corresponds to a real pulse width of 221 fs at optimized conditions. The spatial chirp (i.e., wavelength vs position) is around 0.54 nm/mm along x axis and 0.02 nm/mm along y axis, respectively.

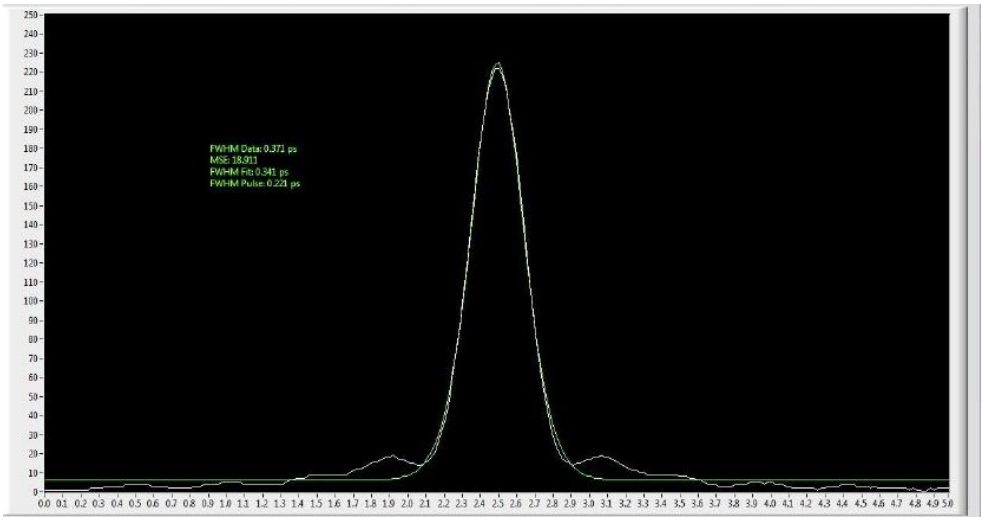


*Fig. 2-6: Laser temporal pulse profile measured by an optical autocorrelator (x axis is time expressed in ps, y axis is intensity with relative units). Cited from* [70].

Initially, the laser beam propagates with its linear polarization oriented in x-y plane (i.e., parallel to the optical table and perpendicular to z axis). A computer controlled half-wave plate and a Glan-laser polarizer are adopted for manipulating the beam power with ensuring the linear polarization of the laser beam. Here, the linear polarization of the laser beam at this position is remained to be horizontal (i.e., along x axis and thus parallel to the ideal plane of the compressor). Subsequently, the laser beam can propagate into two alternative paths: one with acousto-optic modulator for adjusting the final used repetition rate or another without acousto-optic modulator.

The acousto-optic modulator is also manipulated by the computer via a radio-frequency signal. It can generate first-order diffraction beam with diffraction efficiency adjustment in the range of 0-100% of the total laser power. This device can provide a fast switch for the laser beam with a reliable frequency operation up to 2 MHz for the current design. With configuration, direct laser writing Bragg grating waveguides made by periodic segments, volumetric pixels (voxels), and refractive index modulation are possible [202–204].

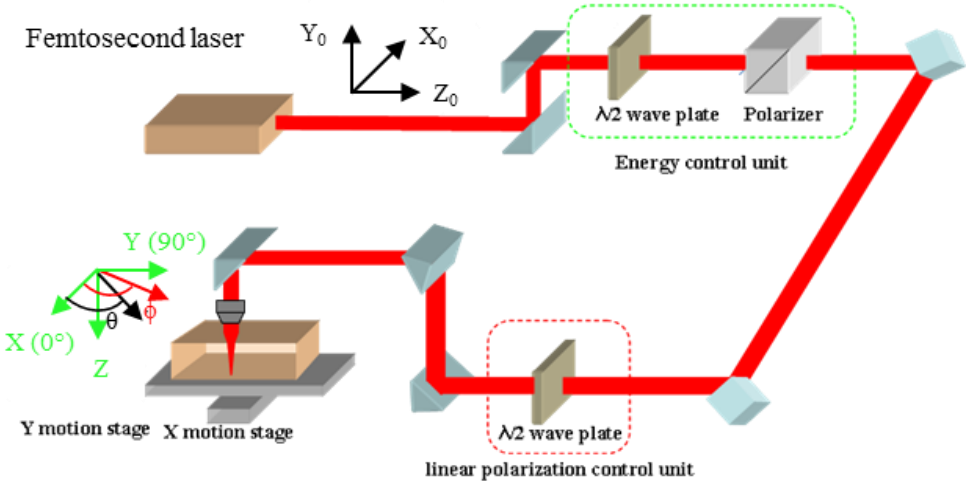


*Fig. 2-7: Schematics of the FLDW experimental setup. Cited from* [70].

The schematics of the experimental setup of the fs laser writing system is depicted in **Fig. 2-7**. The laser beam is aligned in a designed light path experiencing the energy control and linear polarization control. Then it is focused on the targeted silica glass sample mounted on a computer-controlled translation XY-stage with a resolution of 50 nm (one-XY200HA from Newport). The bidirectional repeatability of the stage is 90 nm, and the maximum speed is 200 mm/s. The z axis manipulation is enabled by a computer-controlled stage (UTS100CC from Newport) for focusing the fs light inside the glass sample (typically 200 μm below the upper surface) or realizing the multilayer writing configuration at different z positions. The laser focusing is demonstrated by a series of aspherical lenses with NA ranging from 0.16 to 0.65 with corresponding light spot diameter from 4.5 μm to 1.1 μm (e.g., for 0.55 NA is 1.3 μm). Theoretically, the light spot diameter can be calculated at $1/e^2$ of the

intensity maximum value and can be expressed as:

$$\omega_0 = \frac{M^2\lambda}{\pi \mathrm{NA}} \qquad \text{(Eq. 2-10)}$$

Here, $\omega_0$ is the radius of the spot. $M^2 < 1.1$ is a typical beam quality. $\lambda$ is the wavelength of the laser, in this system it is 1030 nm. The beam is considered as a Gaussian beam.

The linear polarization control unit is consisting of a computer-controlled half-wave plate providing a full adjustment of linear polarization direction with a typical speed of 720°/s via a fast belt driven rotation motor (URB100CC from Newport). By now, due to the design of the system with controlling of pulse energy, repetition rate, scanning, focusing conditions, linear polarization orientation, general laser writing is easy-obtain following any design.

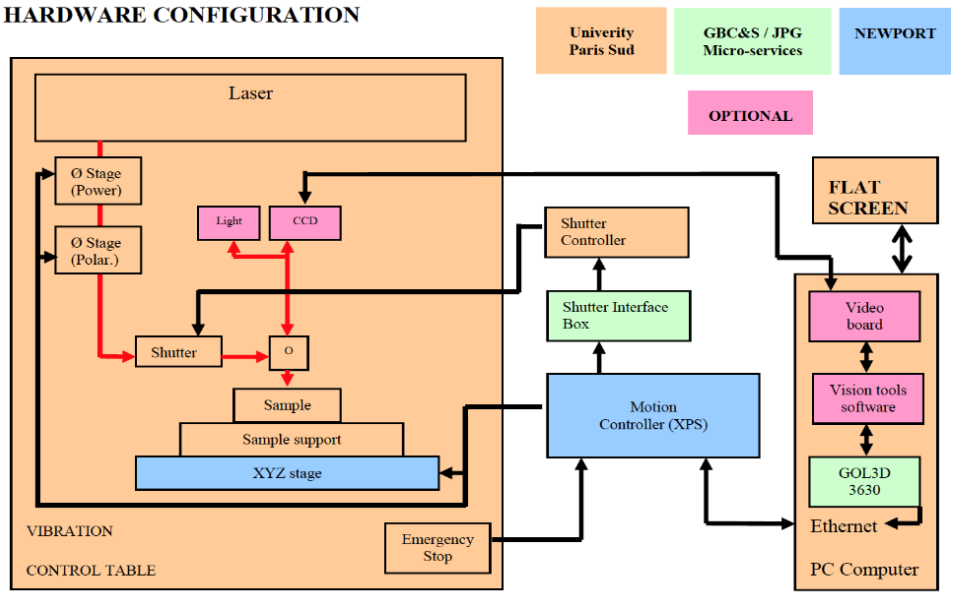


*Fig. 2-8: Schematics of the GOL3D software bus design for assembling and controlling the devices in the laser writing system. Cited from* [70].

Importantly, all the motorized devices are connected to an XPS-8-axis controller from Newport with a computer. A software, namely GOL3D is designed not only for the components assembly but also for translation manipulation of the sample, as depicted in **Fig. 2-8**. This configuration provides possibility in complex trajectories such as

squares, spirals or even patterns. In this complex writing, the writing speed is an important parameter since it affects the pulse accumulation and thus the types of the structural modifications it will induce. Therefore, it requires an identical speed throughout the whole trajectory by optimizing the writing algorithm and the synchronization with the shutter in this case.

### II.4.2 FLDW system in Department of Physics, Shanghai University

The fs laser utilized in this system is a Ti: Sapphire regenerated femtosecond pulsed laser (Spectra-Physics). It consists of three key parts, namely a fs seed pulse oscillator (Mai Tai HP), an ultrafast amplifier (Spitfire Pro-F1KXP) and an optical parameter amplifier (Topas-C).

The fs seed pulse oscillator (Mai Tai HP) delivers an 80±1 MHz 100-fs pulsed light at a center wavelength of 800 nm with a beam quality of $M^2 < 1.1$ and a diameter (according to $1/e^2$ of the intensity maximum value) of 1.2 mm. Then the light is amplified by an ultrafast amplifier (Spitfire Pro-F1KXP) and the laser beam after amplification is typically with a 1 kHz repetition rate, a maximum pulse energy of 4 mJ, a duration of 120 fs, a beam quality of $M^2 < 1.3$. Finally, an optical parameter amplifier (Topas-C) is utilized for wavelength coverage of the kHz ultrafast amplifier and to get the final output light with a maximum pulse energy of 250 μJ. The output light owns a Gaussian intensity profile.

The laser writing system combines a controlling software (Image-Pro MC5.1), an electric shutter (from Newport), a 3D translation stage (H101A Pro Scan model, PSI) and a microscopy system (from Olympus). The schematic of the experimental setup is depicted in **Fig. 2-9**. Firstly, the laser beam is delivered from the Ti: sapphire laser and is narrowed with energy distribution averaged to be uniform by a small aperture. Subsequently, a half-wave plate is used for manipulating the linear polarization orientation of the laser beam while a neutral density filter is utilized for the energy control. A computer-controlled shutter operates the on/off switch of the light. Finally, the light is transmitted through a dichroic mirror and focused into the sample by an objective lens (typically, a 50× objective with a

NA of 0.55, Nikon ECLIPSE 80i). The sample is mounted on the xyz-stage and can be precisely moved with line scanning. The illumination and the charge-coupled device (CCD) enable the monitoring of sample focusing as well as the laser writing process.

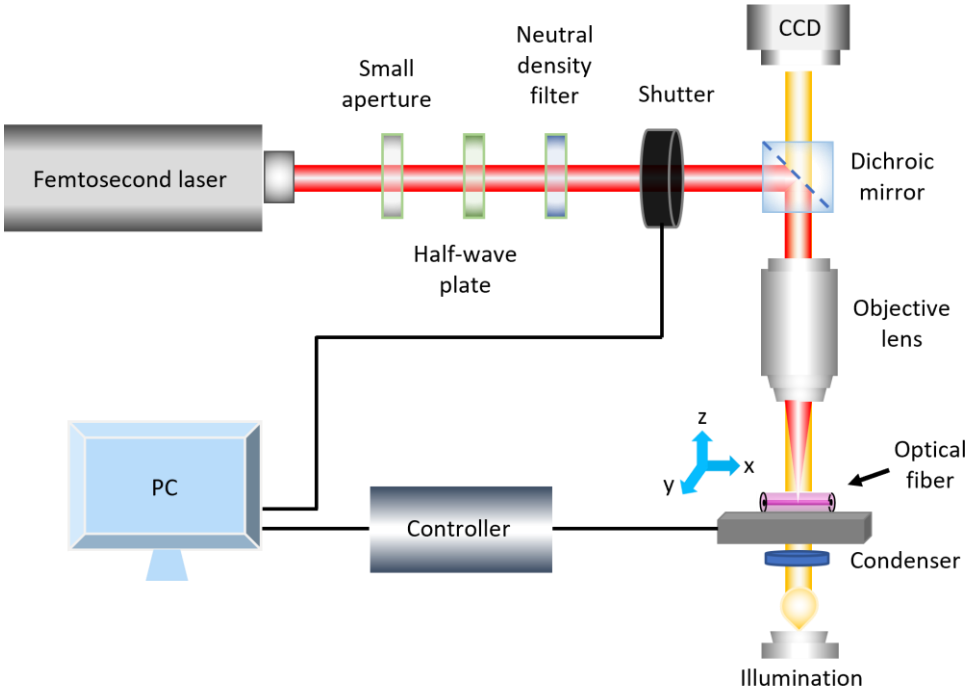


*Fig. 2-9: Schematic of the fs laser writing system. Cited from* [22].

### II.4.3 Sample details

Throughout the works studied in this PhD thesis, the adopted substrates are bulk silica glass and silica fibers. The fused silica glass adopted are Suprasil CG slices (Heraeus, Germany) with typical dimensions of 75 mm length, 25 mm width and 1 mm thickness, of which the double sides are optically polished. The silica fibers adopted are commercial fibers. The utilized single-mode fiber is SMF-28e from Corning with a typical 8.2-μm-diameter core and a 125-μm-diameter cladding. The utilized few-mode fiber is YOFC-4 from YOFC with a typical 18.5-μm-diameter core and 125-μm-diameter cladding.

## II.5 CHARACTERIZATION OF ANISOTROPIC POLARIMETRIC PROPERTIES

### II.5.1 Descriptions of polarization of light

Lightwave, as an electromagnetic wave, has its vibration orientation of vector fields (typically, the electric field) perpendicular to its propagation direction. According to the electric field orientation, light can be categorized into three types: natural light (fully unpolarized light), partially polarized light (not fully polarized light) and polarized light (fully polarized light). Conventionally, scalar polarization fields contain linearly polarized light, elliptically polarized light, and circularly polarized light. This is attributed to the vibration modes of the polarization (generally, it is considered as the electric field). However, for conveniently analyzing and understanding the polarization of the light, it requires an effective mathematical method for descriptions.

#### *II.5.1.1 Jones vector*

Polarization vector emerges to be a significant mathematical solution due to its simple description. In 1940s, R. C. Jones proposed Jones vector to describe the polarization of the light by orthogonal decomposition of the intensity (typically, divided to x axis and y axis). Thus, the electric field can be expressed as:

$$E(r,t) = \begin{pmatrix} E_x \\ E_y \\ 0 \end{pmatrix} e^{i(kz-\omega t)} \qquad \text{(Eq. 2-11)}$$

$E_x$ and $E_y$ are the intensity components of x axis and y axis, respectively. $r = (x, y, z)$ is the vector position of the light. $k$ and $\omega$ are the wave vector and angular frequency, respectively. We assume that the light propagates along z axis, the two-dimensional vector field can be expressed as:

$$E = \begin{bmatrix} E_x \\ E_y \end{bmatrix} = \begin{bmatrix} a_x \cos(\omega t - kz + \varphi_x) \\ a_y \cos(\omega t - kz + \varphi_y) \end{bmatrix} \qquad \text{(Eq. 2-12)}$$

$a_{x/y}$ and $\varphi_{x/y}$ are the amplitude and phase of the component of x/y

axis, respectively. Thus, if one takes a phase difference of $\varphi = \varphi_y - \varphi_x$ and a light intensity of $I_0 = a_x^2 + a_y^2$, the Jones vector can be expressed as:

$$\begin{bmatrix} E_x \\ E_y \end{bmatrix} = \frac{1}{\sqrt{I_0}} \begin{bmatrix} a_x \\ a_y e^{i\varphi} \end{bmatrix} \quad \text{(Eq. 2-13)}$$

Jones vectors possesses a restriction that it can only describe a fully polarized light, despite of its simple and elegant way for describing the state of polarization. However, it is necessary to consider the unpolarized part of the light, which needs a more compatible method.

#### *II.5.1.2 Stokes vector*

Since G. G. Stokes determined a Stokes vector with four elements in 1852, Stokes vector has been proved to be a more commonly used mathematical description for the polarization of light. Stokes vector is represented by a combination of four elements, namely $S_0$, $S_1$, $S_2$, $S_3$ (or also called $I$, $Q$, $U$, $V$):

$$S = \begin{bmatrix} S_0 \\ S_1 \\ S_2 \\ S_3 \end{bmatrix} = \begin{bmatrix} I \\ \rho I cos2\alpha cos2\chi \\ \rho I sin2\alpha cos2\chi \\ \rho I sin2\chi \end{bmatrix} = \begin{bmatrix} I \\ Q \\ U \\ V \end{bmatrix} = \begin{bmatrix} I_x + I_y \\ I_x - I_y \\ I_{+45} - I_{-45} \\ I_- - I_+ \end{bmatrix} \quad \text{(Eq. 2-14)}$$

Here, $I$ is the total intensity of the light. $I_x$ and $I_y$ are the intensities of the linearly polarized light oriented along x axis and y axis, respectively. $I_{+45}$ and $I_{-45}$ are the intensities of the linearly polarized light oriented along 45° axis and -45° axis, respectively. $I_-$ and $I_+$ are the intensities of the circularly polarized light oriented left-handed and right-handed, respectively. $(\rho, 2\alpha, 2\chi)$ are the parameters of spherical coordinates related to the 3D vector of Cartesian coordinates.

Furthermore, the Stokes vector could describe the unpolarized part of the light. Specifically, an unpolarized light possesses same intensity of any direction, thus the $(S_1, S_2, S_3)$ equals to (0, 0, 0). Therefore, if we consider a partially polarized light, it can be expressed as a combination of a fully polarized light and an unpolarized light:

$$S_{par} = \begin{bmatrix} S_0 \\ S_1 \\ S_2 \\ S_3 \end{bmatrix} = S_{pol} + S_{unpol} = \begin{bmatrix} \rho S_0 \\ S_1 \\ S_2 \\ S_3 \end{bmatrix} + \begin{bmatrix} (1-\rho)S_0 \\ 0 \\ 0 \\ 0 \end{bmatrix} \quad \text{(Eq. 2-15)}$$

Here, we could see that ${S_0}^2 > {S_1}^2 + {S_2}^2 + {S_3}^2$. $\rho$ refers to the intensity ratio of polarized light to total light. Actually, it refers to the degree of polarization (DoP) and can be expressed by the Stokes elements as:

$$\rho = \frac{\sqrt{Q^2 + U^2 + V^2}}{I} \quad \text{(Eq. 2-16)}$$

#### *II.5.1.3 Poincaré sphere*

To make the polarization description more intuitive, Henry Poincaré proposed a visualization framework, namely Poincaré sphere, to show the Stokes vectors in a tridimensional space. The graphical description is based on a sphere with a radius of 1. Every point on the surface of the sphere correlates to a certain polarization of a fully polarized light (i.e., with $\rho = 1$). While the points inside the sphere refer to the partially polarized lights, as depicted in **Fig. 2-10**. Worth noting that, the center of the sphere represents the natural light; the two polars refer to two circularly polarized lights; the points on the equator are the lights with linear polarizations.

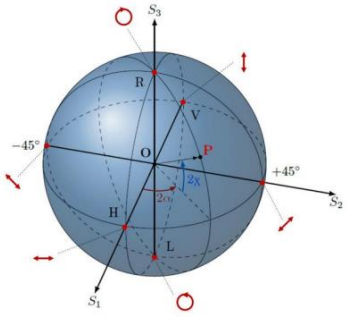


*Fig. 2-10: Illustration of a Poincaré sphere. Cited from* [70].

### II.5.2 Mueller matrix

As there are mathematical descriptions of the state of polarization, it is necessary to construct a mathematical model for the light

propagation in the media with polarizing effects. In general, when the light propagates through a media (a polarizing device), the state of polarization of the light experiences a change related to the polarization effects. This change can be described by a transmission matrix.

A solution that focuses on the Stokes vector called Mueller matrix formalism was proposed by Hans Mueller in 1928. The Mueller matrix possessing four-dimensional elements (4×4), describes the polarimetric interaction between light and the polarizing devices (including the depolarizing effects). The incident light beam expressed as $S_{in}$ will be converted to be an output $S_{out}$ through the polarizing device with a Mueller matrix:

$$S_{out} = MS_{in} = \begin{bmatrix} m_{11} & m_{12} & m_{13} & m_{14} \\ m_{21} & m_{22} & m_{23} & m_{24} \\ m_{31} & m_{32} & m_{33} & m_{34} \\ m_{41} & m_{42} & m_{43} & m_{44} \end{bmatrix} S_{in} \qquad \text{(Eq. 2-17)}$$

It is worth noting that if the light propagates through several polarizing devices one by one, the collective Mueller matrix can be obtained by cascading every Mueller matrix of the polarizing devices:

$$S_{out} = MS_{in} = M_n \cdots M_2 M_1 S_{in} \qquad \text{(Eq. 2-18)}$$

### II.5.3 Mueller matrix decomposition for extraction of polarimetric properties

Indeed, a Mueller matrix itself is quite complex for illustrating the polarimetric properties of the sample at one glance. Thus, to further understanding how the polarizing devices (or the unmeasured samples in the experiments) change the state of polarization of the incident light, a decomposition of Mueller matrix is required. Various decomposition approaches have been studied. In fact, one needs to consider a proper decomposition strategy according to the situation of the sample. That is, each decomposition method has an applicable situation, which is mainly related to the different spatial structure of the sample. In this PhD thesis, we take product decomposition and logarithmic decomposition into account according to our samples.

#### *II.5.3.1 Product decomposition of Mueller matrix*

Product decomposition is usually employed in characterizing the samples with their polarimetric properties parallel to the plane of probe light propagation. The most widely used product decomposition method (also called polar decomposition) was proposed by Lu and Chipman [205]. The product decomposition method got its name since it regards the sample as different polarimetric parts that interact with the incident light. These polarimetric parts can be expressed as a well-defined basic polarimetric properties with their Mueller matrix just like a product from the raw Mueller matrix. Typically, they are composed of three representative properties: a di-attenuator, a retarder, and a depolarizer. Commonly, the ordering of these polarimetric properties could lead to different results, however, Goudail et al. suggested an ordering of depolarizer, retarder, di-attenuator since it contains physical meanings for general optical devices [206]:

$$M = M_\Delta M_r M_d \qquad \text{(Eq. 2-19)}$$

$M_\Delta$ is the depolarizer of the sample, which determines its depolarizing effect. $M_r$ is the retardation property of the sample, which, in a more complex decomposition approach, can be further decomposed to be a linear retarder and a circular retarder. $M_d$ refers to the di-attenuation effect of the sample and as the same it can be further divided into a linear di-attenuator and a circular di-attenuator.

If the di-attenuator and the retarder are expressed in ideal form, the depolarizer is not able to achieve an ideal form due to the polarizance of the Mueller matrix. The depolarizer component in each sample contains both the depolarizing effect caused by the scattering and the polarizance. Thus, the depolarizer component $M_\Delta$ can be expressed by:

$$M_\Delta = \begin{bmatrix} 1 & \mathbf{0}^T \\ \boldsymbol{P} & \boldsymbol{m}_\Delta \end{bmatrix} \qquad \text{(Eq. 2-20)}$$

$\boldsymbol{m}_\Delta$ indicates the depolarizing effect while $\boldsymbol{P}$ refers to the polarizing direction of the polarizance.

### *II.5.3.2 Logarithmic decomposition of Mueller matrix*

Logarithmic decomposition is suitable for the samples that contain polarizing and depolarizing effects together with distributing uniformly across the probing direction of the sample configuration. First logarithmic decomposition method was proposed for linear optically anisotropic samples with non-depolarizing effects and later for fully polarized light. Recently, it has been completely developed by R. Ossikovski with depolarizing media [207]. Subsequently, an interesting revision of the concept from O. Arteaga leads to a modern formalism of the logarithmic decomposition strategy [208]. The logarithmic decomposition considers the samples with continuous media (or homogenous media) so that the gradient of Mueller matrix along the probe light propagating direction, i.e., z axis can be obtained by:

$$\frac{d\boldsymbol{M}(z)}{dz} = \boldsymbol{m} \cdot \boldsymbol{M}(z) \qquad \text{(Eq. 2-21)}$$

Here, $\boldsymbol{M}(z)$ is the Mueller matrix of the sample while $\boldsymbol{m}$ is the differential matrix. The Mueller matrix can be further expressed by using the exponential function:

$$\boldsymbol{M}(z) = \exp\left(\boldsymbol{m} \cdot z\right) \qquad \text{(Eq. 2-22)}$$

Thus, we can define a logarithmic matrix by:

$$\boldsymbol{L} = \boldsymbol{m} \cdot z = \mathrm{In}[\boldsymbol{M}(z)] \qquad \text{(Eq. 2-23)}$$

Indeed, the differential matrix of $\boldsymbol{m}$ contains the elementary properties of the sample in per unit of length along the z axis, including linear birefringence along x-y coordinates (LB), linear birefringence along 45°-135° axes (LB'); linear dichroism along x-y coordinates (LD), linear dichroism along 45°-135° axes (LD'); circular birefringence (CB), circular dichroism (CD), and isotropic absorption ($\alpha$).

In the case of samples with depolarizing effects, the differential matrix is assumed as around an average value, namely $\langle \boldsymbol{m} \rangle$. It contains a statistical fluctuation of the matrices that is necessary to consider the multiple realizations or paths that a photon could

experience when coming across the sample. Specifically, the fluctuations can be expressed as a statistic variance matrix:

$$\boldsymbol{m} = \langle \boldsymbol{m} \rangle + \Delta \boldsymbol{m} \qquad \text{(Eq. 2-24)}$$

A first approximation related to the Mueller matrix with the exponential of the matrix m times of the thickness can be considered when assuming the fluctuations are sufficiently small:

$$\boldsymbol{L}(z) = \boldsymbol{L_m}(z) + \boldsymbol{L_u}(z) = \langle \boldsymbol{m} \rangle z + \frac{1}{2}\langle \boldsymbol{\Delta m}^2 \rangle z^2 \qquad \text{(Eq. 2-25)}$$

Here, $\boldsymbol{L_m}$ and $\boldsymbol{L_u}$ represent the G-antisymmetric and G-symmetric components of the logarithmic matrix $\boldsymbol{L}$, which can be expressed as:

$$\boldsymbol{L_m} = \frac{1}{2}(\boldsymbol{L} - \boldsymbol{G}\boldsymbol{L}^T\boldsymbol{G})$$

$$\boldsymbol{L_u} = \frac{1}{2}(\boldsymbol{L} + \boldsymbol{G}\boldsymbol{L}^T\boldsymbol{G}) \qquad \text{(Eq. 2-26)}$$

Minkowski metric matrix is $\boldsymbol{G} = diag(1, -1, -1, -1)$.

If the sample does not contain depolarizing effect, $\langle \boldsymbol{\Delta m}^2 \rangle = 0$ leads to $\boldsymbol{L_u} = 0$ and $\boldsymbol{L_m} = \boldsymbol{L}$. This in turns indicates that the $\boldsymbol{L_m}$ matrix contains all the elementary polarimetric properties of the sample, which can be expressed as:

$$\boldsymbol{L_m} = \begin{bmatrix} 0 & LD & LD' & CD \\ LD & 0 & CB & -LB' \\ LD' & -CB & 0 & LB \\ CD & LB' & -LB & 0 \end{bmatrix} \qquad \text{(Eq. 2-27)}$$

If the sample contains the depolarizing effect, $\langle \boldsymbol{\Delta m}^2 \rangle \neq 0$ indicates that the diagonal elements of the $\boldsymbol{L_u}$ matrix represent the depolarization coefficients with a quadratic dependence of the z distance: $diag(\boldsymbol{L_u}) = (0, \alpha_1, \alpha_2, \alpha_3)$.

### II.5.4 List of anisotropic properties

In order to characterize the polarimetric properties of the fs irradiated samples, the linear and circular anisotropic properties are extracted from the Mueller formalism.

*Table. 2-5. Linear and circular optical properties [23].*

| Property | Definition | Commonly described in polarimetry | Unit |
|---|---|---|---|
| **LB** (linear birefringence) | $\Delta n_L = (n_x - n_y)$ | $LB = \frac{2\pi}{\lambda}(n_x - n_y) \cdot d$ | radians |
| **LB'** (45°-linear birefringence) | $\Delta n_{L'} = (n_{45°} - n_{-45°})$ | $LB' = \frac{2\pi}{\lambda}(n_{45°} - n_{-45°}) \cdot d$ | radians |
| **TLB** (total linear birefringence) | $\Delta n_{TLB} = (n_e - n_o)$ < *uniaxial material*> | $TLB = \sqrt{LB^2 + LB'^2}$ | radians |
| **TLB fast axis angle** | *Lower refractive index axis* | $\theta_B = \frac{1}{2} \cdot arctan\left(\frac{LB}{LB'}\right)$ | degrees |
| **LD** (linear dichroism) | $\Delta \kappa_L = (\kappa_x - \kappa_y)$ | $LD = \frac{2\pi}{\lambda}(\kappa_x - \kappa_y) \cdot d$ | radians |
| **LD'** (45°-linear dichroism) | $\Delta \kappa_{L'} = (\kappa_{45°} - \kappa_{-45°})$ | $LD' = \frac{2\pi}{\lambda}(\kappa_{45°} - \kappa_{-45°}) \cdot d$ | radians |
| **TLD** (total linear dichroism) | $\Delta \kappa_{TLD} = (\kappa_{high} - \kappa_{low})$ | $TLD = \sqrt{LD^2 + LD'^2}$ | radians |
| **TLD fast axis angle** | *Lower attenuation axis* | $\theta_D = \frac{1}{2} \cdot arctan\left(\frac{LD}{LD'}\right)$ | degrees |
| **CB** (circular birefringence) | $\Delta n_C = (n_- - n_+)$ | $CB = \frac{2\pi}{\lambda}(n_- - n_+) \cdot d$ | radians |
| **Optical rotation** | / | $\theta_{rot} = \frac{\pi}{\lambda}(n_- - n_+) \cdot d \cdot \frac{180°}{\pi}$ | degrees |
| **CD** (circular dichroism) | $\Delta \kappa_C = (\kappa_- - \kappa_+)$ | $CD = \frac{2\pi}{\lambda}(\kappa_- - \kappa_+) \cdot d$ | radians |

$n_{[]}$: refractive index; $\kappa_{[]}$: absorption index; $d$: thickness of anisotropic layer; $\lambda$: probe light wavelength; ***x***: *x* axis; ***y***: *y* axis; ***e***: extraordinary light; ***o***: ordinary light; "-": left-handed; "+": right-handed

Accordingly, all the anisotropic properties are described as phase

difference because it is more practical for polarimetry. Besides, all the anisotropic properties discussed in this PhD thesis are summarized in **Table. 2-5** with their definitions and units.

## II.6 POLARIMETRIC INSTRUMENTATION

Polarimeter, as the effective instrumentation for characterizing the polarimetric properties, has been developed to diverse categories. Initially, Stokes polarimeter can easily come to mind with its complete theory and simplicity. In general, Stokes polarimetry contains a single optical path with a polarization state analyzer (PSA) to identify the elements of the Stokes vectors, namely (I, Q, U, V). The PSA can be a succession of retarders, aiming to obtain the linear and circular retardation together with their orientations and a linear polarizer to identify the di-attenuation effects. Stokes polarimeters are widely used in remote sensing, light source characterization, and astronomy [209]. However, it does not contain an illumination component.

Then, a type of polarimeter with illumination part emerges to be a novel strategy since the illumination part and analysis part can be both well-controlled. The illumination part contains the polarization state generation (PSG) with well-defined polarization states. The sample is inserted between the PSG and the PSA. Therefore, the PSA can record the polarizing effects on the incident light caused by the sample. Normally, the polarizing effects can be calculated from the obtained matrix of the sample.

A Mueller polarimeter based on Mueller matrix method, is a modern polarimeter since it can also measure the partially polarized light. That is, it allows the sample to carry depolarizing effects. It commonly obtains a 4×4 Mueller matrix to depict the polarizing effects of the sample. Regarding the Mueller polarimeter, it could be in two different forms: spectroscopic Mueller polarimeter and imaging Mueller polarimeter. Specifically, the spectroscopic Mueller polarimeter gives the information within a wavelength range (typically in visible band and near infrared band), which is enabled by a wavelength scanning during the measuring process. The imaging Mueller polarimeter provides the possibility of spatial distribution of the polarizing effects in the sample.

### II.6.1 Polarimetric microscopy based on a "de Sénarmont" compensator

A "de Sénarmont" compensator employs a highly precise quarter-wave plate (typically, a quarter-wave birefringent quartz or mica crystalline plate), together with a rotation analyzing polarizer with high-resolution 180-degree rotation capability. This device provides the measurement of quantitative retardation with an accuracy of one thousandth of a wavelength or even less. It is designed to measure the crystals, fibers, optical strain, or even living organisms for birefringence detecting at an optical probe light at 550 nm in the green light region. However, the probing light can be other wavelength when the quarter-wave plate is changed accordingly. The "de Sénarmont" compensator allows emphasizing of the contrast to detect the weak birefringent samples.

As described from the Olympus resource center, the "de Sénarmont" compensator lies on the principle: the electric vector of the elliptically (or circularly) polarized light that emerges after the sample is superimposed on the electric vector of the circularly polarized light induced from the precise quarter-wave plate. This superimposing of the electric vectors leads to a vibration azimuth of the linearly polarized light that generated by the first polarizer, as depicted in **Fig. 2-11**.

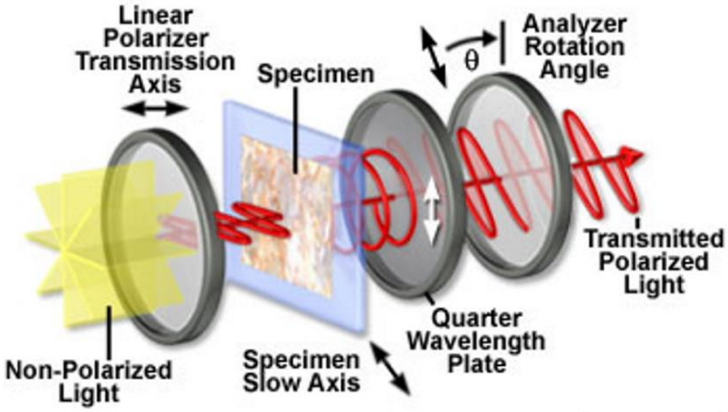


*Fig. 2-11: Illustration of principle of the "de Sénarmont" compensator. Cited from http://www.olympusmicro.com/.*

Specifically, in order to get the linear birefringence and the related

optical path difference of the sample, the "de Sénarmont" compensator is sandwiched in a crossed polarized microscopy after adjusting the slow axis and sign of birefringence by a first-order retardation plate (detailed information in the next section). The probe light is linearly polarized with an orientation according to the polarizer. The subsequent birefringent sample will convert the linearly polarized light into an elliptically polarized light (or circularly polarized light if the sample is just a quarter-wave plate). Then the precise quarter-wave plate will reconvert the elliptically polarized light back into linearly polarized light with an azimuth rotation related to the birefringence information, which can be recorded by rotating the 180-degree analyzer. That is, the azimuth of the output linearly polarized light measured by the rotating analyzer is a direct function of the optical path difference.

The rotation angle obtained in the analyzer with an extinction is indeed one-half value of the full phase shift between ordinary and extraordinary wavefronts when the probe light propagates through the sample, i.e., $\theta = \phi_l/2$. Thus, the related retardation $R$ with a unit of nm can be expressed as:

$$R = \Delta n \cdot d = \theta \cdot \frac{\lambda}{\pi} \qquad \text{(Eq. 2-28)}$$

Or if $\theta$ is expressed in degree, the $R$ should be:

$$R = \Delta n \cdot d = \theta \cdot \frac{\lambda}{180°} \qquad \text{(Eq. 2-29)}$$

Here, $\Delta n$ is the birefringence while $d$ is the length of the measured distance (typically is the thickness of the sample). $\lambda$ is the probe light wavelength.

For example, several lines written by fs laser are depicted in **Fig. 2-12**. The green interference filter in the measuring system has a narrow bandpass at 550 nm. In this example, the measured azimuth angle of the analyzer is 78.7°, which indicates the retardation of the lines is approximately 240 nm at the probe wavelength of 550 nm. For more accurate results, several trials can be demonstrated to get an average value, or one can rotate the sample with 90° and attempt an opposite

direction of the rotation of the analyzer for extinction.

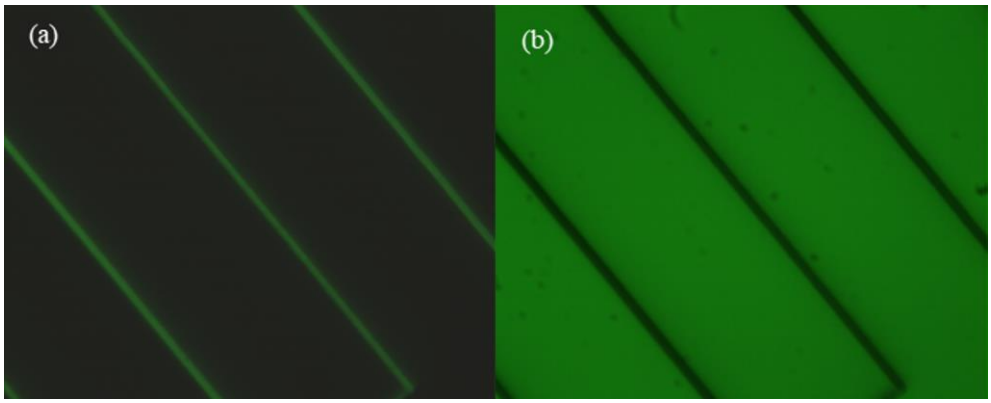


*Fig. 2-12: Microscopic images of fs written fine lines inside a silica slide measured by the crossed polarizer microscopy equipped by a "de Sénarmont" compensator. (a) The image under crossed polarizers with background fully dark. (b) The image under an extinction mode by rotating the analyzer with the lines fully dark. Cited from* [70].

### II.6.2 Full-wave retardation plate

In fact, it is necessary to get the prior knowledge of the sign of birefringent property in the sample for finding the extinction angle of the analyzer rotation (since different rotation direction of the analyzer gets different result of the retardation). For example, a same rotation angle obtained from the analyzer can be derived from an extinction of a sample with positive birefringence that retards the wavefront or a sample with negative birefringence that advances the wavefront. We cannot easily distinguish them.

Here, a full-wave retardation plate substitutes the "de Sénarmont" compensator in the optical path between the rear aperture of the objective and the analyzer. Thus, an optical path difference (exact wavelength is dependent on the manufacturer, here is 530 nm) is introduced to the entire wavefront field. This technique is utilized to determine the index ellipse orientation caused by the birefringent sample before the quantitative retardation measurement by "de Sénarmont" configuration. The full-wave plate is made of thin anisotropic quartz with precise thickness according to the wavelength. It is inserted between two crossed polarizers with diagonally distributed.

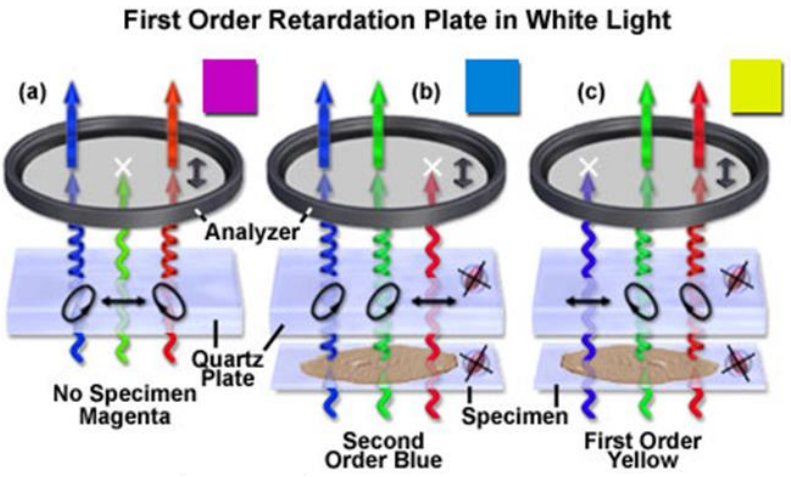


*Fig. 2-13: Principle of the first order full-wave retardation plate. Cited from http://www.olympusmicro.com/primer/techniques/polarized/firstorderplate.html.*

The principle of this technique is depicted in **Fig. 2-13**. Specifically, the polarized white light can be symbolized with three wavefronts, namely blue, green, and red lights. When probe light passes through an isotropic sample (or no sample), the background exhibits a magenta color because the green light is blocked. When the slow axis of the sample is parallel to the full-wave plate, the red light is blocked, and the observed output light is blue. On the contrary, when the slow axis of the sample is perpendicular to the slow axis of the full-wave plate, the blue part will be linearly polarized and blocked. Thus, the result emerges to be yellow.

### II.6.3 Experimental identification of different modification types written by fs laser

In order to achieve the targeted structural modifications written by our fs laser writing system, it is necessary to identify the damage thresholds of the fs written structure types and thus determine the modification window, especially for the Type II window. For demonstrating the calibration of damage thresholds, we set a series of laser writing parameters including polarization, repetition rate and pulse energy. Here, the polarization configuration is defined as "scanning direction + polarization direction", e.g., "Xx" ("Xy") configuration refers to a scanning direction along x axis and the polarization orientation is along x (y) axis. Additionally, the speed is

set according to the repetition rate by fixing the overlapping rate equals to 1000 pulses/μm. The specific parameters are depicted in the **Table. 2-6**.

In this laser writing configurations, we obtain the identification of Type II, Type III, and heat accumulation modifications in the experiment. However, Type I structures are not observed, which is mainly attributed to the fixed overlapping rate (not low enough to excite Type I structures). Then we characterize the modified structures by the microscopy with equipping of crossed polarizers, full-wave plate, and "de Sénarmont" compensator. As depicted in **Fig. 2-14**, clear Type II structures are obtained by both "Xx" and "Xy" writing configurations. As introduced in the previous section, the full-wave retardation plate technique is utilized to confirm the sign of the birefringence of the Type II structures. **Fig. 2-14(A)** exhibits clear yellow color in the laser irradiated line regions indicates the slow axis of Type II nanograting is perpendicular to the slow axis of the full-wave plate, which agrees well with the Xx configuration. Additionally, **Fig. 2-14(B)** shows a blue color of Xy written Type II nanograting with a slow axis parallel to the slow axis of the full-wave plate.

*Table. 2-6. List of the main parameters employed in the calibrations.*

| Conf. | Pulse energy (μJ) | NA | RR (kHz) | Scanning speed (mm/s) | Overlap (pulse/μm) | Pitch (μm) | Depth (μm) |
|---|---|---|---|---|---|---|---|
| Xx | 0.0125-5 | 0.6 | 10 | 0.01 | 1000 | 1 | 200 |
| | | | 50 | 0.05 | | | |
| | | | 100 | 0.1 | | | |
| | | | 250 | 0.25 | | | |
| | | | 500 | 0.5 | | | |
| | | | 1000 | 1 | | | |
| Xy | 0.0125-5 | 0.6 | 10 | 0.01 | 1000 | 1 | 200 |
| | | | 50 | 0.05 | | | |
| | | | 100 | 0.1 | | | |
| | | | 250 | 0.25 | | | |
| | | | 500 | 0.5 | | | |
| | | | 1000 | 1 | | | |

Conf.: configuration; NA: numerical aperture; RR: repetition rate.

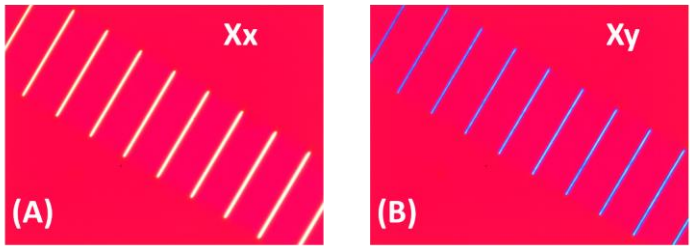


*Fig. 2-14: Crossed polarizer microscopic image of Type II nanograting structures with a full-wave plate: (A) Xx configuration. (B) Xy configuration.*

When the pulse energy approaches the T3 threshold, Type III voids caused by micro-explosion can be observed under both Xx and Xy configurations, as shown in **Figs. 2-15(A) and 2-15(C)**, respectively. The laser track is filled with a series of voids in the irradiated line regions. When the pulse energy increases furthermore, heat accumulation is achieved. In the heat accumulation region, the laser track possesses an obvious spatial broadening profile due to the thermal effects, as depicted in **Figs. 2-15(B) and 2-15(D)**. Since these modifications do not have apparent birefringent properties, they are dark as the background in the crossed polarizers configuration.

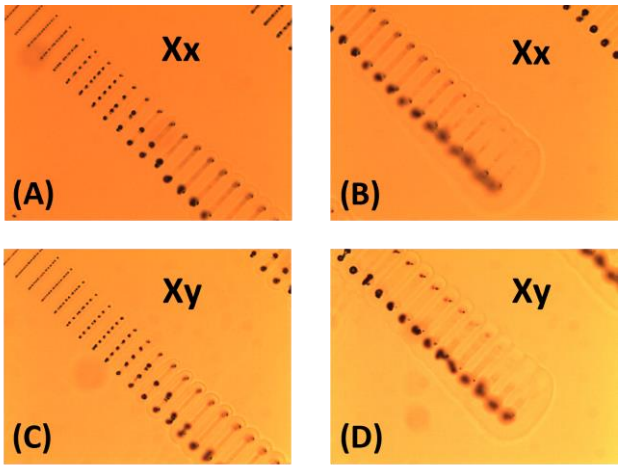


*Fig. 2-15: Characterizations of Xx and Xy configurations fs laser written Type III voids structures and heat accumulation structures by the ordinary microscopy. (A) Ordinary microscopic image of Type III void structures written by Xx configuration. (B) Ordinary microscopic image of heat accumulation structures written by Xx configuration (C) Ordinary microscopic image of Type III void structures written by Xy configuration. (D) Ordinary microscopic image of heat accumulation structures written by Xy configuration.*

To quantitatively identify the modification window, the modification types on the dependence of laser parameters are summarized in **Fig. 2-16** with both Xx and Xy configurations.

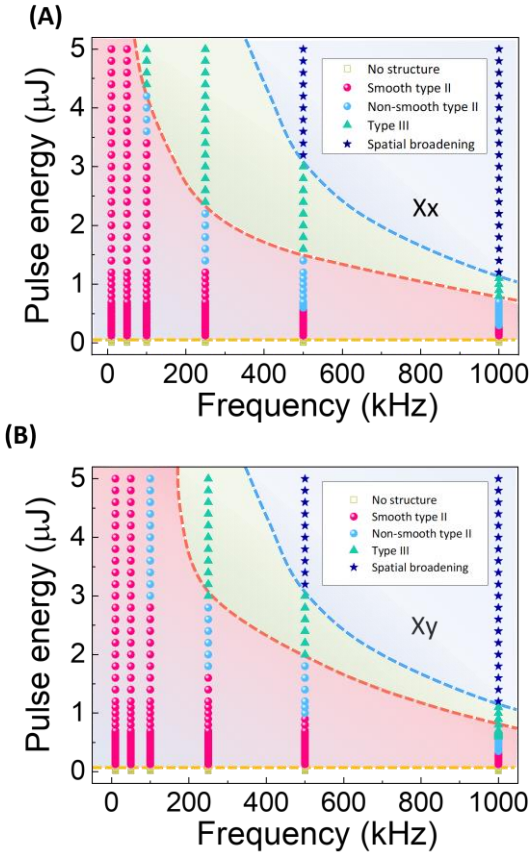


*Fig. 2-16: Summary of fs laser modification type window dependent on different laser parameters. (A) Modification type window with a Xx configuration. (B) Modification type window with a Xy configuration.*

From the experimental results, lower repetition rate is more appropriate for the Type II nanograting imprinting. Specifically, laser writings at the repetition rate of 10 kHz and 50 kHz allow smooth Type II nanograting modifications in the whole calibrated pulse energy range (i.e., up to 5 μJ/pulse). Non-smooth Type II nanogratings start to emerge at high pulse energies at the repetition rate of 100 kHz. At a repetition rate of 1000 kHz, only few pulse energies enable the modification of Type II structure, which is not an appropriate parameter as we expected. The results of Xx configuration and Xy configuration are quite similar, despite of some

small differences especially located in the identification of non-smooth Type II structures and Type III voids structures.

Since Type II nanograting structures exhibit strong birefringent properties, the retardance measurement is very important, which is characterized by the polarimetric microscope equipped with the "de Sénarmont" compensator. Benefit from the identification from full-wave plate characterizations, the rotation direction of the analyzer for extinction is known and the rotated azimuth angle can be easily obtained. Thus, the retardance measurements are summarized in **Fig. 2-17** with both Xx and Xy configurations.

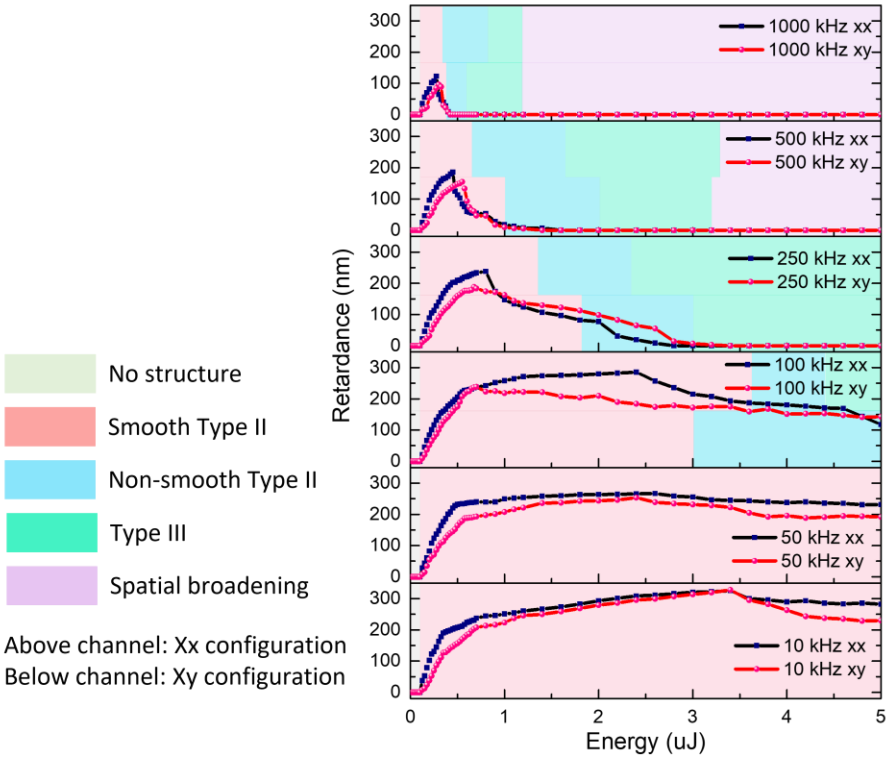


*Fig. 2-17: Summary of fs laser modification type windows with quantitative measurement of retardance.*

From the experimental results, the retardance of smooth Type II nanograting structures can reach 300 nm. The evolution of the

retardance typically exhibits an increase shape at the increase of pulse energy. At lower repetition rates, the retardance will remain the maximum value for several pulse energies. When the pulse energy is relatively high (close to the T3 threshold), the retardance experiences a decline to lower values or even zero when entering in the Type III window. From this summary, one can easily get the appropriate parameters to use for imprinting targeted modification types and even certain retardance it possesses.

### II.6.4 Polarimetric microscopy for optical rotation angle measurement via "uncrossing technique"

In this PhD thesis, we focus on the fs laser creating chirality in silica glasses, which is characterized by imprinting circular optical properties, especially circular birefringence (CB). From a theoretical view, circular birefringence refers to the phase difference between left-handed and right-handed circularly polarized lights when propagating in the chiral sample.

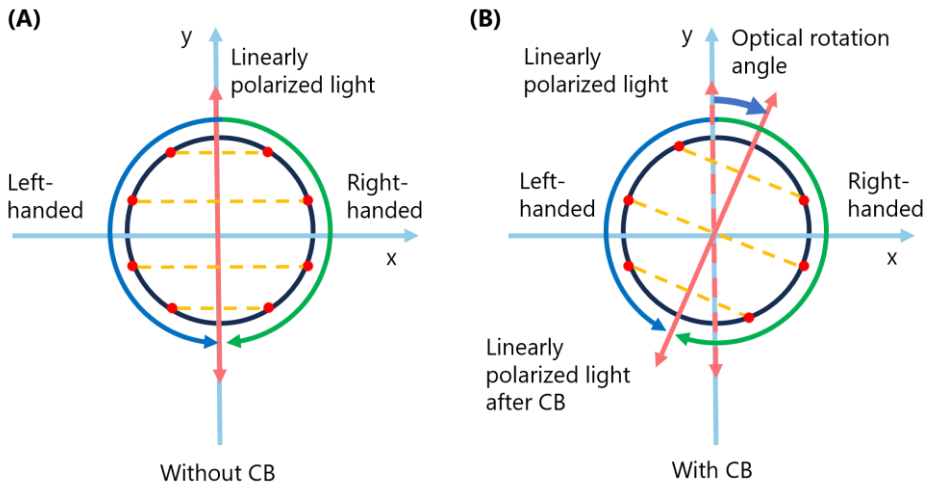


*Fig. 2-18: Schematic of optical rotation caused by CB.*

In general, a linearly polarized light can be divided into two orthogonal circularly polarized lights, namely left-handed and right-handed circularly polarized lights, as depicted in **Fig. 2-18(A)**. If the light propagates through a media without CB, the two circularly polarized lights own same phase and "rotate" synchronously. Thus, their combination remains the original linearly polarized light (i.e., no

changes will add to the incident light). However, if the light propagates through a media that possesses CB optical property, it will introduce a phase difference between the two circularly polarized lights, for example, the right-handed circularly polarized light "rotates" faster than the left-handed one. Thus, their output light beam will be different from the original incident light, which experiences a rotation of the plane of polarization, as depicted in **Fig. 2-18(B)**. Although it is a continuous process (there is a thickness of the anisotropic media), this figure shows a final output caused by CB.

Therefore, one of the significant properties of CB is often called optical rotation. From the opposite view, we can quantify the imprinted CB by measuring the optical rotation angle. A standard crossed polarizer microscope is suitable for such a characterization. Specifically, the first polarizer produces an incident light with linear polarization. Then the sample with CB will rotate the plane of polarization of the incident light. Finally, the analyzer is utilized to extinct the light transmission to quantify the rotated azimuth angle caused by CB, it is a so-called "uncrossing" technique. A typical measurement is depicted in **Fig. 2-19**. For example, an fs laser written multilayer sample that owns a large CB value can lead to a 60.1° optical rotation. Thus, the related CB value can be calculated to be 2.1 rad according to the relationships summarized in **Table. 2-5**.

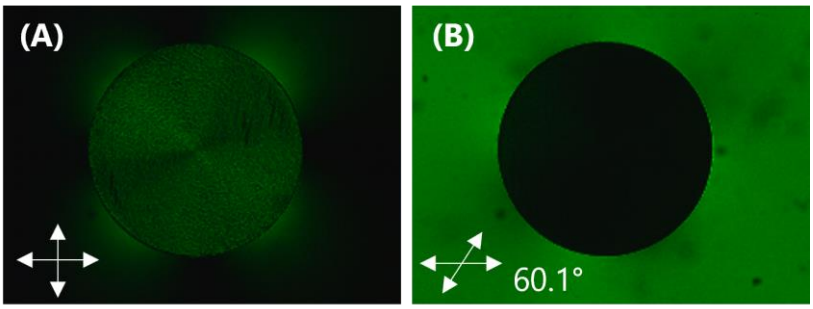


*Fig. 2-19: Illustration of optical rotation measured by an "uncrossing" technique in a crossed polarizer polarimeter. (A) Crossed polarizer microscopic image with the sample. (B) Uncrossed polarizer microscopic image with the sample indicating an optical rotation of 60.1°. Measured at the probe wavelength of 550 nm. The sample is a four-layer spiral sample written with 0°, 45°, 90°, 135° polarization of each layer, respectively. Other laser parameters are 1030 nm, 800 fs, 0.16 NA, 100 kHz, 0.5 mm/s, 0.8 μJ, 450 μm depth (bottom layer), layer gap 100 μm.*

### II.6.5 Vis-Near IR Mueller polarimeter

The visible and near-infrared (Vis-Near IR) Mueller polarimeter can record the polarizing properties of the sample by detecting the Mueller matrix with 16 elements. This device is based on liquid crystal components and has the capabilities for characterizing film thickness and optical constants with extremely high accuracy. The designed system only employs fixed elements with no moving components in the acquisition process and has been optimized for minimizing the errors [210].

A tungsten-halogen lamp together with a blue-LED for ensuring a detective wavelength band from 400 nm to 1000 nm enables the illumination of the system. The input and output heads are identical, which contains a polarizer, two ferroelectric liquid crystals, as well as a fixed retardation plate. A CCD detector is utilized to analyze the result as a spectrograph, which can record 16 elements of the Mueller matrix within 2 seconds at a high accuracy.

Any Mueller polarimeter contains a PSG for generating at least four linearly independent states of polarization $\boldsymbol{S_{in}}$ to form the modulation matrix $\boldsymbol{W}$ and a PSA for analyzing the output $\boldsymbol{S_{out}}$ via characterizing the projections over at least four linearly independent fundamental states of polarization to determine the analytical matrix $\boldsymbol{A}$. Thus, the Mueller matrix $\boldsymbol{M}$ can be obtained by $\boldsymbol{B=AMW}$. A prior calibration step can determine the matrix $\boldsymbol{A}$ and $\boldsymbol{W}$ and then the $\boldsymbol{M}$ matrix can be obtained from $\boldsymbol{B}$.

The calibration is based on eigenvalue calibration method [211], which is rapid and simple. Specifically, we use a linear polarizer and a retardation plate as a known sample. In this method, the detailed description of both PSG and PSA is not required. Besides, the calibration can be done automatically, which is quite user-friendly.

This innovative instrument is capable of Mueller matrix identification ranging from isotropic samples to anisotropic samples no matter they are depolarizing or not. The full Mueller matrix with 16 elements information can be obtained with high accuracy and precision, which allows this spectroscopic Mueller polarimeter to record most

anisotropic phenomena within a large wavelength band. Thus, the users gain easy processes to understand the information on the values of anisotropy and its axis and identify the complex sample types efficiently.

## II.7 CONCLUSION

Methodology and experimental details are quite important to carry out the experimental works and the way to conceive ideas. Form the introductions in this chapter, acousto-optic mode converters can be fabricated accordingly. The transient dynamics in an ultrafast laser is possible to be observed. Additionally, the anisotropic optical properties of the fs laser written structures can be well characterized by several suitable polarimeters.

# Chapter.III DYNAMIC SWITCHING OF VECTOR BEAMS VIA ACOUSTO-OPTIC INTERACTIONS

## III.1 INTRODUCTION

This section depicts the works about dynamic switching of spatial modes by acousto-optic interactions in fibers. This is a basic work of highlights in manipulating spatial modes and further the chiral vortex modes with fast switching capability.

In the first part, we present a work published in ***Optics Letters*** in 2018. It is related to a dual-resonant acousto-optic mode conversion with orthogonal HOMs manipulation. The fundamental mechanism of the dual resonance is caused by the asymmetric geometry of the fibers, which leads to a symmetry breaking in the acoustic and optical birefringence. We proposed a theoretical model to explain the co-effect of acoustic and optical birefringence, which indicates the method to control the conversion efficiency of these two resonant peaks in the spectrum. By combining with the wavelength tunability of the acousto-optic interactions, an orthogonal HOM switching between $LP_{11a}$ and $LP_{11b}$ modes at one single wavelength is demonstrated via altering the applied frequencies of the microwave signals. Thus, with applying a phase difference by polarization controllers, a vortex switching between positive and negative topological charges (namely, +1-order OAM vortex beam and -1-order OAM vortex beam) is realized.

The second part includes a work published in ***IEEE Photonics Journal*** in 2020, which is about utilizing acousto-optic interactions in high-power fiber lasers operating at HOMs for its unique potential in thermal stability. Due to the non-destructive structure of the acousto-optic mode converters, it will not introduce thermal accumulation in the mode conversion region while conventional mode converters like long-period fiber gratings and mode selective couplers do. Besides, this device also possesses dynamic mode switching capability which provides more possibilities in high-power fiber lasers with higher-order modes or likely vortex modes in future studies.

## III.2 DYNAMIC MODE-SWITCHABLE OPTICAL VORTEX BEAMS USING ACOUSTO-OPTIC MODE CONVERTER

# Dynamic mode-switchable optical vortex beams using acousto-optic mode converter

JIAFENG LU,[1] LINGHAO MENG,[1] FAN SHI,[1] XIAOMIN LIU,[2] ZHENGQIAN LUO,[3] PEIGUANG YAN,[4] LIANGJIN HUANG,[5] FUFEI PANG,[1] TINGYUN WANG,[1] XIANGLONG ZENG,[1,*] AND PU ZHOU [5,**]

[1]*Key laboratory of Specialty Fiber Optics and Optical Access Networks, Joint International Research Laboratory of Specialty, Fiber Optics and Advanced Communication, Institute for Advanced Communication and Data Science, Shanghai University, Shanghai 200444, China*
[2] *Max Planck Institute for Polymer Research, Ackermannweg 10, D-55128 Mainz, Germany*
[3] *Department of Electronic Engineering, School of Information Science and Engineering, Xiamen University, Xiamen 361005, China*
[4] *Shenzhen Key Laboratory of Laser Engineering, Shenzhen University, Shenzhen 518060, China*
[5] *College of Advanced Interdisciplinary Studies, National University of Defense Technology, Changsha 410073, China*
[*] *Corresponding author: zenglong@shu.edu.cn*
[**] *Corresponding author: zhoupu203@163.com*

Received XX Month XXXX; revised XX Month, XXXX; accepted XX Month XXXX; posted XX Month XXXX (Doc. ID XXXXX); published XX Month XXXX

**We propose a dynamic scheme to realize mode-switchable generation of $LP_{11a/b}$ modes and ±1-order orbital angular momentum (OAM) modes simultaneously, which are induced by an acoustically-induced fiber grating driven by a radio frequency modulation. $LP_{11a/b}$ mode degeneration in a few-mode fiber is induced by the geometric irregularity of optical fibers. A dual-wavelength resonance of mode coupling from $LP_{01}$ to $LP_{11a/b}$ modes is found based on the combined effects of optical and acoustic birefringence. Within the configuration of CW intra-cavity laser output, we experimentally demonstrate a fast-switchable generation of $LP_{11a/b}$ modes and optical vortex beams with ±1-order OAM at a switching speed up to 4.3 kHz. This approach has potential applications in mode division multiplexing, particle manipulation, stimulated emission depletion microscopy and quantum information science. © 2018 Optical Society of America**

***OCIS codes:*** *(230.1040) Acousto-optical devices; (140.3510) Lasers, fiber; (050.4865) Optical vortices; (060.2330) Fiber optics communications.*

http://dx.doi.org/10.1364/OL.99.099999

The frontier of discovering that optical vortex beams (OVBs) carry orbital angular momentum (OAM) [1] has led to appreciable advances in particle manipulation [2], mode-division multiplexing [3], quantum state manipulation [4], stimulated emission depletion microscopy (STED) [5] and other diverse applications [6-10]. In an effort to extend these applications, fiber-based mode converter is a key component with the implementation of high-order modes (HOMs) generation. Compared to spatial bulk components that require careful alignment of free-space optics, such as q-plates [11] and spatial liquid modulators [12], all-fiber mode converters have the advantage of inherent compatibility to the fiber-optic systems. The long period gratings (LPGs) method couples light from a fundamental core mode into forward propagating core HOMs in a few-mode fiber (FMF). Experimental demonstrations of LPGs with high efficiency of mode conversion have hitherto been reported. The methods of constructing LPGs are mainly clarified by three categories: mechanical micro bending [13], $CO_2$ laser inscription [14] and acousto-optic effect [15-17]. However few works on the degeneration of HOMs and mode-switching in LPGs has been reported, such as OAM states of the OVBs have been only obtained separately [13].

In this paper, based on an acoustically-induced fiber grating (AIFG) we exploit a dynamic scheme to realize mode degeneration of $LP_{11a/b}$ modes and ±1-order OAM modes simultaneously. The geometric irregularity of optical fibers is exploited to mode degeneration and the mechanism of dual-wavelength spectrum is numerically and experimentally demonstrated. The degenerated linear-polarization modes of $LP_{11a/b}$ as well as the OAM states with topological charges of $\pm 1$ can be switched simultaneously by use of RF frequency modulation. This component expands the diversity of AIFG application, which has been implemented in CW intra-cavity laser.

Here the acoustic wave produced by a RF-driven transducer propagates along the unjacketed fiber in the lowest-order acoustic flexural mode, which makes a periodical micro-bend on the fiber and creates a dynamic LPG. To realize the mode conversion from $LP_{01}$ mode to $LP_{11}$ mode, the phase matching condition should be satisfied $L_B = \Lambda$ [18], in which the beat length $L_B$ is $L_B = \lambda/(n_{01} - n_{11})$ and the period of the constructed LPG is expressed as $\Lambda = (\pi R C_{ext}/f)^{\frac{1}{2}}$ due to the acoustic dispersion theory [19]. Here $n_{01}$ and $n_{11}$ represent the effective refractive indices of $LP_{01}$ and $LP_{11}$ modes, respectively, and $\lambda$ is the corresponding wavelength. $\boldsymbol{R}$ refers to the radius of the unjacketed fiber while $C_{ext}$ and $\boldsymbol{f}$ represent the propagating speed of acoustic wave along

silica fiber (5760 m/s) and the applied frequency. Hence the mode conversion occurs at the resonant wavelength of $\lambda_{res} = (n_{01} - n_{11}) \cdot \Lambda$, which can be tuned by altering RF frequency. The coating layer of the fiber is removed in the target acousto-optic interaction region lest it should absorb the acoustic waves. Here the flexural acoustic waves are generated by using a thickness-mode piezoelectric transducer. A 25-cm-long bare few-mode fiber is glued to the top of the silica horn, as depicted in Fig. 1(a). The RF signal is amplified by a high frequency voltage amplifier (Aigtek: ATA-2022H).

The irregularities of optical fibers lead to both optical and acoustic birefringence [20]. As shown in Fig. 1(a), the major and minor axes of the fiber are defined as long and short axes of the ellipse cladding, while ***a*** and ***b*** axes are the short and long axes of the ellipse core, respectively. The ellipticity of the fiber core is defined as the ratio of the short to the long axes, and results in a degeneration of HOMs [21]. $\boldsymbol{\alpha}$ is the angle between the ellipse short axes of fiber core (***a*** axis) and fiber cladding (minor axis) and $\boldsymbol{\beta}$ is the angle between the acoustic vibration direction and the minor axis. The ellipticity of the fiber outer cladding also leads to an acoustic phase velocity difference between the ellipse axes (acoustic eigen axes).

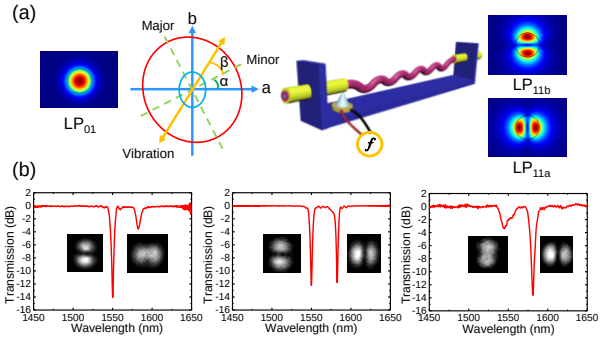


Fig. 1. (a) The proposed AIFG schematics constructed by optical fiber birefringence and acoustic vibration, and the simulated $LP_{11a/b}$ modes. (b) Different efficiencies of dual-wavelength resonance (from $LP_{01}$ to $LP_{11a/b}$) and the corresponding $LP_{11}$ mode patterns when the angle $\beta$ is about 78°, 45° and 12°, respectively.

Thus, the coupling strengths from $LP_{01}$ mode to $LP_{11a/b}$ modes can be formulated by a trigonometric decomposition [20]:

$$\kappa(z) = \begin{bmatrix} \kappa_a(z) \\ \kappa_b(z) \end{bmatrix} = \kappa_0 \begin{bmatrix} -sin\beta \cdot sin\alpha \cdot e^{i\frac{2\pi}{\Lambda_l}} + cos\beta \cdot cos\alpha \cdot e^{i\frac{2\pi}{\Lambda_s}} \\ sin\beta \cdot cos\alpha \cdot e^{i\frac{2\pi}{\Lambda_l}} + cos\beta \cdot sin\alpha \cdot e^{i\frac{2\pi}{\Lambda_s}} \end{bmatrix} \quad (1)$$

The coupling strength $\kappa(z)$ consists of $\kappa_a(z)$ and $\kappa_b(z)$, which represent the coupling between $LP_{01}$ and degenerated $LP_{11a}$ and $LP_{11b}$, respectively. $\kappa_0$ is the coupling strength when $\alpha = 0$ and $\beta = 0$. $\Lambda_l$ and $\Lambda_s$ refer to the AIFG periods along the major axis and the minor axis, respectively. Considering the same ellipse direction of the fiber cladding and core ($\alpha = 0$), the coupling strength can be simplified to be:

$$\kappa(z) = \begin{bmatrix} \kappa_a(z) \\ \kappa_b(z) \end{bmatrix} = \kappa_0 \begin{bmatrix} cos\beta \cdot e^{i\frac{2\pi}{\Lambda_s}} \\ sin\beta \cdot e^{i\frac{2\pi}{\Lambda_l}} \end{bmatrix} \quad (2)$$

Then the coupling strengths $\kappa_a(z)$ and $\kappa_b(z)$ are sine function of the angle $\beta$, which means that one can simply adjust the angle between acoustic vibration and ellipse axes of the fiber to control the coupling efficiencies of $LP_{01}$-$LP_{11a}$ and $LP_{01}$-$LP_{11b}$. The experimental results are shown in Fig. 1(b), which present different coupling efficiencies of $LP_{01}$-$LP_{11a}$ and $LP_{01}$-$LP_{11b}$. The fiber is rotating and gluing to the transducer at the different angle $\beta$ about 78°, 45° and 12°, respectively.

The transverse electric field distributions of $LP_{11a}$ and $LP_{11b}$ modes are calculated using a finite element method (Comsol Multiphysics), as depicted in Fig. 1(a). A small ellipticity of fiber core (radius of short axis: $r_a = 9.2\ \mu m$; radius of long axis: $r_b = 9.3\ \mu m$) is induced to achieve the effective refractive indices difference $\Delta n_{eff}$ (~$2.4*10^{-5}$) between $LP_{11a}$ and $LP_{11b}$, therefore the conventional $LP_{01}$-$LP_{11}$ resonant peak is split into two resonant peaks corresponding to $LP_{11a}$ and $LP_{11b}$, separately. The simulated beat length $L_B$ and the period of AIFG are both shown in Fig. 2(a).

We experimentally observe the dual-wavelength resonance corresponding to $LP_{01}$-$LP_{11a}$ and $LP_{01}$-$LP_{11b}$ modes in Fig. 2(b). Both the transmission depletion for $LP_{11}$ modes are over −15 dB. The two resonance with a wavelength interval of ~30 nm can be simply tuned by the RF frequency, which agrees well with the theoretic calculation as shown in Fig. 2(c) and 2(d).

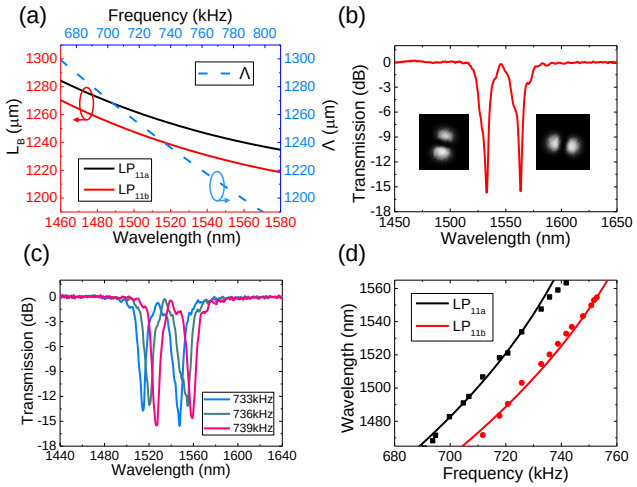


Fig. 2. (a) The simulated beat length $L_B$ of $LP_{11a}$ and $LP_{11b}$ modes in a slightly elliptic fiber and the period of AIFG as a function of applied frequency. (b) A dual-resonant transmission spectrum. (c) The spectra at frequencies of 733 kHz, 736 kHz and 739 kHz. (d) The resonant wavelengths shift as the increase of frequency, compared with calculations (curves) and experimental results (denoted dots).

Due to the dual-resonance and the wavelength-tuning feature, a switchable generation between $LP_{11b}$ and $LP_{11a}$ modes at a certain wavelength (e.g. 1550 nm) can be simply controlled by altering the applied frequency (at 738.0 kHz and 753.0 kHz). The switching time between the modes is mainly determined by the transit time of the acoustic flexural wave propagating through the acousto-optic coupling region of the AIFG [17] and can be expressed as $\tau = L/(\pi \cdot R \cdot C_{ext} \cdot f)^{\frac{1}{2}}$. Here $\boldsymbol{L}$ is the length of the acousto-optic coupling region (25 cm). The switching times of $LP_{01}$-$LP_{11b}$ and $LP_{01}$-$LP_{11a}$ are calculated as 0.274 ms and 0.271 ms.

Here an intensity modulator (IM) structure is demonstrated based on the mode conversion of the AIFG as shown in Fig. 3(a). A light beam at the wavelength of 1550 nm from a tunable laser (TL) is launched into the AIFG. After mode coupling, the HOM part of the output light beam is totally depleted through a mode stripper (MS) to a single-mode fiber (SMF), while the remained fundamental mode propagates through the MS and the SMF without any loss. Thus, different efficiency of mode coupling determines the optical loss as shown in Fig. 3(b). The higher the efficiency, the more loss induced in the IM. The switching time from $LP_{01}$ to $LP_{11}$ is about 0.31 ms, which is close to the calculated transit time τ. Besides, the collapse time of an AIFG is also measured to be about 0.15 ms from $LP_{11}$ to $LP_{01}$. Here different applied voltages are used to obtain different conversion efficiency of $LP_{11a}$ and $LP_{11b}$ in order to distinguish the modes [17]. The switching time between $LP_{11b}$ and $LP_{11a}$ is measured to be 0.23 ms, which means that the switching speed is up to 4.3 kHz. By increasing the applied voltages, the output power is recorded in Fig. 3(c). In the range from 25 $V_{pp}$ (voltage peak-peak) to 150 $V_{pp}$, the output power performs a good linear relation with applied voltage. Notice that when the voltage is over 150 $V_{pp}$ the output power starts to increase due to the over-coupling effect.

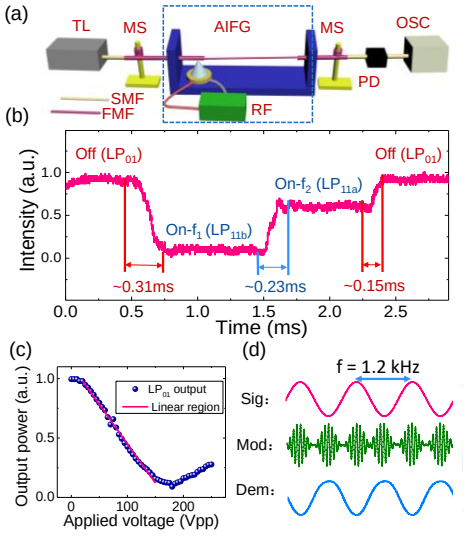


Fig. 3. (a) The setup diagram of intensity modulator based on an AIFG. TL: tunable laser; MS: mode stripper; RF: radio frequency; PD: photoelectric detector; OSC: oscilloscope. (b) The temporal trace of mode switching from $LP_{01}$ to $LP_{11b}$, from $LP_{11b}$ to $LP_{11a}$ and from $LP_{11a}$ to $LP_{01}$. $f_1$: 738.0 kHz; $f_2$: 753.0 kHz. (c) The output power as a function of applied voltage. (d) The signal wave (Sig), amplitude modulation wave (Mod) and demodulation wave (Dem) of the AIFG-based IM.

Furthermore, the AIFG-based intensity modulation is obtained when the amplitude modulation (AM) of HOM is used. Figure 3(d) shows the sine signal wave, the modulation waveform and demodulation waveform. Here the phase of the demodulation waveform is opposite to the signal because the mode conversion is increased with the increase of applied voltage. Thus, the remaining output power of $LP_{01}$ mode reaches the minimum value when the voltage is the maximum value. The maximum frequency of undistorted waveforms is measured to be 1.2 kHz.

To demonstrate the aforesaid applications and devices, a CW intra-cavity laser with an AIFG-based switchable mode converter has been presented as shown in Fig. 4. The schematic diagram of the intra-cavity CW laser is depicted in Fig. 4(a). The gain is provided by a single mode Erbium-doped fiber (EDF) pumped at 980 nm through a wavelength division multiplexer (WDM). A MS made of 5 turns on a 10-mm-diameter rod is utilized to ensure a pure $LP_{01}$ mode into the AIFG. A cavity mirror is made by a $SiO_2$-$Ta_2O_5$ dielectric film coated at the end face of an FMF jumper [22], which reflects 60% of the HOMs at the wavelength of 1550 nm. Then $LP_{11a/b}$ mode is reconverted to $LP_{01}$ mode by the AIFG for laser oscillation. The wavelength of the amplified light is selected by a single mode fiber Bragg grating (FBG), which reflects the light at the central wavelength of 1550.3 nm with a reflectivity > 98% and 3 dB bandwidth of 0.5 nm. The residual light out of the FBG is measured by an optical spectrum analyzer (OSA), which shows the output spectrum in Fig 4(c). The laser output power as a function of pump power is depicted in Fig. 4(d) and the slope efficiency is 18.2%. For the CW laser emission at the wavelength of 1550 nm, the RF frequency is set to 738.0 kHz (753.0 kHz) to achieve the mode conversion of $LP_{01}$-$LP_{11b}$ ($LP_{01}$-$LP_{11a}$). Hence the laser output can be mode-switched between $LP_{11a}$ or $LP_{11b}$ modes, which are determined by different applied frequencies. (see visualization 1).

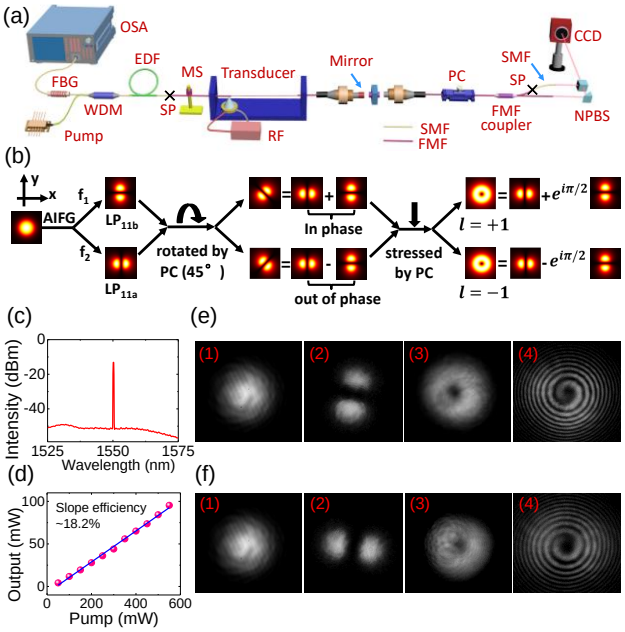


Fig. 4. (a) The setup diagram of the intra-cavity CW laser with interference unit. SP: splice point between SMF and FMF; PC: polarization controller. (b) The mechanism of switching OVBs. (c) The spectrum of CW laser output. (d) The output power as a function of pump power. The intensity distributions of Gaussian beam (1), $LP_{11}$ beam (2), OAM beam (3) and interference pattern (4) for $LP_{11b}$ mode (e) and for $LP_{11a}$ mode (f).

Moreover, the output beams of $LP_{11a/b}$ modes are easily utilized to generate OVBs with switchable OAM modes, as shown in Fig. 4(b). By adjusting the rotation of the PC, the generated $LP_{11}$ mode can be aligned to different directions. For the case of the $LP_{11a}$ mode (setting the frequency at 753.0 kHz) aligned at 45° to the x axis of the fiber cross section, the rotated $LP_{11a}$ mode (defined as

$LP_{11a(rot)}$) can be expressed as a superposition of two in-phase orthogonal $LP_{11}$ modes: $LP_{11a(rot)} = LP_{11}^{even} + LP_{11}^{odd}$. When the stress axis is supposed to coincide with the y axis of the fiber cross section, a phase difference may appear between the two orthogonal modes. This is because the stress changes the effective dimensions of the FMF resulting in different phase velocities of the two modes. By adjusting the pressure appropriately, the two orthogonal modes can achieve a $+\pi/2$ phase difference and the output is a +1-order OAM beam with a symmetric annular intensity profile and a helical phase front [13]. Then under the same situation of PC state, for the case of $LP_{11b}$ mode (setting the frequency at 738.0 kHz) the rotated $LP_{11b}$ mode is $LP_{11b(rot)} = LP_{11}^{even} - LP_{11}^{odd}$. The same phase difference $+\pi/2$ is introduced and the output is a -1-order OAM beam. The two output OAM beams can be respectively expressed as:

$$OAM_{\pm 1} = LP_{11}^{even} \pm i \cdot LP_{11}^{odd} \quad (3)$$

The helical phase $\exp(\pm i\ell h)$ of the ±1-order OVBs signifying $\ell = \pm 1$ per photon is verified by examining their interference patterns with a Gaussian beam. Note that the frequencies of the ±1-order OVBs are down-shifted from that of the $LP_{01}$ mode by an amount of the acoustic flexural wave, however, the reference light requires the same frequency with the OVBs for beam interference. To do so, the output OVB from the FMF is divided into two paths by a 3-dB FMF coupler. One branch is directly spliced to SMF to convert the ±1-order OVBs back to a fundamental mode as a reference beam. Then the reference beam and the optical vortex beam are collimated, attenuated to same power and combined through a non-polarization beam splitter (NPBS) to obtain the interference patterns, which are recorded by a charge-coupled device (CCD), as shown in Fig. 4(e) and 4(f) (see visualization 2).

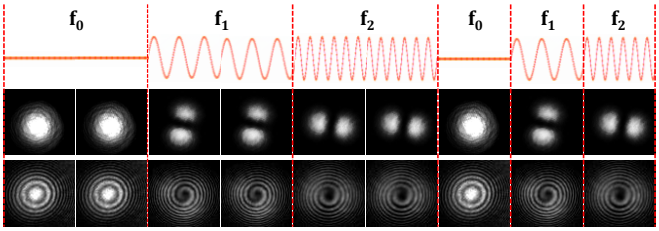


Fig. 5. The schematic diagram of mode switching with the modulation of RF frequencies ($f_0$, $f_1$ and $f_2$). Intensity patterns of modes switching (second row) and the corresponding interference patterns (third row).

Fast-switchable AIFG-based mode converter develops a new idea in OAM generation. This flexible component provides a method for a donut-shaped source, which can be used in STED application to deplete the fluorescence of gaussian beam for achieving the resolution beyond the diffraction limit [5]. Furthermore, fast-switchable OAM beams also has the potential in optical communication and particle manipulation. The modulation schematic diagram is shown in Fig. 5. The $f_1$ refers to the frequency at the mode conversion of $LP_{01}$-$LP_{11b}$ (here is 738.0 kHz) while the $f_2$ refers to the frequency at the mode conversion of $LP_{01}$-$LP_{11a}$ (here is 753.0 kHz). The $f_0$ represents the non-resonant frequency or turning off the RF signal. The corresponding linear polarized beams and ±1-order OVBs are modulated by RF frequencies. The fast-switchable beams between Gaussian beams and ±1-order OVBs can accordingly control the particles trapping, (anti-)clockwise spinning.

In summary, we have experimentally demonstrated a fast-switchable mode converter, which can generate switching $LP_{11a/b}$ modes and ± 1-order OVBs at a switching speed up to 4.3 kHz. The mechanism of dual-wavelength resonant spectrum is numerically and experimentally analyzed. By varying the RF frequency, both the resonant peaks of $LP_{01}$-$LP_{11b}$ and $LP_{01}$-$LP_{11a}$ can be tuned with a spectral tuning rate of 2 nm/kHz. The orthogonal mode switching of both HOMs and OVBs enriches the diversity of AIFGs and the demonstrated intra-cavity CW laser with switching HOMs and OVBs output are advantageous for practical applications.

**Funding.** National Natural Science Foundation of China (NSFC) (91750108, 61635006, 61805280); Science and Technology Commission of Shanghai Municipality (16520720900); Shanghai Municipal Education Commission (16SG35).

**Acknowledgment**. Zeng Xianglong acknowledges the Program for Professor of Special Appointment (Eastern Scholar) at Shanghai Institutions of Higher Learning and Pang Fufei acknowledges "Shuguang Program" supported by Shanghai Education Development Foundation.

## References

1. L. Allen, M. W. Beijersbergen, R. J. C. Spreeuw, and J. P. Woerdman, Phys. Rev. A **45**, 8185 (1992).
2. D. G. Grier, Nature **424**, 810 (2003).
3. N. Bozinovic, Y. Yue, Y. Ren, M. Tur, P. Kristensen, H. Huang, A. E. Willner, and S. Ramachandran, Science **340**, 1545 (2013).
4. A. Mair, A. Vaziri, G. Weihs, and A. Zeilinger, Nature **412**, 6844 (2001).
5. L. Yan, P. Gregg, E. Karimi, A. Rubano, L. Marrucci, R. Boyd, and S. Ramachandran, Optica **2**, 900 (2015).
6. S. Fürhapter, A. Jesacher, S. Bernet, and M. Ritsch-Marte, Opt. Lett. **30**, 1953 (2005).
7. S. W. Hell, Nat. Biotechnol. **21**, 1347 (2003).
8. G. Foo, D. M. Palacios, and J. Swartzlander Jr., Opt. Lett. **30**, 3308 (2005).
9. S. Franke-Arnold, L. Allen, and M. Padgett, Laser Photon. Rev. **2**, 299 (2008).
10. B. J. McMorran, A. Agrawal, I. M. Anderson, A. A. Herzing, H. J. Lezec, J. J. McClelland, and J. Unguris, Science **331**, 6014 (2011)
11. P. Gregg, M. Mirhosseini, A. Rubano, L. Marrucci, E. Karimi, R. W. Boyd, and S. Ramachandran, Opt. Lett. **40**, 1729 (2015).
12. A. S. Ostrovsky, C. Rickenstorffparrao, and V. Arrizón, Opt. Lett. **38**, 534 (2013).
13. S. Li, Q. Mo, X. Hu, C. Du, and J. Wang, Opt. Lett. **40**, 4376 (2015).
14. Y. Zhao, Y. Liu, C. Zhang, L. Zhang, G. Zheng, C. Mou, J. Wen, and T. Wang, Opt. Lett. **42**, 22 (2017).
15. B. Y. Kim, H. E. Engan, H. J. Shaw, and J. N. Blake, Opt. Lett. **11**, 389 (1986).
16. P. Z. Dashti, F. Alhassen, and H. P. Lee, Phys. Rev. Lett. **96**, 043064 (2006).
17. W. Zhang, K. Wei, L. Huang, D. Mao, B. Jiang, F. Gao, G. Zhang, T. Mei, and J. Zhao, Opt. Express **24**, 19278 (2016).
18. K. J. Park, K. Y. Song, Y. K. Kim, J. H. Lee, and B. Y. Kim, Opt. Express **24**, 3543 (2016).
19. T. A. Birks, P. St. J. Russell, and D. O. Culverhouse, J. Lightwave Technol. **14**, 2519 (1996).
20. S. D. Lim, H. C. Park, I. K. Hwang, and B. Y. Kim, Opt. Express **16**, 6125 (2008).
21. L. Wang, and S. Larochelle, Opt. Lett. **40**, 5846 (2015).
22. L. Li, Q. Ruan, R. Yang, L. Zhao, and Z. Luo, Opt. Express **24**, 21020 (2016).
23. L. Carrión-Higueras, E. P. Alcusa-Sáez, A. Díez, and M. V. Andrés, IEEE Photonics J. **9**, 1 (2017).
24. J. Wang, Z. Jiang, H. Chen, J. Li, J. Yin, J. Wang, T. He, P. Yan, and S. Ruan, Photon. Res. **6**, 535 (2018).

## References


1. Allen, L., Beijersbergen, M. W., Spreeuw, R. J. C., & Woerdman, J. P. (1992). Orbital angular momentum of light and the transformation of Laguerre-Gaussian laser modes. Physical Review A, 45(11), 8185.
2. Grier, D. G. (2003). A revolution in optical manipulation. nature, 424(6950), 810.
3. Bozinovic, N., Yue, Y., Ren, Y., Tur, M., Kristensen, P., Huang, H., ... & Ramachandran, S. (2013). Terabit-scale orbital angular momentum mode division multiplexing in fibers. science, 340(6140), 1545-1548.
4. Mair, A., Vaziri, A., Weihs, G., & Zeilinger, A. (2001). Entanglement of the orbital angular momentum states of photons. Nature, 412(6844), 313.
5. Yan, L., Gregg, P., Karimi, E., Rubano, A., Marrucci, L., & Boyd, R., et al. (2015). Q-plate enabled spectrally diverse orbital-angular-momentum conversion for stimulated emission depletion microscopy. Optica, 2(10), 900.
6. Fürhapter, S., Jesacher, A., Bernet, S., & Ritsch-Marte, M. (2005). Spiral interferometry. Optics letters, 30(15), 1953-1955.
7. Hell, S. W. (2003). Toward fluorescence nanoscopy. Nature biotechnology, 21(11), 1347.
8. Foo, G., Palacios, D. M., & Swartzlander, G. A. (2005). Optical vortex coronagraph. Optics letters, 30(24), 3308-3310.
9. Franke‐Arnold, S., Allen, L., & Padgett, M. (2008). Advances in optical angular momentum. Laser & Photonics Reviews, 2(4), 299-313.
10. McMorran, B. J., Agrawal, A., Anderson, I. M., Herzing, A. A., Lezec, H. J., McClelland, J. J., & Unguris, J. (2011). Electron vortex beams with high quanta of orbital angular momentum. science, 331(6014), 192-195.
11. Gregg, P., Mirhosseini, M., Rubano, A., Marrucci, L., Karimi, E., & Boyd, R. W., et al. (2015). Q-plates as higher order polarization controllers for orbital angular momentum modes of fiber. Optics Letters, 40(8), 1729-32.
12. Ostrovsky, A. S., Rickenstorffparrao, C., & Arrizón, V. (2013). Generation of the "perfect" optical vortex using a liquid-crystal spatial light modulator. Optics Letters, 38(4), 534-6.
13. Li, S., Mo, Q., Hu, X., Du, C., & Wang, J. (2015). Controllable all-fiber orbital angular momentum mode converter. Optics letters, 40(18), 4376-4379.
14. Zhao, Y., Liu, Y., Zhang, C., Zhang, L., Zheng, G., Mou, C., ... & Wang, T. (2017). All-fiber mode converter based on long-period fiber gratings written in few-mode fiber. Optics letters, 42(22), 4708-4711.
15. Kim, B. Y., Blake, J. N., Engan, H. E., & Shaw, H. J. (1986). All-fiber acousto-optic frequency shifter. Optics Letters, 11(6), 389-391.
16. Dashti, P. Z., Alhassen, F., & Lee, H. P. (2006). Observation of orbital angular momentum transfer between acoustic and optical vortices in optical fiber. Physical review letters, 96(4), 043604.
17. Zhang, W., Wei, K., Huang, L., Mao, D., Jiang, B., Gao, F., ... & Zhao, J. (2016). Optical vortex generation with wavelength tunability based on an acoustically-induced fiber grating. Optics express, 24(17), 19278-19285.
18. Park, K. J., Song, K. Y., Kim, Y. K., Lee, J. H., & Kim, B. Y. (2016). Broadband mode division multiplexer using all-fiber mode selective couplers. Optics Express, 24(4), 3543.
19. T. A. Birks, P. St. J. Russell, and D. O. Culverhouse, "The acousto-optic effect in single-mode fiber tapers and couplers," J. Lightwave Technol. 14(11), 2519–2529 (1996).
20. Do Lim, S., Park, H. C., Hwang, I. K., & Kim, B. Y. (2008). Combined effects of optical and acoustic birefringence on acousto-optic mode coupling in photonic crystal fiber. Optics express, 16(9), 6125-6133.
21. Wang, L., & LaRochelle, S. (2015). Design of eight-mode polarization-maintaining few-mode fiber for multiple-input multiple-output-free spatial division multiplexing. Optics letters, 40(24), 5846-5849.
22. Lei Li, Qiujun Ruan, Runhua Yang, Luming Zhao, and Zhengqian Luo, "Bidirectional operation of 100 fs bound solitons in an ultra-compact mode-locked fiber laser," Opt. Express 24, 21020-21026 (2016).
23. Carrión-Higueras, L., Alcusa-Sáez, E. P., Díez, A., & Andrés, M. V. (2017). All-fiber laser with intracavity acousto-optic dynamic mode converter for efficient generation of radially polarized cylindrical vector beams. IEEE Photonics Journal, 9(1), 1-7.
24. J. T. Wang, Z. K. Jiang, H. Chen, J. R. Li, J. D. Yin, J. Z. Wang, T. C. He, P. G. Yan, and S. C. Ruan, "High energy soliton pulse generation by a magnetron-sputtering-deposition-grown MoTe2 saturable absorber," Photon. Res. 6, 535–541 (2018).

## III.3 ALL-FIBER LASER WITH AGILE MODE-SWITCHING CAPABILITY THROUGH INTRA-CAVITY CONVERSION

IEEE Photonics Journal
An IEEE Photonics Society Publication

Open Access

# All-Fiber Laser With Agile Mode-Switching Capability Through Intra-Cavity Conversion

Volume 12, Number 2, April 2020

Hanshuo Wu
Jiafeng Lu
Liangjin Huang
Xianglong Zeng
Pu Zhou

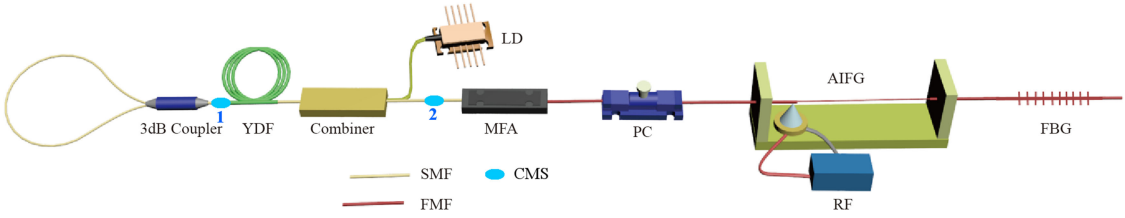


DOI: 10.1109/JPHOT.2019.2911270
1943-0655 © 2018 IEEE

IEEE photonics SOCIETY

IEEE

# All-Fiber Laser With Agile Mode-Switching Capability Through Intra-Cavity Conversion

**Hanshuo Wu**,[1] **Jiafeng Lu**,[2] **Liangjin Huang**,[1] **Xianglong Zeng**,[2] **and Pu Zhou** [1]

[1]College of Advanced Interdisciplinary Studies, National University of Defense Technology, Changsha 410073, China
[2]Key Laboratory of Specialty Fiber Optics and Optical Access Networks, Joint International Research Laboratory of Specialty Fiber Optics and Advanced Communication, Shanghai Institute for Advanced Communication and Data Science, Shanghai University, Shanghai 200444, China

*DOI:10.1109/JPHOT.2019.2911270*


Manuscript received January 6, 2019; revised April 8, 2019; accepted April 11, 2019. Date of publication April 14, 2019; date of current version March 9, 2020. This work was supported in part by the National Natural Science Foundation of China under Grants 61805280 and 91750108, in part by the Open Research Fund of State Key Laboratory of Pulsed Power Laser Technology under Grant SKL2018ZR06, and in part by the Science and Technology Commission of Shanghai Municipality under Grant 16520720900. *(Hanshuo Wu and Jiafeng Lu contributed equally to this work.)* Corresponding authors: Pu Zhou and Xianglong Zeng (email: zhoupu203@163.com; zenglong@shu.edu.cn).
This paper has supplementary downloadable material available at http://ieeexplore.ieee.org. The Supplementary Material contains two videos showing Visualization 1 and Visualization 2. The total size of the files is 17.6 MB.

**Abstract:** Agile mode switching between $LP_{01}$ and $LP_{11}$ modes in an all-fiber laser is demonstrated by exploiting an acoustically induced fiber grating within the laser cavity. The laser exploits a cladding pump configuration and can deliver up to 5.85 W of stable output power in $LP_{11}$ mode at 1070.07 nm and 6.06 W in $LP_{01}$ mode at 1070.48 nm, with a slope efficiency near 50%. Complete mode-switching speed with 250 Hz and partial mode-switching speed with 1 kHz are demonstrated. Based on the obtained switching time between $LP_{11}$ and $LP_{01}$ mode, the maximum complete mode-switching speed is calculated to be ~555.56 Hz. Moreover, variable output beam profiles could be obtained by adjusting the frequency of the modulation signal applied on the acoustically induced fiber grating. This paper could provide an example of realizing a high-power, mode-switchable fiber laser source for practical use.

**Index Terms:** Mode switching, agile, acoustically-induced fiber grating, high order mode.

## 1. Introduction

Fiber lasers with pure high-order-mode (HOM) output have been intensively studied in recent years owing to their unique polarization, amplitude and phase characteristics. Generally, there are several commonly used approaches to realize HOM operation, including adopting spatial light modulators [1], [2], employing long period gratings [3], [4], introducing adaptive control [5]–[7], using few-mode fiber Bragg gratings (FBGs) [8]–[10] and taking advantage of mode selective couplers [11], [12]. Currently, exploration on HOM fiber lasers has focused on power scaling [13], nonlinear conversion [4], [14], vector beam generation [15], etc. However, only a little attention has been paid on fast

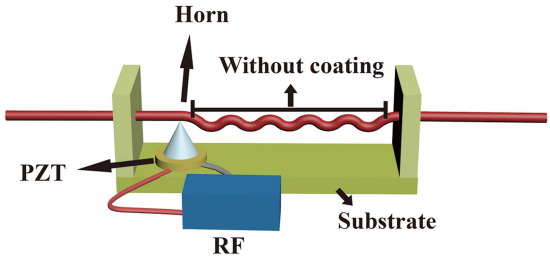


Fig. 1. Configuration of the AIFG. (PZT: piezoceramic transducer, RF: radio frequency source. The red line in this figure stands for few-mode fiber).

mode switching of HOM lasers. In some fields, such as material processing, laser beams with dynamically adaptable transverse profiles could yield substantially higher processing speeds as well as improved cut quality. Meanwhile, the fast-mode switching capability can enable the use of the optimum beam characteristics for each step of the cutting process, not just for cutting of different materials or various thicknesses [16]–[19]. In 2013, J. Daniel *et al.* realized mode selection and switching in a multimode fiber laser oscillator by adopting a few-mode fiber Bragg grating and an acoustic-optic tunable-filter as the free-space wavelength-selective element [18]. They proved that the mode is changing at the frequency of 20 kHz but could not confirm that it was switching between $LP_{01}$ and $LP_{11}$ modes. No further researches have been reported to achieve fast mode switching.

Here, we fabricate an acoustically-induced fiber grating (AIFG) and apply it in a fiber laser to achieve intra-cavity mode conversion and agile mode switching. An AIFG, which consists of a piezoceramic transducer (PZT), a horn and a piece of few-mode fiber (FMF), can provide a flexible method to achieve all-fiber mode conversion and fast mode switching within a wide wavelength range [20]. Applications of such kind of device include mode-locked fiber lasers [21] and Q-switched fiber lasers [22]. In terms of mode conversion, it has also been adopted for generating cylinder beams and optical vortex beams [23]–[27]. It should be noted that fast mode-switching capability of the above-mentioned fiber laser based on AIFG has not been fully studied and the output powers of these fiber lasers are relatively low (less than several tens of milliwatts).

In this paper, intra-cavity mode conversion and agile mode switching between $LP_{01}$ and $LP_{11}$ have been realized through an AIFG. In addition, the output power of $LP_{11}$ mode reaches 5.85 W with a slope efficiency of ~46.58%, while the output power of $LP_{01}$ mode reaches 6.06 W with a slope efficiency of ~48.16%, and the average output power does not change much during the mode switching operation. Variable output beam profiles could be obtained by adjusting the frequency of the modulation signal, which also benefits from the unique characteristics of the AIFG.

## 2. Principle and Experimental Setup

### 2.1 Principle of AIFG

The basic schematic of an AIFG is shown in Fig. 1. It consists of a PZT, a quartz horn and a piece of FMF. The coating of a part of the FMF is removed, which serves as the acoustic-optic coupling region. Both the bottom diameter and the height of the horn are 10 mm. The resonant frequency of the PZT is near 1.7 MHz. The horn is epoxied to the PZT, which is driven by a radio frequency (RF) source. The modulation signal generated by the RF source is a sinusoidal waveform. When a radio frequency is applied onto the PZT, it will vibrate at the same frequency as the applied signal, and the horn will transfer the vibration into ultrasonic wave propagating along the fiber with the same frequency as the applied radio frequency. The propagating ultrasonic wave would generate periodic deformation (i.e., periodic index variation) in the fiber, which leads to the formation of a long period grating. The period of the grating can be calculated with the following formula [25]:

$$\Lambda = \sqrt{(\pi R C_{ext}/f)} \tag{1}$$

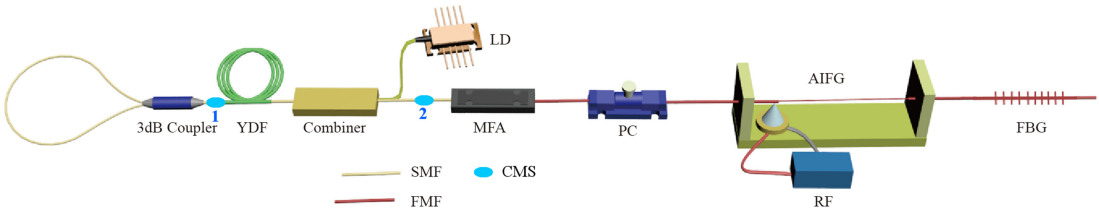


Fig. 2. Experimental setup of the mode-switchable fiber laser. (YDF: ytterbium-doped fiber, LD: laser diode, MFA: mode field adapter, PC: polarization controller, RF: radio frequency source, AIFG: acoustically-induced fiber grating, FBG: fiber Bragg grating, SMF: single mode fiber, FMF: few-mode fiber, CMS: cladding mode stripper).

where $R$ is the cladding radius of the unjacketed FMF, $C_{ext} = 5760$ m/s is the velocity of the acoustic wave in silica fiber, and $f$ is the frequency of the applied signal, which is also the frequency of the acoustic wave. In our work, the FMF used is a piece of germanium-doped fiber (GDF, 15/130 $\mu$m). Therefore, the cladding radius ($R$) of the FMF in Equation (1) is 65 $\mu$m. The core numerical aperture of the GDF is ~0.077 and the corresponding normalized frequency number (V number) is ~3.39 at 1070 nm. Therefore, this GDF can only support two modes, i.e., $LP_{01}$ and $LP_{11}$ mode.

According to the mode coupling theory, mode coupling and conversion occur when the phase matching condition is satisfied. The phase matching condition can be expressed as [28]:

$$\Lambda = L_B = \lambda/(n_{01} - n_{11}) \tag{2}$$

where $\lambda$ is the wavelength of the propagating wave, and $n_{01}$, $n_{11}$ are the effective refractive indexes of $LP_{01}$ and $LP_{11}$ mode, respectively. In this work, $n_{01} \approx 1.45946$ and $n_{11} \approx 1.45865$ at 1070 nm. Therefore, the expected period of the grating $\wedge$ will be ~1.32 mm according to Equation (2), and the applied modulation frequency is expected to be ~674.044 kHz.

Phase matching condition can be met by adjusting the modulation frequency $f$. Up to several MHz modulation frequency can be precisely reached by adjusting the setting of the signal generator for the RF source. This device can realize mode conversion between $LP_{01}$ and $LP_{11}$ mode as well as achieving the mixing state of both modes with variable proportions.

### 2.2 Experimental Setup

Figure 2 shows the experimental setup of the mode switchable fiber laser, which is a typical linear cavity. A 3-dB coupler working at 1080 $\pm$ 20 nm is used to form a fiber loop mirror (FLM) by splicing the two ports on the same side together to provide broadband feedback. A piece of 4-meter-long ytterbium-doped fiber (YDF) is adopted to provide active gain. The nominal cladding absorption coefficient of the YDF is ~5 dB/m at 976 nm. A 976-nm multimode laser diode (LD) is employed as the pump, and the pump laser is injected into the laser cavity through the pump port of a (2 + 1) $\times$ 1 combiner. The signal port of the combiner and the input port of the aforementioned AIFG are connected by a mode field adapter (MFA). The MFA is a home-made device based on a thermally expanded core technique [29]. The output port of the AIFG is further spliced with a few-mode FBG. The output end of the FBG is angle cleaved to 8 degrees to prevent unexpected backward reflection. The pigtail of the 3-dB coupler, the YDF and the signal port of the combiner are single mode fibers (SMFs), with a core/cladding diameter of 10/125 $\mu$m. The pigtails of the AIFG and the FBG are FMFs, with a core/cladding diameter of 15/130 $\mu$m. The core/cladding diameters of input and output ports of the MFA are 10/125 and 15/130 $\mu$m, respectively, which is adopted to reduce the cavity loss. Cladding mode strippers, which are made of a high refractive index glue, are coated on the bare fiber around the splicing points 1 and 2 to remove the cladding mode. A polarization controller (PC) is placed at the 15/130 $\mu$m port of the MFA to adjust the polarization state. Afterward, the output beam goes through a 4$f$ system with an adjustable attenuator before finally recorded by a laser beam analyzer (Ophir-Spiricon, SP620U).

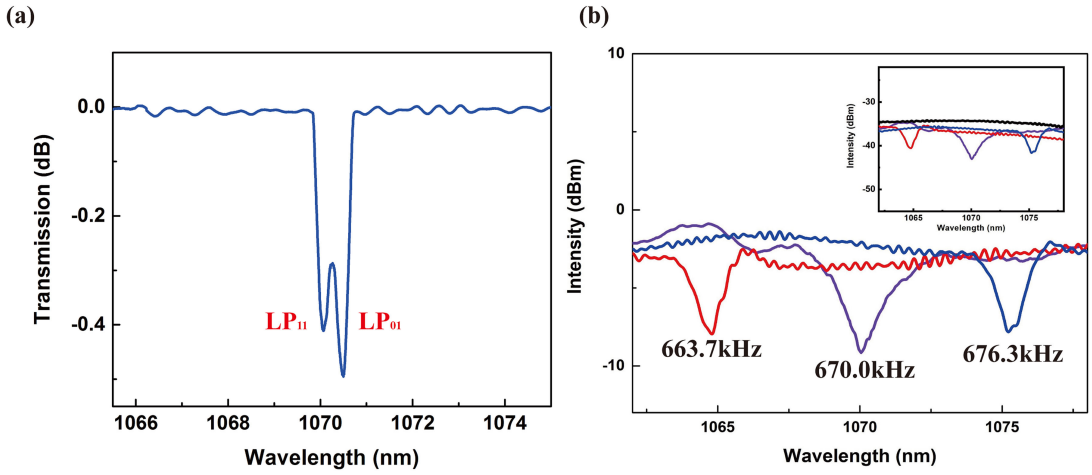


Fig. 3. (a) The transmission spectrum of the few-mode FBG. (b) The transmission spectra of the AIFG with the modulation frequency of 663.7 kHz, 670.0 kHz and 676.3 kHz (Inset: transmission spectra with and without modulation frequency).

The performance of the few-mode FBG and the AIFG is characterized with the optical spectrum analyzer (OSA). The resolution of the OSA is set to 0.02 nm. The transmission spectrum of the FBG is obtained by measuring the transmission spectrum with a hybrid spatial mode broadband source injected into the few-mode FBG. The hybrid mode source is produced by a lateral offset along the fiber to excite high-order modes. As presented in Fig. 3(a), the two transmission dips corresponding to $LP_{11}$ and $LP_{01}$ mode of the FBG locate at 1070.07 nm and 1070.48 nm, respectively. The reflectivity of this FBG is ~10.867% at 1070 nm, with a 3-dB bandwidth of 1.07 nm. Fig. 3(b) shows the transmission spectra of the AIFG at different modulation frequencies, which are obtained by calculating the intensity difference between the transmission spectra with (red, purple and blue curves) and without (black curve) the modulation frequency applied on the AIFG, as shown in the inset of Fig. 3(b). The transmission spectra at different modulation frequencies are measured in one setup by splicing the AIFG between a broadband ASE source and a piece of 10/125 fiber. Both the pigtail of the ASE source and the 10/125 fiber are single mode fibers and the splicing points are coated with high refractive index glue to remove cladding light. The acoustic-light interaction length is 0.5-meter-long, which is defined by the length of the unjacketed FMF. The applied peak-peak voltage on the PZT is optimized to be 120 V. The dips in the transmission spectra indicate the resonance wavelength range, which would vary with the applied modulation frequency. There are high resonance ranges around 1065, 1070 and 1075 nm when the modulation frequency is 663.7, 670.0, and 676.3 kHz, respectively, which indicates that mode coupling from $LP_{01}$ to $LP_{11}$ mode exists. The coupling efficiency from $LP_{01}$ to $LP_{11}$ mode is about 8.78 dB (~86.76%) around 1070 nm, which equals to the absolute intensity of the transmission dip in the transmission spectrum. This experimental frequency (670.0 kHz) and the theoretically calculated value (~674.044 kHz) at 1070 nm have a very good agreement. The small deviation is possibly caused by a slight difference between the actual values and the nominal values of the fiber parameters (i.e., the refractive index and the core diameter). The conversion efficiency can be further improved by changing the length of the acoustic-optic coupling region and optimizing the amplitude of the modulation signal.

## 3. Results and Discussion

Based on the above-mentioned experimental setup, mode switching between $LP_{01}$ and $LP_{11}$ is realized. The PC is used to adjust the polarization state and help to realize higher conversion efficiency [3]. Moreover, the mode purity can be improved in the meantime. As shown in Fig. 4(a), when the modulation signal with the frequency of 670.0 kHz is applied, the output mode of the

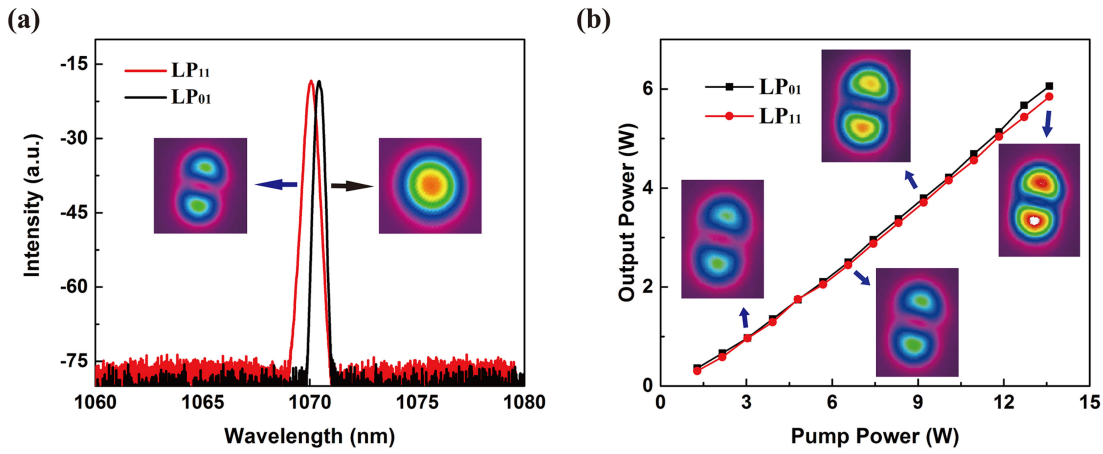


Fig. 4. (a) The output spectra of $LP_{11}$ mode and $LP_{01}$ mode. (b) The output power of $LP_{01}$ and $LP_{11}$ mode as a function of the pump power.

proposed laser switches from $LP_{01}$ to $LP_{11}$, and the corresponding output wavelength shifts from 1070.48 nm to 1070.07 nm, which matches well with the $LP_{01}$ and $LP_{11}$ peaks of the FBG. The linewidths of the $LP_{01}$ and $LP_{11}$ mode output spectra are 0.28 and 0.27 nm, respectively. In our work, the two wavelengths corresponding to $LP_{01}$ and $LP_{11}$ mode of the FBG cannot exist together. Consequently, when the device works in $LP_{11}$ mode, if there are any unconverted $LP_{01}$ mode components, they will be reflected by the FBG and pass through the AIFG, where the $LP_{01}$ mode would be converted into the $LP_{11}$ mode and dissipate in the SMF. Therefore, the single wavelength operation can ensure high mode purity of the $LP_{11}$ mode. The output power as a function of the pump power is shown in Fig. 4(b). The maximum output powers of $LP_{01}$ and $LP_{11}$ mode lasers are 6.06 and 5.85 W with a slope efficiency of ~48.16% and ~46.58%, respectively. As indicated in Fig. 3(b), the conversion loss of the AIFG is ~13.24% from $LP_{01}$ to $LP_{11}$ mode, but the overall efficiencies of both $LP_{01}$ and $LP_{11}$ mode do not differ much. The small efficiency difference can possibly be attributed to the cavity loss difference of these two modes caused by the PC in this configuration. Although only $LP_{01}$ mode experiences the gain in the lasing medium regardless of the output mode, the PC is adjusted to a position where the cavity loss of $LP_{01}$ mode is higher than that of the $LP_{11}$ mode. Therefore, the overall efficiency of the $LP_{01}$ and $LP_{11}$ mode does not differ much in this case.

Since the output mode of the proposed fiber laser is significantly correlated with the output spectrum, the stability of the $LP_{11}$ mode operation can be verified through checking the stability of the central wavelength and the intensity of the output spectra. Fig. 5(a) presents the output spectra of the fiber laser with $LP_{11}$ mode output, which are recorded every 2 minutes within a total time frame of 10 minutes. The central wavelength and intensity of the output spectra are generally stable, the former of which varies from 1070.062 to 1070.085 nm, while the latter of which ranges from −39.436 to −39.375 dB during the whole test. The insignificant central wavelength variation (0.017 nm) and power fluctuation (0.061 dB, equals to 1.39%) indicate that this laser works stably in $LP_{11}$ mode regime.

Owing to the unique advantage of AIFG, this laser can deliver laser output with controllable proportion of high order components simply by changing the modulation frequency. The output beam profiles under different modulation frequencies are shown in Fig. 6. As the modulation frequency comes close to the working point (670.0 kHz), the proportion of the $LP_{11}$ mode increases gradually, which means the components of $LP_{11}$ mode can be tailored to a desired ratio. What should be noted is that the output beam profile is very stable, which can be repeated simply by adjusting the modulation frequency to the corresponding frequency. Future work could adopt modal decomposition to quantify the fraction of power in each mode and better control the proportions of

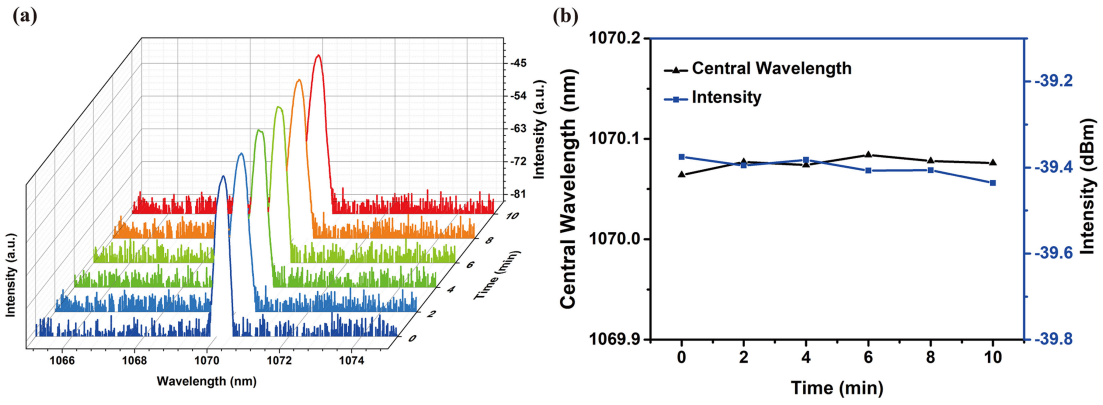


Fig. 5. (a) The output spectra of the fiber laser. (b) The variation of central wavelength and intensity of the output spectra.

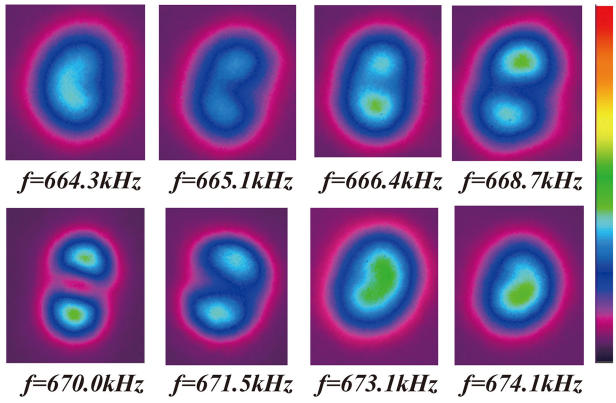


Fig. 6. Output beam profiles at different modulation frequencies.

each mode. The capability of realizing versatile output beam profiles could find potential applications in material processing, light field manipulation, etc.

Benefiting from the flexible modulation frequency property of the AIFG, this laser also possesses agile mode switching ability. The switching time, as well as the prompt mode switching capability, have been intensively studied. At first, we use the laser beam analyzer to record the mode switching operation, and the mode-switching operation recorded with a frame rate of 15 Hz is shown in Visualization 1. Since the maximum frame rate of the laser beam analyzer is only ~30 Hz, it cannot meet the demand for fast mode-switching analysis. Another option is monitoring the power fluctuations sampling from the variable output beam profile, which can be achieved by placing a pinhole before a photon detector (PD). The bandwidths of the oscilloscope and the PD employed in our work are 200 MHz and 150 MHz, respectively.

The position of the pinhole is carefully adjusted to make it close to the center of the lobe of the $LP_{11}$ mode. In this case, the power level at the selected sampling point will be higher when the laser operates in $LP_{11}$ mode compared with that of $LP_{01}$ mode. First of all, fast mode switching between $LP_{01}$ and $LP_{11}$ is investigated under different mode-switching speed. Fig. 7(a) and (b) show the temporal trace read from the oscilloscope when the mode is switched from $LP_{01}$ to $LP_{11}$ mode back and forth by applying 670.0-kHz modulation signal and no modulation to the PZT with at a frequency of 100 and 250 Hz, respectively. Under these circumstances, the mode can be fully switched between $LP_{01}$ and $LP_{11}$ without apparent distortion. In order to obtain the maximum mode-switching speed, the time needed for mode switching from $LP_{01}$ to $LP_{11}$ mode and the mode

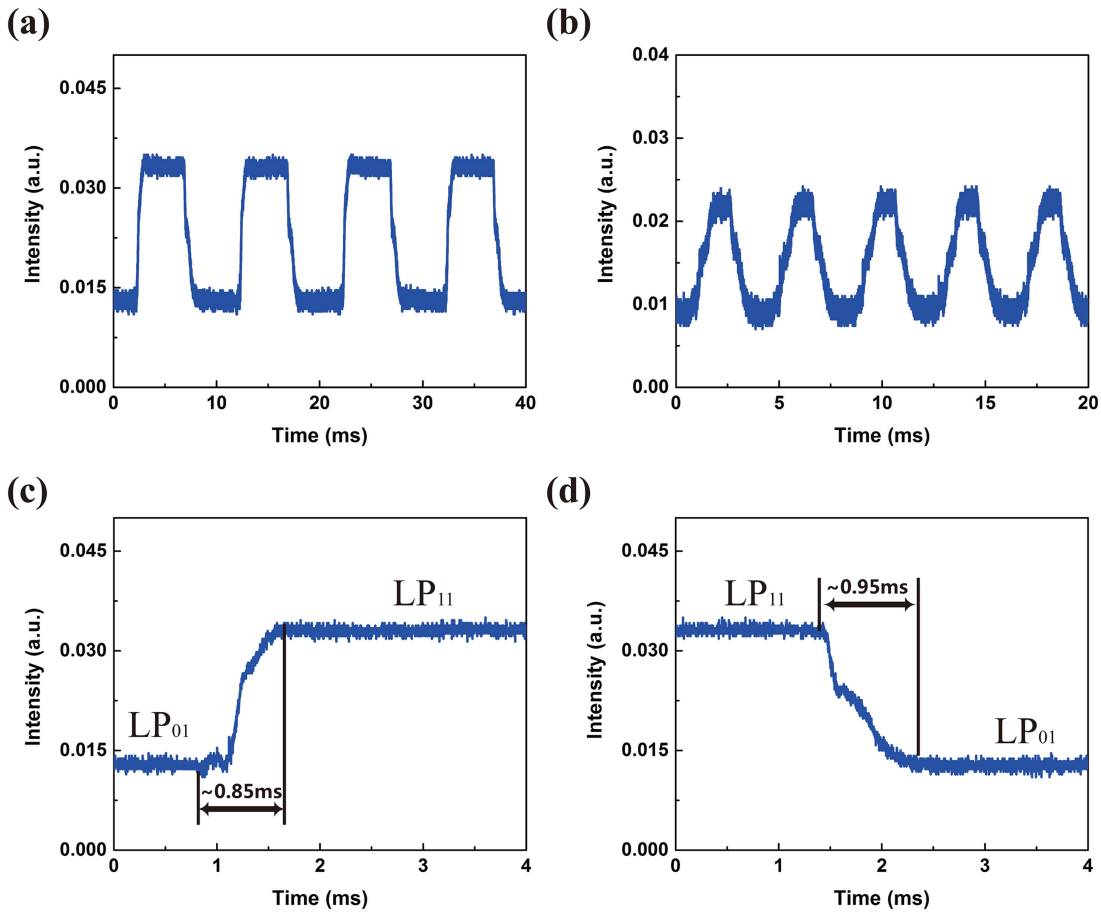


Fig. 7. (a) Temporal trace of mode switching at a switching frequency of 100 Hz. (b) Temporal trace of mode switching at a switching frequency of 250 Hz. (c) Temporal trace of mode switching from $LP_{01}$ to $LP_{11}$. (d) Temporal trace of mode switching from $LP_{11}$ to $LP_{01}$.

switching from $LP_{11}$ to $LP_{01}$ mode is measured. By capturing the rising edge of the temporal trace, the switching time from $LP_{01}$ to $LP_{11}$ mode can be obtained to be ~0.85 ms, as shown in Fig. 7(c). Similarly, the switching time from $LP_{11}$ to $LP_{01}$ mode can be obtained by capturing the falling edge of the temporal trace, which is ~0.95 ms, as shown in Fig. 7(d). Although the switching time of the AIFG can be as short as a few hundred microseconds [30], the switching time in this laser setup is supposed to be mainly determined by the lifetime of $Yb^{3+}$ ions in excited state, which is around ~0.84 ms [31]. Different from our very recent work presented in [30], in which a cavity mirror is used instead of the few-mode FBG in this work, the central wavelength of the laser proposed in this paper also switches accompanying the mode-switching process. This wavelength-switching process would take some time, i.e., the lifetime of $Yb^{3+}$ ions in the excited state, to realize stable oscillation. Therefore, based on the obtained switching time between $LP_{11}$ and $LP_{01}$, the maximum switching speed can be calculated to be ~555.56 Hz. When the switching speed is higher than 555.56 Hz, the output mode cannot be fully switched between the $LP_{01}$ and $LP_{11}$ mode.

Furthermore, the power fluctuation at the mode-switching speed of 1 kHz is also measured, the result of which is shown in Fig. 8(a). Although the mode switching between $LP_{11}$ and $LP_{01}$ mode cannot be fully realized in this case, the power level at the monitored point is still changing at 1 kHz. Moreover, it can also be used to obtain dynamical output beam profiles. We make the modulation frequency sweep from 661 kHz to 670 kHz back and forth periodically. The periodical time is set to 17 seconds, and the setting of the sweeping signal is given in Fig. 8(b). The recorded power

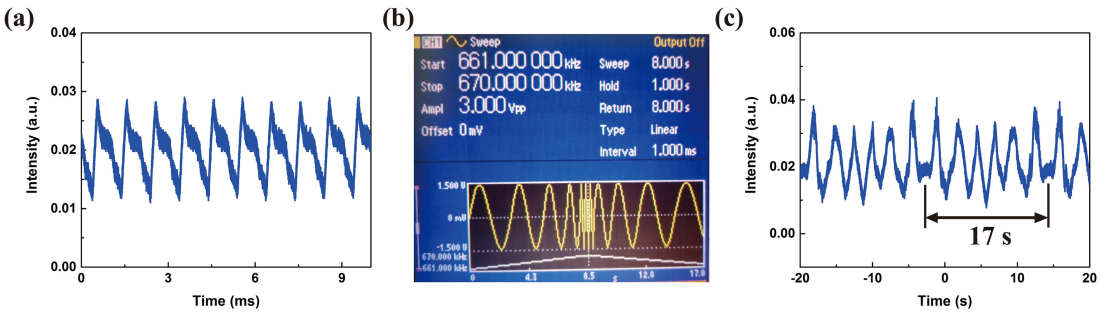


Fig. 8. (a) Temporal trace of mode switching at a switching frequency of 1 kHz. (b) Setting of the arbitrary function generator for the sweeping signal. (c) Temporal trace of the periodical modulation frequency sweeping.

changes regularly in a period the same as that of the modulation signal, as shown in Fig. 8(c). At the same time, the output beam profile also changes fast, and the proportion of $LP_{01}$ and $LP_{11}$ mode is also changing (See visualization 2). These results also indicate this laser has the capability of realizing variable output beam profiles with repeatable patterns.

## 4. Conclusion

In conclusion, we have demonstrated an all-fiber laser with agile mode switching capability. Mode switching is achieved by adopting a self-constructed AIFG, which can be applied to realize mode conversion and agile mode switching at almost arbitrary wavelengths simply by adjusting the modulation frequency. The highest output power of $LP_{11}$ mode obtained in this laser is 5.85 W with a slope efficiency of ~46.58% at 1070.07 nm and the output power of $LP_{01}$ mode reaches 6.06 W with a slope efficiency of ~48.16% at 1070.48 nm. The time needed for mode switching operation has also been measured. The switching time from $LP_{01}$ to $LP_{11}$ mode is ~0.85 ms, while it takes ~0.95 ms to switch from $LP_{11}$ to $LP_{01}$ mode. Mode switching between $LP_{01}$ and $LP_{11}$ at a switching speed of 250 Hz is realized. Besides, this laser could modulate the power distribution at kHz and even higher modulation speed. It should be noted that this work presents a preliminary demonstration for efficient mode switching between the $LP_{01}$ mode and $LP_{11}$ mode. Agile mode-switching between two or more symmetric modes of different orders, aiming at material processing applications, can be expected if adopting proper FMF for the AIFG [32] and well-designed schematic. This work also provides an efficient method to realize relatively high power laser sources with the agile mode-switching ability for practical use. Further power scaling can be expected with higher pump power under the present configuration. However, the master oscillator power amplifier scheme should be employed to achieve high-power output with hundreds or even thousands of watts.

## Acknowledgment

The authors would like to thank Linghao Meng, Jiawei He, Jun Ye, Yanran Gu, Teng Wang, Fan Shi, Yi An, and Yu Hu for their kind help on carrying out the experiments and useful discussions. The authors also thank Binbin Wei and Mohammed Salih for proofreading this manuscript.

## References

[1] S. Ngcobo, I. Litvin, L. Burger, and A. Forbes, "A digital laser for on-demand laser modes," *Nat. Commun.*, vol. 4, 2013, Art. no. 2289.
[2] A. Forbes, A. Dudley, and M. McLaren, "Creation and detection of optical modes with spatial light modulators," *Adv. Opt. Photon.*, vol. 8, no. 2, pp. 200–227, 2016.
[3] R. Chen *et al.*, "High efficiency all-fiber cylindrical vector beam laser using a long-period fiber grating," *Opt. Lett.*, vol. 43, no. 4, pp. 755–758, 2018.

[4] X. Yang, Z. Xu, S. Chen, and Z. Jiang, "High power $LP_{11}$ mode supercontinuum generation from an all-fiber MOPA," *Opt. Exp.*, vol. 26, no. 11, pp. 13740–13745, 2018.
[5] L. Huang, J. Leng, P. Zhou, S. Guo, H. Lü, and X. A. Cheng, "Adaptive mode control of a few-mode fiber by real-time mode decomposition," *Opt. Exp.*, vol. 23, no. 21, pp. 28082–28090, 2015.
[6] R. Su *et al.*, "500 W level MOPA laser with switchable output modes based on active control," *Opt. Exp.*, vol. 25, no. 19, pp. 23275–23282, 2017.
[7] P. Lu, M. Shipton, A. Wang, S. Soker, and Y. Xu, "Adaptive control of waveguide modes in a two-mode-fiber," *Opt. Exp.*, vol. 22, no. 3, pp. 2955–2964, 2014.
[8] B. Sun *et al.*, "Transverse mode switchable fiber laser through wavelength tuning," *Opt. Lett.*, vol. 38, no. 5, pp. 667–669, 2013.
[9] T. Liu, S. Chen, and J. Hou, "Selective transverse mode operation of an all-fiber laser with a mode-selective fiber Bragg grating pair," *Opt. Lett.*, vol. 41, pp. 5692–5695, 2016.
[10] J. Song *et al.*, "High power narrow linewidth LP11 mode fiber laser using mode-selective FBGs," *Laser Phys. Lett.*, vol. 15, no. 11, 2018, Art. no. 115101.
[11] T. Wang *et al.*, "Generation of femtosecond optical vortex beams in all-fiber mode-locked fiber laser using mode selective coupler," *J. Lightw. Technol.*, vol. 35, no. 11, pp. 2161–2166, Jun. 2017.
[12] Y. Huang *et al.*, "High-order mode Yb-doped fiber lasers based on mode-selective couplers," *Opt. Exp.*, vol. 26, no. 15, pp. 19171–19181, 2018.
[13] S. Ramachandran, J. M. Fini, M. Mermelstein, J. W. Nicholson, S. Ghalmi, and M. F. Yan, "Ultra-large effective-area, higher-order mode fibers: A new strategy for high-power lasers," *Laser Photon. Rev.*, vol. 2, no. 6, pp. 429–448, 2008.
[14] W. Zhang *et al.*, "Tunable-wavelength picosecond vortex generation in fiber and its application in frequency-doubled vortex," *J. Opt.*, vol. 20, no. 1, 2018, Art. no. 014004.
[15] H. Wan, J. Wang, Z. Zhang, Y. Cai, B. Sun, and L. Zhang, "High efficiency mode-locked, cylindrical vector beam fiber laser based on a mode selective coupler," *Opt. Exp.*, vol. 25, no. 10, pp. 11444–11451, 2017.
[16] N. Sanner, N. Huot, E. Audouard, C. Larat, and J. P. Huignard, "Direct ultrafast laser micro-structuring of materials using programmable beam shaping," *Opt. Laser. Eng.*, vol. 45, no. 6, pp. 737–741, 2007.
[17] M. Duocastella and C. B. Arnold, "Bessel and annular beams for materials processing," *Laser Photon. Rev.*, vol. 6, no. 5, pp. 607–621, 2012.
[18] J. M. O. Daniel and W. A. Clarkson, "Rapid, electronically controllable transverse mode selection in a multimode fiber laser," *Opt. Exp.*, vol. 21, no. 24, pp. 29442–29448, 2013.
[19] D. A. V. Kliner and B. Victor, "A breakthrough for fiber lasers," *Photon. Views*, vol. 16, no. 1, pp. 51–55, 2019.
[20] W. Zhang *et al.*, "Optical vortex generation with wavelength tunability based on an acoustically-induced fiber grating," *Opt. Exp.*, vol. 24, no. 17, pp. 19278–19285, 2016.
[21] I. L. Villegas *et al.*, "Mode-locked Yb-doped all-fiber laser based on in-fiber acoustooptic modulation," *Laser Phys. Lett.*, vol. 8, no. 3, p. 227, 2011.
[22] C. Cuadrado-Laborde, A. Díez, J. L. Cruz, and M. V. Andrés, "Doubly active Q switching and mode locking of an all-fiber laser," *Opt. Lett.*, vol. 34, no. 18, pp. 2709–2711, 2009.
[23] L. Carrión-Higueras, E. P. Alcusa-Sáez, A. Díez, and M. V. Andrés, "All-fiber laser with intracavity acousto-optic dynamic mode converter for efficient generation of radially polarized cylindrical vector beams," *IEEE Photon. J.*, vol. 9, no. 1, Feb. 2017, Art. no. 1500507.
[24] X. Zhang *et al.*, "All-fiber cylindrical vector beams laser based on an acoustically-induced fiber grating," *J. Opt.*, vol. 20, no. 7, 2018, Art. no. 075608.
[25] W. Zhang *et al.*, "Generation of femtosecond optical vortex pulse in fiber based on an acoustically induced fiber grating," *Opt. Lett.*, vol. 42, no. 3, pp. 454–457, 2017.
[26] W. Zhang *et al.*, "High-order optical vortex generation in a few-mode fiber via cascaded acoustically driven vector mode conversion," *Opt. Lett.*, vol. 41, no. 21, pp. 5082–5085, 2016.
[27] K. Wei *et al.*, "Generation of cylindrical vector beams and optical vortex by two acoustically induced fiber gratings with orthogonal vibration directions," *Opt. Exp.*, vol. 25, no. 3, pp. 2733–2741, 2017.
[28] A. M. Vengsarkar, J. R. Pedrazzani, J. B. Judkins, P. J. Lemaire, N. S. Bergano, and C. R. Davidson, "Long-period fiber-grating-based gain equalizers," *Opt. Lett.*, vol. 21, no. 5, pp. 336–338, 1996.
[29] X. Zhou, Z. Chen, H. Chen, J. Li, and J. Hou, "Mode field adaptation between single-mode fiber and large mode area fiber by thermally expanded core technique," *Opt. Laser Technol.*, vol. 47, pp. 72–75, 2013.
[30] J. Lu *et al.*, "Dynamic mode-switchable optical vortex beams using acousto-optic mode converter," *Opt. Lett.*, vol. 43, no. 23, pp. 5841–5844, 2018.
[31] R. Paschotta, J. Nilsson, P. R. Barber, J. E. Caplen, A. C. Tropper, and D. C. Hanna, "Lifetime quenching in Yb-doped fibres," *Opt. Commun.*, vol. 136, no. 5/6, pp. 375–378, 1997.
[32] D. Song, H. Su Park, B. Y. Kim, and K. Y. Song, "Acoustooptic generation and characterization of the higher order modes in a four-mode fiber for mode-division multiplexed transmission," *J. Lightw. Technol.*, vol. 32, no. 23, pp. 3932–3936, Dec. 2014.

## III.4 CONCLUSION

It is a new strategy to develop a dynamic switching method. Compared to conventional static mode conversion strategy, acousto-optic interaction with dual-resonant property is a novel approach to satisfy both the dynamic switching ability and the wavelength tunability. To summarize the key results that we have obtained in this chapter:

**In normal fiber lasers**:

1. Dual-resonance has been discovered in a few-mode fiber (YOFC-4) based acousto-optic mode converter at the communication band. According to both simulation results and experimental observations, these two resonant peaks in the spectrum are related to two orthogonal HOMs, namely $LP_{11a}$ and $LP_{11b}$ modes due to a degeneration mechanism.
2. The depths of two resonant peaks (two mode conversion efficiencies) are investigated to be tunable by adjusting the adhere angle of fiber and horn.
3. The fundamental mechanism of dual resonances is revealed to be a co-effect of acoustic and optic birefringence. Basically, it is the geometric inhomogeneity that leads to a mismatch of acoustic neutral axis and optical neutral axis. Thus, the effective refractive indices of $LP_{11a}$ and $LP_{11b}$ modes are degenerated and exhibit an obvious difference. This difference results in different resonant wavelengths in the mode conversion.
4. Combined with the inherent wavelength tunability of acousto-optic converter, the vortex mode switching is demonstrated by altering the frequency of the microwave signal. This is an external and dynamic switching strategy of vortex modes control in fiber optics.
5. This vortex mode switching owns a fast-switching speed up to 4.3 kHz. Specifically, the switching time between $LP_{01}$ mode and $LP_{11a}$ mode is about 0.15 ms; the switching time between $LP_{01}$ mode and $LP_{11b}$ mode is about 0.31 ms; the switching time between $LP_{11a}$ mode and $LP_{11b}$ mode (and the related -1-order OAM and +1-order OAM mode) is about 0.15 ms.
6. The vortex mode switching is realized in a linear fiber laser cavity

with an output slope efficiency of 18.2%.

**In high-power fiber lasers**:

1. Dynamic mode switching of HOMs ($LP_{11a}$ and $LP_{11b}$ modes) is demonstrated at the 1.0-μm band. This result indicates a good potential in high-power fiber laser with HOMs operation because 1.0-μm band is suitable with high-power output due to a Yb-doped gain fiber.
2. The maximum powers obtained in this work are investigated to be 6.06 W and 5.85 W at the operation of $LP_{01}$ mode and $LP_{11}$ modes, respectively. Despite the output power for now is not very high, this result shows implications with good thermal stability of the acousto-optic mode conversion device in high-power fiber lasers.
3. Slight difference of the output wavelength is observed with 1070.48 nm at $LP_{01}$ mode and 1070.07 nm at $LP_{11}$ mode, respectively. This is due to the different reflection wavelength of the few-mode FBG utilized as cavity mirror.
4. The output spectrum remains stable during 10 mins with high-power operation.
5. The switching time from $LP_{01}$ mode to $LP_{11}$ modes investigated in this work is carried out to be 0.85 ms while the switching time from $LP_{11}$ modes to $LP_{01}$ mode is measured to be 0.95 ms. These switching times are longer than the results measured in our results at 1.5-μm band because it is restricted by the laser oscillation time in this fiber laser cavity.

In conclusion, we have developed a novel acousto-optic mode converter with HOM switching and vortex mode switching with a high switching speed. This device is of great potential in fiber lasers that require HOMs or vortex modes operations and high-power outputs. This might open the door towards new fiber lasers with agile mode switching dynamics and endow more functions to the fiber laser community.

# Chapter.IV SWITCHING DYNAMICS IN ULTRAFAST FIBER LASERS VIA ACOUSTO-OPTIC INTERACTIONS

## IV.1 INTRODUCTION

Ultrafast fiber lasers are of great interest in the laser study due to its unique ultrahigh peak powers and ultrashort durations. These fiber lasers operated at ultrashort pulses exhibit diverse nonlinear effects themselves and in interactions with matters. Previous researchers pour their passions in fabricating different kinds of ultrafast lasers to meet different requirements for the performance. Recently, more studies of operating mechanisms in ultrafast fiber lasers are carried out due to the development of time-stretched dispersive Fourier transform technique. Transient processes in ultrafast fiber lasers exhibit interesting phenomena that reveal a lot of inner mechanisms of the ultrafast light behaviors in the laser cavity. This is fundamentally new since it provides the physical descriptions of each stage where the light evolves in a mode locking formation process. Especially for the build-up and collapse processes [196,198,201], they describe the birth and death of the pulses.

To go beyond the limitations of the static cavities in conventionally reported fiber lasers (i.e., only pump supply can be utilized as a "trigger" of the transient process), dynamic switching strategy enabled by acousto-optic interactions in fibers allows more possibilities for external perturbation introductions in the laser cavity and provides new potentials in observing diverse behaviors of light pulses operating between different mode locking states.

In this Chapter, we realize the real-time observation of vortex modes switching dynamics in a mode locked fiber laser with a linear cavity, which is related to a published work in ***Photonics Research*** in 2020. With the dynamic tunability of the acousto-optic mode converter, the "trigger" between different modes is easily obtained. Thus, by time-stretched dispersive Fourier transform technique, the transient dynamics is available to be observed. The whole process from one stable mode locking state to another stable mode locking state is

recorded.

In addition, with a special design of the laser cavity incorporation with acousto-optic interactions, a pulse width switching between femtosecond scale and picosecond scale is realized. This result provides a new sight of dynamic switching at temporal view, which is different from spatial mode switching. Pulse width is an important parameter in ultrafast lasers and thus its manipulation would extend the applications of the lasers. However, the previous control of pulse width is quite static by adjusting the band pass or manual attenuation control. This idea is a kind of combining two lasers in one laser cavity, which exhibits a bit of clumsy. Furthermore, this manual strategy is not capable of dynamics observation. However, we proposed a dynamic control of the pulse width switching enabled by a dynamic manipulation of the attenuation in one single laser cavity to achieve the oscillation altering between broadband and narrow band, which correlates to a femtosecond pulsed output and a picosecond pulsed output. Besides, the transient dynamics is also available due to the excellent “trigger” property of the acousto-optic device.

## IV.2 Real-time observation of vortex mode switching in a narrow-linewidth mode-locked fiber laser

# Real-time observation of vortex mode switching in a narrow-linewidth mode-locked fiber laser

JIAFENG LU,[1] FAN SHI,[1] LINGHAO MENG,[1] LONGKUN ZHANG,[1] LINPING TENG,[1] ZHENGQIAN LUO,[2] PEIGUANG YAN,[3] FUFEI PANG,[1,4] AND XIANGLONG ZENG[1,*]

[1]*Key laboratory of Specialty Fiber Optics and Optical Access Networks, Joint International Research Laboratory of Specialty Fiber Optics and Advanced Communication, Shanghai University, Shanghai 200444, China*

[2] *Department of Electronic Engineering, School of Information Science and Engineering, Xiamen University, Xiamen 361005, China*

[3] *Shenzhen Key Laboratory of Laser Engineering, Shenzhen University, Shenzhen 518060, China*

[4] *ffpang@shu.edu.cn*

**Corresponding author: zenglong@shu.edu.cn*

Received XX Month XXXX; revised XX Month, XXXX; accepted XX Month XXXX; posted XX Month XXXX (Doc. ID XXXXX); published XX Month XXXX

**Temporal and spatial resonant modes are always possessed in physical systems with energy oscillation. In the ultrafast fiber lasers, enormous progress has been made toward controlling the interactions of many longitudinal modes, which results in temporally mode-locked pulses. Recently optical vortex beams have been extensively investigated due to their quantized orbital angular momentum, spatially donut-like intensity and spiral phase front. In this paper we have demonstrated the first observation of optical vortex modes switching and their corresponding pulse evolution dynamics in a narrow-linewidth mode-locked fiber laser. The spatial mode switching is achieved by incorporating a dual-resonant acousto-optic mode converter in the vortex mode-locked fiber laser. The vortex mode switching dynamics have four stages, including quiet-down, relaxation oscillation, quasi-mode locking and energy recovery prior to the stable mode locking of another vortex mode. The evolution dynamics of the wavelength shifting during the switching process are observed via time-stretch dispersion Fourier transform method. The spatial mode competition through optical nonlinearity induces energy fluctuation on the time scale of ultrashort pulses, which plays an essential role in the mode switching dynamic process. The results have great implications in the study of spatially mode-locking mechanism and ultrashort laser applications.** 

http://dx.doi.org/10.1364/prj.99.099999

## 1. Introduction

Transient phenomenon dynamics are of significance for revealing the evolution mechanism of numerous nonlinear systems [1-4]. Mode-locked lasers can exhibit profound nonlinear optical dynamics and have moved into the spotlight of optical research due to their unique intriguing properties of temporal and spatial oscillation [5-9]. Recent years have seen increased interests in mode-locked fiber lasers and largely in anticipation of particle manipulation [10, 11], ultrafast laser fabrication [12], high-capacity optical communication [13], and Bose-Einstein condensates [14].

The mode-locked fiber laser provides an ideal platform for exploring the ultrashort nonlinear dynamics, where mode locking (ML) pulses arise from the balance among optical nonlinearity, dispersion, intracavity gain and loss [15]. Despite of the ultimate stable ML state, mode-locked lasers experience a series of unstable phenomena when detuned from steady state or originating as stable ML pulses from the noise [16]. These instabilities are important as they reveal the landscape of the pulse evolution during the self-starting process and ML process. The self-starting dynamics in the passive mode-locked fiber lasers have been established by a rich variety of theoretical and experimental results [17-20]. Recently, researchers have pioneered the time-stretch dispersive Fourier transform (TS-DFT) technique to the exploration of build-up dynamics in the ML fiber lasers [21-24]. They have revealed the detailed information of underlying dynamics in the self-starting process and generalized the build-up process into three stages: relaxation oscillation, quasi-mode locking (Q-ML) stage and stable ML. Polarization change in the laser cavity, energy fluctuation of pump power and extra environmental perturbations can influence the formation dynamics of the ML pulses. Therefore, the entire observation of the ML process has great implication in the laser operation.

Temporal mode-locked fiber lasers have major influence on both laser physics and practical applications through lasing spatially at the fundamental mode. However, the so-called "capacity crunch" is anticipated, whereby the single mode fibers (SMFs) are unable to meet the increasing demand of data

telecommunications. At present, the optical spatial division multiplexing (SDM) technique emerges to provide a promising solution to this potential bandwidth crisis [25, 26]. The few-mode-fibers (FMFs) and multimode fibers (MMFs) exploited in SDM systems can support a few spatial eigenmodes, each with different propagating constants and spatial distributions. Vortex light multiplexing has obtained great attentions due to its new multiplexing dimension of orbital angular momentum (OAM). Recently, terabit free space communication employing vortex light has been demonstrated [13]. These modes can interact with each other in the FMFs and MMFs through optical nonlinearity, disorder (random linear mode coupling) and laser gain [27]. The spatial modes interaction in ultrafast mode-locked fiber lasers is much more interesting and finally evolves into the spatiotemporal ML. Previous reports mainly focus on the overall effect and joint interaction between 10-100 spatial modes in spatiotemporal mode-locking, but the specific interaction between the identified individual spatial modes remains to be further explored [28-31].

In this paper, we have demonstrated the first observation of vortex mode switching dynamics This result helps scientists understanding the rich variety of instability phenomena in the mode switching dynamic process and the influence of spatial mode interactions on ML states. Previously, static spatial mode-switching has been demonstrated in both fiber [32] and free space [33]. Nevertheless, the static mode switching of different spatial modes requires manual adjustment of polarization controller or cavity mirror. However, these static mode switching methods often suffer from the following restrictions: (1) complexity of manual adjustments; (2) low switching speed for capturing the dynamic mode switching process; (3) environmental sensitivity. To realize the real-time observation of mode switching dynamics, here a dual-resonant acousto-optic mode converter (AOMC) is employed to provide a tunable mode switching with fast switching speed in a narrow-linewidth mode-locked laser cavity.

## 2. Theory: acoustic displacement-based model of dual-resonant AOMC

The AOMC components exploit electro-acoustic conversion effect in piezoceramic (PZT) materials and acousto-optic interaction effect in silica fiber media to construct a dynamic tunable spatial mode conversion [34-37]. In our previous report [38, 39], we preliminarily utilized the AOMC in a continuous-wave fiber laser, yet complete theoretical analysis was not demonstrated to reveal the entire property of dual-resonant AOMC. Here we introduce the mode switching mechanism of AOMC into a mode-locked fiber laser to discover the mode switching dynamics on ML states, which broadens the practical value of dual-resonant AOMC and enriches the ultrafast physical fundamentals.

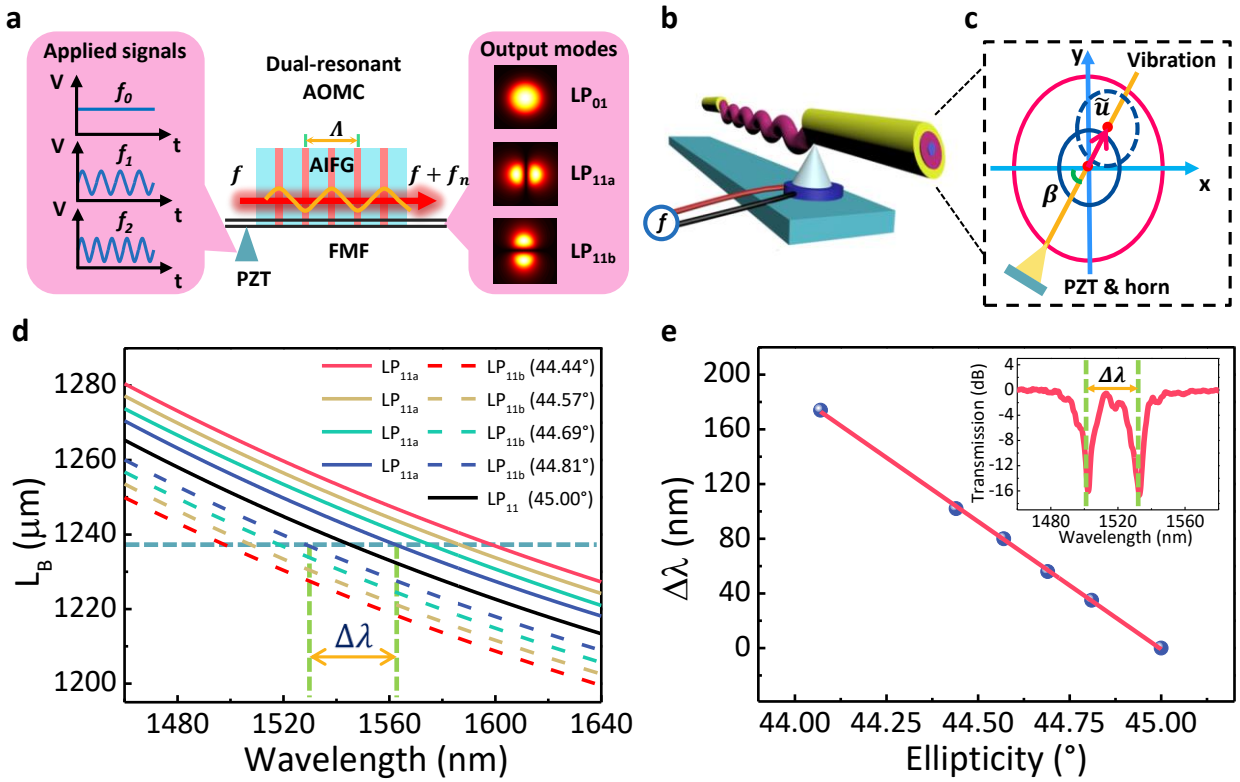


Fig. 1. The diagram of an AOMC and the simulation of the switching mechanism based on optical and acoustic birefringence. (a) The schematic diagram of the dual-resonant AOMC and the mode switching mechanism. (b) The setup of an AOMC component. (c) The schematic diagram of the fiber end face. (d) The simulation of beat lengths between $LP_{01}$ mode and $LP_{11a/b}$ modes with different ellipticities of the fiber core. The straight lines and dash lines represent the beat lengths from $LP_{01}$ mode to $LP_{11a}$ and $LP_{11b}$, respectively. (e) The **$\Delta\lambda$** shifts as the decrease of ellipticity of fiber core. Inset figure shows the wavelength separation in the transmission spectrum of dual-resonant AOMC.

The interaction of light beams and acoustic waves enables the optical field controlling in silica fibers, which is mainly derived from the photon-phonon scattering. It is a common belief that a travelling flexural acoustic wave (FAW) produces a periodic micro-bending, which causes an interlaced density of fiber medium as shown in **Fig. 1(a)**. The FAW propagating along the unjacketed silica fiber at the lowest-order mode ($F_{11}$ mode) leads to an acoustically induced displacement vector (AIDV) of $\tilde{\boldsymbol{u}}$ on the fiber medium, which is asymmetric with respect to the direction of applied vibration. **Figure 1(b)** and **1(c)** show the schematic drawing of the AOMC component and the schematic diagram of the fiber end face with acoustic wave, respectively. Therefore, the permittivity deformation of the FAW-endowed ellipse fiber can be classified into two principle contributions [40]: geometric perturbation of $\boldsymbol{\varepsilon_g}$ and photo-elastic effect of $\boldsymbol{\varepsilon_p}$. The whole effect induced by the FAW on the fiber can be explained via a permittivity deformation as: $\delta\hat{\varepsilon}(x,y,z,t) = \delta\varepsilon_g(x,y,z,t) + \delta\varepsilon_p(z,t)$.

Geometrical deformation wave introduces the acoustic displacement and modifies the unperturbed permittivity $\varepsilon_0(x,y)$ as followed:

$$\varepsilon_0(x,y) \to \varepsilon_0(x-u_x, y-u_y) \tag{1}$$

$u_x$ and $u_y$ represent the orthogonal components of acoustic displacement $\tilde{\boldsymbol{u}}$. The ellipticity of silica fiber leads to an acoustic birefringence, which can be allowed for by making use of the following trigonometric decomposition:

$$u_x = u_0 \cos(Kz - f_n t)\cdot cos\beta \cdot e^{i\frac{2\pi}{\Lambda_s}},$$
$$u_y = u_0 \cos(Kz - f_n t)\cdot sin\beta \cdot e^{i\frac{2\pi}{\Lambda_l}}. \tag{2}$$

Here, $u_0$ represents the amplitude of the acoustic vibration displacement. $f_n$ is the applied frequency of the radio frequency (RF) signal (subscript $n$ refers to different resonant mode conversions). $K$ is the wave vector of the FAW. Axes $\boldsymbol{x}$ and $\boldsymbol{y}$ represent the short and long axes of the fiber in the view of fiber end face, respectively. Axis $\boldsymbol{z}$ is the fiber axial direction. $\Lambda$ stands for the period of acoustically induced fiber grating (AIFG), which can be expressed as $\Lambda = (\pi \cdot C_{ext} \cdot R/f_n)^{\frac{1}{2}}$, where $C_{ext} = 5760\ m/s$ is the velocity of acoustic wave propagating in silica media. $R$ is the radius of the fiber cladding. In an ellipse fiber, the AIFG periods are different at the two orthogonal directions because the radii of fiber cladding short axis and long axis are different. Therefore, $\Lambda_s$ and $\Lambda_l$ are defined as the AIFG periods at the short axis and the long axis, respectively. Angle $\boldsymbol{\beta}$ is defined as the angle between Axis $\boldsymbol{x}$ and the direction of acoustic vibration.

Thus, the geometrically induced correction of permittivity $\delta\varepsilon_g$ can be obtained by utilizing the standard framework of micro-bending-based model while the photo-elastic correction of permittivity $\boldsymbol{\delta\varepsilon_p}$ can be obtained by combining the photo-elastic tensor in the fiber medium, respectively [34, 35, 40]:

$$\delta\varepsilon_g = \begin{bmatrix}\delta\varepsilon_g^x \\ \delta\varepsilon_g^y\end{bmatrix} = \begin{bmatrix}n_{co}K^2u_x\cdot x \\ n_{co}K^2u_y\cdot y\end{bmatrix},$$
$$\delta\varepsilon_p = \varepsilon_{co}^2 pKu_0\begin{pmatrix}0&0&1\\0&0&0\\1&0&0\end{pmatrix}\sin(Kz - f_n t). \tag{3}$$

Here $n_{co}$ is the refractive index of fiber core. $\varepsilon_{co} = n_{co}^2$ is the permittivity of fiber core material and $p$ is the constant of photo-elasticity of fiber medium. The geometric induced correction has two orthogonal components and further influences the dual-resonant mode conversion in the AOMC.

The mismatching coefficient can be expressed as $\xi = K - \widetilde{K}$, where $\widetilde{K} = \beta_{01} - \beta_{11}$ is the resonant value of the acoustic wave vector. The propagation constants $\beta_{11a}$ and $\beta_{11b}$ are slightly different due to the degeneration of $LP_{11}$ mode by the ellipticity of the fiber. Therefore, it requires different frequencies of applied RF signals to obtain the mode conversions from $LP_{01}$ mode to $LP_{11a/b}$ modes according to the distinct values of resonant acoustic wave vector. Thus, the mode conversion efficiency can be expressed as [35]:

$$K_{a/b} \propto \frac{\pi}{\lambda}\sqrt{\frac{\varepsilon_0}{\mu_0}}n_{\mathrm{co}}\int E_{01}^*(x,y)\cdot\delta\hat{\varepsilon}\cdot E_{11a/b}(x,y)dxdy. \tag{4}$$

$K_{a/b}$ represents the conversion efficiencies of mode conversion from $LP_{01}$ mode to $LP_{11a}$ and $LP_{11b}$ modes, respectively. $E_{01}(x,y)$ and $E_{11a/b}(x,y)$ are the electric field distributions of $LP_{01}$ mode and $LP_{11a/b}$ modes, respectively. The overall influence of energy coupling between $LP_{01}$ mode and $LP_{11}$ modes exhibits the co-effect of acoustic and optical birefringence. The mode conversions from $LP_{01}$ mode to $LP_{11a}$ and $LP_{11b}$ modes have distinct resonances due to the contribution of geometric permittivity deformation. Obviously, the mode conversion can be simply controlled by the AIFG period via tuning the applied RF signals.

**Figure. 1(d)** shows the simulation result of the beat lengths between $LP_{01}$ mode and $LP_{11a/b}$ modes with different ellipticities of the adopted FMF. The numerical simulation of the ellipse-fiber-based AIFG employs a finite element method (Comsol Multiphysics). The step-index FMF adopted in the experiment has a small ellipticity. The ellipticity is defined as $E = arctan\frac{x}{y}$. Once the frequency of the applied RF signal is set, the period of the AIFG is determined. Here we employ the beat length between different modes to obtain the simulation results. Based on mode coupling theory, phase match condition $L_B = \Lambda$ should be satisfied, where $L_B = \lambda\cdot(n_{01} - n_{11a/11b})^{-1}$ is the beat length. Here $\lambda$ is the resonant wavelength and $n_{01}$ ($n_{11a/11b}$) represents the effective refractive index of the $LP_{01}$ ($LP_{11a/11b}$) mode.

$LP_{11a}$ and $LP_{11b}$ modes have their own resonant wavelengths and consequently there exists a wavelength separation ($\boldsymbol{\Delta\lambda}$). As shown in **Fig. 1(e)**, $\boldsymbol{\Delta\lambda}$ has a nearly linear relationship with the ellipticity. The larger the ellipticity, the larger the dual-resonant wavelength separation, which can be used to shape the different optical filters and excite hybrid high-order modes output with different wavelength combination.

## 3. Experimental setups and methods

### A. AOMC component fabrication

Here a thickness-mode PZT is utilized for generating acoustic waves and the RF signal produced by a function generator is amplified by a high-frequency voltage amplifier (Aigtek: ATA-2022H), as shown in **Fig. 1(b)**. A silica horn adhered to the PZT via epoxy gum is employed for amplifying the acoustic waves and making the acoustic waves from longitudinal mode to transverse mode. A 25-cm-long unjacketed fiber is glued to the top of the silica horn. The acoustic wave then propagates along the unjacketed fiber as a flexural mode. The existence of the AIFG structure is determined by the applied RF signal, which means that the AIFG has a dynamic tunability. The transmission spectra are measured via a broadband optical source and an optical spectrum analyzer (OSA, AQ6370, YOKOGAWA).

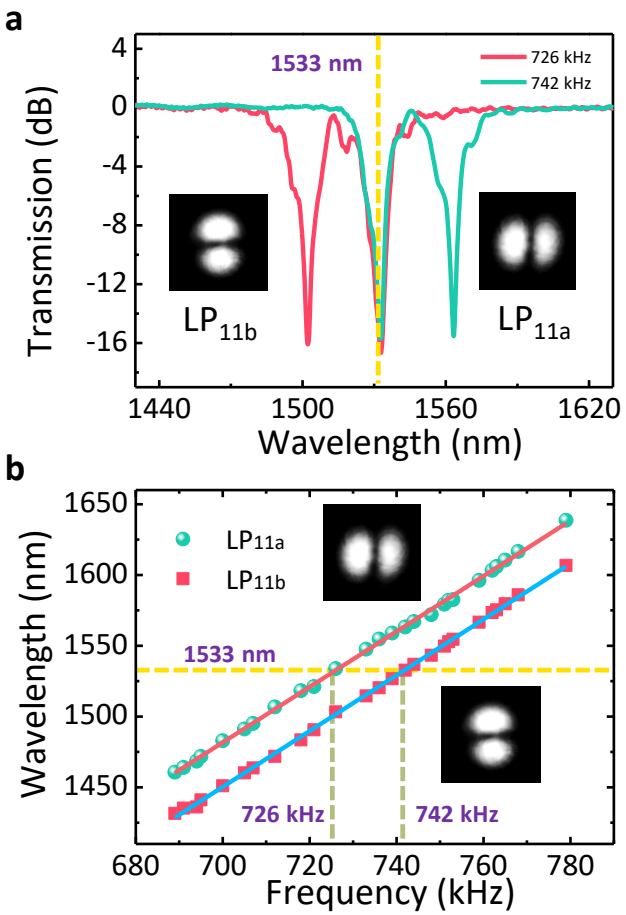


Fig. 2. The transmission spectra (a) of AOMC with two different applied RF signal frequencies of 726 kHz and 742 kHz and the frequency dependent wavelength shift performance (b) of the applied dual-resonant AOMC.

In **Fig. 2(a),** the dual-resonant response is observed and the mode conversions from $LP_{01}$ mode to $LP_{11a}$ and $LP_{11b}$ mode are demonstrated. The resonant depths of $LP_{11a}$ and $LP_{11b}$ modes are both larger than -15 dB, which means that the mode conversion efficiencies of both $LP_{11a}$ and $LP_{11b}$ modes are higher than 97%. The ellipticity of the FMF used in the experiment is about 44.81° and $\Delta\lambda$ is measured to be 30 nm, which agrees well with the theoretic calculation. On the other hand, the mode conversion of $LP_{01}$-$LP_{11a}$ and $LP_{01}$-$LP_{11b}$ can be achieved at a same resonant wavelength (1533 nm) by utilizing two different RF frequencies (726 kHz, 742 kHz).

**Figure 2(b)** shows the center wavelength tuning property of AOMC dependent on RF frequency. The center wavelengths of the two resonant peaks ($LP_{01}$-$LP_{11a}$ and $LP_{01}$-$LP_{11b}$) both have an approximate linear property of red shift as the increase of applied RF frequencies. The insets are the corresponding mode patterns of $LP_{11a}$ and $LP_{11b}$ modes.

### B. Experimental setup of mode-locked fiber laser

A mode-locked narrow-linewidth fiber laser based on an intracavity AOMC is demonstrated to achieve vortex mode switching pulses. Narrow-linewidth fiber lasers have the advantages of good stability, high coherence and low noise [41, 42]. The narrow-linewidth mode-locked fiber laser is a good platform for studying spatial mode switching processes because different spatial mode pulses with narrow-linewidth have strong spectral discrimination.

**Figure. 3(a)** shows the schematic of the mode-locked fiber laser setup. The laser oscillator is obtained by using a linear cavity configuration with half cavity of the SMF and half cavity of the FMF. The single-mode cavity consists of a single-mode SESAM, a 50-cm-long Erbium doped fiber (EDF), a wavelength-division-multiplexed coupler (WDM), a 5:95 coupler and a 10-meter-long SMF. The few-mode part of the laser cavity consists of a mode stripper (MS), an AOMC and a few-mode FBG (FM-FBG). The 980 nm-LD provides energy pump via a 980-1550 nm WDM. The coupler with a 5% output port is employed to extract the laser energy out of the cavity. A 10-meter-long SMF is inserted into the cavity to optimize the net dispersion. The SESAM-based mode locker is used for forming temporal pulses and reflecting the light back to the laser cavity, simultaneously. The $PC_1$ (polarization controller) is utilized to optimize the mode-locking status by adjusting the birefringence of the linear cavity.

In the FMF part, the MS is exploited to ensure a pure $LP_{01}$ mode light beam propagating into the AOMC because direct splicing between the SMF and the FMF may introduce high-order modes in FMFs. Here the intracavity AOMC achieves a switchable mode conversion from $LP_{01}$ mode to $LP_{11a/b}$ modes while the FM-FBG plays the role of selecting laser wavelength and reflecting the light back to the cavity. When the high-order mode is reflected and propagates through the AOMC, it will be reconverted to $LP_{01}$ mode and comes back to the SMF cavity. While any unconverted $LP_{01}$ mode is reflected by the FM-FBG and passes through the AOMC, which would convert into the high-order mode and dissipate in the SMF. Therefore, high purity of high-order mode is ensured in the few-mode cavity. The $PC_2$ is utilized to adjust the mode phase and generate OAM modes.
The lasing mode at the operation wavelength around 1533 nm is controlled by the applied RF signal frequency ($f_n$). When the applied RF signal is set to $f_1$ (726 kHz) or $f_2$ (742 kHz), the laser operates at the state of $LP_{11a}$ or $LP_{11b}$ mode, respectively. When the applied RF signal is set to $f_0$ (a non-resonant frequency or an off state), the laser operates at the state of $LP_{01}$ mode. To obtain a spatial mode switching in a mode-locked fiber laser, the applied RF signal is modulated via a frequency shift keying (FSK) method, which provides a periodic frequency modulation way for controlling the mode switching process.

### C. Generation of switching vortex pulses

To achieve the generation of vortex pulses, the optical field tuning technique is adopted as follows. Firstly, the $LP_{11a}$ mode and $LP_{11b}$ mode pulses can be rotated with a degree of 45° by the $PC_2$ and the rotated $LP_{11}$ modes can be orthogonally decomposed as $LP_{11a(rot)} = LP_{11}^{even} - LP_{11}^{odd}$ and $LP_{11b(rot)} = LP_{11}^{even} + LP_{11}^{odd}$, respectively.

Actually, the linear polarization modes are only approximations of the eigen-mode combinations of the radially polarized mode ($TM_{01}$), the azimuthally polarized mode ($TE_{01}$) and two strictly degenerated hybrid modes ($HE_{21}^{odd}/HE_{21}^{even}$) [43, 44]. Therefore, the rotated LP modes can be further expressed by eigen-modes of degeneracy:

$$LP_{11a(rot)} = TM_{01} - HE_{21}^{odd} - (TE_{01} + HE_{21}^{even}),$$
$$LP_{11b(rot)} = TM_{01} - HE_{21}^{odd} + (TE_{01} + HE_{21}^{even}). \quad (5)$$

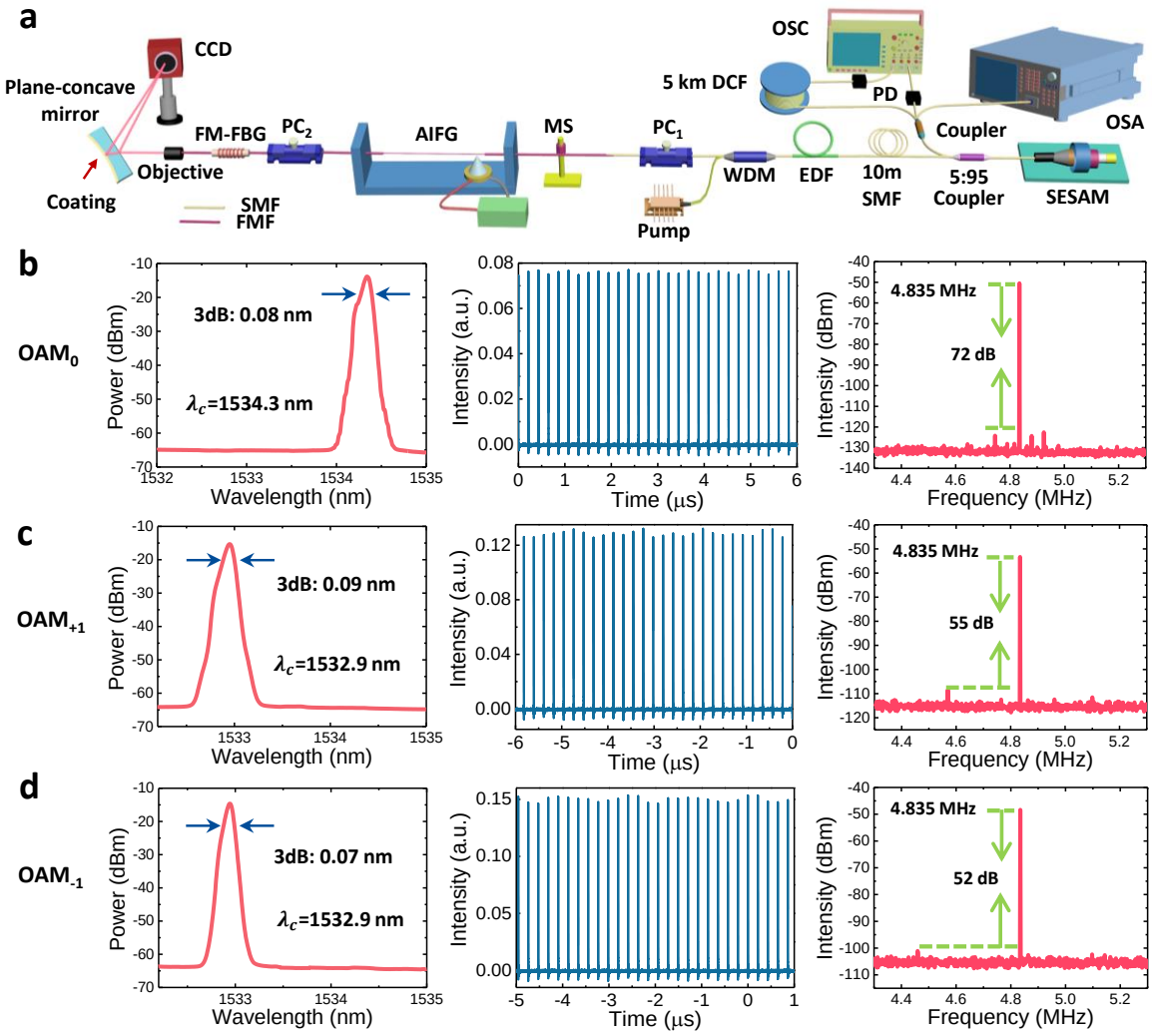


Fig. 3. The experimental setup and results of spatial mode switching in a mode-locked fiber laser. (a) The schematic diagram of spatial mode switching fiber laser setup. OSA: optical spectrum analyzer; PC: polarization controller; MS: mode stripper. The stable ML with $OAM_0$ (b), $OAM_{+1}$ (c) and $OAM_{-1}$ (d). The results include laser spectra, pulse trains and RF signals. (see spatial mode switching processes of $LP_{01}$-$LP_{11a}$, $LP_{01}$-$LP_{11b}$, $LP_{11a}$-$LP_{11b}$ and $OAM_{+1}$-$OAM_{-1}$ in **visualization 1**, **visualization 2**, **visualization 3** and **visualization 4**, respectively).

Then the stress provided by $PC_2$ changes the effective dimensions of the FMF, resulting in different phase velocities of the eigen modes. When tuning the stress appropriately a phase difference of "$\pi/2$" ("$i$") can be changed to the eigen-modes. Finally, the adjusted $LP_{11a}$ mode and $LP_{11b}$ mode become the corresponding -1-order OAM mode and +1-order OAM mode and can be expressed as:

$$LP_{11a(adj)} = TM_{01} - HE_{21}^{odd} - iTE_{01} - iHE_{21}^{even} = OAM_{-1},$$
$$LP_{11b(adj)} = TM_{01} - HE_{21}^{odd} + iTE_{01} + iHE_{21}^{even} = OAM_{+1}. \quad (6)$$

Thus, the mode switching OAM pulses are successfully demonstrated by altering the applied RF signal frequency.

## 4. Results

### A. Mode-locked fiber laser with OAM mode switching output

The OAM-switching pulses with the topology numbers of +1 and -1 are successfully demonstrated. **Figure. 3(b-d)** exhibit the outputs of the mode-locked fiber laser at three different vortex modes: $OAM_0$ ($LP_{01}$ mode), $OAM_{+1}$ mode and $OAM_{-1}$ mode, respectively. The laser spectra show a wavelength difference due to the different reflection wavelengths of the FM-FBG with $OAM_0$ mode and $OAM_1$ mode. The laser operating wavelengths of $OAM_0$ mode and $OAM_1$ mode are 1534.3 nm and 1532.9 nm, respectively.

Due to the narrow bandwidth of the FM-FBG reflection, the 3-dB widths of the laser spectra at the ML states of $OAM_0$, $OAM_{+1}$ and $OAM_{-1}$ are 0.09 nm, 0.07 nm and 0.08nm, respectively. The pulse trains recorded by a real-time oscilloscope (OSC, Keysight, DSOS404A) via a high-speed photoelectric detector (PD) confirm stable mode-locked states of three OAM modes.

The repetition rate of the mode-locked fiber laser is 4.835 MHz, which agrees well with the calculated one corresponding to the cavity length (~21.5 m and the repetition rate is 4.81 MHz). The operating vortex mode states are modulated by modulating the applied RF signal frequency rather than changing the laser

cavity so that the repetition rate has no difference in three vortex modes. However, the signal-noise ratio (SNR) has lower values at the states of $OAM_1$ mode than $OAM_0$ modes, since mode conversion introduces intracavity modal perturbation and slightly declines the SNR.

The interference patterns are obtained by employing a plane-concave mirror (PCM)-based interference technique [45, 46]. The OAM-switching pulsed laser beam is collimated by using an objective lens and then reflected by the PCM as shown in **Fig. 3(a)**. The concave face of the mirror is coated with a reflectivity of >99% at 1550 nm while the plane face of the mirror is uncoated. Therefore, when the OAM pulsed laser beam is incident into the PCM, both the plane face (Fresnel reflection ~4%@1550 nm) and the concave face (>99% @1550 nm) reflect the laser beam. The two reflected laser beams are overlapped and spatially interfered at the cross point by properly adjusting the position and the angle of the PCM.

The mode patterns as well as interference patterns are recorded by using the charge coupled device (CCD, InGaAs camera, model C10633-23, from Hamamatsu Photonics), as depicted in **Fig. 4(a)**. As seen in **Fig. 4(b)**, the pulse widths of three modes are measured to be approximately 400 ps.

The slope efficiencies of three distinct mode states are demonstrated as shown in **Fig. 4(c)**. The slope efficiencies of $OAM_0$, $OAM_{+1}$ and $OAM_{-1}$ modes are 5.5%, 7.13% and 7.64%, respectively. The distinction between the slope efficiencies of two $OAM_1$ modes is because of the slight difference of mode conversion efficiency. Additionally, the difference between the slope efficiencies of $OAM_0$ mode and $OAM_1$ mode is mainly due to the reflectivity difference of FM-FBG.

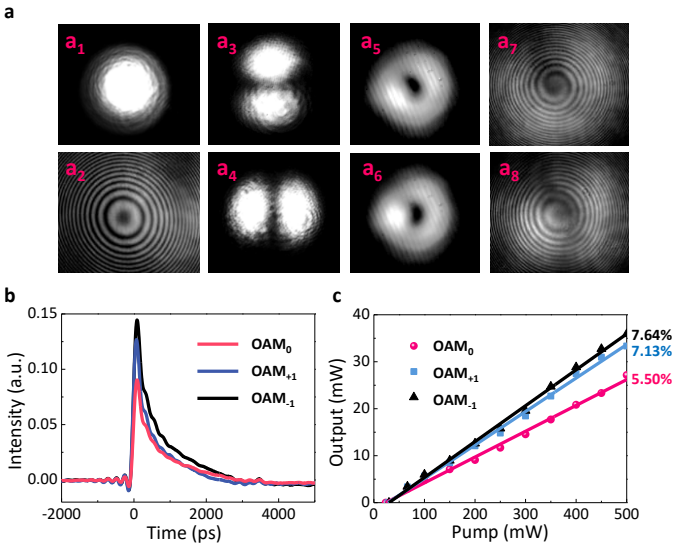


Fig. 4. The output results of the mode switching mode-locked fiber laser. (a) The mode patterns recorded by a CCD include mode intensity pattern ($a_1$) and interference pattern ($a_2$) of $OAM_0$ mode; $LP_{11}$ mode intensity patterns ($a_3$, $a_4$), doughnut mode patterns ($a_5$, $a_6$) and interference patterns ($a_7$, $a_8$) of $OAM_{+1}$ and $OAM_{-1}$ modes. (b) The real-time pulse shapes of three OAM modes. (c) The slope efficiencies of the mode-locked fiber laser with three OAM mode states.

### B. Real-time observation of vortex mode switching in the mode-locked fiber laser

Vortex mode switching introduces intracavity perturbation and the mode switching dynamics become an interesting phenomenon. Real-time pulse evolution in the mode switching process is demonstrated as depicted in **Fig. 5**. OAM-mode switching causes a quasi-broken and reconstructing process of ML states. The pulse train signals in **Fig. 5(a)** reveal that there exists an evident laser strike region before the appearance of a stable pulse train (i.e. the stable ML state) at every OAM-mode switching process.

**Figure. 5(b) and 5(c)** exhibit the corresponding detailed information of every laser strike region of the mode switching process named as **I-VI**. Additionally, strike region **I** (mode switching from $OAM_0$ mode to $OAM_{-1}$ mode) and **II** (mode switching from $OAM_{-1}$ mode to $OAM_{+1}$ mode) are interpreted particularly. The duration times of whole strike region are ~1 ms (between $OAM_0$ mode and $OAM_{-1}$ mode), ~1.8 ms (between $OAM_{-1}$ mode and $OAM_{+1}$ mode) and ~2.2 ms (between $OAM_0$ mode and $OAM_{+1}$ mode).

As shown in **Fig. 5,** the experimental results reveal that the whole mode switching dynamic process includes a quiet-down state, relaxation oscillation, Q-ML stage, and finally the reconstructed ML phase. At the beginning of the strike region, there exists a quiet-down process, which is mainly on account of the microstructure change of the AIFG, such as the fiber long period grating formation ($OAM_0$-$OAM_1$), grating collapse ($OAM_1$-$OAM_0$) and period variation ($OAM_{-1}$-$OAM_{+1}$).

The time durations of three kinds of quiet-down process are ~120 ms, ~50 ms and ~80 ms, respectively, which correspond to the switching times of the AOMC. Note that all the quiet-down times are marginally smaller than the switching time of AOMC component measured in (ref. 38), because a partial mode perturbation is enough for destroying the stable ML state and introducing the instability in the laser cavity. Then the number of cavity photons comes to an initial low value as determined by quantum field fluctuation.

After a short time, a series of laser strikes are generated, which is mainly originated from the relaxation oscillation. The separation of the neighboring laser strikes is ~70 ms. Liu et al reported a raised relaxation oscillation phenomenon in the build-up process in mode-locked fiber lasers [21]. Differently, the laser strikes observed in this experiment are not regularly raising type, which are mainly modulated by the spatial mode competition. Spatially lasing modes can interact through the optical nonlinearity at the time scale of a mode-locked pulse, which leads to an energy fluctuation at the temporal and spatial domains. Additionally, the rare-earth gain media introduces a temporally averaging nonlinear interaction in the relaxation oscillation process [28]. Prior to the stable ML state formation, there co-exist two modes (i. e., the original mode and the target converted mode) and their intermediate states. The competition of these spatial modes leads to a fluctuation of energy accumulation in the cavity and further influences the amplitude of the formed laser strikes. It is worth noting that the mode competition between two $OAM_1$ modes is weaker than that between $OAM_0$ mode and $OAM_1$ mode. Hence the peak envelope change of laser strikes during the process of mode switching between two $OAM_1$ modes is much weaker than that between $OAM_0$ mode and $OAM_1$ modes. The Q-ML is also observed in the temporal information with a duration time of ~120 ms. Typical pulses arise and form a pulse train with the shifting of laser wavelength (detailed discussion in next section).

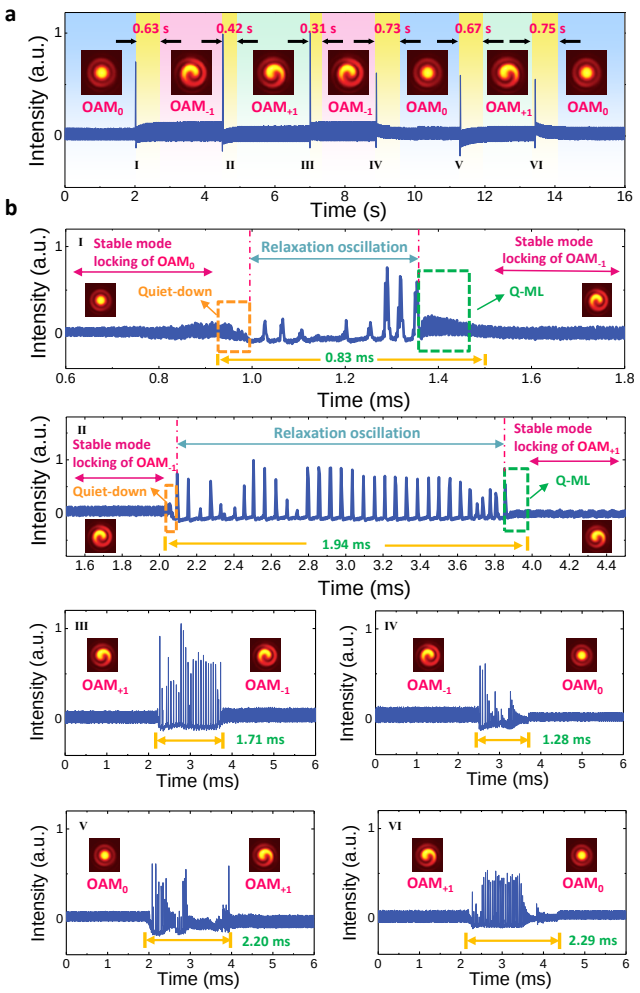


Fig. 5. The real-time information of mode switching dynamics. (a) The real-time information of the whole mode switching dynamic process among three vortex modes ($OAM_0$, $OAM_{-1}$ and $OAM_{+1}$). The detailed information of the strike regions named as **I-II**(b), **III-VI**(c), respectively.

The final reconstructed ML state has two stages including temporal stable ML and temporal-amplitude stable ML. At the beginning of the reconstructing ML state, the pulse train has a recover time to obtain a stable energy level of pulse amplitude. The recovery time between $OAM_0$ mode and $OAM_1$ mode is ~0.7 s while it is ~0.4 s between two $OAM_1$ modes. The laser oscillating and reconstructing processes between different OAM- modes are much more difficult than that between same order modes, thus it takes more time for recovering ML pulses.

### C. Vortex mode switching dynamics observed by TS-DFT method

To overcome the limited electronic bandwidth of the real-time OSC, the TS-DFT method is exploited to reveal the detailed spectral and temporal information of transient vortex OAM-mode switching process in the mode-locked laser. As shown in **Fig. 3(a)**, the real-time spectral information is obtained from the dispersing pulses detected after a dispersion compensation fiber (DCF). The dispersion ($D$) and length ($L$) of the employed DCF are -648 ps·nm$^{-1}$·km$^{-1}$ and ~5 km. The spectral information can be mapped into the temporal waveform recorded by an OSC. The mapping relationship between temporal and spectral resolutions can be expressed as: $\Delta t = |D| \cdot L \cdot \Delta\lambda = 3.24\ ns \cdot nm^{-1} \cdot \Delta\lambda$, where $\Delta t$ and $\Delta\lambda$ represent the temporal and spectral resolutions, respectively. Besides, the roundtrip time is 206.8 ns.

**Figure. 6** show the experimental observation of vortex mode switching from $OAM_{+1}$ mode to $OAM_0$ mode via TS-DFT method. Since the lasing wavelengths of $OAM_{+1}$ mode and $OAM_0$ mode are different, the spectrum evolution exhibits a corresponding wavelength change of OAM-switching pulses. **Figure. 6(a)** depicts the energy envelope evolution of vortex OAM-mode switching dynamic process. Note that the end of this data shows a fluctuation after roundtrips of ~6000 (corresponding to time of ~1.24 ms). According to Fig. 5(c-VI), the duration time of the whole laser strike process is 2.29 ms, which means there exists an energy fluctuation process in the tail part of the laser strike region.

**Figure. 6(b)** shows the whole spectrum evolution dynamics. Firstly, the laser cavity operates at the stable $OAM_{+1}$ mode. As depicted in **Fig. 6($b_1$)**, the single-shot spectrum shows a stable state at the wavelength of ~1532.9 nm. When the applied RF signal changes, the stable ML state collapses and the laser output evolves as a quantum initial situation, which is characterized as a low energy state. As the cavity energy accumulates enough, there arise some laser spikes that mainly originate from the variation of population inversion in the EDF. The laser spikes vary irregularly until one laser spike dominates the energy fluctuation. Then the laser operating wavelength goes through a shift process to the final targeted lasing wavelength (1534.3 nm) of $OAM_0$ mode as shown in **Fig. 6($b_3$)**. **Figure. 6($c_1$)** and **6($c_2$)** show the DFT signals and optical spectra of stable ML states of $OAM_{+1}$ mode and $OAM_0$ mode, respectively, which are well matched with each other.

## 5. Conclusion

In this work, we have experimentally demonstrated the vortex mode switching dynamics in a mode-locked fiber laser by introducing the mode switchable AOMC. The real-time pulse evolution exhibits that a mode switching process mainly consists of a quiet-down moment, a relaxation oscillation process, a Q-ML stage and an energy recovering process. The vortex mode switching dynamics provides a new way to study the formation process of ML pulses under the view of spatial degree of freedom. In the mode switching dynamic process, we found that the energy fluctuation of mode switching between different vortex modes is strong enough to form irregular laser strikes. Hence, most likely the mode conversion and mode competition inside the laser cavity are responsible for the energy perturbation. The energy perturbation is supposed to be the main factor affecting the pulse evolution dynamic process. Furthermore, the unveiled evolution process of spatial mode switching is currently instructive for the development of ultrafast lasers and transient nonlinearity. The experimental result of vortex mode switching dynamics reveals the physical mechanism of vortex mode state transition process in a mode-locked fiber laser, which enriches the ultrafast photonics and advances the practical applications.

In addition, the novel result of generating switching optical vortex pulses is also demonstrated and paves the way toward quantum information science [47], stimulated emission depletion microscopy (STED) [48] and ultrafast laser fabrication [49].

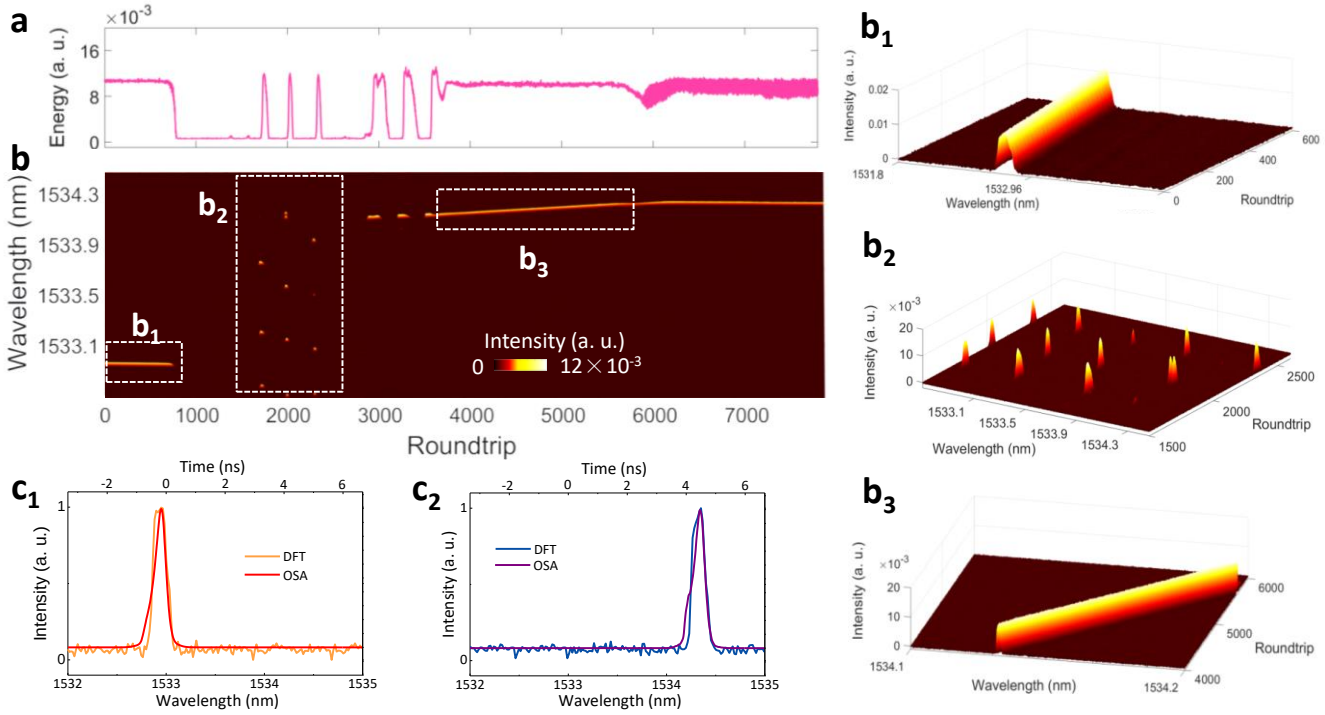


Fig. 6. The experimental observation of vortex mode switching from $OAM_{+1}$ mode to $OAM_0$ mode via TS-DFT method. (a) The energy envelope evolution of DFT signal. (b) The whole spectrum evolution of vortex mode switching dynamics with close-ups pictures of initial ML ($b_1$), laser spikes ($b_2$) and wavelength shift ($b_3$). Comparisons of DFT signals and optical spectra of $OAM_{+1}$ mode ($c_1$) and $OAM_0$ mode ($c_2$). (see dynamic single-shot spectrum evolution in **Visualization 5**).

For instance, traditional vortex mode converters employed in quantum optical communication are free-space elements which need complicated optical alignment to fiber system. Our method of generating switchable vortex modes has the following advantages: (1) eliminate the space-fiber coupling process due to the all-fiber configuration; (2) allow marshalling of data information by dynamic switching. Our method of generating switchable vortex beam provides a switchable light source between gaussian distribution and donut distribution in STED systems. The fluoresce radiation and stimulated depletion can be flexibly controlled by mode switching between 0-order and 1-order vortex modes. In field of laser fabrication, the switchable OAM ultrafast laser pulses can enrich the types of nanostructures fabricated by vortex laser and broaden the dimensions of vortex laser processing. For example, the chiral-alternating nanogratings can be fabricated by switching $OAM_{+1}$ mode and $OAM_{-1}$ mode alternatively.

Meanwhile, the detailed AIDV-based model of a dual-resonant AOMC further enriches the physical mechanism of acoustic and optical birefringence and gives an instructive pathway for extending the practical applications of the AOMCs. Consequently, all these findings will enable the development of a new class of strategies for studying ML mechanism through controlling the spatial mode switching.

**Disclosure.** The authors declare no conflicts of interest.

**Funding Information.** National Science Foundation of China (NSFC) (91750108, 61635006); 111 Project (D20031).

**Acknowledgment.** X. Zeng acknowledges the support of the Program for Professor of Special Appointment (Eastern Scholar) at Shanghai Institutions of Higher Learning. We are grateful to Dr. Junsong Peng at East China Normal University for invaluable discussions on ML dynamics.

## References

1. K. Goda, K. K. Tsia, and B. Jalali, "Serial time-encoded amplified imaging for real-time observation of fast dynamic phenomena," Nature **458**, 1145–1149 (2009).
2. H. Guo, M. Karpov, E. Lucas, A. Kordts, M. H. P. Pfeiffer, G. Lichachev, V. E. Lobanov, M. L. Gorodetsky, and T. J. Kippenberg, "Universal dynamics and deterministic switching of dissipative Kerr solitons in optical microresonators," Nat. Phys. **13**, 94-102 (2017).
3. B. Li, S. W. Huang, Y. Li, C. W. Wong, and K. K. Y. Wong, "Panoramic-reconstruction temporal imaging for seamless measurements of slowly-evolved femtosecond pulse dynamics," Nat. Commun. **8**(1), 61 (2017).
4. J. Kim and Y. Song, "Ultralow-noise mode-locked fiber lasers and frequency combs: principles, status, and applications," Adv. Opt. Photon. **8**, 465–540 (2016).
5. U. Teğin, E. Kakkava, B. Rahmani, D. Psaltis, and C. Moser, "Spatiotemporal self-similar fiber laser," Optica **6**, 1412-1415 (2019).
6. T. Mayteevarunyoo, B. A. Malomed, and D. V. Skryabin, "Spatiotemporal dissipative solitons and vortices in a multi-transverse-mode fiber laser," Opt. Express **27**, 37364-37373 (2019).
7. U. Teğin, B. Rahmani, E. Kakkava, N. Borhani, C. Moser, and D. Psaltis, "Controlling spatiotemporal nonlinearities in multimode fibers with deep neural networks," APL Photonics **5**, 030804 (2019).

8. S. V. Smirnov, S. Sugavanam, O. A. Gorbunov, and D. V. Churkin, "Generation of spatio-temporal extreme events in noise-like pulses NPE mode-locked fibre laser," Opt. Express **25**, 23122-23127 (2017).
9. H. Wu, C. Huang, and J. Huang, "Spatiotemporal dynamics of a passively mode-locked Nd:$GdVO_4$ laser," Opt. Express **15**, 2391-2397 (2007).
10. M. Padgett, and R. Bowman, "Tweezers with a twist," Nat. Photon. **5**(6), 343-348 (2011).
11. D. G. Grier, "A revolution in optical manipulation," Nature **424**, 810 (2003).
12. S. Kawata, H. B. Sun, T. Tanaka and K. Takada, "Finer features for functional microdevices," Nature **412**, 697 (2001).
13. J. Wang, J. Y. Yang, I. M. Fazal, N. Ahmed, Y. Yan, H. Huang, Y. Ren, Y. Yue, S. Dolinar, M. Tur, and A. E. Willner, "Terabit free-space data transmission employing orbital angular momentum multiplexing," Nat. Photon. **6**(7), 488-496 (2012).
14. J. Denschlag, J. Simsarian, D. Feder, C. W. Clark, L. Collins, J. Cubizolles, L. Deng, E. W. Hagley, K. Helmerson, and W. P. Reinhardt, "Generating solitons by phase engineering of a Bose-Einstein condensate," Science **287**, 97 (2000).
15. A. F. J. Runge, N. G. R. Broderick, and M. Erkintalo, "Observation of soliton explosions in a passively mode-locked fiber laser," Optica **2**, 36 (2015).
16. P. Ryczkowski, M. Närhi, C. Billet, J.-M. Merolla, G. Genty and J. M. Dudley, "Real-time full-field characterization of transient dissipative soliton dynamics in a mode-locked laser," Nat. Photon. **12**, 221–227 (2018).
17. F. Krausz, T. Brabec, and C. Spielmann, "Self-starting passive mode locking," Opt. Lett. **16**(4), 235–237 (1991).
18. E. Kelleher and J. Travers, "Chirped pulse formation dynamics in ultra-long mode-locked fiber lasers," Opt. Lett. **39**(6), 1398–1401 (2014).
19. A. Chong, L. Wright, and F. Wise, "Ultrafast fiber lasers based on self-similar pulse evolution: a review of current progress," Rep. Prog. Phys. **78**(11), 113901 (2015).
20. J. Peng, and H. Zeng, "Build-Up of Dissipative Optical Soliton Molecules via Diverse Soliton Interactions," Laser Photonics Rev. 12(8), 1800009 (2018).
21. X. Liu and Y. Cui, "Revealing the behavior of soliton buildup in a mode-locked laser," Adv. Photon. **1**, 016003 (2019).
22. Y. Cui, and X. Liu, "Revelation of the birth and extinction dynamics of solitons in SWNT-mode-locked fiber lasers," Photon. Res. **7**(04), 53-60 (2019).
23. X. Liu, and M. Pang, "Revealing the Buildup Dynamics of Harmonic Mode-Locking States in Ultrafast Lasers," Laser Photonics Rev. **13**(9), 1800333 (2019).
24. X. Liu, D. Popa, and N. Akhmediev, "Revealing the transition dynamics from Q switching to mode locking in a soliton laser," Phys. Rev. Lett. **123**, 093901 (2019).
25. D. J. Richardson, J. M. Fini, and L. E. Nelson, "Space-division multiplexing in optical fibres," Nat. Photon. **7**, 354–362 (2013).
26. H. R. Stuart, "Dispersive multiplexing in multimode optical fiber," Science **289**, 281–283 (2000).
27. L. G. Wright, Z. M. Ziegler, P. M. Lushnikov, Z. Zhu, M. A. Eftekhar, D. N. Christodoulides, and F. W. Wise, "Multimode Nonlinear Fiber Optics: Massively Parallel Numerical Solver, Tutorial, and Outlook," IEEE J. Sel. Top. Quant. Electron. **24**(3), 5100516 (2018).
28. L. G. Wright, D. N. Christodoulides, and F. W. Wise, "Spatiotemporal mode-locking in multimode fiber lasers," Science **358**, 94 (2017).
29. W. H. Renninger, and F. W. Wise, "Optical solitons in graded-index multimode fibres," Nat. Commun. **4**(4), 1719 (2013).
30. L. G. Wright, D. N. Christodoulides, and F. W. Wise, "Controllable spatiotemporal nonlinear effects in multimode fibres," Nat. Photon. **9**(5), 306-310 (2015).
31. H. Qin, X. Xiao, P. Wang, and C. Yang, "Observation of soliton molecules in a spatiotemporal mode-locked multimode fiber laser," Opt. Lett. **43**(9), 1982-1985 (2018).
32. R. Chen, F. Sun, J. Yao, J. Wang, H. Min, A. Wang, and Q. Zhan, "Mode locked all-fiber laser generating optical vortex pulses with tunable repetition rate," Appl. Phys. Lett. **112**, 261103 (2018).
33. Z. Li, J. Peng, Q. Li, Y. Gao, J. Li, and Q. Cao, "Generation of picosecond vortex beam in a self-mode-locked Nd: $YVO_4$ laser," Optoelectron. Lett. **13**, 188-191 (2017).
34. S. D. Lim, H. C. Park, I. K. Hwang, and B. Y. Kim, "Combined effects of optical and acoustic birefringence on acousto-optic mode coupling in photonic crystal fiber," Opt. Express **16**(9), 6125-6133 (2008).
35. W. Zhang, K. Wei, L. Huang, D. Mao, B. Jiang, F. Gao, G. Zhang, T. Mei, and J. Zhao, "Optical vortex generation with wavelength tunability based on an acoustically-induced fiber grating," Opt. Express **24**(17), 19278 (2016).
36. P. Z. Dashti, F. Alhassen, and H. P. Lee, "Transfer of orbital angular momentum between acoustic and optical vortices in optical fiber," Phys. Rev. Lett. **96**, 043064 (2006).
37. Y. Li, L. Huang, H. Han, L. Gao, Y. Cao, Y. Gong, W. Zhang, F. Gao, I. P. Ikechukwu, and T. Zhu, "Acousto-optic tunable ultrafast laser with vector-mode-coupling-induced polarization conversion," Photon. Res. **7**(7), 798-805 (2019).
38. J. Lu, L. Meng, F. Shi, X. Liu, Z. Luo, P. Yan, L. Huang, F. Pang, T. Wang, X. Zeng, and P. Zhou, "Dynamic mode-switchable optical vortex beams using acousto-optic mode converter," Opt. Lett. **43**(23), 5841-5844 (2018).
39. J. Lu, L. Meng, F. Shi, and X. Zeng, "A mode-locked fiber laser with switchable high-order modes using intracavity acousto-optic mode converter," presented at Optical Fiber Communication Conference (OFC), San Diego, paper W3C.3 (March 2019).
40. M. A. Yavorsky, D. V. Vikulin, E. V. Barshak, B. P. Lapin, and C. N. Alexeyev, "Revised model of acousto-optic interaction in optical fibers endowed with a flexural wave," Opt. Lett. **44**(3), 598-601 (2019).
41. R. Li, J. Zou, W. Li, K. Wang, T. Du, H. Wang, X. Sun, Z. Xiao, H. Fu, and Z. Luo, "Ultrawide-space and controllable soliton molecules in a narrow-linewidth mode-locked fiber laser," IEEE Phot. Tech. Lett. **30**(16), 1423-1426 (2018).
42. Y. Shen, G. Ren, Y. Yang, S. Yao, Y. Wu, Y. Jiang, Y. Xu, W. Jin, and S. Jian, "Switchable narrow linewidth fiber laser with LP11 transverse mode output," Optics & Laser Technology **98**, 1-6 (2018).
43. S. Ramachandran and P. Kristensen, "Optical vortices in fibers," Nanophotonics **2**(5-6), 455-474 (2013).
44. J. Wang and A. E. Willner, "Twisted Communications using Orbital Angular Momentum (Tutorial Talk)," Optical Fiber Communication Conference, OSA Technical Digest (online), paper Th1H.5 (2016).
45. J. Zou, H. Wang, W. Li, T. Du, B. Xu, N. Chen, Z. Cai, and Z. Luo, "Visible-wavelength all-fiber vortex laser," IEEE Phot. Tech. Lett. **31**, 18 (2019).
46. J. Zou, Z. Kang, R. Wang, H. Wang, J. Liu, C. Dong, X. Jiang, B. Xu, Z. Cai, G. Qin, H. Zhang and Z. Luo, "Green/red pulsed vortex-beam oscillations in all-fiber lasers with visible-resonance gold nanorods," Nanoscale **11**, 15991 (2019).
47. A. Mair, A. Vaziri, G. Weihs, and A. Zeilinger, "Entanglement of the orbital angular momentum states of photons," Nature **412**, 313 (2001).
48. L. Yan, P. Gregg, E. Karimi, A. Rubano, L. Marrucci, R. Boyd, and S. Ramachandran, "Q-plate enabled spectrally diverse orbital-angular-momentum conversion for stimulated emission depletion microscopy," Optica **2**, 900 (2015).
49. J. Lu, Y. Dai, Q. Li, Y. Zhang, C. Wang, F. Pang, T. Wang, and X. Zeng, "Fiber nanogratings induced by femtosecond pulse laser direct writing for in-line polarizer," Nanoscale **11**(3), 908-914 (2019).

## IV.3 DYNAMIC PULSE WIDTH SWITCHING BETWEEN FEMTOSECOND AND PICOSECOND BY ACOUSTO-OPTIC ATTENUATION CONTROL

### IV.3.1 Principle of acousto-optic interaction enabled attenuation strategy

To transfer the concept of acousto-optic interactions in fibers for chiral light generation and manipulation, acousto-optic interactions could be also a good strategy for controlling other parameters in the ultrafast laser cavity due to its external dynamic tunability.

For instance, it is highly suitable for the dynamic control of attenuation with a sandwich structure of single-mode fiber, few-mode fiber, single-mode fiber (i.e., SMF-FMF-SMF). Specifically, the acousto-optic device is applied on the few-mode fiber region and can achieve a dynamic mode conversion of the light from fundamental mode to HOMs with mode conversion efficiency tunability and switching capability. When the microwave signal is not applied on the acousto-optic mode converter (i.e., the acousto-optic device is off), the fundamental mode $LP_{01}$ mode can stably propagating across the SMF-FMF-SMF sandwich structure without loss (neglecting the slight mode stimulation caused by imperfect fusion between the single-mode fiber and the few-mode fiber). However, when the acousto-optic device is switched on, the fundamental mode will be converted to HOMs (e.g., $LP_{11}$ modes) with a controllable mode conversion efficiency (ideally continuous tunability from 0% to 99%) when it propagates through the acousto-optic interaction region. Finally, the HOM part of the light will then exponentially decay in the evanescent field since the single-mode fiber cannot support HOM propagation. Therefore, the higher the mode conversion efficiency, the higher the attenuation (the lower power the remaining fundamental mode at the output port). Thus, with a tunability of mode conversion efficiency of acousto-optic interaction (typically by controlling the applied voltage of the microwave signal), a dynamic attenuation strategy is obtained.

Such an acousto-optic interaction-based attenuator would bring new possibilities in fiber lasers, especially in mode locked fiber lasers.

Because the equilibrium of gain and loss is the main topic in the lasers, which strongly influences the mode locking formation and stability. A dynamic attenuator can effectively manipulate the oscillation states in the laser cavity and extend the fundamental research or improve the performance of the ultrafast lasers. In this section, we present an innovative work about dynamic pulse width switching enabled by the acousto-optic interaction-based attenuation mechanism, as depicted in **Fig. 4-1**.

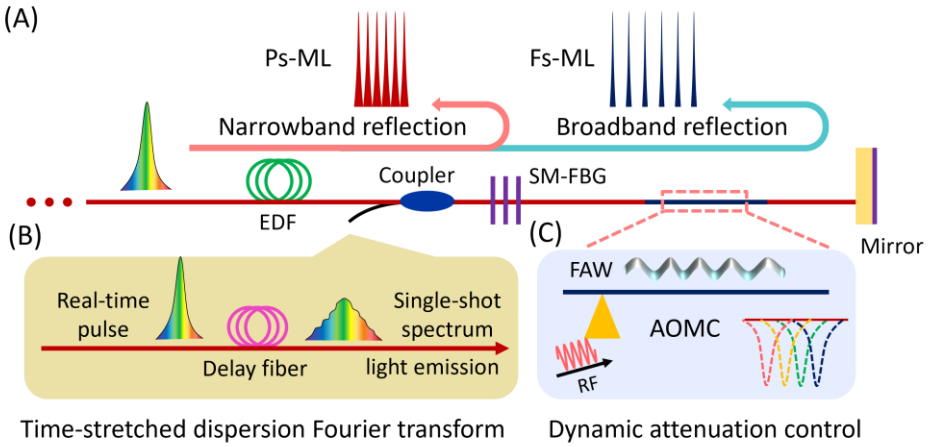


*Fig. 4-1: Illustration of the dynamic pulse width switching mechanism. (A) Schematic of a linear fiber laser cavity with narrowband reflection and broadband reflection to achieve picosecond (ps) mode locking (ML) and femtosecond (fs) ML states controlled by acousto-optic interactions. (B) Schematic of the time-stretched dispersive Fourier transformation technique. (C) Schematic of the dynamic attenuation control by acousto-optic mode converter (AOMC) with applied flexural acoustic wave (FAW), which is manipulated by the microwave radiofrequency (RF) signal.*

In general, in a linear fiber laser cavity, the side reflection components are FBGs (with narrow wavelength reflection) and mirror-like optics (with broadband reflection such as dielectric films or Faraday rotation mirrors). Normally, the FBGs are always used for a wavelength selection device when there is no bandpass filter in the cavity. Currently, the other side reflection component can be a broadband mirror (if one puts a second FBG, it should be rigorously same wavelength reflection as the first FBG, otherwise the laser cannot oscillate successfully). However, if we make a cascaded structure of a FBG and a broadband mirror at one side (keep the other side a broadband mirror for simplicity), what could happen? No

doubt it will be the same as one single broadband mirror (considering a same reflection efficiency of these two components) since the narrow part will be firstly reflected by the FBG and the remaining part will be reflected by the broadband mirror. Importantly, when compared to the broadband part of the oscillated light, the narrow part exhibits very little effect which can be ignored.

However, if there is an attenuator that suppresses the remaining light part, there will be no broadband light reflection and thus the light oscillation will be only determined by the narrowband selection of the FBG. That is, this structure will equal to a single FBG structure. Therefore, incorporating a cascaded structure of a FBG and a broadband mirror component with an attenuation mechanism, the narrowband and broadband light oscillation states can be altered.

Previously, our group has reported a manual switching strategy employing a squeezing based attenuator by adjusting a polarization controller between the FBG and the broadband mirror [212]. Specifically, a polarization controller is put in a coupler-based fiber loop (i.e., a broadband fiber loop mirror) to adjust the attenuation. The output pulse width can be switched between 24.5 ps and 1.04 ps with narrowband and broadband spectra, respectively. However, this switching is not a real "switch" since the attenuation is controlled by manually squeezing the polarization controller. It is easy to achieve the switching from broadband to narrowband because increasing the attenuation can be fast. But the switching from narrowband to broadband takes much longer time to create the broadband mode locking state. In conclusion, it is in fact a strategy for fabricating two mode locked fiber lasers with different pulse widths within one single laser cavity but not a mode locked fiber laser with dynamic switchable pulse widths.

### IV.3.2 Laser cavity of the pulse width switchable mode locked fiber laser

Therefore, in this PhD thesis, we innovatively introduce the acousto-optic attenuation control to achieve a dynamic pulse width switching with a fast-switching speed up to several kHz.

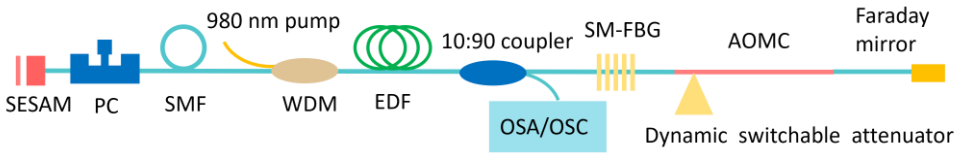


*Fig. 4-2: Schematic of the linear cavity of the pulse width switchable mode locked fiber laser. SESAM: semiconductor saturable absorber mirror; PC: polarization controller; SMF: single-mode fiber; WDM: wavelength division multiplexer; EDF: Erbium-doped fiber: OSA: optical spectrum analyzer; OSC: oscilloscope; SM-FBG: single-mode fiber Bragg grating; AOMC: acousto-optic mode converter.*

The laser cavity of the pulse width switchable mode locked fiber laser is depicted in **Fig. 4-2**. On the left side of the cavity, a SESAM (Batop SESAM-1550-30-10 ps) plays the role of both a broadband cavity mirror and a saturable absorber (the mode locking device). Then a polarization controller is utilized to adjusting the polarization state and loss in the whole laser cavity to ensuring a stable mode locking state. Note that, once it is set at the appropriate position, it is fixed all the time during the switching between fs mode locking and ps mode locking. A 10 m-long single-mode fiber (with a dispersion of −22 $ps^2$/km) is inserted to ensure a negative dispersion in the whole laser cavity. A 980 nm-pump is inserted into the laser cavity by a 980 nm/1550 nm wavelength division multiplexer. The gain is provided by a 5 m Er-doped fiber (NUFERN, EDFC-980-HP). Subsequently, a 10:90 optical coupler acts as an output port and is further connected to the analyzing units such as an optical spectrum analyzer (OSA, Yokogawa AQ6370) and an oscilloscope (OSC, DSA-X-96204Q). On the right part is the cascaded structure of the single-mode FBG and the broadband mirror (a commercial Faraday rotation mirror) sandwiched with the acousto-optic mode converter for attenuation control.

### IV.3.3 Characteristics of the pulse width switchable mode locked fiber laser

By switching on and off the microwave signal, the attenuation is dynamically controlled and the two stable mode locking states with narrow band and broadband are obtained in **Fig. 4-3**.

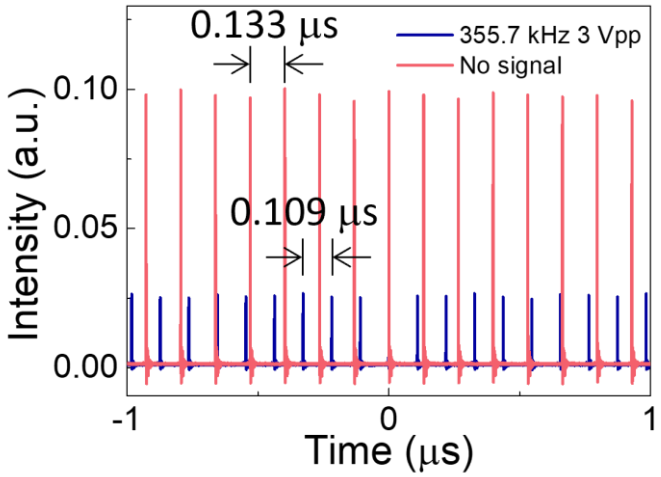


*Fig. 4-3: Experiment result of the obtained mode locked pulse trains with both narrowband mode locking (blue color, acousto-optic interaction activated by applying a microwave signal with 355.7 kHz frequency and 3 Vpp peak power) and broadband mode locking (red color, acousto-optic interaction disabled by switching off the microwave signal).*

From the experimental proof, the two mode locking states possess different repetition rates due to their different cavity length. The narrowband mode locked pulses oscillate only between the SESAM and the SM-FBG, which correlates to a shorter cavity length and thus a shorter roundtrip time of 0.109 µs (a repetition rate of 9.160 MHz). However, the broadband mode locked pulses oscillate between the SESAM and the Faraday rotation mirror that exhibits a longer roundtrip time of 0.133 µs (a repetition rate of 7.545 MHz). Another difference locates at the pulse energy. The broadband mode locking state corresponds to a low loss oscillation which leads to a higher pulse energy than the narrowband mode locking state. It agrees well with the slope efficiency result as depicted in **Fig.4-4**. The two mode locking states have the same pump power threshold of mode locking but own different slope efficiencies with 1.8% for broadband mode locking and 1.1% for narrowband mode locking.

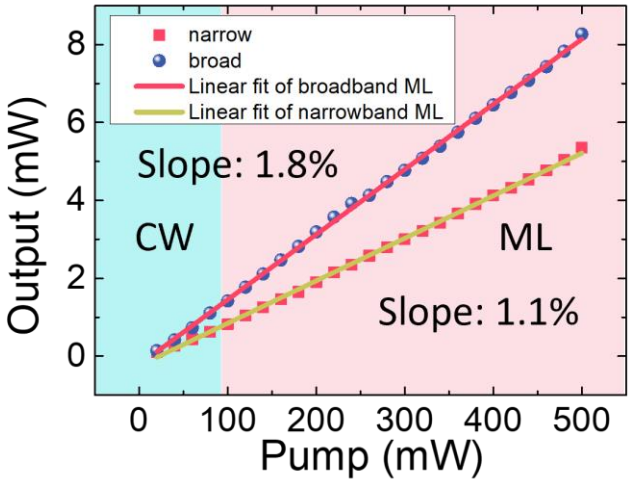


*Fig. 4-4: Experiment result of the obtained slope efficiencies with both narrowband mode locking (red rectangle, acousto-optic interaction activated by applying a microwave signal with 355.7 kHz frequency and 3 Vpp peak power) and broadband mode locking (blue sphere, acousto-optic interaction disabled by switching off the microwave signal) and their linear fittings.*

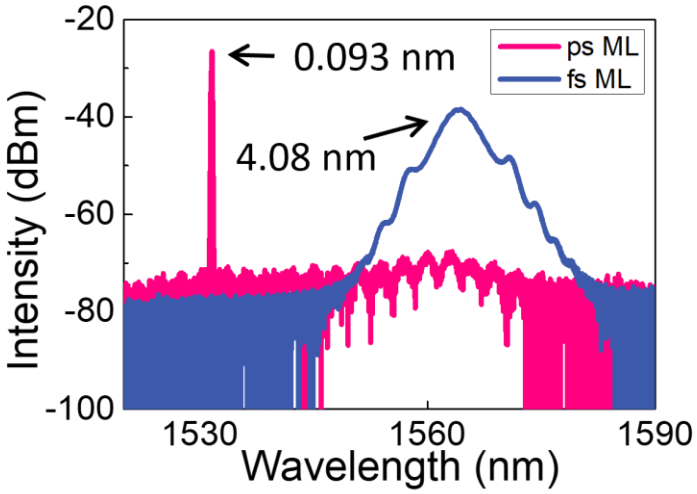


*Fig. 4-5: Experiment result of the obtained spectra with both narrowband mode locking (red color, acousto-optic interaction activated by applying a microwave signal with 355.7 kHz frequency and 3 Vpp peak power) and broadband mode locking (blue color, acousto-optic interaction disabled by switching off the microwave signal).*

The output spectra of both broadband and narrowband mode locking states are shown in **Fig. 4-5**. The narrowband mode locking

spectrum owns an FWHM of 0.093 nm with a center wavelength of 1531.3 nm. The broadband mode locking spectrum owns an FWHM of 4.08 nm with a center wavelength of 1564.2 nm. Here, the center wavelengths are quite different due to the equilibrium of the loss and gain in the laser cavity (mainly attributes to the dynamic attenuation control) which will be explained in the next section.

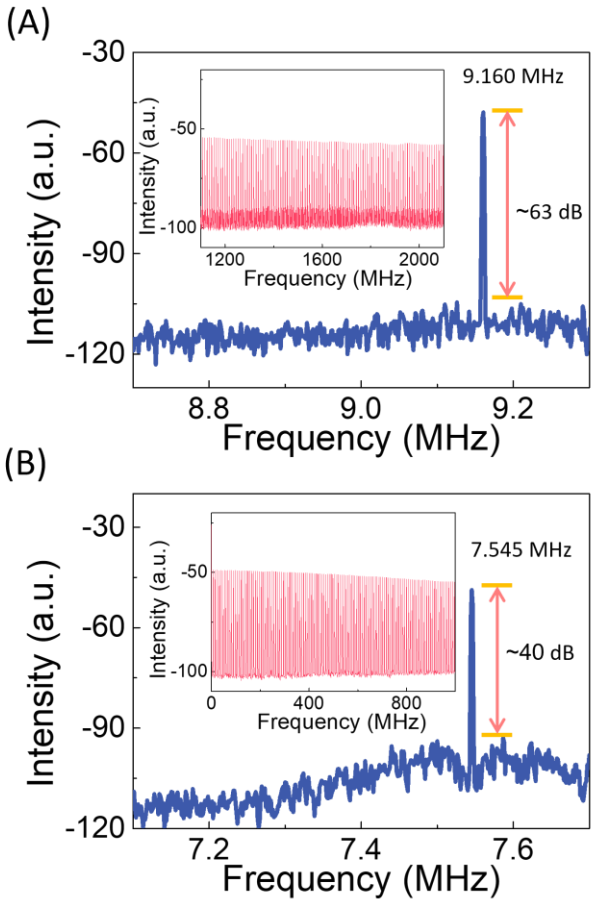


*Fig. 4-6: Experiment results of the obtained radio frequency (RF) spectra with both (A) narrowband mode locking (acousto-optic interaction activated by applying a microwave signal with 355.7 kHz frequency and 3 Vpp peak power) and (B) broadband mode locking (acousto-optic interaction disabled by switching off the microwave signal). Insets are the RF spectra in a wide frequency range.*

The radio frequency spectra are investigated as shown in **Fig. 4-6**. The radio frequency spectra show stable mode locking states of both narrowband reflection and broadband reflection. The narrowband mode locking state and the broadband mode locking state own

fundamental frequencies of 9.160 MHz and 7.545 MHz, which agree well with the temporal pulse train results. Besides, compared to broadband mode locking state, narrowband mode locking state exhibits a higher signal-to-noise ratio (SNR) of about 63 dB. This is strongly dependent on the high reflectivity of the FBG.

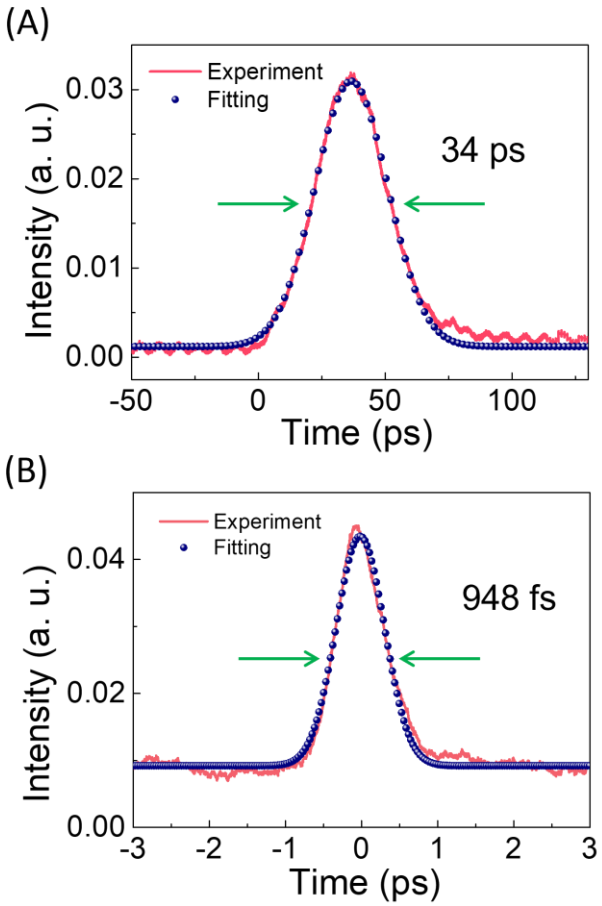


*Fig. 4-7: Experiment results of the obtained autocorrelation traces with both (A) narrowband mode locking (acousto-optic interaction activated by applying a microwave signal with 355.7 kHz frequency and 3 Vpp peak power) and (B) broadband mode locking (acousto-optic interaction disabled by switching off the microwave signal).*

To characterize the pulse width of each mode locking state, an autocorrelator (AC, FR-103XL) is employed. Due to a negative net dispersion in the laser cavity, a Gaussian-like profile is utilized to fit the AC trace, as depicted in **Fig. 4-7**. Thus, the pulse widths of the two mode locking states are calculated to be 34 ps (for narrowband

mode locking) and 948 fs (broadband mode locking). Due to the time-stretched dispersive effect, the pulse width is slightly broadened by the single-mode fiber between the pigtail of the output coupler and the AC. Therefore, the real pulse widths are both slightly shorter than the measurement results. However, the AC results already show the switching between fs pulses and ps pulses, which is highly flexible by simple modulation of the external microwave signal.

### IV.3.4 Mode locking state evolution under dynamic attenuation manipulation via acousto-optic interactions

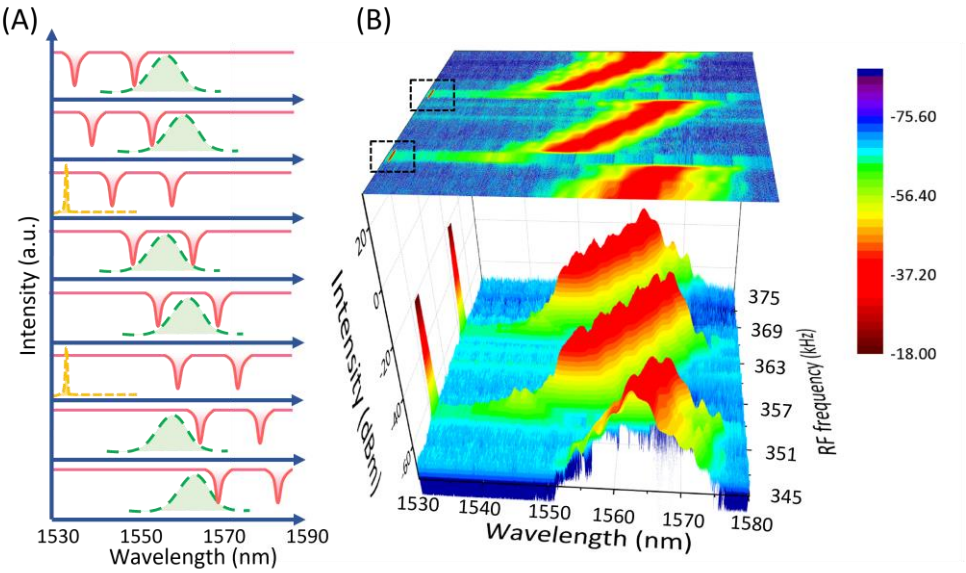


*Fig. 4-8: Theoretical analysis (A) and experiment results (B) of the mode locking state evolution by increasing the applied frequency of the microwave signal to adjusting the attenuation.*

Except for the switching mechanism between fs pulses and ps pulses, this mode locked fiber laser owns another interesting property of wavelength shifting. As investigated in the previous section, our adopted acousto-optic mode converter owns a dual-resonance property. In general, the 3-dB width of each resonant peak is about 10 nm and the interval between the two resonant peaks is about 30 nm [213]. However, the operation band of the Er-doped gain fiber (EDFC-980-HP) is 1530-1565 nm. Normally, the lasing wavelength is strongly dependent on the loss in a simple laser cavity using this gain fiber without any wavelength selection strategy. That is, any

wavelength within the range of 1530-1565 nm is possible. Thus, the only way to effectively control the consequent lasing wavelength is the loss adjusted by the attenuation control in our laser cavity. However, the 3-dB bandwidth of acousto-optic resonance (~10 nm) cannot cover the whole band of the gain fiber (35 nm). This means if the center resonant wavelength (and thus it is the center attenuation wavelength) is not located at the center wavelength of the gain band, the broadband mode locking is still possible.

Due to the wavelength tunability of the acousto-optic interaction, we gradually moving the applied frequency to shift the center attenuation wavelength to investigate the mode locking state evolution, as depicted in **Fig. 4-8**. In **Fig. 4-8(A)**, the applied frequency increases from the top to the bottom and so as the resonant wavelength of both resonant peaks. Note that the interval between two resonant peaks is fixed (only determined by the ellipticity of the fiber shape) [213].

The mode locking state evolution is found to be five stages. (1) At the beginning, the right resonant peak is just touching the left side of the gain band so that the broadband mode locking is achieved, and the center wavelength exhibits a redshift according to the increase of the applied frequency. (2) When the right resonant peak reaches the center of the gain band, the attenuation breaks the broadband oscillation. That is, neither the left part nor the right part of the unattenuated gain band is impossible to support a mode locking state. Thus, the fiber laser transfers to a narrowband reflection and form a ps mode locking state. (3) With the resonant wavelength further increases, the gain band will be in the middle of the two resonant peaks. Here, the interval of 30 nm between two resonant peaks provides a window for broadband mode locking. Subsequently, the right resonant peak will completely leave the gain band, but the left resonant peak begins to approach the gain band. This contributes to a similar result of broadband mode locking with a redshift of center wavelength at the increase of applied frequency. (4) When the left resonant peak locates at the center of the gain band, the mode locking state transfer to the narrowband mode locking again due to the strong attenuation. (5) Finally, with the left resonant peak comes to the right part of the gain band, the broadband mode locking will

take place at the left part of the gain band and exhibit a redshift according to the increase of the applied frequency.

We can clearly observe the five stages of the mode locking state evolution in the experimental results depicted in **Fig. 4-8(B)**, which agree well with the above theoretical analysis. This result helps us deeply understand the oscillation manipulation mechanism under the equilibrium of gain and loss and provides a novel strategy for not only a switching between narrowband mode locking and broadband mode locking, but also a wavelength tunability of the mode locking states.

### IV.3.5 Real-time observation of pulse width switching dynamics via acousto-optic interactions

To further investigate the pulse width switching dynamics in the mode locked fiber laser, the time-stretched dispersive Fourier transform technique is employed to realize the real-time observation. Specifically, here a single-mode fiber (YOFC SMF) with length of $L_{SMF} = 7.5\ km$ and dispersion of $D = -18\ ps/(nm \cdot km)$ is utilized to provide enough delay. Thus, the mapping relationship between time domain ($\delta t$) and frequency domain ($\delta\lambda$) can be calculated as:

$$\delta\lambda = \frac{\delta t}{|D| \cdot L_{SMF}} = \frac{\delta t}{135\ ps/nm} \qquad \text{(Eq. 4-1)}$$

Here, the photodetector adopted has a response bandwidth of 33 GHz and we set the acquisition repetition of the OSC at 40 GHz. The dynamic switching is realized by a frequency shift keying (FSK) technique from the signal generator. The altering speed is set at 200 Hz which is suitable for both the acquisition frequency and recording length of the OSC. One frequency is set at 364.4 kHz to create a large attenuation for ensuring a narrowband mode locking state and the other frequency is set at 30 kHz for non-resonance in the gain band which leads to the broadband mode locking state. Here, the second frequency cannot be set at 0 or switched off due to the FSK inherent property, but a non-resonance signal exhibits same effects as "off" state in this case. More importantly, due to the different repetition rates of the two mode locking states (because of different oscillation

cavity lengths as discussed above), the roundtrip time should be processed separately.

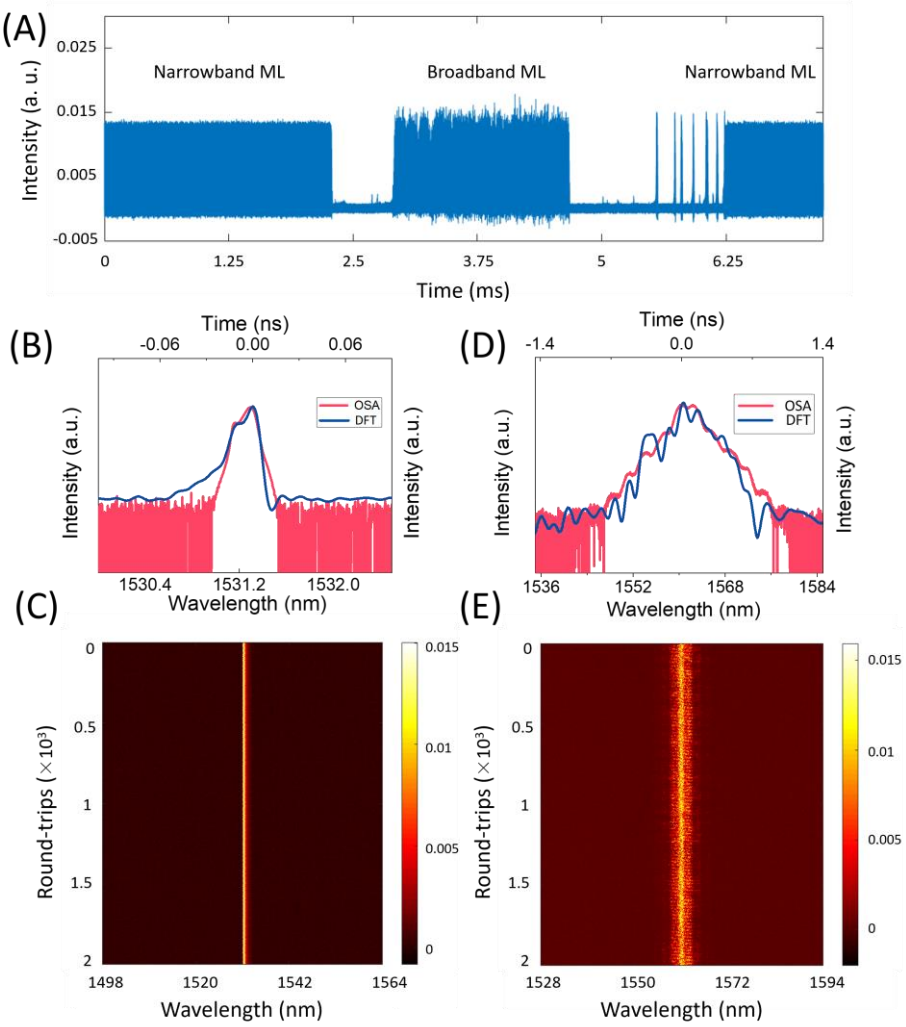


*Fig. 4-9: Real-time observations of pulse width switching by time-stretched dispersive Fourier transformation technique. (A) Real-time pulse train of the switching sequence of narrowband mode locking-broadband mode locking-narrowband mode locking after the delay by a 7.5 km single-mode fiber. (B) The comparison of stretched pulse shape and OSA spectrum of the narrowband mode locking state. (C) The evolution of a stable narrowband mode locking state. (D) The comparison of stretched pulse shape and OSA spectrum of the broadband mode locking state. (E) The evolution of a stable broadband mode locking state.*

The real-time pulse trains and their shapes compared to OSA spectra are depicted in **Fig. 4-9**. From the experimental result presented in **Fig. 4-9(A)**, the narrowband mode locking state is flatter than the

broadband mode locking state which is due to a higher SNR. More importantly, the switching from narrowband mode locking state to broadband mode locking state takes about 0.75 ms while the switching from broadband mode locking state to narrowband mode locking state takes about 1.56 ms. The latter takes a longer switching time which is mainly attributed to (1) a larger attenuation (and thus the larger loss) caused by the acousto-optic interaction contributes to a result that the light oscillation takes more time to reform a stable mode locking state from instability; (2) a shorter cavity length leads to less longitudinal modes and thus larger longitudinal mode intervals, which increases the difficulty in mode locking and thus a longer mode locking formation time.

The comparisons between pulse shapes after time-stretched dispersive Fourier transform and OSA spectra of both narrowband and broadband mode locking states indicate a good mapping relationship between two characterizing techniques. The dynamics evolutions without any switching process show good stabilities of both two mode locking states.

A pulse width dynamic switching process with a sequence of "narrowband mode locking-broadband mode locking-narrowband mode locking" is clearly observed as shown in **Fig. 4-10**. At first, the stable narrowband mode locking state suffers a quiet-down when the acousto-optic interaction is "off" and then the light is calmed down to the initial quantum state. Later, the relaxation oscillation takes place, but no large laser strikes are observed. This indicates a weak mode competition and after a short time the broadband mode locking is formed. Here, an obvious spectral intensity oscillation is observed, which lasts about 1000 roundtrips. The strong spectral intensity oscillation is mainly attributed to the soliton shaping evolution by saturable absorption effects [214]. Prior to the stable mode locking state, the soliton shape experiences an evolutionary process with different transient structural solitons according to the nonlinear effect of saturable absorption. Thus, in the spatiotemporal observation, the spectral evolution shows different structures of the spectra at different roundtrip positions with likely a periodic trend that is strongly dependent on the parameters set in the laser cavity.

The dynamics of switching from broadband mode locking state to narrowband mode locking state also experiences firstly a quiet-down process. But in the relaxation oscillation process, there are more laser strikes appeared due to a strong mode competition toward the final dominant pulse. Before the final stable narrowband mode locking state, the spectral intensity seems to exhibit only an intensity increase shape. However, it could also be attributed to the narrow bandwidth of the spectrum. The 3D profile of the whole switching dynamics is depicted in **Fig. 4-10(D)**.

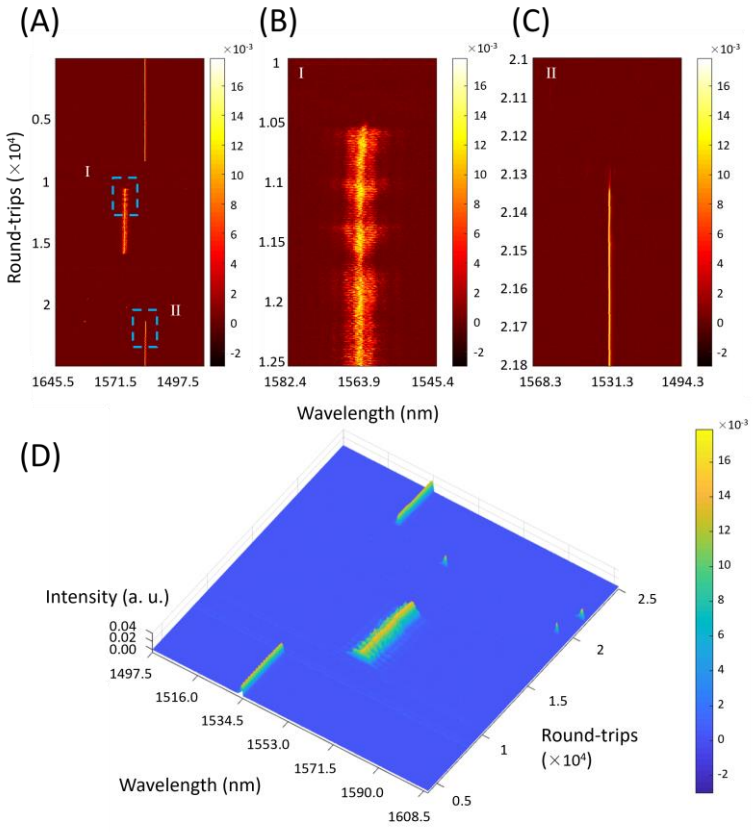


*Fig. 4-10: Dynamics evolutions of pulse width switching enabled by time-stretched dispersive Fourier transformation technique. (A) The overall 2D illustration of the pulse width dynamic switching process with a sequence of narrowband mode locking-broadband mode locking-narrowband mode locking. (B) The detailed image of the dashed rectangle region named as region I in figure A showing the formation of broadband mode locking state. (C) The detailed image of the dashed rectangle region named as region II in figure A showing the formation of narrowband mode locking state. (D) The overall 3D illustration of the pulse width dynamic switching process same as in figure A.*

## IV.4 CONCLUSION

Introduction of acousto-optic interaction into ultrafast fiber lasers to enable external manipulation as a controllable "trigger" for diverse transient dynamics observations is a fundamentally new strategy. This indeed paves the way for studying unique dynamic behaviors in ultrafast fiber lasers that are far from the normal build-up or shutting-down transient processes enabled by conventional pump injection. Our strategy using acousto-optic interactions can somehow provide the opportunity to observe some "middle" state transfers in the ultrafast lasers such as dynamic switching of mode locking states between different spatial modes (especially vortex modes) and different pulse width.

In this Chapter, we have tentatively obtained many important pioneered works:

**Real-time observation of vortex switching dynamics:**

1. A revised model of dual resonance in acousto-optic interactions in fibers is proposed. The acoustically induced displacement vector is utilized to describe the physical mechanism caused by the co-effect of acoustic and optical birefringence. This could extend the practical applications of the acousto-optic devices.
2. Novel demonstrations of mode locked vortex switching both between 0-order (Gaussian pulses) and 1$^{st}$-order vortex pulses (+1-order OAM or -1-order OAM) and between different topological charge signs (between +1-order OAM and -1-order OAM) are carried out successfully and well controlled. These results show great implications in flexible manipulation of ultrafast vortex pulses to meet more possibilities in ultrafast optics such as super-resolution imaging, quantum information science and ultrafast laser processing.
3. Transient switching process between different vortex mode locked states is observed. This is the first observation of spatial mode switching dynamics in the ultrafast fiber lasers, to the best of our knowledge. The transient dynamics of vortex mode switching includes a quiet-down phase, a relaxation oscillation stage, a quasi-mode locking state and an energy recovery process prior to

the final stable mode locked state with an operation of another vortex mode.

4. The energy fluctuation induced by acousto-optic mode switching contributes to irregular lasing strikes. We believe that the mode conversion and the mode competition within the laser cavity result in the energy perturbation, which is the main factor in the pulse evolution process.
5. Interestingly, there exists a continuous evolution of a wavelength shifting process before achieving the final targeted vortex mode locked state.

**Real-time observation of pulse width switching dynamics:**

1. A dynamic attenuation strategy is demonstrated in a cascaded FBG and broadband mirror incorporating with an acousto-optic device. This strategy is not only capable of switching-on/off the attenuation but also can adjust the attenuation ratio continuously.
2. The dynamic switching between narrowband and broadband mode locked states is realized by the acousto-optic interaction based dynamic attenuation strategy in a linear fiber laser cavity. This further enables the dynamic switching of pulse width between femtosecond scale and picosecond scale.
3. Due to the wavelength tunability, complex mode locking state evolution is investigated according to the frequency manipulation of the applied microwave signal. The results not only show the evolution between narrowband mode locking and broadband mode locking but also the lasing wavelength shifting in broadband mode locking states. This further enriches the mode locking mechanisms and provides a new strategy of tunable mode locked fiber laser fabrication.
4. Real-time observation of pulse width switching dynamics is demonstrated by means of time-stretched dispersive Fourier transform technique. The pulse width switching dynamics experiences a quiet-down process, a relaxation oscillation stage prior to the final stable mode locking state with another pulse width.
5. However, there exists an extra spectral intensity oscillation phase in the switching dynamics from narrowband mode locking to broadband mode locking. It is mainly attributed to the structured

soliton shaping according to the saturable absorption effects. Besides, the relaxation oscillation in the switching dynamics from broadband mode locking to narrowband mode locking is more intense to form some large laser strikes than the switching dynamics from narrowband mode locking to broadband mode locking. It can be interpreted as a larger loss introduced by the acousto-optic attenuation to break the equilibrium of gain and loss in the laser cavity.

The work demonstrated in this Chapter is based on the chiral light manipulation via acousto-optic interactions in fibers and extends it into ultrafast fiber lasers. It is only a starting point for studying diverse transient dynamics in ultrafast fiber lasers by employing the acousto-optic interactions. One can imagine some other interesting dynamics to observe, e.g., switching dynamics between conventional solitons and dissipated solitons, Q-switching states, and mode locked states. We believe that it would open the door for highly flexible chiral light field manipulations in ultrafast lasers as well as the dynamics research in ultrafast optics.

# Chapter.V FEMTOSECOND LASER DIRECT WRITING FIBER NANOGRATINGS

## V.1 INTRODUCTION

The objective of this PhD thesis is not only focusing on the novel chiral manipulation of light fields with dynamic tunability, but also related to the in-depth study of the light induced chirality in transparent materials, namely silica materials. This approach will enrich the physical mechanisms of light-matter interactions and endow new functional properties in the matter to create advanced photonic materials.

In this Chapter, we tentatively investigate fs laser direct writing fiber nanograting structures in silica fibers to seek a new strategy of nanograting-based functional in-line optics by imprinting anisotropic linear optical properties and chiral optical properties. This work could be a starting point of the fs laser direct writing fiber nangoratings and the related chirality as well to provide new possibilities in fiber optics.

In the first section, a published work in ***Nanoscale*** in 2019 is presented, which is about fs laser direct writing fiber nanogratings with both SEM evidence and characteristics. It contains the morphology observations related to the nanograting periodic structures, continuous writing property, erasure rewriting advantages. For characterizing the anisotropic polarimetric properties of the fiber nanogratings, both cross-polarized microscopy and Mueller polarimeter are utilized to unveil the strong birefringence and polarizing effects. More importantly, due to the strong linear dichroism of the fiber nanograting structures, an in-line polarizer is fabricated and characterized by fs laser direct writing fiber nanograting arrays distributed surrounding the fiber core. Thus, the evanescent field is restructured to manipulate the light propagation in the fiber core with an ultralow loss.

In the second section, a full control of 3D rotation of the fiber

nanograting structures is demonstrated. This work is related to a published paper in ***Applied Surface Science*** in 2023. With the investigation of polarization dependence of the nanograting orientation evolution, the fiber nanograting distribution can be well manipulated to form complex patterns with a synchronous polarization control. By the calibration of the pulse energy and the scanning speed, the retardance of the fiber nanogratings can also achieve the targeted values. Thus, the space variant fiber nanograting structures with expected distributions are enabled. This result meets the requirements of novel "Lab-on-fiber" and "Lab-in-fiber" systems and creates more functions benefit from the unique optical properties of nanograting structures. Besides, chiral optical property is discovered at the first time in fiber nanogratings and could lead to more interesting and functional in-line devices due to this chirality.

## V.2 FIBER NANOGRATINGS INDUCED BY FEMTOSECOND PULSE LASER DIRECT WRITING FOR IN-LINE POLARIZER

Journal Name

ARTICLE

# Fiber nanogratings induced by femtosecond pulse laser direct writing for in-line polarizer

Received 00th January 20xx,
Accepted 00th January 20xx

DOI: 10.1039/x0xx00000x

www.rsc.org/

Jiafeng Lu,[a] Ye Dai,*[b] Qin Li,[b] Yali Zhang,[a] Chunhua Wang,[a] Fufei Pang,[a] Tingyun Wang [a] and Xianglong Zeng *[a]

Self-organized fiber nanogratings (FNGs) induced by femtosecond pulse laser direct writing are demonstrated in optical silica fibers, for the first time. The Ge doping in silica fiber core plays an important role in the formation of nanogratings. Negative changes of refractive index with sawtooth fluctuation and strong birefringence of FNGs are investigated by optical fiber refractive index analyzer and crossed polarization microscope, respectively. The polarization features of FNGs are characterized by Mueller matrices analytical method and in-line polarizers based on FNGs are fabricated. FNGs are promising integrated components because of their prominent properties of polarization and salient compatibility with most fiber-optic systems.

## Introduction

Femtosecond pulse lasers have become irreplaceable processing tools due to their ultrashort durations and ultrahigh peak powers.[1] In the past decades, femtosecond pulse lasers have been widely used in various materials machining, such as nanostructures fabricating,[2-4] 3D printing,[5-6] 3D photonics integrating,[7] microfluids constructing,[8] materials internal modifying,[9] materials cutting and welding.[10-12] The thermal diffusion inhibition which is resulted from ultrashort pulse duration affords the benefits of adiabatic processing and high machining accuracy. The nonlinear effects induced around the irradiation area lead to intense light absorption, i.e. multiphoton absorption in transparent materials. Hence the threshold effect of multiphoton absorption and ionization could be applied for internal processing of transparent materials including fused silica,[13-15] germanate glasses,[16-18] sapphires[19] and lithium niobate crystals.[20-22] The laser-direct-writing technique has developed a new way to produce waveguides.[9, 23] Chen et al have reported on fabricating optical waveguides in diverse crystalline dielectric materials.[24] Moreover, the femtosecond laser fabricated circuits has been exploited in quantum information science.[25] Depending on the incident laser intensity levels, three kinds of induced microstructures are classified qualitatively.[26] At a low intensity irradiation, type-I structure is observed as a refractive index increase in the central part of irradiation area. With the increase of incident laser intensity, type-II structure manifesting as a subwavelength periodic structure, i.e. nanograting, becomes dominant. In this case, the electric field of femtosecond laser is responsible for both the excitation efficiency and orientation of the periodic nanostructures.[27] The resulting grating consists of alternate high and low refractive index nanoplanes and orientates perpendicular to the polarization of incident pulses. The induced nanogratings are self-organized structure with the period less than the laser wavelength, which enables laser processing to obtain fine structure size breaking through the Abbe diffraction limit. As further increasing the irradiation intensity, type-III structure originates mainly from the plasma blast and comes to be micro-voids and micro-cracks.[28, 29]

A nanograting phenomenon mainly exhibits both of strong birefringence effect and anisotropically chemical sensitivities.[30] The morphological anisotropy of nanogratings can lead to polarization dependent scattering, which was proposed to a potential application for fabricating polarizing components in integrated photonic circuits.[19] Conventional nanograting fabrication is usually achieved in bulk transparent dielectric material, such as fused silica[13, 14, 27] and Ge doped silica glass.[16-18] These components have been widely exploited in free-space optics, but few FNGs was found in the waveguide due to the lack of efficient coupling, especially in optical fibers with cylindrical structure and axially refractive index distribution.

Silica fiber is one of the most widely used media for optical communication and information process because of low transmission loss and potentially nonlinear effects. Moreover, different fiber components can be easily spliced together with ignorable coupling loss. Recent progresses in femtosecond laser processing in optical fibers have opened new frontiers of physics and technology in light-matter interaction. Fiber Bragg

[a] Key laboratory of Specialty Fiber Optics and Optical Access Networks, Joint International Research Laboratory of Specialty, Fiber Optics and Advanced Communication, Institute for Advanced Communication and Data Science, Shanghai University, Shanghai 200444, China. E-mail: zenglong@shu.edu.cn
[b] Department of Physics, Shanghai University, Shanghai 200444, China. E-mail: yedai@shu.edu.cn

gratings (FBGs) are demonstrated in optical fibers by using phase mask techniques[31, 32] and point-by-point techniques[33, 34] under a femtosecond laser irradiation. Ultrafast laser enhanced Rayleigh backscattering in optical fibers was investigated to fabricate distributed optical fiber sensors.[35] Lab-in-fibers were inscribed with multiple layers structure by femtosecond laser pulses, which have developed a new optical integration platform.[36] Very recently we also reported a work on how to fabricate nanogratings in silica optical fibers.[37]

Polarization properties of nanograting array inside optical fibers provide new optical functions in silica fibers. We firstly propose a new in-line fiber polarizer based on femtosecond pulse laser direct writing FNGs. Conventional polarizers can be classified into three main types: prism polarizer by refraction, sheet polarizer based on anisotropic absorption and Brewster-angle by reflection. These polarizing components are mostly used in free-space optics. Recent developments of in-line polarizers integrated with optical fibers have been reported in photonic circuits. In-line polarizers based on 45° tilted fiber gratings and partially liquid-filled hollow-core photonic crystal fibers are demonstrated.[38, 39] Bao et al also proposed an in-line fiber polarizer using ultrathin two-dimensional carbon material, which shows a good broadband polarizing performance.[40] These fiber polarizers require complex manufacturing processes such as graphene fabrication, phase mask processing and liquid filling technology. The proposed in-line fiber polarizer in current case presents the polarization dependent scattering of femtosecond laser direct writing nanogratings, which is proven to a promising alternative because of its broadband polarizing feature and simple fabricating procedure.

The self-organized nanogratings induced by femtosecond laser pulses direct writing are successfully demonstrate in optical fibers. The FNGs are observed morphologically by using transmission scanning electron microscopy (SEM) images. We confirm the polarization birefringence of FNGs due to their anisotropic structure and experimentally investigate the retardation and depolarization effects by Mueller matrix analytical method. For the first time as we know, the proof-of-concept implementation of an in-line polarizer based on FNGs in optical fibers is demonstrated due to polarization dependent attenuation. The FNGs-based fiber develops a promising application in all-fiber functional components, such as polarization mode control and high-order vector mode selection.

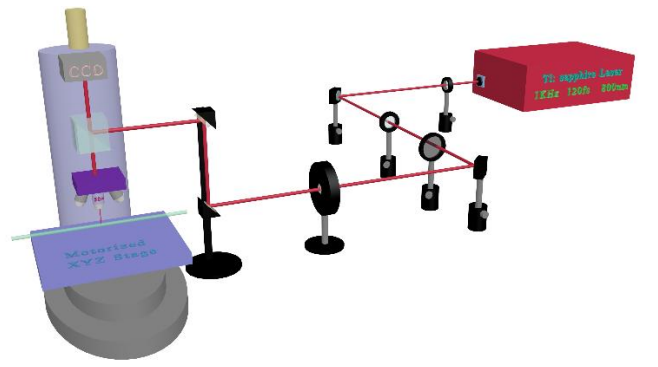


Fig. 1. FNGs processing schematic of experimental setup

## Results and Discussion

### FNGs fabrication setup

The FNGs can be fabricated both in single-mode-fibers (SMFs) and few-mode-fibers (FMFs) by a focused beam from a mode-locked, regenerated amplified Ti: sapphire laser system. The laser pulses are delivered at a center wavelength of 800 nm with a repetition rate of 1 kHz and a pulse duration time of 120 fs. A small aperture is utilized to narrow the laser beam and to average the energy of light spot distribution uniformly. A half-wave plate and a continuous neutral density filter are utilized to adjust the polarization azimuth angle and the pulse energy, respectively. The optical fibers are mounted onto a computer-controlled xyz translation stage (H101A ProScan model, PSI) and are irradiated with a 50x objective (NA=0.55, Nikon ECLIPSE 80i). The processing system is illustrated in Fig. 1.

### Self-organization of the nanogratings in optical fibers

The microstructures of optical silica fibers are different from that of bulk silica glass. The Ge doping in the core and the stress produced in the drawing process both possibly influence the formation of nanogratings.[18, 41-43] In addition, the relatively slow quenching rate of glass melt in the cladding contributes to the radial stress distribution in optical fibers.

Figure 2 shows the SEM (JSM 7500F) images of nanogratings inscribed in optical fibers. After femtosecond laser writing, the fiber samples are mechanically polished and then etched by 1 mol% hydrofluoric (HF) acid aqueous for 90 s at ambient temperature. The longitudinal cross-sections of nanograting array are observed in a carrot-like shape of approximately 15 μm in length and 2 μm in width, which is dependent on self-focused energy distribution of femtosecond laser pulses. Figure 2a and 2b show the whole view of fiber end face and the enlarged local area of nanogratings embedded inside a commercial SMF (SMF 28e), respectively. The femtosecond laser with a polarization of **E** propagates along the direction of **k** and scans along the direction of **S**. The nanogratings orientate perpendicular to the polarization of incident laser pulses. The region enclosed by a red dotted circle is the fiber core with a small amount of doped Ge. It is found that the bottom region of nanograting #3 written in the fiber core is about 1.2 μm wider than the top region of nanograting #3 and the other nanogratings, which are located in the fiber cladding with the same laser irradiation. This can be attributed to the defect centers induced by Ge-doping random networks of $SiO_4$ in the fiber core material.[44] The multi-photon ionization threshold is determined by the band gap of the material in a multi-photon absorption process. The band gap of core material is lower than that of no-doping silica glass in fiber cladding, which makes a larger area of ionized region in fiber core by the same irradiation intensity, resulting in a larger nanograting size.[26, 27]

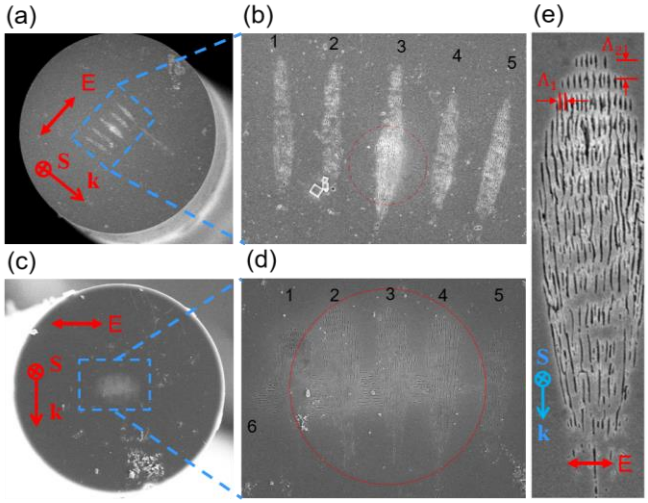


Fig. 2 SEM images of fabricated FNGs. Overall images of fiber end face with nanogratings inscribed by 1.38 μJ pulses in a SMF (a) and an FMF (c). Detailed images of FNGs in the SMF (b) and FMF (d). A dual period nanograting structure inscribed in a SMF (e) by 1.32 μJ pulses. All the FNGs were written at the scanning speed of 5 μm/s.

Nanogratings imprinted in a few-mode fiber with a larger core diameter (YOFC, four-mode SI 18/125) are shown in Fig. 2c and 2d. The nanogratings #2, #3 and #4 inscribed in the fiber core show about 1 μm wider and 1.6 μm longer than nanogratings #1 and #5 inscribed in the fiber cladding. These results well explain that free electrons density induced by multiphoton absorption is critically essential to the nanograting formation. Figure 2e exhibits a double-periodic nanograting structure in an optical fiber, which possibly results from the asymmetric growth of plasma and its local field intensity distribution.[45-47] The period $\Lambda_1$ parallel to the polarization of incident laser is measured to be 180 nm while the period $\Lambda_2$ perpendicular to the polarization gradually increases along the propagation direction of the incident laser. Nanoplasma spheres are preferentially formed from the inhomogeneity and defect areas in optical fibers under the irradiation of femtosecond laser pulses. The positive feedback of the interaction between incident light and plasma spheres induces the asymmetric local enhancement of the optical field, which leads to the asymmetric growth of the plasma spheres to be ellipsoid. With the increase of incident focusing depth inside the fiber, the size of the formed ellipsoid plasma gradually increases along the propagation of the incident light, which causes the gradual increase of period $\Lambda_2$.

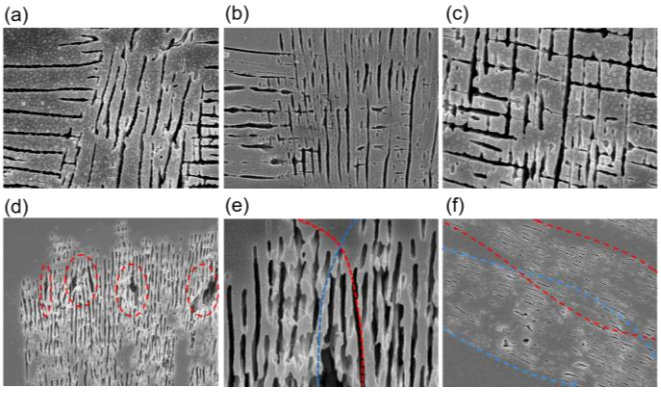


Fig. 3 SEM images of different levels of erasure and rewriting. The complete erasure (a), partial erasure (b) and the coexist phenomenon (c). (d) SEM images of parallel multi-scanning by 1.29 μJ pulses. Junctions of two nanogratings written by parallel partially overlapping in a SMF (e) and an FMF (f).

The erasure and rewriting properties of nanogratings in optical fibers are observed in Fig. 2d and a detailed investigation is depicted in Fig. 3a-3c. The horizontal nanogratings are imprinted firstly in the core region of an FMF at a scanning speed of 5 μm/s and the vertical nanogratings are inscribed at the same scanning speed to erase the formers. The horizontal nanogratings are written by using pulse energy of 1.38 μJ, while the vertical nanogratings are written by using 1.41 μJ, 1.38 μJ and 1.35 μJ, respectively. The laser rewriting capability strongly depends on the erasing pulse energy. When the erasing pulse energy is large enough, the former nanograting can be erased completely and a new nanograting is rewritten with the orientation perpendicular to the polarization of the erasing laser pulses. Once the erasing laser power comes to a threshold value, the two nanogratings with different orientations will reach a balance and coexist as a two-dimensional periodic nanostructure, which is illustrated in Fig. 2c.

Nanogratings imprinted in optical fibers also show a good connection with a parallel multi-scanning technique. Figure 3d shows the large area distribution of multiple embedded nanogratings in a SMF. The nanogratings inscribed by parallelly scanning with partial overlapping can connect one by one as a law of extension. Any two adjacent nanogratings remain the same spatial regularity. The collapses marked by red dotted circles are interpreted to excessive etching of HF caused by aggregation of high density structure defects suffering overlapping irradiation. Overlapping areas of two nanogratings in a SMF and an FMF are depicted in Fig. 3e and 3f, respectively.

**Characterization of nanogratings in optical fibers**

Nanogratings inscribed in optical fibers have strong birefringence signals under a cross-polarized optical microscope and are characterized by measuring the brightness of the written lines using an image analyzing software (NIS-Elements, Nikon). The birefringence signal is defined as the optical intensity of light transmission through the inscribed FNGs placed between two crossed polarizers. The principle of birefringence characterizing is given by:[48] $\mathrm{I} \propto sin^2\left(\frac{\pi \cdot \Delta \cdot L}{\lambda}\right)$. The value of birefringence ($\Delta$) is the difference between the ordinary and extraordinary indices of refraction. The parameters L and $\lambda$ are the length of the nanograting along the illuminated light propagation direction and the corresponding wavelength, respectively. Therefore, the birefringence signal intensity can roughly represent the retardance and the development levels of the formed nanogratings. Figure 4a and 4b show the birefringence distributions of the focal plane and a

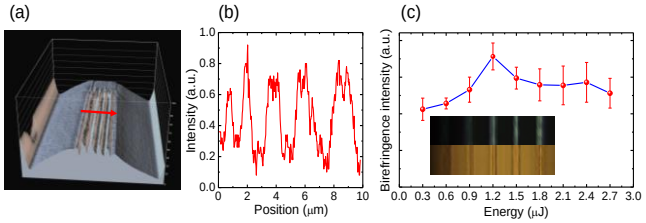


Fig. 4 (a) The birefringence distribution of the focal plane with five nanogratings inside. (b) The corresponding birefringence signal measured by line scanning. (c) The change of the birefringence intensities at varying the writing pulse energies. Inset: The written lines captured by cross-polarized and normal optical microscopes with the pulse energies of 0.6 μJ, 0.9 μJ, 1.2 μJ, 1.5 μJ and 1.8 μJ.

line scanning perpendicular to the axial direction of fiber, respectively. Considering that the brightness of birefringence signal in unexposed areas is much lower than that in the written lines, the inherent birefringence of optical fibers can be ignored. Strong intensities emerge from laser scanning lines, verifying that the signals are caused mainly by the birefringence of the nanogratings formed in optical fibers. The dependence of birefringence signal intensities on different pulse energies are depicted in Fig. 4c with cross-polarized and normal optical microscope images, which show that the optimal writing energy is around 1.2 μJ at a repetition rate of 1 kHz. When the laser power is lower than 1.2 μJ, the birefringence increases rapidly with the power increasing which indicates the formation of nanogratings. With the power increasing over 1.2 μJ, the birefringence decreases because high laser intensities are especially prone to induce micro-cracks belonging to the type-III, which destroys the formed nanograting structure and recedes the birefringence intensity.

The refractive index distribution of nanogratings in optical fibers is investigated by optical fiber refractive index analyzer (S14). The optical fiber with fabricated nanogratings was mechanically polished

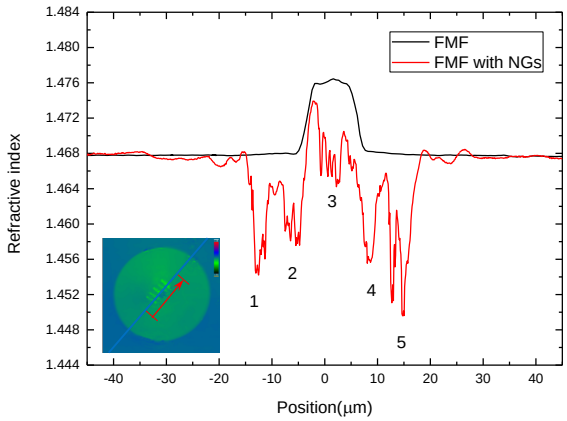


Fig. 5 The refractive index distribution of an FMF end face with five nanogratings.

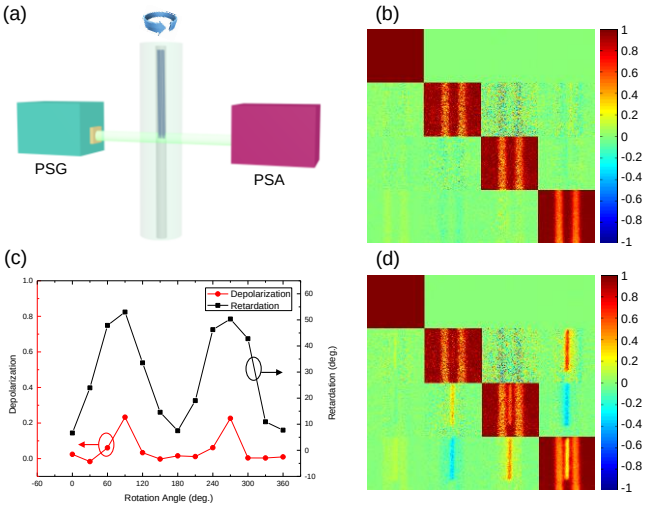


Fig. 6 (a) The Mueller matrices measuring system. The Mueller matrices images of an optical fiber with nanogratings at the rotation angle of 0° (b) and 90° (d). (c) The depolarization and retardation of an FNG at different rotation angles.

and then immersed in the index-matching fluid under the measurement using refracted near-field technique.[49] Figure 5 shows the refractive index distribution of five nanogratings in an FMF with line scanning measurement. A negative change of refractive index of approximate 0.015 is induced after irradiation, while every nanograting seems as a whole. Sawtooth changes of refractive indices are observed in nanogratings #1, #2, #3 and #5, which confirms that nanograting consists of alternant low and high refractive index nanoplanes. Sawtooth structure does not emerge in nanograting #4 due to the limit of device resolution and the poorly quality of the formed nanograting.

Nanogratings orientate perpendicular to the polarization of femtosecond laser pulses, which makes nanogratings polarization sensitive components. A 4×4 Mueller matrix is deemed to be the most comprehensive measurement of polarization due to its ability of characterizing all polarization effects. Mueller matrices are measured by collecting and analyzing the output states of polarization (SOP) from a Mueller matrix measuring system.[50] An optical fiber written with nanogratings is placed perpendicular to the propagation direction of probe light and sandwiched between a polarization state generator (PSG) and a polarization state analyzer (PSA) as shown in Fig. 6a. Figure 6b and 6d show the Mueller matrices images of an optical fiber with nanogratings by rotating the fiber at 0° and 90°, respectively. In the Fig. 6b, the nanostructure is almost invisible in Mueller matrices images, which indicates that the normal direction of nanogratings is parallel to the propagating direction of the probe light. The structure is isotropous and makes a weak impact on the propagation of probe light. Differently, the written lines are observed clearly in the Fig. 6d. The fiber has been rotated at 90° so that the normal direction of nanogratings is perpendicular to the propagating direction of the probe light. Due to the alternate low and

Journal Name

ARTICLE

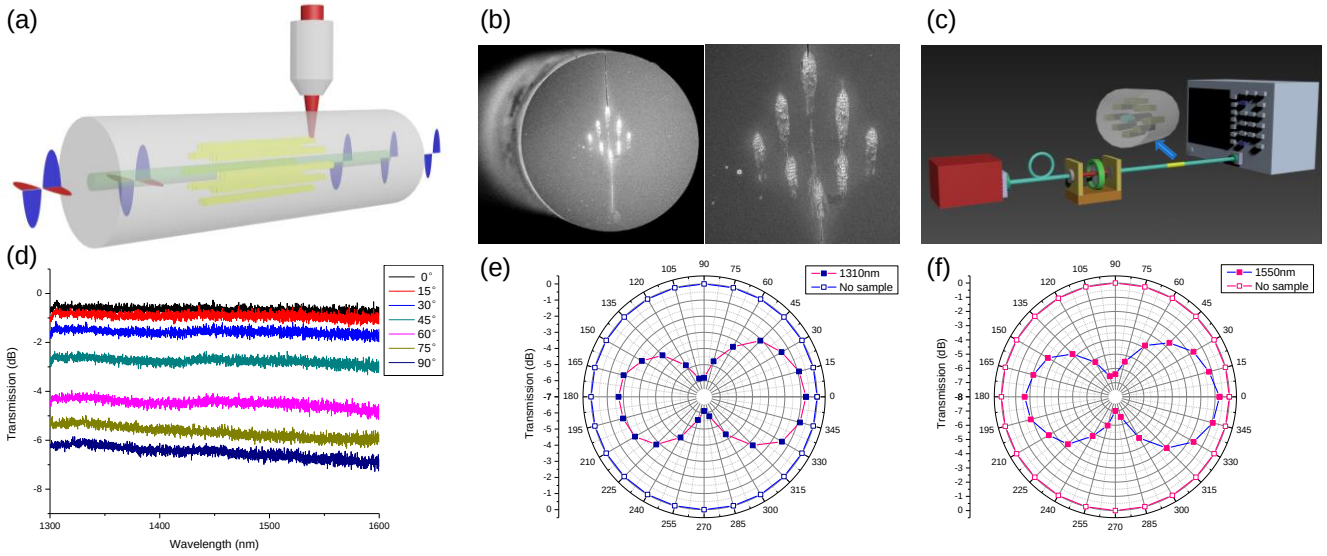


Fig. 7 (a) The schematic diagram of the in-line polarizer based on FNGs. (b) SEM images of the fiber end face with nanogratings embedded around fiber core for in-line polarizer. (c) The schematic diagram of in-line polarizer testing setup. (d) The loss spectra at varying the input polarization angles. The polarization distribution of the in-line fiber polarizer (■) and a bare fiber (□) at the wavelength of 1310 nm (e) and 1550 nm (f).

high refractive index nanoplanes, the structure shows strong anisotropy, which causes a large optical retardation. The Mueller matrices are measured from 0° to 360° and decomposed by the method given by:[51]

$$M = \begin{bmatrix} m_{00} & m_{01} & m_{02} & m_{03} \\ m_{10} & m_{11} & m_{12} & m_{13} \\ m_{20} & m_{21} & m_{22} & m_{23} \\ m_{30} & m_{31} & m_{32} & m_{33} \end{bmatrix} = M_\Delta M_R M_D \quad (1)$$

Here $M$ is the Mueller matrix of the FNG, which includes 16 polarization dependent elements. $M_\Delta$ refers to the depolarization factor, $M_R$ stands for the birefringence factor, and the $M_D$ represents the diattenuation factor. After data processing, the depolarization and retardation of nanogratings inscribed in optical fibers are dotted at varying rotation angles in Fig. 6c. Both of the depolarization and retardation reach the maximum at either 90° or 270°. The depolarization of nanogratings is interpreted to the elastic and inelastic scattering resulting from the nanoplanes and other defect structures. The results show the measured maximum of the retardance is about 53°, which is mainly caused by the nanograting birefringence, while the minimum is not zero because of the inherent birefringence of optical fibers.

**In-line polarizer based on FNGs**

Nanograting consists of alternant low and high refractive index nanoplanes with the thickness $w_{1,2}$ and dielectric constant $\varepsilon_{1,2}$, respectively. The effective dielectric constant parallel to the direction of nanoplanes is defined as $\varepsilon_\parallel$ while the effective dielectric constant perpendicular to the direction of nanoplanes is defined as $\varepsilon_\perp$, which can be respectively expressed as[52]:

$$\varepsilon_\parallel = (w_1\varepsilon_1 + w_2\varepsilon_2)/(w_1 + w_2) \quad (2)$$

$$\varepsilon_\perp = (w_1 + w_2)\varepsilon_1\varepsilon_2/(w_1\varepsilon_2 + w_2\varepsilon_1) \quad (3)$$

Consequently, nanograting shows a strong birefringence like a negative uniaxial crystal. On the basis of effective medium theory,[53] the light with polarization perpendicular to the normal direction of nanogratings can propagate through nanogratings with weakest scattering and reflection, while the light with polarization parallel to the normal direction of nanogratings is severely attenuated by nanograting due to the strong scattering and reflection. The attenuation mechanism is depicted in Fig. 7a.

This polarization sensitive attenuation of the FNGs is utilized to fabricate in-line optical polarizers. The nanogratings are inscribed in the cladding of optical fibers interacting with the evanescent fields, meanwhile the transmission loss of the light propagation is less increased. Here the extinction ratio (ER) of the in-line polarizer is measured by using Malus-law method.

The experimental setup is shown in Fig. 7c. A linearly polarized source which consists of a broadband light source and a polarizer is launched to the in-line polarizer based on FNGs and finally pigtailed by an optical spectrum analyzer (OSA) (Yokogawa 6370c). By varying the polarization of input beam, the intensity of the output beam changes periodically according to Malus law as $I = I_O cos^2\theta$.[54] Here $\theta$ is the angle between transmission axes of the polarizer and the transmission axes of the in-line polarizer. We define the maximum and the minimum transmission intensities as $I_{max}$ and $I_{min}$, respectively. The ratio of maximum to minimum transmitted intensity is defined as the ER in terms of dB, as follows:

$$\text{ER (dB)} = 10log\left(\frac{I_{max}}{I_{min}}\right) = I_{max}\ (dB) - I_{min}\ (dB) \quad (4)$$

The insertion loss (IL) of in-line fiber polarizer is defined as the ratio of the input light intensity $I_0$ over the $I_{max}$ in the following formula:

$$\text{IL (dB)} = 10log\left(\frac{I_0}{I_{max}}\right) = I_0\ (dB) - I_{max}\ (dB) \quad (5)$$

The SEM images of in-line polarizer based on FNGs and the measured optical loss spectra at varying angles of input polarization from 0° to 90° are shown in Fig. 7b and 7d, respectively. The fiber polarizer based on FNGs shows a polarizing behavior in a broadband, and the polarizing perfomance at the wavelengths of 1310 nm and 1550 nm is displayed in Fig. 7e and 7f.

The ERs of the fabricated fiber polarizer are 5.43 dB and 6.319 dB at 1310 nm and 1550 nm, respectively, which can be further improved by optimizing the writing parameters including the length of scanning lines, pulse energy and arrangment modes of nanograting arrays. Here the unsymmetrical structure of polarization performance is mainly attributed to the chiral property of FNGs, which is interpreted to the action of light-induced torque[55, 56] and leads to a different attenuation when the polarization of the input light are 0° and 180°. The IL of the in-line polarizer is 0.69 dB both at 1310 nm and 1550 nm, which is mostly linked to the continuity and uniformity of the nanograting arrays. By optimizing the writing parameters and the arrangement of nanograings arrays, such polarizers with better performances can be obtained. A nanograting structure is maintained up to the glass transition temperature $T_g$ of ~1200 ℃,[57-59] which ensures a high thermal stability of FNG-based devices for extensive practical applications.

## Conclusions

We report on the fabrication and characterization of FNGs induced by femtosecond laser pulses direct writing. The Ge doping plays an important role in formation of nanogratings in optical fibers. The strong birefringence and the negative refractive index distribution with sawtooth structure of nanogratings in optical fibers are both characterized. Mueller matrix analytical method is utilized to characterize the depolarization and retardance of the fabricated FNGs. The polarization-dependent attenuation existed in a broadband spectrum range and therefore the in-line polarizer has been achieved. We also discuss the optimum proposal for improving the extinction ratio of the polarizer. The in-line polarizers based on FNGs are very competitive to the polarization management in photon integration field with the advantages of compact size, simple fabrication, strong stability and high compatibility to most fiber-optic systems.

## Conflicts of Interest

There are no conflicts of interest to declare.

## Acknowledgements

This work was supported by the National Natural Science Foundation of China (Grant Nos. 91750108, 11774220, 61575118, 61635006). X. Zeng acknowledges the support of the Program for Professor of Special Appointment (Eastern Scholar) at Shanghai Institutions of Higher Learning and Science and Technology Commission of Shanghai Municipality (16520720900). F. Pang was supported by "Shuguang Program" of Shanghai Education Development Foundation and Shanghai Municipal Education Commission (16SG35).

## Notes and references

1 D. Tan, K. N. Sharafudeen, Y. Yue, and J. Qiu, Progress in Materials Science, 2016, **76**, 154.
2 S. Richter, M. Heinrich, S. Döring, A. Tünnermann, and S. Nolte, Applied Physics A, 2011, **104**, 503.
3 F. Liang, R. Vallée, and S. L. Chin, Optics Express, 2012, **20**, 4389.
4 P. G. Kazansky, and Y. Shimotsuma, Journal of the Ceramic Society of Japan,2008, **116**, 1052.
5 S. Kawata, H. B. Sun, T. Tanaka, and K. Takada, Nature, 2001, **412**, 697.
6 Y. Hu, Z. Lao, B. P. Cumming, D. Wu, J. Li, H. Liang, J. Chu, W. Huang, and M. Gu, Proceedings of the National Academy of Sciences, 2015, **112**, 6876.
7 K. Itoh, W. Watanabe, S. Nolte, and C. B. Schaffer, MRS bulletin, 2006, **31**, 620.
8 C. Hnatovsky, R. S. Taylor, E. Simova, P. P. Rajeev, D. M. Rayner, V. R. Bhardwaj, and P. B. Corkum, Applied Physics A, 2006, **84**, 47.
9 K. M. Davis, K. Miura, N. Sugimoto, and K. Hirao, Optics Letters, 1996, **21**, 1729.
10 K. Sugioka, and Y. Cheng, Light: Science and Applications, 2014, **3**, e149.
11 T. Tamaki, W. Watanabe, J. Nishii, and K. Itoh, Japanese Journal of Applied Physics, 2005, **44**, L687.
12 S. Richter, S. Döring, A. Tünnermann, and S. Nolte, Applied Physics A, 2011, **103**, 257.
13 C. Hnatovsky, R. S. Taylor, P. P. Rajeev, E. Simova, V. R. Bhardwaj, D. M. Rayner, and P. B. Corkum, Applied Physics Letters, 2005, **87**, 014104.
14 L. P. R. Ramirez, M. Heinrich, S. Richter, F. Dreisow, R. Keil, A. V. Korovin, U. Peschel, S. Nolte and A. Tünnermann, Applied Physics A, 2010, **100**, 1.
15 V. R. Bhardwaj, E. Simova, P. P. Rajeev, C. Hnatovsky, R. S. Taylor, D. M. Rayner, and P. B. Corkum, Physical Review Letters,2006, **96**, 057404.

 

16 F. Zhang, A. Cerkauskaite, R. Drevinskas, P. G. Kazansky, and J. Qiu, Advanced Optical Materials,2017, **5**, 1700342.
17 R. Desmarchelier, B. Poumellec, F. Brisset, S. Mazerat, and M. Lancry, World Journal of Nano Science and Engineering, 2015, **5**, 115.
18 F. Zimmermann, M. Lancry, A. Plech, S. Richter, B. H. Babu, B. Poumellec, A. Tünnermann, and S. Nolte, Optics Letters, 2016, **41**, 1161.
19 J. Bai, G. Cheng, X. Long, Y. Wang, W. Zhao, G. Chen, R. Stoian, and R. Hui, Optics Express, 2012, **20**, 15035.
20 C. Fan, B. Poumellec, H. Zeng, M. Lancry, W. Yang, B. Bourguignon, and G. Chen, Journal of Laser Micro/Nanoengineering, 2011, **6,** 2.
21 J. Lv, Y. Cheng, J. R. V. de Aldana, X. Hao, and F. Chen, Journal of Lightwave Technology, 2016, **34**, 3587.
22 J. Cao, B. Poumellec, F. Brisset, and M. Lancry, Optics Express, 2018, **26**, 7460.
23 A. Crespi, Y. Gu, B. Ngamsom, H. J. Hoekstra, C. Dongre, M. Pollnau, R. Ramponi, H. H. van den Vlekkert, P. Watts, G. Cerullo, and R. Osellame, Lab on A Chip, 2010, **10**, 1167.
24 F. Chen, and J. R. V. D. Aldana, Laser and Photonics Reviews, 2014, **8**, 251.
25 T. Meany, M. Gräfe, R. Heilmann, A. Perez-Leija, S. Gross, M. J. Steel, M. J. Withford, and A. Szameit, Laser and Photonics Reviews, 2015, **9**, 363.
26 Y. Dai, A. Patel, J. Song, M. Beresna, and P. G. Kazansky, Optics Express, 2016, **24**, 19344.
27 Y. Shimotsuma, P. G. Kazansky, J. Qiu, and K. Hirao, Physical Review Letters, 2003, **91**, 247405.
28 X. Wang, F. Chen, Q. Yang, H. Liu, H. Bian, J. Si, and X. Hou, Applied Physics A, 2011, **102**, 39.
29 J. Qiu, The Chemical Record, 2004, **4(1)**, 50-58.
30 F. Zhang, Y. Yu, C. Cheng, Y. Dai, and J. Qiu, Optics Letters, 2013, **38**, 2212.
31 J. Thomas, E. Wikszak, T. Clausnitzer, U. Fuchs, U. Zeitner, S. Nolte, and A. Tünnermann, Applied Physics A, 2007, **86**, 153.
32 C. Hnatovsky, D. Grobnic, D. Coulas, M. Barnes, and S. J. Mihailov, Optics Letters, 2007, **42**, 399.
33 Y. Lai, K. Zhou, K. Sugden, and I. Bennion, Optics Express, 2007, **15**, 18318.
34 T. Geernaert, K. Kalli, C. Koutsides, M. Komodromos, T. Nasilowski, W. Urbanczyk, J. Wojcik, F. Berghmans, and H. Thienpont, Optics Letters, 2010, **35**, 1647.
35 A. Yan, S. Huang, S. Li, R. Chen, P. Ohodnicki, M. Buric, S. Lee, M. Li, and K. P. Chen, Scientific Reports, 2017, **7**, 9360.
36 M. Haque, K. K. Lee, S. Ho, L. A. Fernandes, and P. R. Herman, Lab on A Chip, 2014, **14**, 3817.
37 J. Lu, Q. Li, Y. Dai, Y. Zhang, C. Wang, F. Pang, T. Wang, and X. Zeng, Conference on Lasers and Electro-Optics, 2018, JTu3O.2.
38 Z. Yan, K. Zhou, and L. Zhang, Optics Letters, 2012, **37**, 3819.
39 W. Qian, C. L. Zhao, Y. Wang, C. C. Chan, S. Liu, and W. Jin, Optics Letters, 2011, **36**, 3296.
40 Q. Bao, H. Zhang, B. Wang, Z. Ni, C. H. Y. X. Lim, Y. Wang, D. Y. Tang, and K. P. Loh, Nature Photonics, 2011, **5**, 411.
41 P. G. Kazansky, H. Inouye, T. Mitsuyu, K. Miura, J. Qiu, K. Hirao, Physical Review Letters, 1999, **82**, 2199.
42 A. Champion, and Y. Bellouard, Optical Materials Express, 2012, **2**, 789.
43 A. Champion, M. Beresna, P. Kazansky, and Y. Bellouard, Optics Express, 2013, **21**, 24942.
44 J. X. Wen, W. Y. Luo, Z. Y. Xiao, T. Y. Wang, Z. Y. Chen, and X. L. Zeng, Journal of Applied Physics, 2010, **107**, 145.
45 A. Y. Arai, E. Bricchi, J. Bovatsek, P. G. Kazansky, and W. Yang, Optics Express, 2006, **14**, 10117.
46 M. Beresna, M. Gecevičius, P. G. Kazansky, T. Taylor, and A. V. Kavokin, Applied Physics Letters, 2012, **101**, 219.
47 M. Gong, Y. Dai, J. Song, and G. Ma, Acta Optica Sinica, 2016, **36**, 1.
48 R. Taylor, C. Hnatovsky, and E. Simova, Laser and Photonics Reviews, 2008, **2**, 26.
49 K. I. White, Optical and Quantum Electronics, 1979, **11**, 185.
50 C. Wang, S. Zhang, Q. Yu, and L. Li, Journal of Modern Optics, 2013, **60**, 1869.
51 J. Morio, and F. Goudail, Optics Letters, 2004, **29**, 2234.
52 M. Born and E. Wolf, "Principles of Optics, 7th ed," Publishing House of Electronics Industry, 2009, Beijing, China.
53 P. Lalanne, and D. Lemercier-lalanne, Optica Acta International Journal of Optics, 1996, **43**, 2063.
54 H. Esmaeilzadeh, E. Arzi, M. Mozafari, and A. Hassani, Sensors and Actuators A Physical, 2012, **185**, 59.
55 B. Poumellec, M. Lancry, R. Desmarchelier, E. Hervé, and B. Bourguignon, Light Science and Applications, 2016, **5**, e16178.
56 R. Desmarchelier, M. Lancry, J. Tian, and B. Poumellec, Applied Physics Letters, 2017, **110**, 021112.
57 E. Bricchi, and P. G. Kazansky, Applied Physics Letters, 2006, **88**, 3329.
58 J. Zhang, M. Gecevičius, M. Beresna, and P. G. Kazansky, Physical Review Letters, 2014, **112**, 033901.
59 F. Zhang, Y. Yu, C. Cheng, Y. Dai, H. Zhang, and J. Qiu, Applied Physics B, 2014, **117**, 53.

## V.3 SPACE VARIANT FIBER NANOGRATINGS INDUCED BY FEMTOSECOND LASER DIRECT WRITING

# Space variant fiber nanogratings induced by femtosecond laser direct writing

**JIAFENG LU,[1] LINPING TENG,[1] QINXIAO ZHAI,[2] CHUNHUA WANG,[1] MATTHIEU LANCRY,[3] YE DAI,[2,4] AND XIANGLONG ZENG[1,*]**

[1] *Key Laboratory of Specialty Fiber Optics and Optical Access Networks, Joint International Research Laboratory of Specialty Fiber Optics and Advanced Communication, Shanghai Institute for Advanced Communication and Data Science, Shanghai University, Shanghai 200444, China*
[2] *Department of Physics, Shanghai University, Shanghai 200444, China,*
[3] *Institut de Chimie Moléculaire et des Matériaux d'Orsay, Université Paris Saclay, Orsay cedex 91405, France*
[4] *yedai@shu.edu.cn*
* *zenglong@shu.edu.cn*

**Abstract:** Light-matter interaction within ultrashort duration time contributes to the nonlinear photoionization that allows diverse nanostructures, especially subwavelength nanogratings, which comprises strong negative birefringence and recently chiroptic properties. Fiber nanograting, namely nanograting integrated in optical fibers, encountering the new possibility of realizing both "lab-on-fiber" and "lab-in-fiber" engineering, is leading to a novel and intriguing topic in ultrafast optics and integrated optics. However, the state-of-the-art fiber nanograting based technologies normally focus on the unidirectional distributions of nanogratings, which restricts the freedom of functionality. Here, we report a full control of the fiber nanogratings orientation by manipulating the laser polarization and a tailoring of space variant fiber nanogratings to extend the diversity towards on-demand fiber nanogratings engineering. As such, we believe that this will be beneficial for optical manipulation in fiber lasers, fiber communications and fiber based integrated systems.

Key words: Silica fibers, Nanograting, Femtosecond laser, Light matter interaction, Chirality

## 1. Introduction

Processing of materials in the domains of data storage, nanoscale photonics, bioscience and plasmonic structures requires high throughout structuring and refined nano-patterning. Generally, small feature size and high precision are incompatible corresponding to Tennant's law[1,2]. However, femtosecond (fs) laser emerges with Abbe diffraction limit breaking due to self-organization from nonlinear effects, may encounter the balance of these two alternatives. Fs laser manufacturing delivers photo energies of laser pulses with ultrahigh peak power precisely to defined local volumes of the transparent materials via nonlinear effects e.g., two/multi-photon excitations[3,4]. Such a complex process takes place at a time scale much smaller than the thermal diffusion and the electron-phonon transfer between photon-excited plasma and lattice ions, which enables diverse photon-modifications dedicated in sub 100 nm sized region lithography, very importantly with a non-restricted three-dimensional (3D) capability[2]. The permanent optical modifications that are dependent on the light energy deposition and transfer efficiency to the materials, are cataloged into three kinds: isotropic refractive index modifications due to point defects and specific volume changes (Type I); anisotropic index changes due to subwavelength nanostructures so called nanogratings (Type II); and micro/nano-voids mainly caused by micro-explosions (Type III)[5]. The thresholds of these different modification regimes depend not only on the controllable laser parameters but also on the optical and thermo-mechanical properties of the materials themselves.

A self-organized nanograting[6] mainly exhibits a strong negative form birefringence, attributing to the alternatively distributed nano-porous layers with anisotropic filling factor. Such a unique refined nanostructure originates for example, from the scattered waves interference leading to spatial structuration of the plasma density distribution[7,8]. Recently, Lancry et al. revealed that the nanoscale free-electron density modulation is determined by a decomposition of $SiO_2$ leading to oblate nanopores formation[9]. Subsequently, the oxygen atoms are expulsed from the lattice and thus recombine to molecular oxygen in the nanopores. This theory has now been developed and revisited by a plasma mediated nano-cavitation model[8]. Although the nature of the origin of nanogratings remains under discussion, type II nanogratings modification exhibits useful physical-chemical properties i.e., strong birefringence, high thermal stability, erasure rewriting, chemical sensitivity[8,10–12]. Recently, Poumellec et al. revealed that fs laser pulses can create optical chirality in an achiral material (silica glass)[13], as confirmed by our two-layers model that this fs induced chirality is imprinted based on two linear contributions i.e., a form birefringence and a stress-related birefringence with non-parallel and non-perpendicular neutral axes [14]. To date, fs laser written nanogratings have encountered diverse applications ranging from plasma physical fundamentals, materials science to nano-photonics and quantum information science[4,15–17].

From fundamental optical communication system to micro-sensing in extreme environments, optical fiber has brought revolutionary development in light science due to its much lower transmission loss as well as, the cheaper fabrication cost[18]. Thus, towards on-demand manipulations of light propagating in the optical fibers, fiber-based elements are essential to unlock the functionalities of fiber-based light technology. Given the micrometric sizes and complex structures manufacturing, fs laser 3D processing has brought new possibility to nano-micro fabrications in fibers. For instance, mature technologies of fs laser written fiber Bragg gratings (FBGs) have been demonstrated via phase mask and point-by-point technique[19,20]. In addition, an enhanced Rayleigh backscattering is investigated by fs laser processing in fibers, which encounters distributed fiber sensors[21]. Normally, lab-on-a-chip devices require cm dimensions with functional elements sizes featuring around 100 μm, which corresponds to the cross sections of normal optical fibers[22]. Following the perspective, fiber-tip based elements or even lab-on-fiber and lab-in-fiber develop rapidly from a proof-of-principle stage to a useful platform for manipulating light interacted with fibers and of course, inside fibers. This significant technology with advanced functional materials at micro-nano scale gives disparate properties and functions to the optical fiber media, leading to the new possibilities in nano-photonics, plasmon physics and nano-sensing[23–25].

Fs written nanograting in optical fibers i.e., fiber nanograting (FNG) exploits both the anisotropic optical properties of nanograting and fiber compatibility, which is now growing as a novel strategy for fiber-based functional element fabrications. For instance, potential birefringent waveplates would be realized by embedding nanogratings inside optical fibers for phase control of fast and slow light beams. Owing to the chemical sensitivity of nanogratings, on-demand structural fabrications of FNG-based micro-fluidic channels are possible. Recent advances that multilayer strategy enabled chiral waveplates can control the polarization of the light in silica glass[26] indicate instructive perspectives in FNGs due to the compatibility of the cylindrical structure of an optical fiber. Previously, we have reported a fs laser implanted polarization selective array assembled by a set of FNGs distributed around fiber core can thus form an in-line polarizer[27]. This in turn provides new perspectives in fs laser written in-line/on-fiber optical element fabrications and further, in micro-fluidic channels and surface plasma resonance in optical fibers, via complex assemblies of FNGs. However, the state-of-the-art of FNGs only exploits the nanogratings orientated with same directions, which somewhat restricts their functionality.

In this paper, we present a unified strategy that enables dynamic control of laser polarization to demonstrate the tailoring of space variant FNGs induced by fs laser pulses. In a simple view, the orientation of the FNG distribution is manipulated by the laser polarization (considering no tilt effect) and the optical retardance remains related to the laser fluence[6]. Firstly, the polarization dependences of the FNG distribution in the planes both parallel and perpendicular to the light propagating direction are investigated with a design of polarization evolution. Calibrations of retardance are performed via different laser pulse energies and writing speeds, which are measured by crossed polarized microscopy. In addition, the Mueller matrix of the FNG structure is recorded and then decomposed to characterize the polarization properties. Furthermore, continuous evolutions of FNG orientation variation i.e., space variant FNG constructions are enabled by fs laser scanning combined with a synchronous polarization control technique. This tailoring of space variant FNGs would extend the manipulation freedom of FNGs inscriptions towards five-dimension (5D, 3D space control combined with FNG orientation and retardance) control.

## 2. Experimental setup and methods

### *2.1 Fs laser setup*

The illustration of the fs laser setup is depicted in **Fig. 1(a)**. The fs laser pulses of 120 fs duration are delivered from a Ti: sapphire laser system (Spectra-Physics) at a repetition rate of 1 kHz with a central wavelength of 800 nm. A small aperture narrows the laser beam size and allows a uniform distribution of the light spot whereas a continuous neutral density filter is utilized to manipulate the power. Besides, a computer controlled half-wave plate is employed to rotate the laser polarization azimuth. Benefit from a fast belt driven rotation motor (URB100CC, Newport), the half-wave plate can be rotated at a very fast speed up to 720°/s. The fs laser beam is then focused into the optical fiber via an objective with a low numerical aperture (NA) of 0.55 for minimizing the spherical aberration. The laser scanning is enabled by mounting the optical fiber on a computer-controlled *xyz* transition stage (H101A Pro Scan model, PSI) with a line scanning trajectory. Here, we have two schemes of laser scanning. Scheme 1 (scheme 2) refers to a focusing configuration that the laser propagation direction is perpendicular (parallel) to the fiber axis, respectively. The transition stage and the rotation motor can operate synchronously by computer control. The optical fibers adopted in this paper are commercial single-mode fibers (SMFs, Corning SMF-28e) and few-mode fibers (FMFs, YOFC-4). The pulse energy and scanning speed are set at appropriate parameters enabling a smooth writing of Type II nanogratings formation (typ. 1.2 μJ/pulse, 5 μm $s^{-1}$).

### *2.2 Retardance measurements*

FNGs own strong birefringence due to its inherent anisotropic periodic nanostructures (alternative nanoporous layers of lower refractive index[9]), which results in high optical retardance related to $R = (n_e - n_o) \cdot d$ when expressed in nanometers[14]. $d$ is the thickness of the birefringent layer whereas $n_{e/o}$ represents the refractive index of extraordinary/ordinary light (considering uniaxial materials in our case), respectively. Experimentally, a polarimetric microscope system (EXICOR Micro Imager) is used for quantitative retardance measurements. Considering the skin depth of the FNG samples, the light source of the crossed polarized microscope is set at blue light (475 nm). A charge coupled device (CCD) camera is used to record the intensity of the probe light and calculate the retardance distribution as well as slow axis distribution combined with two compensators.

### *2.3 Scanning electron microscopy (SEM) measurements*

Firstly, the cross-sections of the fs written FNG samples are polished and then etched by a hydrofluoric acid (HF) solution (1 vol%) for 80 s. Secondly, the etched samples are treated by ultrasonic cleaning for 10 mins and dried in the oven for 75 ℃, 20 mins. Afterwards, the

samples are metal-sprayed and then observed by a SEM (Nava NanoSEM 450) using the secondary electron field emission mode.

### *2.4 Mueller imaging characterizations*

Mueller matrix is deemed as one of the most efficient methods to unveil the overall polarimetric properties of the sample. Here, the measurement is demonstrated in a Mueller formalism instead of a Jones matrix because our fs written samples may contain some depolarization effect, in addition, it is more suitable since linear and circular anisotropic properties are co-existing[14]. The Mueller imaging system is constructed by a polarization state generator (PSG) consist of a half-wave plate (HWP), and a quarter-wave plate (QWP), FNG sample focusing and a polarization state analyzer (PSA) consist of a QWP and a HWP[28]. The probe light source is operated at 632 nm and a complementary metal-oxide-semiconductor transistor (CMOS) camera is utilized to record the 4×4 Mueller matrix. Then the obtained Mueller matrix is decomposed by using a logarithmic decomposition method[29,30] to "disentangle" all the anisotropic properties:

$$M_{dec} = \begin{bmatrix} 0 & LD & LD' & CD \\ LD & 0 & CB & -LB' \\ LD' & -CB & 0 & LB \\ CD & LB' & -LB & 0 \end{bmatrix} \quad (1)$$

More detailed information can be found in "supplementary materials". The obtained anisotropic optical properties include both linear optical properties: linear birefringence (LB), 45°-linear birefringence (LB'), linear dichroism (LD), 45°-linear dichroism (LD'), and circular optical properties: circular birefringence (CB), circular dichroism (CD).

## 3. Results

### *3.1 Manipulation of FNG orientations via laser polarization*

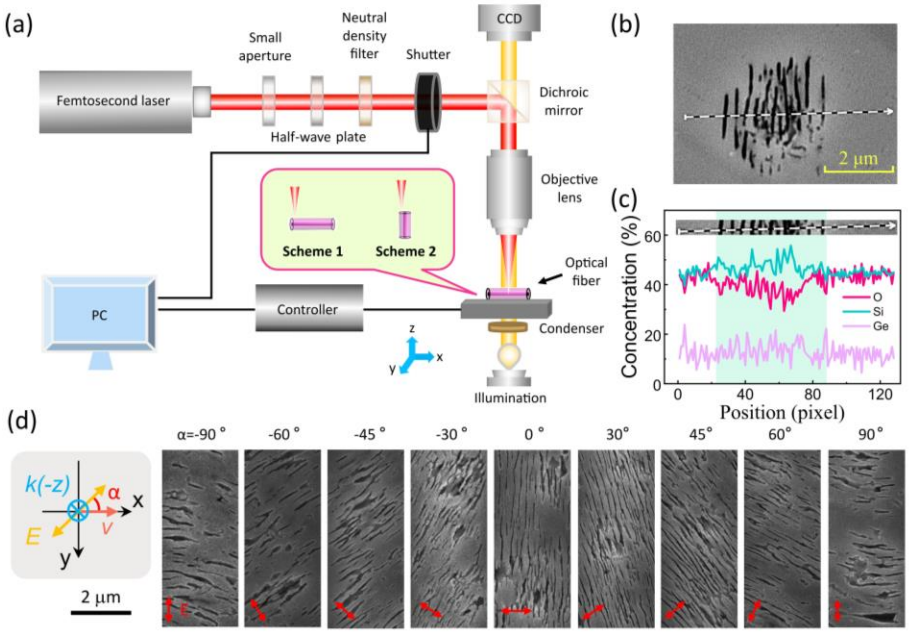


Fig. 1. Fs laser direct writing system, fs laser written FNGs, and the polarization dependence of fs written FNG orientation (scanning perpendicular to fiber axis). (a) Schematics of the fs laser writing system. Here, scheme 1 refers to a focusing configuration that the laser propagation direction is perpendicular to the fiber axis. Scheme 2 refers to a focusing

configuration that the laser propagation direction is parallel to the fiber axis. (b) SEM image of the fs written FNG in a few-mode fiber (YOFC-4) core by 1.2 μJ/pulse, 5 μm $s^{-1}$. Black-white-alternative arrow line: analytical region of the EDS measurement. (c) EDS measurement result of element distributions including Oxygen (O), Silicon (Si) and Germanium (Ge). (d) Polarization dependence of fs written FNG orientations observed in the plane perpendicular to laser propagation direction. FNGs are written in a few-mode fiber (YOFC-4) core with scheme 2, 1.2 μJ/pulse, 5 μm $s^{-1}$.

To impart the desirable manipulation of space variant FNGs, one should, at a first step, control the spatial distribution orientation of FNGs. In simple cases, fs laser written nanogratings are distributed perpendicular to the laser polarization direction, considering no tilt effect that could be caused by pulse front tilt (PFT) or stress effects [14,31,32]. Experimentally, the fs laser system is carried out to demonstrate FNG inscriptions inside optical fibers. **Figure. 1(b)** exhibits a typical FNG SEM image with a black-white-alternative arrow line, which indicates the analytical region of the energy dispersion spectrum (EDS) measurement. The EDS measurement is depicted in **Fig. 1(c)**. Obviously one can observe the irradiated region possesses three elements corresponding to the basic $GeO_2$-doped $SiO_2$ optical fibers. In the FNG region, the concentration of Silicon (Si) is less than that of Oxygen (O), while they are quite close in the non-irradiated region. Furthermore, the element distribution has a prominent variation that corresponds to the nano-lines distribution. This, in turn, indicates a conspicuous relationship showing that the element has been likely periodically modulated by fs laser irradiation.

*Towards FNG orientation manipulation in the plane perpendicular to laser propagation direction*: To investigate the polarization dependence of the FNG distribution with the observation plane perpendicular to laser wavevector direction, we tentatively employ a set of laser polarization evolution from $\alpha = -90°$ to $\alpha = 90°$ with a step of 30°. $\alpha$ is defined as the angle between x axis and the laser polarization direction. In addition, since $\alpha = -45°$ and $\alpha = 45°$ are quite unusual e.g., in implanting optical chirality inside transparent materials, they are also included here. Experimentally, the FNG orientations are well controlled by the laser polarization as they appear with an almost perpendicular connection.

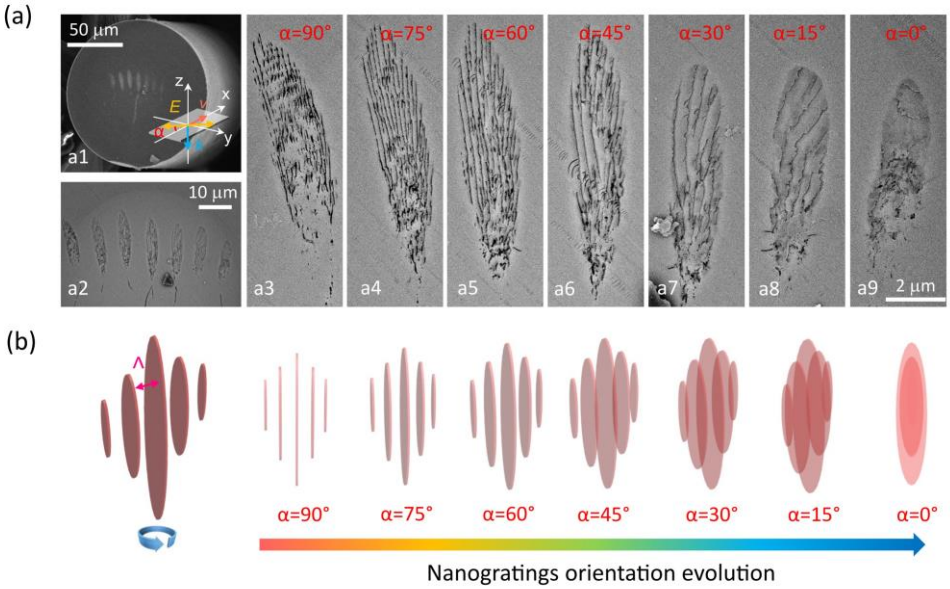


Fig. 2. Polarization dependence of fs written FNG orientation in the plane parallel to laser propagation direction. (a) SEM images of fs written FNGs by different laser polarizations. FNGs are written in a few-mode fiber (YOFC-4) core by scheme 1, 1.2 μJ/pulse, 5 μm $s^{-1}$:

Overview of the fiber cross-section (a1); observation of fiber core region (a2); detailed images of each FNG written by different laser polarizations (a3-a9). (b) Schematics of FNG orientation evolution controlled by laser polarization. Λ refers to the period of FNG.

*Towards FNG orientation manipulation in the plane parallel to laser propagation direction*: In addition, investigating the polarization dependence of the FNG distribution with the observation plane parallel to the laser wavevector direction is also essential for manipulating the orientation of the FNG. As depicted in **Fig. 2(a)**, obvious nanolayers (namely nano-lines) appear at a laser polarization of $\alpha = 90°$ and nano-planes emerge at a laser polarization of $\alpha = 0°$. Whereas at a laser polarization of around $\alpha = 45°$, there is a co-existence of nanolayers and nano-planes which shows the projection image of an out-of-plane structure. Note that one should observe some nanopores structures[9,12], however, here it is not clearly observed because the HF etching destroys the nanopores. Obviously, the experimental results show a good perpendicular relationship between laser polarization and FNG orientation.

### *3.2 Manipulation of retardances of FNGs via fs laser fluence*

Nanogratings that own an inherent periodic arrangement of nanolayers with a large refractive index contrast exhibit an obvious anisotropy, leading to strong negative linear birefringence and thus a related retardance[14]. Such a form birefringence makes nanogratings to be a useful strategy for birefringent device fabrications, which can be also integrated in optical fibers. Thus, investigating and tailoring both the retardance amplitude and its orientation lie on the core of unlocking the functionality of FNGs.

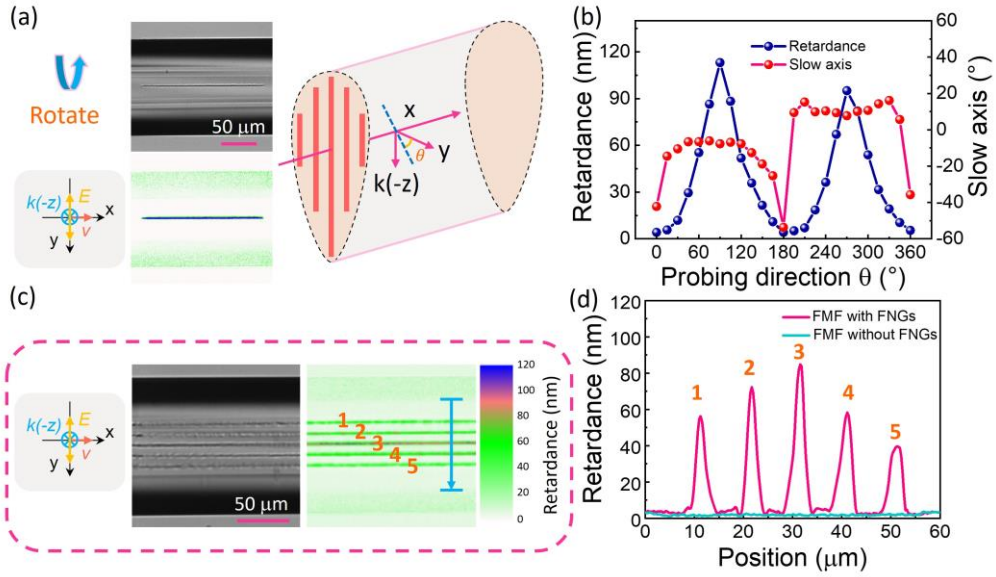


Fig. 3. Retardance and slow axis measurements of FNGs. (a) Microscope image (top) and crossed polarized microscope image (bottom) of a FNG sample written in a few-mode fiber (YOFC-4) core by scheme 1, 1.2 μJ/pulse, 5 μm $s^{-1}$. Illustration of rotating the FNG sample to achieve different probing direction (right). (b) Retardance and angle of slow axis of the investigated FNG sample distribution at different probing directions. (c) Microscope image (left) and crossed polarized microscope image (right) of five laser tracks (FNGs) written in different positions of a few-mode fiber (YOFC-4) by scheme 1, 1.2 μJ/pulse, 5 μm $s^{-1}$. Laser track 1 and 5: in fiber cladding; Laser track 2 and 4: at the border of fiber core and cladding; Laser track 3: in fiber core. Blue arrow shows the line scanning direction of retardance measurement. (d) Retardance distribution recorded by line scanning compared to a non-irradiated few-mode fiber.

Here, we use the crossed polarized microscope to identify the retardance as well as the slow axis of a FNG structure with different probing directions, as depicted in **Fig. 3(a)**. **Figure. 3(b)** shows the retardance and slow axis distribution obtained by rotating the fiber from $\theta = 0°$ to $\theta = 360°$. $\theta$ refers to the angle between probe direction and the y axis (perpendicular to FNG orientation) as shown in the right schematic picture of **Fig. 3(a)**. Obviously depicted in **Fig. 3(b)**, the retardance achieves maximum values at 90° and 270° because the probe light propagation direction is along the nanolayers (nano-lines). Whereas the retardance achieves minimum values at 0° (360°) and 180° because the probe light propagates through a set of nano-planes which can be deemed as isotropic layers as a first approximation (assuming a random distribution of spherical nanopores). Furthermore, the slow axis shows three values over a 360° fiber rotation. Firstly, the slow axis is measured to be non-significant values (here around -45°) at 0° (360°) and 180° due to a nearly zero linear birefringence. Secondly, the slow axis achieves around -10° (theoretically it should be 0°) from 15° to 165°, which means the sample is a little tilted in the measuring process. Further, the slow axis measured to be 10° from 195° to 345° well confirms the tilt of the sample and more importantly, the anisotropic orientation of FNGs.

**Figure. 3(c)** depicts the microscope image of five laser tracks written in a few-mode fiber. Besides, the retardances are quantitatively recorded in **Fig. 3(d)**. Firstly, the FNGs exhibit large retardance compared to non-irradiated few-mode fibers. Furthermore, the retardance of the central laser track has a higher value, which could be attributed to (1) a shorter periodicity of nanogratings and higher porosity filling factor[33]; (2) the higher Ge-doping in the fiber core, inducing more defect centers to the $SiO_4$ random networks[34], which lower the band gap of the fiber core material and thus result in a lower threshold of multi-photon ionization[27].

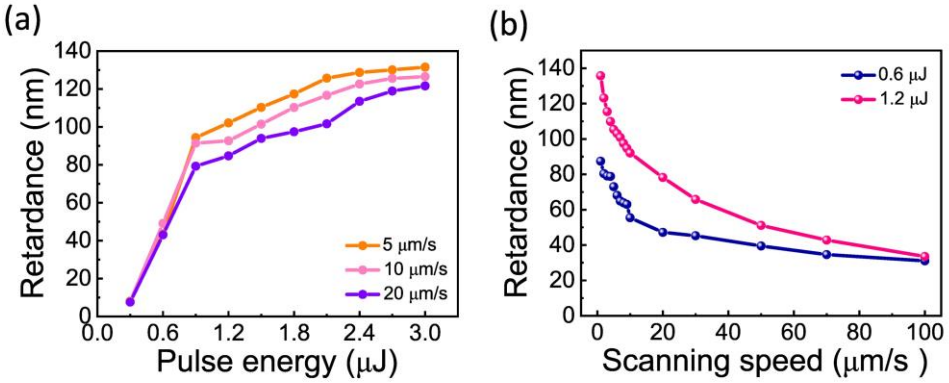


Fig. 4. Tailoring of retardance of FNGs by laser fluence. (a) Retardance evolutions at different laser pulse energies for scanning speeds of 5 μm $s^{-1}$, 10 μm $s^{-1}$ and 20 μm $s^{-1}$. (b) Retardance evolutions at different scanning speeds for laser pulse energies of 0.6 μJ and 1.2 μJ. FNGs are written in the few-mode fiber (YOFC-4) core by scheme 1.

Experimentally, one can demonstrate the tailoring of retardances of written FNGs by controlling the laser fluence, namely manipulating pulse energy or scanning speed. This is depicted in **Figure. 4(a)** and **4(b)** respectively. Normally, within smooth Type II nanogratings window, higher pulse energy allows a high energy deposit inside the transparent material while lower scanning speed leads to a shorter period of nanogratings and a higher porosity filling factor, which both result in a stronger linear birefringence and thus the related retardance.

### *3.3 Anisotropic optical properties of FNGs*

Since nanogratings own anisotropic sub-wavelength structures, FNGs are expected not only to possess anisotropic linear optical properties, but also remarkable circular ones due to an optical symmetry breaking. According to the "two-layer model" proposed in our previous work[14], the circular optical properties are originated from a chiral combination of form birefringence contribution and stress related birefringence contribution. Thus, one can set two linear retarders to predict the circular birefringence of FNGs. Here, we only take circular birefringence as a representative chiral optical property. Thus, only the linear birefringence property is considered in the linear retarder because the circular birefringence only originates from the chiral combination of linear birefringence. The Mueller matrix of the linear retarder can be expressed as:

$$M_{LR}(R) = \begin{bmatrix} 1 & 0 & 0 & 0 \\ 0 & 1 & 0 & 0 \\ 0 & 0 & cos\,(R) & sin\,(R) \\ 0 & 0 & -sin\,(R) & cos\,(R) \end{bmatrix} \tag{2}$$

$R$ refers to the retardance expressed in rad, which correlates to the linear birefringence. The circular birefringence consists of a form birefringence and a stress related birefringence with their neutral axes non-parallel and non-perpendicular. For sake of large asymmetry, we set an angle of 45° between the slow axes of these two linear retarder layers. Thus, we can simply define a 45° slow axis of form birefringence layer and 0° slow axis of stress layer. Therefore, the Mueller matrix of the first linear retarder (refers to form birefringence) and the Mueller matrix of the second linear retarder (refers to stress related birefringence) can be obtained:

$$M_{form} = M_r(-45°) \cdot M_{LR}(R_1) \cdot M_r(45°) \tag{3}$$

$$M_{stress} = M_{LR}(R_2) \tag{4}$$

Here, $M_r$ is the rotation matrix and can be expressed as:

$$M_r(\alpha) = \begin{bmatrix} 1 & 0 & 0 & 0 \\ 0 & cos\,(2\alpha) & sin\,(2\alpha) & 0 \\ 0 & -sin\,(2\alpha) & cos\,(2\alpha) & 0 \\ 0 & 0 & 0 & 1 \end{bmatrix} \tag{5}$$

Finally, the collective Mueller matrix of the whole structure can be calculated by:

$$M = M_{stress} \cdot M_{form} \tag{6}$$

Thus, with a logarithmic decomposition method introduced in "*2.4 Mueller imaging characterizations*" section, we can obtain the circular birefringence. According to previous investigations [14,27] and the experiment results of FNGs, the retardance values of form birefringence and stress related birefringence are set as -0.75 rad and 0.55 rad, respectively. The final circular birefringence is calculated to be 0.204 rad.

Experimentally, a Mueller imaging polarimeter is used to investigate all the anisotropic optical properties as depicted in **Fig. 5**. Specifically, eight FNGs are imprinted in a few-mode fiber core with a focusing configuration of scheme 2 and a polarization of 45° one by one by rotating the fiber. These FNGs are then characterized by a Mueller polarimeter, as shown in **Fig. 5(a)**. A non-inscribed few-mode fiber is also investigated for sake of comparison. The whole Mueller matrices of few-mode fibers cross-sections with and without FNG inscriptions are depicted in **Fig. 5(b)** and **Fig. 5(c)**, respectively. Obviously, the Mueller matrix images of FNGs show different behavior compared to the non-inscribed fiber. Moreover, **Fig. 5(d)** exhibits a comparison between microscope images and the Mueller matrix $M_{22}$ elements of few-mode fibers cross-sections both with and without FNG inscriptions, respectively. Obviously, the $M_{22}$ element of FNG inscriptions exhibits large values with different signs and amplitudes whereas the $M_{22}$ element of non-inscriptions exhibits a nearly zero value. Here, one element of Mueller matrix can only tell the difference, however, it is not enough to extract the polarimetric properties of the sample. Thus, the whole Mueller matrix is then decomposed by a logarithmic method as described in "*2.4 Mueller imaging characterizations*" section. An average circular birefringence value of 0.21 rad probed at 632 nm is observed, as

shown in **Fig. 5(e)**, which is quite close to the predict one (0.204 rad) with theoretical calculation. This result is the first report of a circular optical property imprinted through a FNG structure, to the best of our knowledge.

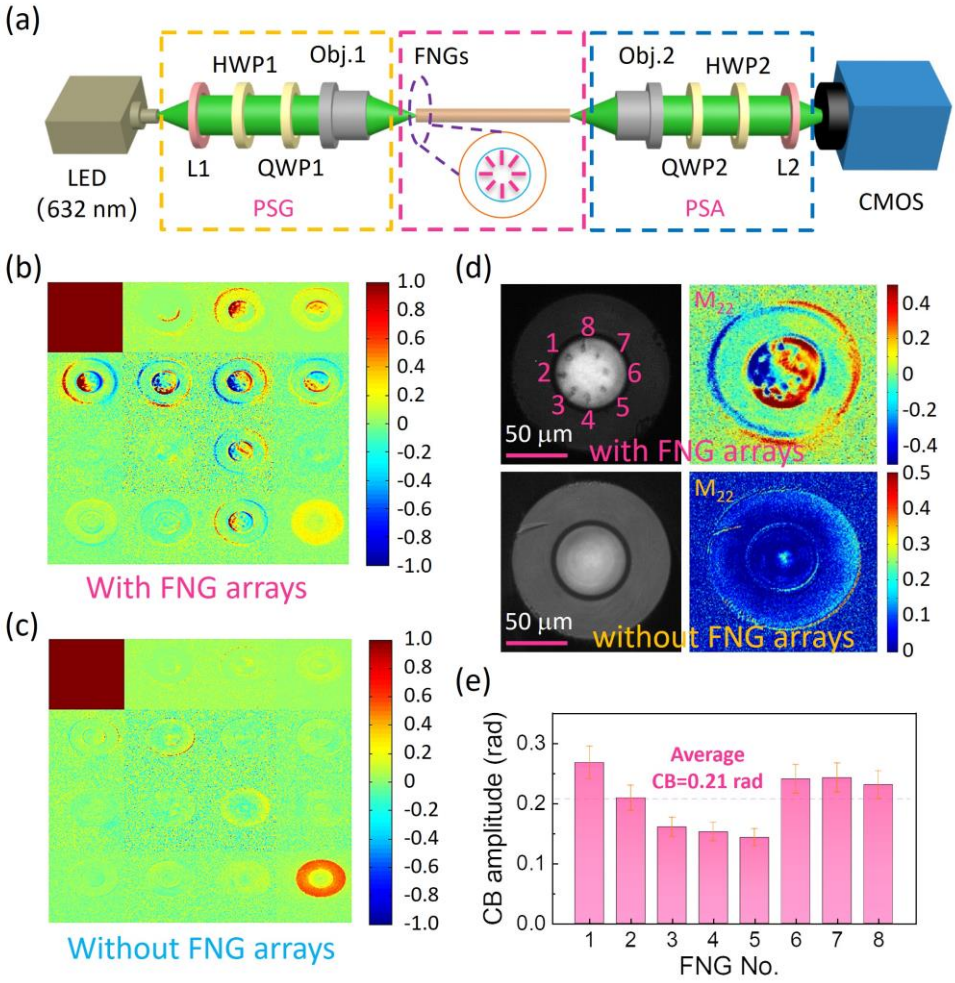


Fig. 5. Characteristics of anisotropic optical properties of FNGs by Mueller formalism. (a) Schematics of the Mueller polarimeter: LED: light emitting diode; L1,2: lens; HWP1,2: half-wave plate; QWP1,2: quarter-wave plate; Obj.1,2: objective; FNG: fiber nanograting; CMOS: complementary metal-oxide-semiconductor transistor camera; PSG: polarization state generator; PSA: polarization state analyzer. Full Mueller matrices of few-mode fiber cross-sections with (b) and without (c) FNG arrays imprinted. (d) Microscopic images (left) and Mueller element $M_{22}$ images (right) of few-mode fiber cross-sections with (above) and without (below) FNG arrays imprinted. (e) CB values of each FNG (labeled in the microscopic image with FNGs of (d)) obtained by Mueller matrix decomposition using a logarithmic method. FNGs are written by scheme 2 and a 45° polarization with each FNG laser track to achieve the large asymmetry.

### *3.4 3D tailoring of space variant FNGs*

Due to the interesting optical properties of FNGs, their flexible manipulation in space will definitely extend the functionality of FNG-based technologies. To imprint such space variant FNGs, the half-wave plate located in fs laser system was computer-controlled with a specific function of time. In other words, the laser polarization can be accurately adjusted during laser

scanning and thus the imprinted FNG distributions. Following this approach, space variant FNGs with any distribution can be obtained.

Experimentally, 90 μm-long laser tracks are written by fs laser pulses scanning by scheme 2, 1.2 μJ/pulse, 5 μm $s^{-1}$ with simultaneous polarization evolution e.g., rotation. **Figure. 6(a)** shows an overview of a single-mode fiber cross-section with several scanning lines of space variant FNGs. Note that the scanning direction perpendicular to the fiber axis is only an easy-obtain configuration for cross-section observation. However, one can utilize an arbitrary scanning direction e.g., along fiber axis (so-called z-scan method) to obtain a space variant FNG evolving along the fiber itself, which can, for instance, fabricate a 3D structured "twisted nanogratings" along the fiber axis that is similar to our previous work in silica glass (but with different strategy)[35].

In **Fig. 6(b)**, both clockwise and anticlockwise evolutions of FNG distribution are demonstrated by rotating the half-wave plate at a constant speed of 10° $s^{-1}$. Thus, due to a 5 μm $s^{-1}$ scanning speed, the FNG orientation rotates from 0° to 180°. Besides, using a 20° $s^{-1}$ speed allows a rotation of FNG orientation from 0° to 360° as depicted in **Fig. 6(c)**. Here, a slight difference of the FNG morphology between clockwise and anticlockwise is mainly attributed to (1) a difference caused in the polishing process (polishing depth and polishing quality); (2) a difference of HF etching effect. Obviously, the FNGs evolve continuously following the expected design, which can be further exploited to construct an arbitrary space variant FNG.

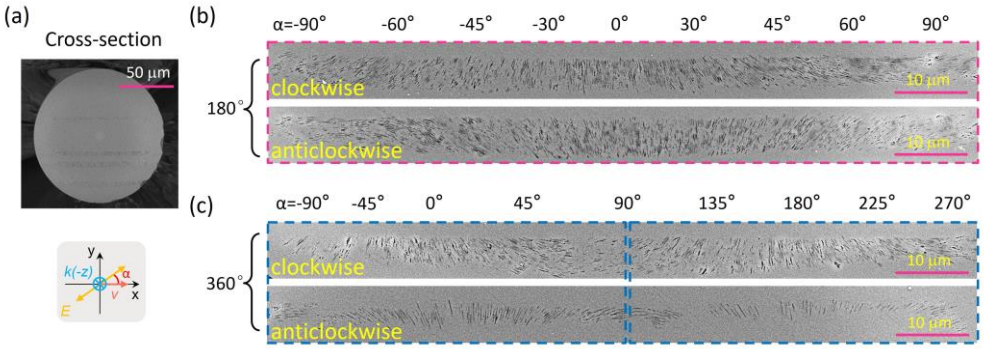


Fig. 6. Space variant FNGs within a line scanning geometry. (a) A SEM image of a single-mode fiber cross-section profile with several line scanning laser tracks of space variant FNGs, combined with laser scanning configuration schematics below. (b) SEM images of 180° rotation of FNGs with both clockwise (above) and anticlockwise (below) evolutions enabled by rotating the half-wave plate at a constant speed of 10° $s^{-1}$. (c) SEM images of 360° rotation of FNGs with both clockwise (above) and anticlockwise (below) evolutions enabled by rotating the half-wave plate at a constant speed of 20° $s^{-1}$. Samples are written in a single-mode fiber by scheme 2, 1.2 μJ/pulse, 5 μm $s^{-1}$.

Furthermore, one can also control the scanning along any directions to construct more complex distributions of FNGs as shown in **Fig. 7**. For instance, **Fig. 7(a)**, **7(b)** and **7(c)** show octagon configurations with different FNG orientations of each side. Besides, one can expect to use a spiral trajectory scanning, instead of polygon configuration, combined with simultaneous polarization evolution to smooth the shape of the FNG structure and thus the effect of optical field manipulations. Additionally, square-like distributions and line arrays with different FNG orientations are also validated by different laser polarizations as shown in **Fig. 7(d)**, **7(e)** and **7(f)**, respectively. This kind of FNG-based complex structures around fiber core is promising in vectorial manipulation of fiber modes by evanescent field interaction. Furthermore, by utilizing the circular birefringence property, space variant fiber nanogratings arrays show great potentials in precisely controlling the linear polarization

rotation of the guiding mode inside fiber core at different positions. This can be further used to create chiral light beams with complex polarization distributions.

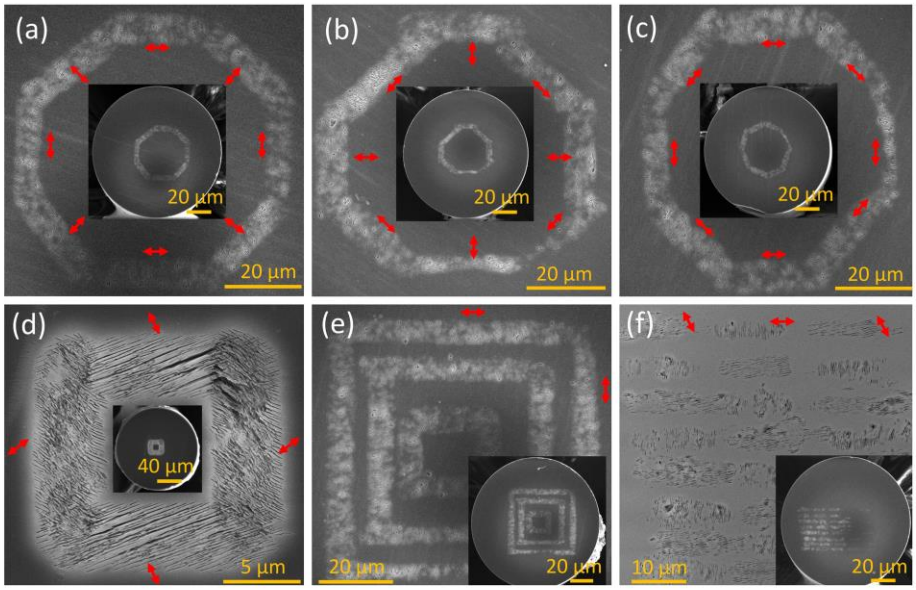


Fig. 7. SEM images of space variant FNGs within complex scanning geometries. (a-c) Octagon configurations with different FNG orientations of each side. (d) Square configuration with different FNG orientations of each side. (e) Square arrays configuration with different FNG orientations of each side. (f) Line arrays configuration with different FNG orientations of each line. Red arrows refer to laser polarization direction. Samples are written in few-mode fibers by scheme 2, 1.2 μJ/pulse, 5 μm $s^{-1}$.

## 4. Discussion and Conclusion

*Origin of element distribution:* Although the origin of nanograting formation is still under discussion, nanopores are proved to exist in nanolayers and play an essential role in nanograting formation. The case appears as well in FNG structures. From experimental EDS result depicted in **Fig. 1(c)**, the Oxygen element exhibits lower concentration in the FNG region. This can be interpreted by the Oxygen migration from lattice to form Oxygen molecules in nanoporous regions, which is located in nanolayers. However, nanolayers are more sensitive to HF etching, which is related to the formation of nanoporous layers with stoichiometrically less silica around nanopores (a large amount of oxygen deficient centers is formed together with nanopores filled with molecular $O_2$).

*Effect of pulse front tilt (PFT):* Anyhow, the orientation of FNG is mainly determined by the laser polarization however a PFT can lead to some deviations. At the focus of the fs light, the spatial chirp caused by the misalignment of the compressor, angular dispersion and PFT grow exponentially and thus can attribute to "quill writing" and anisotropic photo-sensitive absorption[36–38]. However, it can only lead to few degrees tilt of nanolayer orientation at a hundred fs/mm[31]. Thus, controlling FNG orientation using PFT is not obvious and lack of flexibility.

*Controlling the propagating light in fibers by FNGs:*

(1) FNGs that own strong birefringent effect can be exploited for polarization control of propagating light in optical fibers. For instance, FNGs written by appropriate laser parameters can possess a quarter-wave retardance of a targeted wavelength light. Theoretically, this kind of quarter-wave plate can transform the propagating linearly polarized light to be a circularly

polarized light or more generally an elliptically polarized light. Moreover, a space variant FNG or a FNG array can achieve the continuous manipulation of the propagating light both in transverse plane and even along the propagating axis. For example, one can employ a slow axis rotating space variant FNGs with quarter-wave retardance along the fiber axis to generate a novel elliptically polarized light with ellipticity-evolution in the fiber, which is highly flexible.

(2) FNGs are strongly anisotropic nanostructures, which exhibit obvious polarization dependent loss property namely apparent linear or even circular dichroism. Such an effect is useful for fabricating in-line polarizers[27] and even promisingly, vectorial optical field manipulation. Since a single FNG can ensure a high transmittance according to its distribution orientation, a FNG array that includes several FNGs with different orientations can expectedly select a certain vectorial light mode from a hybrid mode of the propagating light.

(3) The chiral optical properties observed here for the first time in a FNG structure are useful for controlling the optical phase of circularly polarized lights. More importantly, circular birefringence possesses inherent optical rotation property that can directly rotate the plane of polarization of light whatever the orientation angle between incoming light polarization and neutral axis of the FNG structure. This effect can be efficiently exploited for in-line linearly polarization rotator, passive fiber isolators and other chiral devices. Compared to traditional optical rotators such as half-wave plates and Faraday rotator, FNG-based rotators are more compact, passive (no need for magnetic field) and less sensitive to the misalignment.

(4) Normally, a FNG structure exhibits non-negligible optical loss mostly due to the Rayleigh scattering from its intrinsic nano-porous nature, which owns a $1/\lambda^4$ relationship[14,39]. However, one can organize the FNG arrays around the fiber core namely, imprinting FNGs in the cladding to ensure an ultralow optical loss and manipulate the propagating light via evanescent field. In addition, a Type X writing strategy can also partly or totally solve this issue owning to its ultrahigh transmittance at the expense of a lower retardance, which was recently studied by Kazansky group [16,40,41].

*Tailoring the Retardance spectral dependence:* The retardance $R = (n_e - n_o) \cdot d$ generated in this paper is above 100 nm, it can be utilized as a quarter-wave plate targeting to a visible light e.g., 400-500 nm for blue light. However, this is not suitable for propagating in a single-mode fiber or few-mode fiber as they are usually designed for near infrared light. Expectedly, there are many strategies to create more retardance in FNG: (1) using higher deposited energy to get a higher $(n_e - n_o)$; (2) using lower NA focal lenses or a multilayers approach to imprint a thicker $d$. Therefore, we can achieve the desired functionality in the near infrared range such as within C-band.

In summary, a full control of 3D FNG orientation distribution is demonstrated by manipulating the fs laser polarization[35]. Both linear optical property (linear birefringence and related retardance) and circular optical property (circular birefringence) are investigated. More importantly, both complex scanning and functionalized polarization manipulation construct space variant FNGs during the laser writing process. Our work provides a wide point of view of tailoring 3D space variant FNGs and may open new possibilities in FNG-based technologies such as, complex in-line birefringent devices fabrication, fiber rotators and isolators, vector modes converters and laser manufacturing in “lab-in-fiber” and “lab-on-fiber” systems.

**Funding.** Science and Technology Commission of Shanghai Municipality (STCSM) (No. 20JC1415700); National Natural Science Foundation of China (NSFC) (12274281, 61635006); China Scholarship Council (CSC) (202006890077) and 111 Project (No. D20031)

**Acknowledgments.** Xianglong Zeng acknowledges the Program for Professor of Special Appointment (Eastern Scholar) at Shanghai Institutions of Higher Learning.

**Disclosures.** The authors declare no conflicts of interest.

**Data availability.** Data underlying the results presented in this paper are available from corresponding author.

## References


[1] M. Juhl, J.P.B. Mueller, K. Leosson, Metasurface Polarimeter on Optical Fiber Facet by Nano-Transfer to UV-Curable Hybrid Polymer, IEEE J. Sel. Top. Quantum Electron. 25 (2019) 4500107. https://doi.org/10.1109/JSTQE.2019.2893757.

[2] M. Malinauskas, A. Žukauskas, S. Hasegawa, Y. Hayasaki, V. Mizeikis, R. Buividas, S. Juodkazis, Ultrafast laser processing of materials from science to industry, Light Sci. Appl. 5 (2016) e16133.

[3] Y. Shimotsuma, M. Sakakura, P.G. Kazansky, M. Beresna, J. Qiu, K. Miura, K. Hirao, Ultrafast manipulation of self-assembled form birefringence in glass, Adv. Mater. 22 (2010) 4039–4043. https://doi.org/10.1002/adma.201000921.

[4] K. Sugioka, Y. Cheng, Ultrafast lasers-reliable tools for advanced materials processing, Light Sci. Appl. 3 (2014) e149. https://doi.org/10.1038/lsa.2014.30.

[5] F. Zhang, Z. Nie, H. Huang, L. Ma, H. Tang, M. Hao, J. Qiu, Self-assembled three-dimensional periodic micro-nano structures in bulk quartz crystal induced by femtosecond laser pulses, Opt. Express. 27 (2019) 6442. https://doi.org/10.1364/oe.27.006442.

[6] Y. Shimotsuma, P.G. Kazansky, J. Qiu, K. Hirao, Self-organized nanogratings in glass irradiated by ultrashort light pulses, Phys. Rev. Lett. 91 (2003) 247405. https://doi.org/10.1103/PhysRevLett.91.247405.

[7] R. Buschlinger, S. Nolte, U. Peschel, Self-organized pattern formation in laser-induced multiphoton ionization, Phys. Rev. B. 89 (2014) 184306. https://doi.org/10.1103/PhysRevB.89.184306.

[8] A. Rudenko, J.P. Colombier, T.E. Itina, Nanopore-mediated ultrashort laser-induced formation and erasure of volume nanogratings in glass, Phys. Chem. Chem. Phys. 20 (2018) 5887–5899. https://doi.org/10.1039/c7cp07603g.

[9] M. Lancry, B. Poumellec, J. Canning, K. Cook, J.C. Poulin, F. Brisset, Ultrafast nanoporous silica formation driven by femtosecond laser irradiation, Laser Photon. Rev. 7 (2013) 953–962. https://doi.org/10.1002/lpor.201300043.

[10] E. Bricchi, B.G. Klappauf, P.G. Kazansky, Form birefringence and negative index change created by femtosecond direct writing in transparent materials, Opt. Lett. 29 (2004) 119–121. https://doi.org/10.1364/ol.29.000119.

[11] C. Hnatovsky, R.S. Taylor, E. Simova, P.P. Rajeev, D.M. Rayner, V.R. Bhardwaj, P.B. Corkum, Fabrication of microchannels in glass using focused femtosecond laser radiation and selective chemical etching, Appl. Phys. A Mater. Sci. Process. 84 (2006) 47–61. https://doi.org/10.1007/s00339-006-3590-4.

[12] Y. Wang, M. Cavillon, J. Ballato, T. Hawkins, T. Elsmann, M. Rothhardt, R. Desmarchelier, G. Laffont, B. Poumellec, M. Lancry, 3D laser engineering of molten core optical fibers: toward a new generation of harsh environment sensing devices, Adv. Opt. Mater. 10 (2022) 2200379. https://doi.org/10.1002/adom.202200379.

[13] B. Poumellec, M. Lancry, R. Desmarchelier, E. Hervé, B. Bourguignon, Parity violation in chiral structure creation under femtosecond laser irradiation in silica glass?, Light Sci. Appl. 5 (2016) e16178. https://doi.org/10.1038/lsa.2016.178.

[14] J. Lu, J. Tian, B. Poumellec, E. Garcia-caurel, R. Ossikovski, X. Zeng, M. Lancry, Tailoring chiral optical properties by femtosecond laser direct writing in silica, Light Sci. Appl. 12 (2023) 46. https://doi.org/10.1038/s41377-023-01080-y.

[15] T. Meany, M. Gräfe, R. Heilmann, A. Perez-Leija, S. Gross, M.J. Steel, M.J. Withford, A. Szameit, Laser written circuits for quantum photonics, Laser Photonics Rev. 9 (2015) 363–384. https://doi.org/10.1002/lpor.201500061.

[16] H. Wang, Y. Lei, L. Wang, M. Sakakura, Y. Yu, G. Shayeganrad, P.G. Kazansky, 100-layer error-free 5D optical data storage by ultrafast laser nanostructuring in glass, Laser Photon. Rev. 16 (2022) 2100563. https://doi.org/10.1002/lpor.202100563.

[17] A. Crespi, R. Osellame, L. Sansoni, P. Mataloni, F. Sciarrino, R. Ramponi, Fabrication of Quantum Photonic Integrated Circuits by Means of Femtosecond Laser Pulses, Found. Phys. 44 (2014) 843–855. https://doi.org/10.1007/s10701-014-9800-6.

[18] A. Ricciardi, M. Consales, G. Quero, A. Crescitelli, E. Esposito, A. Cusano, Lab-on-Fiber devices as an all around platform for sensing, Opt. Fiber Technol. 19 (2013) 772–784. https://doi.org/10.1016/j.yofte.2013.07.010.

[19] T. Geernaert, K. Kalli, C. Koutsides, M. Komodromos, T. Nasilowski, W. Urbanczyk, J. Wojcik, F. Berghmans, H. Thienpont, Point-by-point fiber Bragg grating inscription in free-standing step-index and photonic crystal fibers using near-IR femtosecond laser, 2010.

[20] C. Hnatovsky, D. Grobnic, D. Coulas, M. Barnes, S.J. Mihailov, Self-organized nanostructure formation during femtosecond-laser inscription of fiber Bragg gratings, Opt. Lett. 42 (2017) 399–402. https://doi.org/10.1364/ol.42.000399.

[21] A. Yan, S. Huang, S. Li, R. Chen, P. Ohodnicki, M. Buric, S. Lee, M.J. Li, K.P. Chen, Distributed Optical Fiber Sensors with Ultrafast Laser Enhanced Rayleigh Backscattering Profiles for Real-Time Monitoring of Solid Oxide Fuel Cell Operations, Sci. Rep. 7 (2017) 9360. https://doi.org/10.1038/s41598-017-09934-3.

[22] H. Craighead, Future lab-on-a-chip technologies for interrogating individual molecules, Nature. 442 (2006) 387–393.

[23] M. Principe, M. Consales, A. Micco, A. Crescitelli, G. Castaldi, E. Esposito, V. La Ferrara, A. Cutolo, V. Galdi, A. Cusano, Optical fiber meta-tips, Light Sci. Appl. 6 (2017). https://doi.org/10.1038/lsa.2016.226.
[24] M. Zou, C. Liao, S. Liu, C. Xiong, J. Zhao, Z. Gan, Y. Chen, K. Yang, D. Liu, Y. Wang, Y. Wang, Fiber-tip polymer clamped-beam probe for high-sensitivity nanoforce measurements, Light Sci. Appl. 10 (2021) 171.
[25] M. Haque, K.K.C. Lee, S. Ho, L.A. Fernandes, P.R. Herman, Chemical-assisted femtosecond laser writing of lab-in-fibers, Lab Chip. 14 (2014) 3817–3829. https://doi.org/10.1039/c4lc00648h.
[26] J. Lu, E. Garcia-Caurel, R. Ossikovski, F. Courvoisier, X. Zeng, B. Poumellec, M. Lancry, Femtosecond laser direct writing multilayer chiral waveplates with minimal linear birefringence, Opt. Lett. 48 (2023) 271–274. https://doi.org/10.1364/ol.479447.
[27] J. Lu, Y. Dai, Q. Li, Y. Zhang, C. Wang, F. Pang, T. Wang, X. Zeng, Fiber nanogratings induced by femtosecond pulse laser direct writing for in-line polarizer, Nanoscale. 11 (2019) 908–914. https://doi.org/10.1039/c8nr06078a.
[28] C. Wang, S. Zhang, Q. Yu, L. Li, Measurement of physical polarization parameters by system estimation, J. Mod. Opt. 60 (2013) 1869–1877. https://doi.org/10.1080/09500340.2013.865088.
[29] R. Ossikovski, Differential matrix formalism for depolarizing anisotropic media, Opt. Lett. 36 (2011) 2330–2332. https://doi.org/10.1364/ol.36.002330.
[30] R. Ossikovski, O. Arteaga, Statistical meaning of the differential Mueller matrix of depolarizing homogeneous media, Opt. Lett. 39 (2014) 4470–4473. https://doi.org/10.1364/ol.39.004470.
[31] Y. Dai, J. Ye, M. Gong, X. Ye, X. Yan, G. Ma, J. Qiu, Forced rotation of nanograting in glass by pulse-front tilted femtosecond laser direct writing, Opt. Express. 22 (2014) 28500–28505. https://doi.org/10.1364/oe.22.028500.
[32] Y. Bellouard, A. Champion, B. McMillen, S. Mukherjee, R.R. Thomson, C. Pépin, P. Gillet, Y. Cheng, Stress-state manipulation in fused silica via femtosecond laser irradiation, Optica. 3 (2016) 1285–1293. https://doi.org/10.1364/optica.3.001285.
[33] M. Lancry, J. Canning, K. Cook, M. Heili, D.R. Neuville, B. Poumellec, Nanoscale femtosecond laser milling and control of nanoporosity in the normal and anomalous regimes of GeO2-SiO2 glasses, Opt. Mater. Express. 6 (2016) 321–330. https://doi.org/10.1364/ome.6.000321.
[34] J.X. Wen, W.Y. Luo, Z.Y. Xiao, T.Y. Wang, Z.Y. Chen, X.L. Zeng, Formation and conversion of defect centers in low water peak single mode optical fiber induced by gamma rays irradiation, J. Appl. Phys. 107 (2010) 044904. https://doi.org/10.1063/1.3273363.
[35] J. Lu, M. Hassan, F. Courvoisier, E. Garcia-Caurel, F. Brisset, R. Ossikovski, X. Zeng, B. Poumellec, M. Lancry, 3D structured Bessel beam polarization and its application to imprint chiral optical properties in silica, APL Photonics. 8 (2023) 060801. https://doi.org/10.1063/5.0140843.
[36] P.G. Kazansky, W. Yang, E. Bricchi, J. Bovatsek, A. Arai, Y. Shimotsuma, K. Miura, K. Hirao, "Quill" writing with ultrashort light pulses in transparent materials, Appl. Phys. Lett. 90 (2007) 12–15. https://doi.org/10.1063/1.2722240.
[37] B. Poumellec, M. Lancry, R. Desmarchelier, E. Hervé, F. Brisset, J.C. Poulin, Asymmetric orientational writing in glass with femtosecond laser irradiation, Opt. Mater. Express. 3 (2013) 1586–1599. https://doi.org/10.1364/ome.3.001586.
[38] P.G. Kazansky, Y. Shimotsuma, M. Sakakura, M. Beresna, M. Gecevičius, Y. Svirko, S. Akturk, J. Qiu, K. Miura, K. Hirao, Photosensitivity control of an isotropic medium through polarization of light pulses with tilted intensity front, Opt. Express. 19 (2011) 20657. https://doi.org/10.1364/oe.19.020657.
[39] J. Tian, R. Li, S.H. Yoo, B. Poumellec, E. Garcia-Caurel, R. Ossikovski, M. Stchakovsky, C. Eypert, J. Canning, M. Lancry, Spectral dependence of femtosecond laser induced circular optical properties in silica, OSA Contin. 2 (2019) 1233–1242. https://doi.org/10.1364/osac.2.001233.
[40] M. Sakakura, Y. Lei, L. Wang, Y.H. Yu, P.G. Kazansky, Ultralow-loss geometric phase and polarization shaping by ultrafast laser writing in silica glass, Light Sci. Appl. 9 (2020) 15. https://doi.org/10.1038/s41377-020-0250-y.
[41] Y. Lei, G. Shayeganrad, H. Wang, M. Sakakura, Y. Yu, L. Wang, D. Kliukin, L. Skuja, Y. Svirko, P.G. Kazansky, Efficient ultrafast laser writing with elliptical polarization, Light Sci. Appl. 12 (2023) 74. https://doi.org/10.1038/s41377-023-01098-2.

## V.4 CONCLUSION

This Chapter develops around the main topic of fs laser direct writing fiber nanograting structures in/on the tip of silica fibers for endowing controllable anisotropic optical properties such as linear birefringence and circular birefringence. This idea combines the fiber compatibility and functional fabrication to form a new platform of integrated devices in fiber optics.

In order to validate the conception to construct this innovative functional in/on-fiber devices, the first step locates at the complete control of the nanograting structure, e.g., its orientation, retardance, circular optical properties. Therefore, we have experimentally characterized the performances of fiber nanogratings by utilizing SEM, polarimetric microscopy, Mueller polarimeter, etc. Based on these results, we have obtained some important conclusions:

1. Fiber nanogratings can exhibit dual-period distribution under appropriate parameters, which can be interpreted by an asymmetric local enhancement of the plasma spheres. Fiber nanogratings also show good continuous distribution and erasure rewriting, which are potential in high-dimensional data storage.
2. Fiber nanogratings located in fiber core owns a higher retardance than ones in fiber cladding. This could be attributed to the small-amount Ge-doping in the fiber core that leads to a shorter nanograting period and a higher porosity filling factor.
3. Benefit from the Mueller polarimeter, small depolarizing effects and strong chiral optical properties are detected. Especially for the circular birefringence, it is a discovery which could be a beginning for more functional devices enabled by tailoring chiral optical properties.
4. In-line polarizers based on fiber nanogratings pave the way for a new kind of integrated polarizer fabrication method with broadband responses and ultralow losses.
5. Besides, space variant tailoring of fiber nanogratings is promising for the future nano/micro-structures integration in “Lab-in/on-fiber” systems.

Fs laser writing fiber components is not fundamentally new since fs

laser writing long-period fiber gratings, FBGs or some micro cavities are developed as a mature and sometimes commercial technology. However, fiber nanogratings that correspond to structures at nanoscale level with unique anisotropic optical properties, could lead the fs writing in fibers to a new level with more complex but useful properties.

# Chapter.VI FEMTOSECOND LASER WRITTEN CHIRALITY IN SILICA: MECHANISMS AND STRATEGIES

## VI.1 INTRODUCTION

The discovery that fs lights can directly induce chirality inside silica materials is a milestone because it is a chirality creation by the interaction between two achiral objects, namely an achiral light and an achiral material [14]. However, the subsequent question is to figure out the origin of the chirality formation. The first concern is based on the light twisting the material by a volume torque. But no evidence directly shows the existence of this kind of torque or other micromechanical force to indeed reshape the atomic arrangement in the molecules. In addition, the light induced chirality exhibits a high value of circular birefringence above our expectation, which also leads us to another tentative explanation: an extrinsic chirality imprinted by fs laser lights.

In the first section of this Chapter, we present a published paper in ***Light Science & Applications*** in 2023. In this paper, we tentatively proposed a new conceptional view that the fs light induced chirality is an extrinsic chirality that originates from a chiral arrangement of linear optical properties. Thus, it is an optical chirality and shows a stronger circular optical property than an intrinsic chirality (molecular chirality) can do. Specifically, this chiral arrangement is realized by the coexistence of form birefringence and stress-induced birefringence with non-parallel and non-perpendicular neutral axes. By conceiving a simple but powerful two-layers model based on Mueller formalism, this assumption is well confirmed by the numerical simulation. Besides, the investigations of polarization dependence of both the circular optical properties and the two contributions (form birefringence and stress related birefringence) are also strong evidence of this origin of fs light induced chirality. After revealing the origin of this optical chirality and taking profit of the proposed two-layers model, we are able to tailor the chiral optical properties of fs written structures inside optical glasses.

As an easy-obtain approach, a multilayer strategy can be directly utilized to construct controllable circular optical properties by designable chiral arrangement of the multilayer structures. Thus, in the second section of this Chapter, we present a published paper in ***Optics Letters*** in 2023. This method is capable of ultrahigh circular optical properties when compared to molecular chirality due to its larger scale and programming of 3D "helix-like" chiral structures. Surprisingly, with an appropriate design of a four-layers structure, we are able to achieve a chiral waveplate with strong circular birefringence (in fact it can achieve arbitrary phase difference between $-\pi$ and $\pi$) with suppressed linear birefringence close to zero. This result is important in chiral waveplate manufacturing because it can almost remove the perturbation caused by the linear optical properties.

After the understanding of chiral light field manipulation mechanism and the origin of light induced chirality in materials, we delivered a fundamentally novel idea to transfer the chirality of structured chiral light field to the silica materials via fs laser direct writing. This work is related to a published work in ***APL Photonics*** in 2023. Experimentally, we combine a polarization distribution control of the fs laser beam by a space variant birefringent waveplate and an axicon focusing technique to generate a chiral Bessel beam with the linear polarization orientation slightly rotating along the optical path in the Bessel core. This is a kind of "helical polarized" beam and can directly imprint "twisted nanograting" structures in silica glasses without a scanning. Such a twisted nanograting owns strong circular optical properties due to its inherent chiral distribution in 3D, which confirms the chirality transfer from light to matter.

## VI.2 TAILORING CHIRAL OPTICAL PROPERTIES BY FEMTOSECOND LASER DIRECT WRITING IN SILICA

Official journal of the CIOMP 2047-7538
www.nature.com/lsa

ARTICLE Open Access

# Tailoring chiral optical properties by femtosecond laser direct writing in silica

Jiafeng Lu[1,2], Jing Tian[1], Bertrand Poumellec[1], Enrique Garcia-Caurel[3], Razvigor Ossikovski[3], Xianglong Zeng[2] and Matthieu Lancry[1]✉

**Abstract**

An object that possesses chirality, that is, having its mirror image not overlayed on itself by rotation and translation, can provide a different optical response to a left- or right-handed circular polarized light. Chiral nanostructures may exhibit polarization-selective optical properties that can be controlled for micro-to-nano optical element engineering. An attractive way to induce such complex nanostructures in three-dimension in glass is femtosecond laser direct writing. However, the mechanism of femtosecond laser induced chirality remains to be unveiled due to complex physical and chemical processes occurring during the ultrashort light-matter interaction. Here, a phenomenological model is proposed and is built on two-layers phase shifters to account for this laser-induced optical chirality in an initially achiral material (silica glass). This model is based on the observation that femtosecond laser induced nanogratings own two principal contributions to its aggregate birefringent response: a form and a stress-related one. By refining this formalism, a multilayer approach is developed to imprint on demand optical rotation. Values up to +/-60° at 550 nm within an optimal 80 µm thickness in silica glass are possible, corresponding to the highest value in a glass to date. These results provide new insights of circular-optical control in micro-nano optical manufacturing and open new opportunities for photonics applications.

## Introduction

From fundamental physics of light-matter interaction to fabrication of targeted optical properties in highly complex optical engineering, femtosecond (fs) laser plays a key role in laser manufacturing. Ultrashort light pulses can precisely deposit light energy in a given transparent material volume by controllable focusing conditions. Nonlinear absorption of high-density photon energy leads to the creation of free electrons plasma within few fs, that is before the electron-phonon energy transfer to the lattice (typ. >10 ps in silica). Thus, at low repetition rate, the glass network heating is decoupled from light exposure and from the plasma itself, which enables localized modifications or even breakdown without surrounding damage. Such nonlinear processes contribute to multiple types of modifications according to laser parameters: (1) an isotropic average index variation (Type I); (2) anisotropic subwavelength nanogratings yielding to high form birefringence (Type II); (3) micro/nano voids due to localized micro-explosions (Type III)[1]. To date, these fs laser-induced modifications have found many applications in most branches of nonlinear science, ranging from plasma physics and nano-photonics to material science, bio-photonics and quantum information science[2,3].

Recent progress highlights that a fs laser beam (axially symmetric intensity distribution, linear polarized with orthogonal incidence) can create optical chirality inside an achiral material through a laser direct writing within Type II regime[4–6]. This concept shed light on a new approach for tailoring chiral optical properties in three dimensional (3D) providing a wider landscape of laser manufacturing.

Correspondence: Matthieu Lancry (matthieu.lancry@universite-paris-saclay.fr)
[1]Institut de Chimie Moléculaire et des Matériaux d'Orsay, Université Paris Saclay, Orsay 91405, France
[2]Key Laboratory of Specialty Fiber Optics and Optical Access Networks, Joint International Research Laboratory of Specialty Fiber Optics and Advanced Communication, Shanghai Institute for Advanced Communication and Data Science, Shanghai University, Shanghai 200444, China
Full list of author information is available at the end of the article

A prerequisite to exploit such new potentials is to elucidate the mechanism how one can manipulate these chiral optical properties. As a first model Poumellec et al.[6] suggested that the breaking of symmetry arises from a volume torque due to the combined action of a stress field and a direct current (DC) electric field. This torque is the source of the chirality originating from pulse front tilt (PFT), focusing conditions and laser polarization. The misalignment between DC electric field $\vec{E}_{DC}$ and the material polarization field $\vec{P}$ generates a volume torque $\vec{P}\Lambda\vec{E}_{DC}$. Its orientation and sign are controllable and may twist the matter to create chiral atomic arrangements. Although the quenched glass network records evidence of a part of molecular activities during the light-matter interaction, the origin of this optical chirality imprinting remains unknown. There is no information to support if the observed circular properties and related optical rotation originate from a laser-induced molecular optical activity such as for sucrose or α-quartz with its chiral lattice arrangement i.e., a so-called intrinsic chirality.

However, if we transfer the concept from molecular activity to optical fundamentals, it can lead to another plausible explanation, that is, circular optical properties can originate from several internal linear birefringence and dichroism contributions with non-parallel, non-perpendicular eigen axes[7] i.e., an extrinsic chirality[8]. Typically, fs laser irradiation in silica glass can result in a Type II modification with nanograting structures and associated mechanical stress at appropriate laser parameters. These nanogratings mainly exhibit an obvious structural anisotropy resulting in a strong uniaxial negative form birefringence[9]. The origin of this anisotropic optical property lies on the subwavelength regular arrangement of nanolayers with a refractive index contrast. It is the specific morphology of nanogratings firstly carried out by Shimotsuma et al. in 2003 that leads to the exciting development of both physical research and practical applications of fs laser induced nanogratings[10]. In addition, irradiation of silica glass in this regime results to a net volume expansion[11], which correlates with the formation of porous nanolayers inside the nanogratings[12,13]. This, in turn, creates a significant birefringence due to the photoelastic tensor of glass. Several teams[14–16] have highlighted the presence of such stress fields within both Type I and Type II regimes. Following this view, we propose here that fs laser induced circular optical properties could originate from the concomitant contributions of a form birefringence and a stress-induced birefringence.

In this paper we tentatively "disassemble" the dependence of the form and stress contributions with respect to the laser polarization direction. In a simple view, the slow/fast axis of the form birefringence is controlled by the laser polarization direction and the related retardance amplitude by the laser fluence. In addition, the polarization dependence of the stress-induced birefringence is investigated through a simple approach based on stress-engineered waveplates as described in previous works[15,17]. A two-layers model is then developed based on Mueller formalism to quantitatively explain the creation of both linear and circular anisotropic optical properties. Finally, we exploit this model to engineer chiral optical properties following two different designs, namely multilayer "nanogratings based waveplates" and "stress-engineered waveplates". The following results provide the evidence that the origin of fs laser induced circular properties includes two contributions and propose a strategy for tailoring chiral optical properties in any glasses by fs laser direct writing.

## Results

### Writing polarization dependence of fs laser induced chiral optical properties

The proposed concept that the Type II nanostructures written by fs laser consists of two contributions (form birefringence and stress birefringence) is schematically shown in Fig. 1a. In the following it is further experimentally demonstrated by fs laser direct writing homogeneous squares made of a set of lines inside bulk silica glass, using appropriate laser parameters within the Type II processing window (more details can be found in "Materials and methods section").

To characterize the overall anisotropic optical properties after fs irradiation, one can use Mueller spectropolarimetry in transmission mode and related definitions namely: linear birefringence (LB), 45°-linear birefringence (LB'), total linear birefringence (TLB), linear dichroism (LD), 45°-linear dichroism (LD'), total linear dichroism (TLD), circular birefringence (CB), and circular dichroism (CD). Since, it is more practical in polarimetry, all these properties are described as linear (or circular) phase difference in this paper. All the definitions, descriptions and units are depicted in Table 1. In addition, since CB will effectively rotate the plane of polarization, we can define an optical rotation $\theta_{rot}$ in degrees. Note that optical activity is mostly used for describing intrinsic chirality but CB and optical rotation are more general and thus more appropriate for this paper. Finally, CD is defined as the difference of absorptions between left- and right-handed circular polarized beams and can result in an elliptical light polarization.

Transmission electron microscope (TEM) analysis confirm that nanogratings are formed by the alternation of "uniform" and nanoporous glass layers, as depicted in Fig. 1a$_1$ and Fig. 1a$_2$. The nanoporous areas represent the nanoplanes that have been cleaved in their plane, the areas between them appearing black are areas that, although having been irradiated, have remained dense[18].

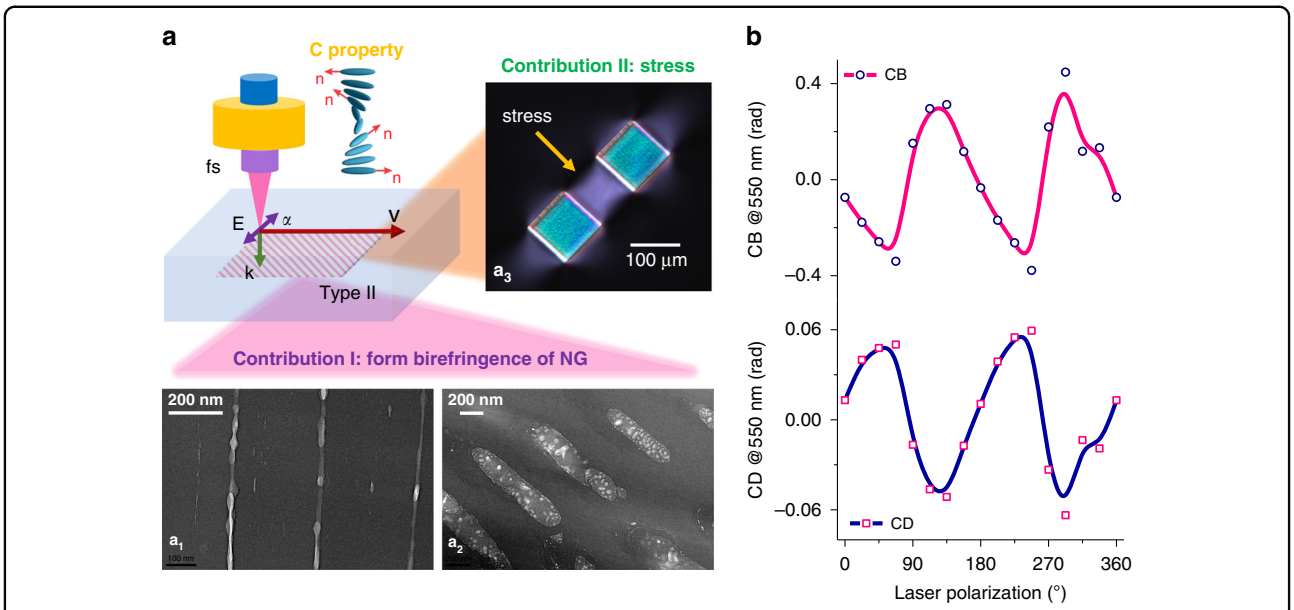


**Fig. 1 Fs laser induced circular properties and their contributions. a** Conceptual scheme of fs laser inscription of nanogratings possessing circular properties with two contributions; TEM images of nanogratings with cleaving perpendicular ($a_1$) and parallel ($a_2$) to the laser propagation direction; ($a_3$) crossed polarizers microscope image of a stress-engineered waveplate between two irradiated zones (called stress bars). **b** CB (upper) and CD (below) evolutions according to laser polarization. Measurements are done at 550 nm

**Table 1 Linear and circular optical properties**

| Property | Definition | Commonly described in polarimetry | Unit |
|---|---|---|---|
| LB (linear birefringence) | $\Delta n_L = (n_x - n_y)$ | $LB = \frac{2\pi}{\lambda}(n_x - n_y)\cdot d$ | radians |
| LB′ (45°-linear birefringence) | $\Delta n_{L'} = (n_{45°} - n_{-45°})$ | $LB' = \frac{2\pi}{\lambda}(n_{45°} - n_{-45°})\cdot d$ | radians |
| TLB (total linear birefringence) | $\Delta n_{TLB} = (n_e - n_o)$ *< for a uniaxial material >* | $TLB = \sqrt{LB^2 + LB'^2}$ | radians |
| TLB fast axis angle | *Lower refractive index axis* | $\theta_B = \frac{1}{2}\cdot arctan\left(\frac{LB}{LB'}\right)$ | degrees |
| LD (linear dichroism) | $\Delta\kappa_L = (\kappa_x - \kappa_y)$ | $LD = \frac{2\pi}{\lambda}(\kappa_x - \kappa_y)\cdot d$ | radians |
| LD′ (45°-linear dichroism) | $\Delta\kappa_{L'} = (\kappa_{45°} - \kappa_{-45°})$ | $LD' = \frac{2\pi}{\lambda}(\kappa_{45°} - \kappa_{-45°})\cdot d$ | radians |
| TLD (total linear dichroism) | $\Delta\kappa_{TLD} = (\kappa_{high} - \kappa_{low})$ | $TLD = \sqrt{LD^2 + LD'^2}$ | radians |
| TLD fast axis angle | *Lower attenuation axis* | $\theta_D = \frac{1}{2}\cdot arctan\left(\frac{LD}{LD'}\right)$ | degrees |
| CB (circular birefringence) | $\Delta n_C = (n_- - n_+)$ | $CB = \frac{2\pi}{\lambda}(n_- - n_+)\cdot d$ | radians |
| Optical rotation | / | $\theta_{rot} = \frac{\pi}{\lambda}(n_- - n_+)\cdot d\cdot\frac{180°}{\pi}$ | degrees |
| CD (circular dichroism) | $\Delta\kappa_C = (\kappa_- - \kappa_+)$ | $CD = \frac{2\pi}{\lambda}(\kappa_- - \kappa_+)\cdot d$ | radians |

$n_{[]}$: refractive index; $\kappa_{[]}$: absorption index; $d$: thickness of anisotropic layer; $\lambda$: probe light wavelength; *x*: *x* axis; *y*: *y* axis; *e*: extraordinary light; *o*: ordinary light; "-": left-handed; "+": right-handed

The net volume expansion, induced by the formation of these nanopores, creates a strong compressive stress field in and around the irradiated zone. Such effect is clearly visible from Fig. 1$a_3$.

To explore the underpinning mechanisms yielding to chiral optical properties and their relationships with laser parameters, the effect of laser polarization dependence is investigated firstly. Experimentally, a set of different laser polarization directions are adopted to imprint a set of milimeter size homogeneous samples with keeping fixed all other parameters. Figure 1b exhibits the laser polarization dependence of CB and CD of the fs laser-irradiated $SiO_2$ samples, measured at the probe light wavelength of 550 nm. The maximum CB (or CD) can be observed from X + 45° writing configuration (linear polarization azimuth $\alpha$ = 45°, 135°, 225° and 315°). However, there is almost no CB (or CD) when the polarization is along $\alpha$ = 0°, 90°, 180° and 270°. In addition, anisotropic circular

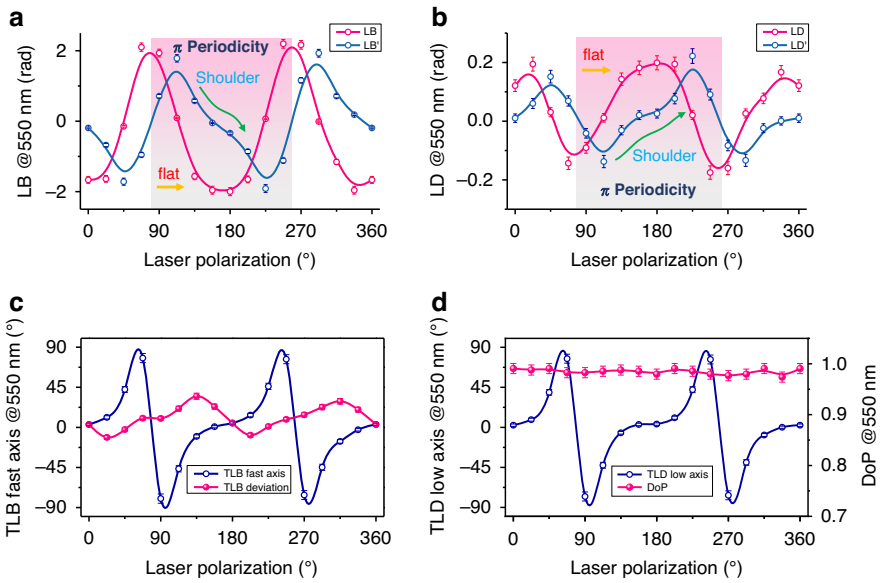


**Fig. 2 Laser polarization dependence of anisotropic properties of fs laser irradiated $SiO_2$ sample. a** LB and LB' evolutions according to laser polarization. **b** LD and LD' evolutions according to laser polarization. **c** TLB fast axis evolution and its deviation (its difference compared to laser polarization $\alpha$, $-90° <$ deviation $\leq 90°$). **d** TLD "low attenuation axis" evolution and the degree of polarization (DoP). **e** SEM images of fs laser irradiated region using a X + 45° writing configuration. Measurements are done at the wavelength of 550 nm

properties exhibit a non-symmetric angular response with a 180° periodic dependence at different azimuth $\boldsymbol{\alpha}$ (with respect to the scanning direction that was chosen along x-axis i.e., 0°).

### Writing polarization dependence of the form birefringence, $LB_{form}$

Fs laser written nanogratings exhibit a linear birefringence that is strongly related to the laser polarization[9]. Note that if the samples are solely made of a birefringent layer whose orientation is linearly dependent of the laser polarization (that is, "ideal nanogratings" with neither tilt nor stress effect on their orientation), both LB and LB' functions will be perfectly periodic with a 45° shift with respect to each other. It is worth noting that when neutral axis of the birefringence is parallel/perpendicular to x (or y) axis, the LB comes to be 0 but LB' reaches maximum whereas the TLB remains almost constant. However, as shown in Fig. 2a, a LB deviation is observed from an ideal sinusoidal shape, exhibiting a "flat zone" around 180°. Following the same trend, LB' owns a periodic modulo 180° evolution, but its angular response also deviates from sinusoidal shape and presents a "shoulder" around 180°±22°. Besides, the LD and LD' show similar results as shown in Fig. 2b.

To figure out the inner mechanism of these irregularities with respect to the linear polarization azimuth, both TLB fast axis and its deviation (its difference compared to $\boldsymbol{\alpha}$) are displayed in Fig. 2c. Similar results, from the TLD "low attenuation axis" are shown in Fig. 2d. For completeness, the degree of polarization (DoP) measured at 550 nm is included and appears larger than 98% revealing a quite negligible depolarization in the investigated spectral range. Finally Fig. 2e shows typical SEM (scanning electron microscope) micrographs of the fs laser track (written nanogratings) using a X + 45° configuration. This configuration gives the opportunity to observe not only regularly spaced nanolayers but also their intrinsic nanoporous nature in a single image. The laser track appears quite homogeneous, and its typical length is around 40 µm.

### Writing polarization independence of the stress-induced birefringence, $LB_{stress}$

For crystalline materials amorphized by fs laser irradiation, it is possible to observe a guiding zone in the surrounding region having undergone compressive mechanical stresses all around the irradiated zone, which exhibits a volume expansion[11]. Similar results have been demonstrated in silica glass within the Type II regime (i.e., nanogratings formation)[14]. When a stress load is applied to a material, the latter develops a linear birefringence according to the photoelastic effect. To perform stress profile measurements, Champion et al. have used fs laser-written specific design and derived an equation to model the stress field accordingly[11]. Their results indicate that the amplitude of the compressive stress should depend on the nanolayers orientation with respect to the writing direction[14] but not the stress orientation[18].

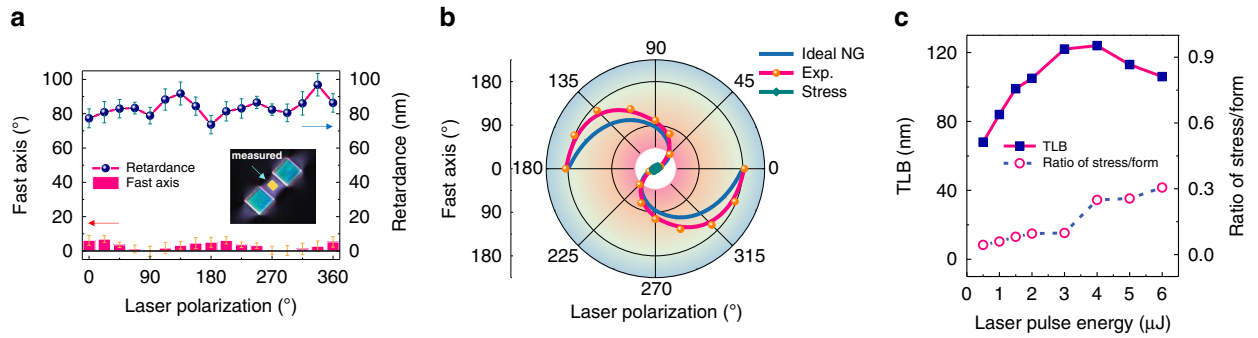


**Fig. 3 Laser polarization independence of stress-induced birefringence. a** $LB_{stress}$ fast axis orientation and retardance according to the laser polarization direction; inset refers to the crossed polarizers microscope image of the stress bars (in blue) creating a pure stress zone with the mark of the measured area (the 0° reference is the direction of the written lines i.e., along x axis). **b** TLB fast axis direction evolutions of "ideal nanogratings" (blue), measured fs laser-induced nanogratings (pink) and pure stress (green) versus laser polarization direction. **c** Evolutions of TLB and $LB_{stress}/LB_{form}$ ratio at different laser pulse energies. All measurements are done at 550 nm

Thus, to experimentally investigate such effects we designed a set of dedicated samples (see experimental details in "Materials and methods section"). This is exemplified in Fig. 1$a_3$ inset where the crossed polarizers image reveals the formation of birefringence not only within the two irradiated areas (blue interference color) but also in-between these two stress bars and around which is attributed to mechanical stress[15]. The measurements of both its related retardance and fast axis to the laser polarization azimuth $\boldsymbol{\alpha}$ are shown in Fig. 3a. We could confirm that the fast/slow axis direction is primarily determined by the writing geometry and does not depend on the laser writing polarization as a first approximation (excepted at the edges of the written lines where the slow axis is azimuthally distributed[14]). Thus, for single lines or superposition of lines, there is a quasi-uniaxial loading along the line and the fast axis direction of the stress-induced birefringence is parallel to the lines for volume expansion[11]. In other words, whether the laser writing polarization is aligned along x or y, the fast/slow axis orientation of the stress-induced birefringence remains unchanged. However, there exists a slight perturbation of the retardance function that indicates a variation of the birefringence amplitude within 20% in agreement with ref. [14]. For completeness, the fast axis orientation is found to deviate by a maximum of 8° from the line direction especially when the nanolayers are perpendicular to the scanning direction. This deviation could be caused by a non-uniform stress field distribution across the sample thickness[17] since there is no compensation for spherical aberration.

Figure 3b summarizes evolutions, as a function of laser polarization, of (1) the fast axis for "ideal nanogratings" (a form birefringence with nanolayers perpendicular to laser polarization), (2) experimental Type II nanogratings, and (3) a pure stress zone. The stress related data are close to the center of the polar plot, which indicates a laser polarization independence of $LB_{stress}$ orientation as discussed above. The measured fast axis of the nanogratings possesses an obvious deviation compared to the theory for "ideal nanogratings". Furthermore, we have tentatively decoupled the $LB_{form}$ contribution from the one coming from stress. The measured TLB and $LB_{stress}/LB_{form}$ ratio according to the laser pulse energy are shown in Fig. 3c. Here, as a simplified approach, "X + 45°" configuration is used to ensure that the measured LB mostly originates from stress-induced birefringence whereas the measured LB' comes from the form birefringence. It is worth pointing out that $LB_{stress}$ contributes from 5% up to 30% when increasing the energy. Within the experimental conditions (1030 nm, 250 fs, 1.5 μJ/pulse), $LB_{stress}$ contributes around 10% to the overall birefringence TLB, which is in good agreement with the thermal stability of TLB[15] (also reproduced for comparison in Fig. 5e).

## A simple but powerful two-layers quantitative model

### *Overview of the model*

In this section, a two-layers model is proposed to reveal the inner mechanism of the fs laser-induced circular optical properties as shown in Fig. 4a. To obtain a robust understanding of the circular optical properties imprinting, this model is constructed in the Mueller formalism instead of Jones matrix, because (1) the light is partially polarized after passing through the laser irradiated area and (2) it is more suitable when all properties are coexisting. The main hypothesis is built on the basis of the propagation of light in inhomogeneous media composed of anisotropic linear layers. In a simple view, every "interaction volume" in the irradiated area is considered to have two linear contributions, which are finally "sumed" through Mueller formalism.

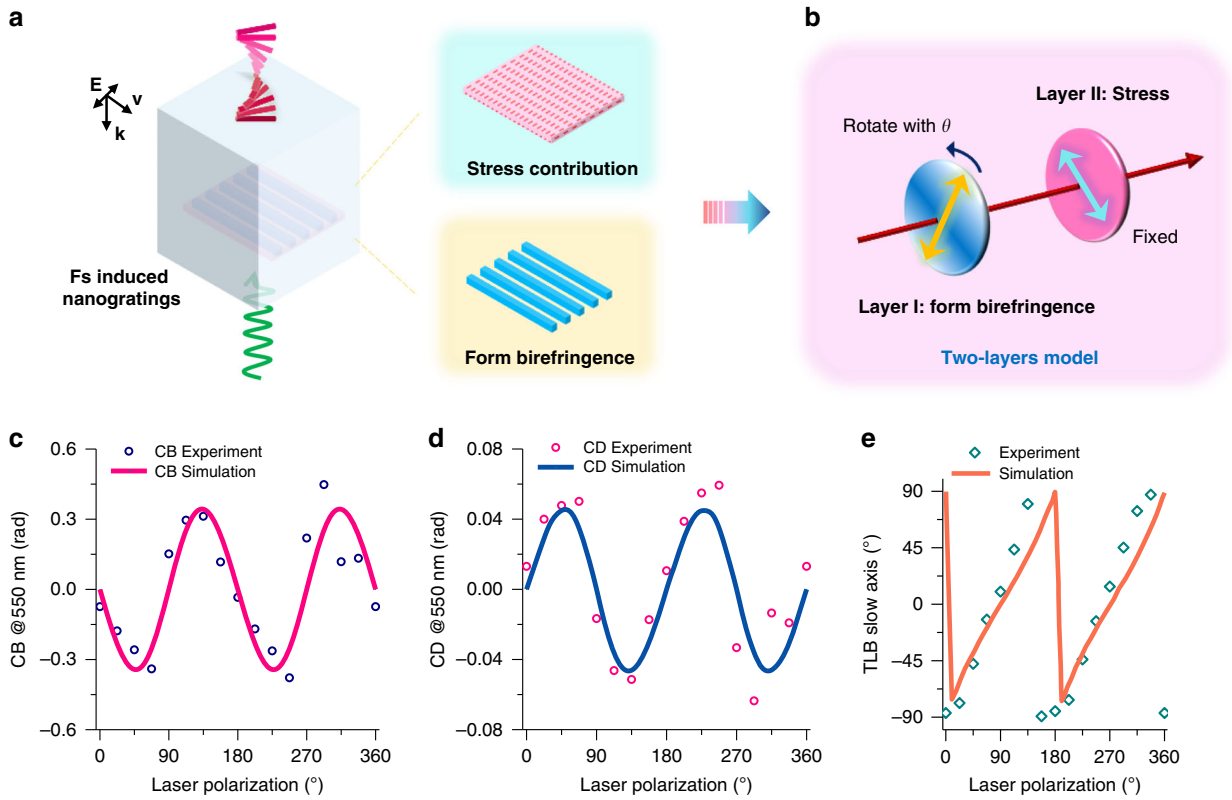


**Fig. 4 The two-layers model and the simulation results. a** The schematic of the two contributions that lead to the laser induced circular optical properties. **b** The schematic of two-layers model consists of two linear retarders. Simulated evolutions according to laser polarization compared with experimental results for CB (**c**), CD (**d**) and TLB slow axis (**e**). Calculations and measurements are done at 550 nm

In the following, we consider the case of two layers with linear anisotropic optical properties, and whose neutral axis orientations may be different, as depicted in Fig. 4b. This fulfills the minimum condition to create an object exhibiting both linear and circular properties (not entangled or entangled depending on the type of decomposition applied). As a direct consequence, the CB would originate from several (at least 2) internal LB contributions with both non-parallel and non-perpendicular neutral axes[7]. Similarly, CD band would result from the cumulative action of LD and LB present in respectively two different layers, also having non-parallel and non-perpendicular neutral axes. Following this model, the amplitude of the observed CD and CB will not only be related to the LD or LB optical phase shift of each contribution, but also to the misalignment between their respective neutral axes.

### *Mathematical description*

It is recalled that the anisotopic properties are associated with a potentially attenuating phase shifter (dichroic) and therefore contain a linear birefringence term LB and a linear dichroism term LD, both expressed in radians unit. In the Mueller formalism chosen here, the optical phase shifter MDR (a linear retarder) is written according to the following relation:

$$MDR(R, P_{si}) = \begin{bmatrix} 1 & -\cos(2P_{si}) & 0 & 0 \\ -\cos(2P_{si}) & 1 & 0 & 0 \\ 0 & 0 & \sin(2P_{si}) \cdot \cos(R) & \sin(2P_{si}) \cdot \sin(R) \\ 0 & 0 & -\sin(2P_{si}) \cdot \sin(R) & \sin(2P_{si}) \cdot \cos(R) \end{bmatrix} \quad (1)$$

where $R$ is the linear phase shift (corresponds to TLB when expressed in radians, here we assume the fast axis along to 0° so that TLB is equal to LB) and $P_{si}$ translates the di-attenuation (or dichroism) property of the phase shifter (corresponds to TLD when expressed in radians). Note that a zero linear dichroism corresponds to a value of $P_{si} = \pi/4$. The angle $\theta_{1,2}$ is defined as the angle between the fast axis of the layer (layer 1 and layer 2, respectively) and the x-axis of the benchmark of the laboratory (defined by the laser compressor plane). After determining the Mueller matrix $M$ corresponding to the assembly of these two phase shifters as shown in Eq. (2), the resulting matrix can be formally decomposed by exploiting the logarithmic approach developped by Ossikovski et al.[19]. Here, $M_R$ represents the rotation matrix. The effective anisotropic optical properties then

can be extracted from the modeled medium.

$$\boldsymbol{M} = \left[\boldsymbol{M_R}(\theta_2)\cdot \boldsymbol{MDR}\left(2^{\boldsymbol{nd}}\ \boldsymbol{layer}\right)\cdot \boldsymbol{M_R}(-\theta_2)\right] \cdot \left[\boldsymbol{M_R}(\theta_1)\cdot \boldsymbol{MDR}(1^{\boldsymbol{st}}\ \boldsymbol{layer})\cdot \boldsymbol{M_R}(-\theta_1)\right] \quad (2)$$

### *Physical origin of the two layers*

Correspondingly, one of the two phase shifters will be representative of the form birefringence attributed to ideal nanogratings (i.e., no tilt, no stress effect on their orientation) and thus exhibits a strong uniaxial negative linear birefringence as reported by Bricchi et al. [9] and a non-zero "apparent" linear dichroism related to anisotropic light scattering. Note that LD is attributed to nanopores formation and their arrangement in nanolayers (positive for Xx writing, negative for Xy writing) so it is not directly related to the birefrigence through a Kramers-Kronig relationship. As the angle between the laser polarization and the writing direction is changing during the writing process (different laser polarization configurations), the direction $\theta_1$ of the fast axis has to be varied accordingly. The second phase shifter is attributed to the presence of a stress-induced birefringence (but no LD) that will guide us in the definition of its properties, of which the amplitude is lower (typically an order of magnitude) than the first layer. This model may seem very simplistic, however, it retains the essential physics to represent the results because it takes into account the more likely sources of birefringence: $LB_{form}$ and $LB_{stress}$, as shown in Fig. 4b.

### *Exploiting the two-layers model*

Quantatively, the value of the parameters $(\boldsymbol{R}, \boldsymbol{P_{si}})$ adopted were adjusted on our experimental results. Generally, the first layer representing the form contribution of nanogratings is assigned at $-\pi/2$ for the parameter $R_1$ related to the TLB i.e., a delay of $\lambda/2$ with a fast axis aligned along x (for example 275 nm at the wavelength of 550 nm) and 0.70 rad for the parameter $\boldsymbol{P_{si1}}$ related to the TLD. Concerning the second layer, a typical value of 0.44 rad is found for the parameter $R_2$ and $\pi/4$ for the parameter $\boldsymbol{P_{si2}}$ corresponding to no dichroism. The first layer will rotate linearly with the $\boldsymbol{\alpha}$ orientation of the laser polarization, that is, $\theta_1 = \alpha$. In contrast, the stress layer is proved to be laser polarization independent (see Fig. 3a). Therefore, the fast axis angle is parallel (respectively slow axis is perpendicular) to the laser scaning direction (here, it is along x axis) and thus $\theta_2 = 0°$. Now the Mueller matrix of the model can be simplifed to be:

$$\boldsymbol{M} = \boldsymbol{MDR}\left(2^{\boldsymbol{nd}}\ \boldsymbol{layer}\right)\cdot \left[\boldsymbol{M_R}(\theta_1)\cdot \boldsymbol{MDR}(1^{\boldsymbol{st}}\ \boldsymbol{layer})\cdot \boldsymbol{M_R}(-\theta_1)\right] \quad (3)$$

Consequently, CB and CD polarimetric results computed by employing the Mathcad© software are shown in Fig. 4c and Fig. 4d, respectively. Obviously, the simulation accounts for the experimental results quite well. Apparently, CB and CD both exhibit a $\pi$ period with the polarization azimuth $\alpha$ (with respect to the scanning direction i.e. along x axis). We demonstrate here that CB arises from a combined effect of the $LB_{form}$ and $LB_{stress}$ contributions with non-parallel and non-perpendicular eigen axes. In the meanwhile CD comes from a combined effect of the LD (co-existing with the $LB_{form}$ in the 1st layer) and the $LB_{stress}$ with non-parallel and non-perpendicular eigen axes. Furthermore, CB and CD approach the maximum value when the angular misalignment between the two eigen axes is ±45°. Note that CB and CD amplitudes depend on the polarization orientation with respect to the scanning direction, which could be related to some "asymmetric orientational writing"[20]. In addition, the calculated TLB slow axis is directly related to the observed deviation of the TLB slow axis orientation that is not perfectly linearly dependent on the laser writing polarization azimuth angle, as depicted in Fig. 4e.

## Optical chirality engineering employing a multilayer configuration

From a practical point of view, the operating principle of the proposed two-layers model provides a powerful framework (e.g., multilayer configuration) towards circular optical properties engineering both in amplitude and sign. To demonstrate the feasibility of inscribing high chiral optical properties, we investigated multilayers-based designs built either on "nanogratings based waveplate" or on "stress-engineered waveplate". For sake of comparison, we also developed a "two-layers $LB_{form}$ waveplate" made from two-layers nanogratings subsequently annealed for 30 minutes at 1150 °C to relax the stress field.

### *CB engineering using "nanogratings based waveplate"*

To obtain the maximum CB property, a misalignment of 45° between the two nanogratings layers should be used as shown in Fig. 5a. Figure 5b depicts the circular properties spectral dispersion extracted from Mueller spectropolarimetry, which highlights a CB up to −2.5 rad measured at 450 nm, the highest value reported in a glass to the best of our knowledge. In comparison to our previous best result of −0.4 rad, the CB value of −2.1 rad (measured at 550 nm) is raised to more than 5 times. In principle, this CB value refers to an optical rotation of −60° within an optimal compactness of 80 µm, which is 20 times more than the optical rotation (calculated to be 2.7° at 550 nm for the same 80 µm thickness) in quartz[21].

Here the spectral dependence of the circular properties originates from the linear ones[15]. Indeed, within the form birefringence model, the retardance $(\boldsymbol{n_x} - \boldsymbol{n_y})\cdot \boldsymbol{d}$ is relatively independent of the wavelength $(\boldsymbol{\lambda})$ especially

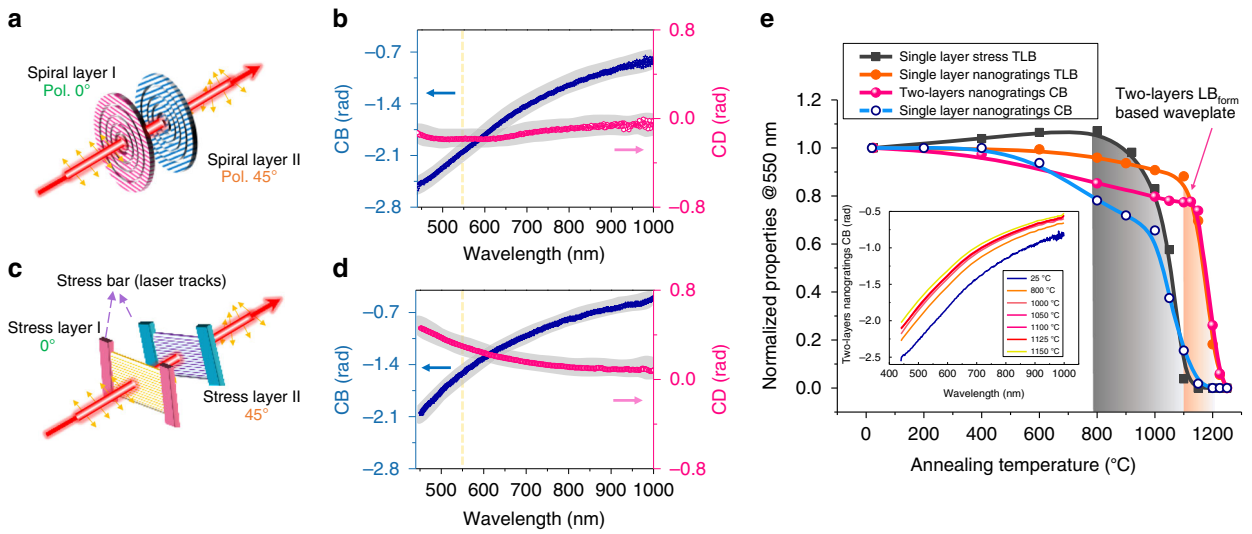


**Fig. 5 Circular anisotropic optical property engineering by exploiting a multilayer writing strategy. a** Diagram of two layers of nanogratings, 45° misaligned. **b** Spectral circular properties of the "nanogratings based waveplate" within 450–1000 nm. **c** Diagram of two layers of stress, 45° misaligned. **d** Spectral circular properties of the "stress engineered waveplate" within 450–1000 nm. **e** Thermal stability of linear and circular properties. Measurements are done at 550 nm. Inset depicts the CB spectral evolution of two-layers "nanogratings based waveplate". *Single layer stress TLB and single layer nanogratings TLB data are reproduced with the permission from ref.* [15]

for long wavelengths ($\lambda >> \Lambda$, nanogratings period). However, when expressed in radians unit, the corresponding LB (or LD) increases at short wavelengths following the expression: $\boldsymbol{LB} = \frac{2\pi}{\lambda} \cdot (\boldsymbol{n_x} - \boldsymbol{n_y}) \cdot \boldsymbol{d}$ (rad). The same explanation typically stands for $LB_{stress}$[15]. As a result, the CB amplitude that depends on (1) $LB_{form}$, $LB_{stress}$ amplitudes and (2) their angular misalignment increases at short wavelengths.

Towards further engineering applications, one should consider the spectral loss of the multilayered waveplates. For "nanogratings-based waveplate", the main losses originate from the Rayleigh scattering due to the intrinsic nanoporous nature of nanogratings[5]. This light scattering owns a $1/\lambda^4$ dependence leading to strong anisotropic losses in the UV-Vis range (transmittance >70% measured at 550 nm) but can be minimized by working within the Type X regime[22] where transmittance can be higher than 95% at 550 nm.

### *CB engineering using "stress-engineered waveplate"*

The "stress-engineered waveplate" exhibits only LB (with no LD) whose orientation is mostly dictated by the laser scanning geometry. Following this approach, we exploit fs laser direct writing to imprint stress bars (a set of lines) thus creating an irradiation-free stress zone in between[17]. Note that the birefringence orientation is manipulated by changing the direction of the stress bars arrangement. Experimentally, a 45° misalignment is employed between the two stress-engineered layers as shown in Fig. 5c. By measuring the Mueller matrix within the "irradiation-free aperture", a high CB up to −2.1 rad can be measured at 450 nm as depicted in Fig. 5d. Similar to the previous design, we take the CB value of −1.57 rad measured at 550 nm into account for comparison. Quantitatively, one can easily create an optical rotation of +/−45° measured at 550 nm. In comparison to nanogratings, the absorption coefficient for the "stress engineered waveplates" reveals negligible absorption losses below 1 $cm^{-1}$ over the whole spectral range from 200 nm up to 1600 nm (i.e., very close to the one of pristine $SiO_2$)[15], which is further strengthen this approach.

### *On the relative influence of stress and nanogratings*

Furthermore, not only to fabricate a two-layers "$LB_{form}$-based waveplate" but also to gain insights in the understanding of fs laser-induced circular properties, we perform step isochronal annealing. From previous results shown in Fig. 5e, stress-induced birefringence can nearly be erased after annealing temperature of 1100 °C (fully after 30 minutes at 1150 °C), which is accompanied by a full erasure of CB for a single nanogratings layer. On the contrary, the TLB only exhibits a decay of only 10% in the same annealing conditions. This confirms that the form birefringence contribution is much larger than the one from stress.

### *Now turning to the CB thermal stability*

The two-layers "nanogratings based waveplate" depicts two principal features. First, from 400 °C to 1100 °C, the CB slightly decreased to around 80% of its initial value

(prior annealing), which correlates with the stress relaxation. Above this temperature, a sort of two-layers "$LB_{form}$ only" waveplate is obtained from which stress effects were released. Here the CB can still achieve −1.59 rad measured at 550 nm, which corresponds to an optical rotation of −45.6°. Secondly, above 1175 °C, the CB experiences a steep decay together with TLB that is attributed to nanopores erasure[18]. Therefore, this clearly indicates that (1) CB can effectively be achieved by non-parallel non-perpendicular assembly of "ideal nanogratings" without any stress assistance and (2) the major contribution to the measured CB is related to the nanogratings form birefringence.

## Discussion

From the previous sections, it has been demonstrated that, following a single-layer writing geometry, the fs laser-induced circular properties originate from the coexistence of (1) form birefringence and (2) stress-induced birefringence. Theoretically, circular birefringence can be observed, not only in chiral materials with a chiral molecular arrangement (called intrinsic chirality, like sugar or quartz that are optically active chiral media) but also in achiral materials that exhibit a chiral arrangement considering the probe light propagation direction (for instance, oblique incidence or chiral arrangement at larger scale, micrometric scale discussed in this paper). Specifically, in our model, the written object is a "chiral object" related to an extrinsic chirality. Indeed, the structure of two linear layers ($LB_{form}$ and $LB_{stress}$) that own non-parallel non-perpendicular slow axes cannot be superimposed by its mirror image. This chiral optical object shows a chiral optical arrangement of optical properties, which thus creates CB as confirmed by the model based on Mueller formalism.

### Effect of the form birefringence

The form birefringence of "ideal nanogratings" (no tilt of their orientation with respect to laser polarization) has its fast axis aligned with the laser polarization direction. At first, Kazansky et al. proposed that nanogratings are mainly caused by the interference of the laser field and bulk plasma wave, which was then revisited by different authors as a multiple scattered wave interference pattern that structures the free electrons plasma density[10]. Recently, it was revealed that nanogratings are formed by an ultrafast decomposition of silica i.e., nanopores formation inside these nanolayers[12]. Three cornerstones prove the existence of nanopores embedded in a step-by-step nanogratings formation process. First, the SEM investigation reported in 2013 (ref. [13]) revealed the nanopores. Second, the TEM investigations presented herein (Fig. 1$a_1$ and Fig. 1$a_2$) provide a clear picture that nanolayers are made of an assembly of elongated nanopores. The formation of nanopores is attributed to $SiO_2$ decomposition into $\boldsymbol{SiO_{2(1-x)} + x \cdot O_2}$. This leads to an expulsion of ionized oxygen atoms from the lattice based on a tensile stress-assisted decomposition mechanism[23] that was recently revisited as plasma mediated nanocavitation process[24]. The oxygen atoms are thus found in the interstitial position and recombine to form molecular oxygen. The typical diameter of nanopores ranges from 10 to 50 nm depending on the deposited energy[25]. Finally, the last cornerstone is attributed to small-angle X-ray scattering measurements that further confirmed the formation of elongated nanoporous structures within the nanolayers[26,27]. All the proposed theories and experimental results confirm that the nanogratings orientate ideally or theoretically perpendicular to the laser polarization. However, from our polarimetric data, the observed TLB angular deviation indicates either a presence of a nanogratings tilt and/or a presence of at least one more contribution to the TLB that is non-parallel non-perpendicular to the form birefringence[7] e.g., the stress-induced birefringence.

### Effect of the PFT

The effect of PFT could be a possible contribution to the observed deviation creating a tilt in the nanolayers orientation as investigated by Dai et al. in 2014 (ref. [28]). The polarization dependence arises due to the spatio-temporal properties of the ultrafast laser beam quantified by spatial chirp, PFT and angular dispersion[29,30]. The PFT produced by temporal and spatial chirps (e.g., due to a slight misalignment of the laser compressor) can lead to both the "quill writing" and the anisotropic photosensitivity phenomena[20,29,31,32]. However, the PFT is capable of interpreting only a small part of the deviation because the PFT-induced nanograting rotation achieves only a few degrees at a hundred fs/mm tilt[28]. Indeed, the experimental proof of neutral axis deviation in our results exhibits an amplitude up to 35°, which is far above the level that PFT can usually achieve. Moreover, note that the polarization dependence of this deviation matches quite well with the one of the circular properties. This deviation is thus likely related to the stress field.

### Effect of the stress field

Ultrashort laser pulses enable the formation of a "quasi-free" electron plasma as an intermediate step between light absorption and structural modifications in the glass network. In particular within the Type II regime, the plasma is structured under the influence of light in relation with the solid. The spatial structuring of the plasma density gives rise to a force field in the solid, which then leads, after extinction of the light pulse, to the imprinting of a stress field. More specifically, there are two possible processes:

(1) "Self-structuring" of the quasi-free electron plasma under the electromagnetic field creates a structured DC field. This DC field distorts the ionized atomic network (partly elastically and plastically). When the laser light is off and after electron relaxation, the elastic part that was balanced by the electromagnetic force disappears, but a plastic strain and a stress field still survive.

(2) The structured plasma imprint structural changes like point defects or nanovoids, the concentration of which follows the plasma density. This may correspond to a change of lattice density and thus to the development of a stress field. For example, in $SiO_2$, this agrees with a reported net volume expansion[11], which correlates with the formation of porous nanolayers[12,13]. Locally, the effective glass volume is expanded and induces a permanent strain field[12], and therefore a stress field appears within and around the laser-modified region. Depending on the laser exposure conditions (including polarization), the overall stress can be enhanced or minimized[14,33] leading to tunable stress-induced birefringence values from $10^{-5}$ up to ~$10^{-3}$ accordingly[34–36]. Note that such stress-induced birefringence influences the written anisotropic optical properties but also likely the nanogratings themselves[37]. Therefore, within the Type II regime[14,38–42], the formation of nanogratings is not solely creating form birefringence but also a stress-induced birefringence contribution that participate to the measured total birefringence[38,43,44].

### About TLB neutral axis deviation

The fast axis evolutions of these two contributions are summarized in Fig. 3b and compared to the one of nanogratings, revealing some deviations. Based on the above discussion we suggest that the significant deviation of the TLB fast axis is due to the stress birefringence that is in general non-parallel and non-perpendicular to the nanolayers themselves. This results in a rotation of TLB neutral axis whose amplitude increases with (1) ratio of stress birefringence to the form birefringence and (2) the misalignment between their respective neutral axes (the maximum being 45°).

### Towards chiral optical properties exploitation

Finally, the fs-induced anisotropic circular properties originate not solely from the form birefringence but from a "cooperation" of this contribution and the stress one, but how do they quantitatively contribute to the imprinted optical chirality? Firstly, from the annealing results shown in Fig. 5e, the CB of two-layers "nanogratings-based waveplate" is dominated by the $LB_{form}$, which can be easily controlled by laser writing parameters (e.g., pulse energy or writing speed)[45]. To further answer this question, our two-layers model not only provides the quantitative meaning of fs laser-induced optical chirality but also can be expanded to other more complex situations. This includes multilayers contributing to diverse anisotropic properties, including circular properties by simply adjusting the layers 3D assembly and the parameters adopted in each layer. Furthermore, such a multilayer strategy opens the door to a new strategy in laser manufacturing optical devices that require circular optical properties and even circular properties without any linear ones. Note this is not a simple linear accumulation of single layers but a vectorial combination for high optical chirality construction. One could arrange different layers including pure $LB_{form}$ (accompanied by annealing strategy), pure stress or their combination with diverse amplitudes and angular misalignment. Interestingly also, the circular optical property cannot only be accumulated but also be compensated by creating the circular property with reverse sign.

## Conclusion

In the light of the current state of the art, we quantitatively interpreted the fs laser-induced optical chirality observed and characterized in silica glass. This property is attributed to the co-existence of two phenomena: nanogratings anisotropic properties (linear form birefringence and dichroism) and a stress-induced linear birefringence. Besides, the misalignment between eigen axes of these two contributions results in a symmetry breaking (a so-called extrinsic chirality) and creates chiral optical properties (CB and CD). It is worth pointing out that one can tailor both the amplitude and sign of the circular properties by adjusting the optical design and laser parameters.

The fundamental interest in fs laser-induced nanostructures that possesses the intrinsic parameters (periodicity, nanoporosity, 3D rotation), allows an effective control of birefringence slow/fast axis and even inducing circular optical properties that lead to the engineering of unique integrated optical devices with 3D space variant birefringence, 3D geometric phase optics and more generally refractive index tensor profiling. This result brings further understanding of the vectorial nature of light-matter interaction and allows designing any kind of 3D structured light beam in terms of phase, amplitude and polarization.

In addition, this approach can be implemented with a multilayer strategy to achieve on-demand optical rotation between [−90°, 90°] and within less than 200 µm. This ability to manipulate optical rotation opens possibilities to optical property engineering of any given transparent material. For instance, developing birefringent devices operating in a broad spectral range—including achromatic components or passive optical isolators—would benefit to many fields such as photonics integrated circuits, polarimetry, spectroscopy, attosecond pulse generation, terahertz, military and domotics applications.

## Materials and methods

### Definitions

LB and LB' are defined as the difference of refractive indices between two othogonal linear polarized beams with a dimentionless unit. However, it is more practical in polarimetry to use linear phase difference to describe the LB and LB' properties, which is adopted in this paper. Because it shows the collective influence to the probe light manipulated by our samples. Hence TLB can be calculated by $\boldsymbol{TLB} = \sqrt{\boldsymbol{LB}^2 + \boldsymbol{LB}'^2}$ in radians with its fast axis angle. CB is defined as the difference of refractive indices between left- and right-handed circular polarized beams with a dimensionless unit. Similarly, it is common using circular phase difference to describe the CB property. LD, LD', TLD and CD refer to the difference of the absorption between two othogonal linear/circular polarized beams respectively and are treated similarly as birefringence ones, as shown in Table 1.

### Femtosecond laser set-up

The laser beam is delivered from a fs laser system operating at $\lambda = 1030\ nm$, $\Delta t_{sp} = 250\ fs$ and outputting at a repetition rate of 100 kHz with an average power up to 10 W (Amplitude Systèmes, Pessac, France). Aspheric lens of 0.6 numerical aperture (NA) and 0.16 NA are adopted for fabricating Type II structure and stress bars, respectively, with a focusing depth of 500 μm below the surface. Based on the preliminary calibrations, the laser parameters are settled with appropriate pulse energy and scanning speed falling into the Type II window (typically 1 mm $s^{-1}$ writing speed at 1.5 μJ for getting a smooth writing) inside a 1-mm-thick silica glass (Suprasil CG, Heraeus, Hanau, Germany). According to the theory reported in ref. [46] and using the plasma absorption reported in ref. [47], i.e., around 15% at 1.5 μJ and 0.16 NA, we can estimate the intensity of our used fs laser beam to be 8.8 TW $cm^{-2}$ (0.16 NA). Then it is difficult to give a reliable intensity at 0.6 NA due to the lack of absorption data, but it should be very close to the clamping intensity that has been estimated to be around 50-60 TW $cm^{-2}$ in silica[48].

### Laser writing configurations

We define the laser configuration as "scanning direction $\boldsymbol{v}$ + laser polarization $\boldsymbol{\alpha}$", for example, here X + 45° refers to the laser scanning direction is along the x axis and the laser polarization $\boldsymbol{\alpha} = 45°$, with a typical error smaller than 0.5°. For simplicity, X + 0° and X + 90° are often replaced by "Xx" and "Xy". A wide range of writing configurations is investigated here. Homogeneous squares generally with a size of 1.5 mm × 1.5 mm are carried out by unidirectional line scanning with 1 μm increment (to avoid "quill writing" and diffraction effects), which are suitable for the Mueller matrix spectro-polarimetry. Towards investigating the laser polarization dependence, the laser linear polarization is oriented from 0° (along the x axis defined by the laser compressor plane taken as a reference) up to 360° with a step of 22.5°.

#### *For "nanogratings-based waveplates"*

Two uniform disks (one using 0° polarization, and another using 45° with fixed other parameters) are written using a spiral trajectory with a diameter of 1.5 mm and a 1 μm pitch. The laser track length is 40 μm in z-axis (depth) and we put 100 μm distance in-between two layers, which means the two layers are almost independent layers. In addition, since the stress decreases exponentially out of the laser tracks, we can neglect the influence of the stress induced by the first layer when writing the second one.

#### *For "stress-engineered waveplates"*

The stress bars consisting of two squares (or two rectangles) made of lines are written for creating a strong stress field in between. Each stress bar is made of 5 written layers with a 35 μm increment along z-axis for ensuring a continuous writing of thick stress bars. Then we write another two stress bars to create the second stress layer with a 45° rotation. The increment between two stress layers is 100 μm to ensure almost independent layers. More details can be found in our previous work[15].

### TEM observations

The interior of the nanogratings has been examined by cleaving the sample after laser irradiation. If the nanograting planes are parallel to the cleavage, the interior structure could be observed with field emission electron microscope, which could reveal small features otherwise covered by conductive coating. Further, high-resolution transmission electron microscopy could be applied to analyze the internal structure of nanogratings through transversal and longitudinal views with FIB technique (see Fig. 1($a_1$) and Fig. 1($a_2$)). Here, we used commercial TOPCON 002B electron microscope (200 kV with a resolution of 0.18 nm). This gives a better understanding of the internal structure of nanoplanes generation and nanopores distribution in the irradiated region of the silica glass. The FIB technique (Zeiss Neon 60, current 50 pA, accelerating voltage 30 kV) is used to dissect nanogratings embedded in silica into small slices with a thickness of 50 nm without invasive nanoplanes in the modified region.

### Mueller matrix characteristics

Spectral normalized Mueller matrices are recorded with a spectroscopic Mueller ellipsometer (Smart SE, JY HORIBA) in transmission at normal incidence in the wavelength range $\lambda \in 450–1000\ nm$. Normally a Smart SE spectroscopic ellipsometer is used to measure the properties of thin films with a reflection mode. But here we used in fact a

modified version of this ellipsometer to create a Mueller spectro-polarimeter as described in the literatures[49,50]. Specifically, a polarization state generator and a polarization state analyzer were added in such equipment to determine the whole Mueller matrices in transmission mode. The sample is probed with at least four (sometimes more) different input polarized states that are generally elliptical, this allows to determine the whole 16 elements of the Mueller matrix, including the mixed information of linear and circular anisotropic optical properties with their sign or orientation and also the degree of polarization. The samples are oriented in such a way that their writing/scanning axis is set horizontal (+/−1°) in the reference frame of the Mueller ellipsometer. To extract these properties, the Mueller matrices measured experimentally are then decomposed using the logarithmic decomposition method[51,52] to tentatively "disentangle" the anisotropic optical properties. In that way the effective values of LB, LB', LD, LD', CB, and CD, can be treated independently. What has a physical meaning is the so-called TLB, which represents the effective birefringence seen by a light probe. For a complete view TLB has to be associated with its neutral axes angle (i.e., fast/slow axis in our uniaxial case). Typical error bars within investigating spectral range remains smaller than 1° for all these properties. Thus, TLB and TLD can be calculated as well as their neutral axis (typ. within +/−2°). Apart from the multi-spectral behavior, all anisotropic optical properties are then extracted at a fixed wavelength of 550 nm.

### Imaging and birefringence measurement

Optical images are measured using an Olympus BX51 polarizing optical microscope (Olympus, Tokyo, Japan) equipped with a "de Sénarmont" compensator. A "de Sénarmont" strategy employs a highly precise quarter-waveplate companied with a feasible 180-degree-rotation polarization analyzer to achieve the retardance measurement with an accuracy of few nanometers at 550 nm. Notice that in only crossed polarized configuration, the birefringence image has different colors due to different values of retardance according to Michel-Levy scale. For example, in Fig. 1($a_3$), the color of the "stress bars" is blue because of a relatively high retardance while the grey part between the stress bars refers to a lower retardance in the pure stress area. In addition, we have performed quantitative linear birefringence imaging measurements at 550 nm using "Open Polscope". Note that, we use small size of samples (typically 0.1 mm × 0.1 mm) for these measurements since the equipment are microscopes themselves. Therefore, the overall cartography of the birefringence amplitude together with its slow axis orientation can be determined successfully.

### Simulation method

We define a two linear retarders model under Mathcad® software. Separately, the parameters of LB and LD can be added into the two linear retarders with both amplitudes and signs. The fast axis of the first retarder (refers to form birefringence contribution) is varied from 0° up to 360°, which is corresponding to the laser polarization direction change. Differently, the fast axis of the second retarder (refers to the stress birefringence contribution) is fixed at 0° in agreement with the writing geometry i.e., a set of lines written along x axis.

#### Acknowledgements

This research was funded by Agence Nationale pour la Recherche, FLAG-IR project, grant number ANR-18-CE08-0004-01 and CNRS Défi Instrumentation aux Limites, UltraBragg project, Science and Technology Commission of Shanghai Municipality (20JC1415700). Jiafeng Lu acknowledges the China Scholarship Council (CSC) for the funding No. 202006890077. We greatly acknowledge Dr. Maxime Cavillon for valuable discussions.

#### Author details

[1]Institut de Chimie Moléculaire et des Matériaux d'Orsay, Université Paris Saclay, Orsay 91405, France. [2]Key Laboratory of Specialty Fiber Optics and Optical Access Networks, Joint International Research Laboratory of Specialty Fiber Optics and Advanced Communication, Shanghai Institute for Advanced Communication and Data Science, Shanghai University, Shanghai 200444, China. [3]LPICM, CNRS, Ecole Polytechnique, Institut Polytechnique de Paris, Palaiseau 91128, France

#### Author contributions

M.L. supervised the project. J.L., B.P. and M.L. wrote the manuscript. J.L. and J.T. carried out the laser writing, sample treatment and characterization. J.L., J.T. and E.G.-C. demonstrated the Mueller spectroscopy and imaging tests. J.L., J.T., and M.L. processed and analyzed the data. M.L., E.G.-C., R.O. and X.Z. discussed the experimental results. J.T., M.L., E.G.-C. and R.O. assisted the theoretical simulation of two-layers model. The TEM test is carried out by M.L. All authors commented and discussed this work.

#### Data availability

Data is available from corresponding author upon reasonable requirements.

#### Conflict of interest

The authors declare no competing interests.

Received: 25 April 2022 Revised: 10 January 2023 Accepted: 15 January 2023
Published online: 20 February 2023

#### References

1. Dai, Y. et al. Void-nanograting transition by ultrashort laser pulse irradiation in silica glass. *Opt. Exp.* **24**, 19344–19353 (2016).
2. Meany, T. et al. Laser written circuits for quantum photonics. *Laser Photo. Rev.* **9**, 363–384 (2015).
3. Lu, J. F. et al. Fiber nanogratings induced by femtosecond pulse laser direct writing for in-line polarizer. *Nanoscale* **11**, 908–914 (2019).
4. Desmarchelier, R. et al. Chiroptical properties photo-induced by femtosecond laser irradiation in silica glass. *Appl. Phys. Lett.* **110**, 021112 (2017).
5. Tian, J. et al. Spectral dependence of femtosecond laser induced circular optical properties in silica. *OSA Contin.* **2**, 1233–1241 (2019).
6. Poumellec, B. et al. Parity violation in chiral structure creation under femtosecond laser irradiation in silica glass? *Light Sci. Appl.* **5**, e16178 (2016).
7. Yoo, S. H., Ossikovski, R. & Garcia-Caurel, E. Experimental study of thickness dependence of polarization and depolarization properties of anisotropic turbid media using Mueller matrix polarimetry and differential decomposition. *Appl. Surf. Sci.* **421**, 870–877 (2017).
8. Arteaga, O. A note on optical activity and extrinsic chirality. Print at http://arxiv.org/abs/1508.02422 (2015).

9. Bricchi, E., Klappauf, B. G. & Kazansky, P. G. Form birefringence and negative index change created by femtosecond direct writing in transparent materials. *Opt. Lett.* **29**, 119–121 (2004).
10. Shimotsuma, Y. et al. Self-organized nanogratings in glass irradiated by ultrashort light pulses. *Phys. Rev. Lett.* **91**, 247405 (2003).
11. Champion, A. & Bellouard, Y. Direct volume variation measurements in fused silica specimens exposed to femtosecond laser. *Opt. Mater. Express* **2**, 789–798 (2012).
12. Canning, J. et al. Anatomy of a femtosecond laser processed silica waveguide [Invited]. *Opt. Mater. Express* **1**, 998–1008 (2011).
13. Lancry, M. et al. Ultrafast nanoporous silica formation driven by femtosecond laser irradiation. *Laser Photo. Rev.* **7**, 953–962 (2013).
14. Champion, A. et al. Stress distribution around femtosecond laser affected zones: effect of nanogratings orientation. *Opt. Express* **21**, 24942–24951 (2013).
15. Tian, J. et al. A comparison between nanogratings-based and stress-engineered waveplates written by femtosecond laser in silica. *Micromachines* **11**, 131 (2020).
16. Heilmann, R. et al. Arbitrary photonic wave plate operations on chip: Realizing Hadamard, Pauli-X, and rotation gates for polarisation qubits. *Sci. Rep.* **4**, 4118 (2014).
17. McMillen, B., Athanasiou, C. & Bellouard, Y. Femtosecond laser direct-write waveplates based on stress-induced birefringence. *Opt. Express* **24**, 27239–27252 (2016).
18. Wang, Y. T. et al. An overview of the thermal erasure mechanisms of femtosecond laser-induced nanogratings in silica glass. *Phys. Status Solidi (A)* **218**, 2100023 (2021).
19. Ortega-Quijano, N. et al. Experimental validation of Mueller matrix differential decomposition. *Opt. Express* **20**, 1151–1163 (2012).
20. Poumellec, B. et al. Asymmetric orientational writing in glass with femtosecond laser irradiation. *Opt. Mater. Express* **3**, 1586–1599 (2013).
21. Dimitriu, D. G. & Dorohoi, D. O. New method to determine the optical rotatory dispersion of inorganic crystals applied to some samples of Carpathian Quartz. *Spectrochim. Acta A Mol. Biomol. Spectrosc.* **131**, 674–677 (2014).
22. Sakakura, M. et al. Ultralow-loss geometric phase and polarization shaping by ultrafast laser writing in silica glass. *Light Sci. Appl.* **9**, 15 (2020).
23. Lancry, M. et al. Nanoscale femtosecond laser milling and control of nanoporosity in the normal and anomalous regimes of $GeO_2$-$SiO_2$ glasses. *Opt. Mater. Express* **6**, 321–330 (2016).
24. Rudenko, A., Colombier, J. P. & Itina, T. E. Nanopore-mediated ultrashort laser-induced formation and erasure of volume nanogratings in glass. *Phys. Chem. Chem. Phys.* **20**, 5887–5899 (2018).
25. Desmarchelier, R. et al. In the heart of femtosecond laser induced nanogratings: from porous nanoplanes to form birefringence. *World J. Nano Sci. Eng.* **5**, 115–125 (2015).
26. Richter, S. et al. On the fundamental structure of femtosecond laser-induced nanogratings. *Laser Photo. Rev.* **6**, 787–792 (2012).
27. Zimmermann, F. et al. Femtosecond laser written nanostructures in Ge-doped glasses. *Opt. Lett.* **41**, 1161–1164 (2016).
28. Dai, Y. et al. Forced rotation of nanograting in glass by pulse-front tilted femtosecond laser direct writing. *Opt. Express* **22**, 28500–28505 (2014).
29. Kazansky, P. G. et al. "Quill" writing with ultrashort light pulses in transparent materials. *Appl. Phys. Lett.* **90**, 151120 (2007).
30. Vitek, D. N. et al. Spatio-temporally focused femtosecond laser pulses for nonreciprocal writing in optically transparent materials. *Opt. Express* **18**, 24673–24678 (2010).
31. Akturk, S. et al. Pulse-front tilt caused by spatial and temporal chirp. *Opt. Express* **12**, 4399–4410 (2004).
32. Kazansky, P. G. et al. Photosensitivity control of an isotropic medium through polarization of light pulses with tilted intensity front. *Opt. Express* **19**, 20657–20664 (2011).
33. Bellouard, Y. et al. Stress-state manipulation in fused silica via femtosecond laser irradiation. *Optica* **3**, 1285–1293 (2016).
34. Yuan, L. et al. Stress-induced birefringence and fabrication of in-fiber polarization devices by controlled femtosecond laser irradiations. *Opt. Express* **24**, 1062–1071 (2016).
35. Fernandes, L. A. et al. Stress induced birefringence tuning in femtosecond laser fabricated waveguides in fused silica. *Opt. Express* **20**, 24103–24114 (2012).
36. Fernandes, L. A. et al. Strong birefringence tuning of optical waveguides with femtosecond laser irradiation of bulk fused silica and single mode fibers. *J. Lightwave Technol.* **31**, 3563–3569 (2013).
37. Gecevičius, M. et al. Extraordinary anisotropy of ultrafast laser writing in glass. *Opt. Express* **21**, 3959–3968 (2013).
38. Poumellec, B. et al. Femtosecond laser irradiation stress induced in pure silica. *Opt. Express* **11**, 1070–1079 (2003).
39. Sudrie, L. et al. Writing of permanent birefringent microlayers in bulk fused silica with femtosecond laser pulses. *Opt. Communications* **171**, 279–284 (1999).
40. Gorelik, T. et al. Transmission electron microscopy studies of femtosecond laser induced modifications in quartz. *Appl. Phys. A* **76**, 309–311 (2003).
41. Sudrie, L. et al. Study of damage in fused silica induced by ultra-short IR laser pulses. *Opt. Commun.* **191**, 333–339 (2001).
42. Zhang, X. R., Xu, X. & Rubenchik, A. M. Simulation of microscale densification during femtosecond laser processing of dielectric materials. *Appl. Phys. A* **79**, 945–948 (2004).
43. Bhardwaj, V. R. et al. Stress in femtosecond-laser-written waveguides in fused silica. *Opt. Lett.* **29**, 1312–1314 (2004).
44. Dürr, F. et al. Tomographic measurement of femtosecond-laser induced stress changes in optical fibers. *Appl. Phys. Lett.* **84**, 4983–4985 (2004).
45. Lancry, M. et al. Compact birefringent waveplates photo-induced in silica by femtosecond laser. *Micromachines* **5**, 825–838 (2014).
46. Schaffer, C. B., Brodeur, A. & Mazur, E. Laser-induced breakdown and damage in bulk transparent materials induced by tightly focused femtosecond laser pulses. *Meas. Sci. Technol.* **12**, 1784–1794 (2001).
47. Wang, H. J. et al. 100-layer error-free 5D optical data storage by ultrafast laser nanostructuring in glass. *Laser Photo. Rev.* **16**, 2100563 (2022).
48. Rolle, J. et al. Filamentation of ultrashort laser pulses in silica glass and KDP crystals: a comparative study. *Phys. Rev. A* **90**, 023834 (2014).
49. Hu, H. F. et al. Simplified calibration procedure for Mueller polarimeter in transmission configuration. *Opt. Lett.* **39**, 418–421 (2014).
50. Ossikovski, R. et al. Polarizer calibration method for Mueller matrix polarimeters. *Appl. Opt.* **59**, 10389–10395 (2020).
51. Ossikovski, R. Differential matrix formalism for depolarizing anisotropic media. *Opt. Lett.* **36**, 2330–2332 (2011).
52. Ossikovski, R. & Arteaga, O. Statistical meaning of the differential Mueller matrix of depolarizing homogeneous media. *Opt. Lett.* **39**, 4470–4473 (2014).

## VI.3 FEMTOSECOND LASER DIRECT WRITING MULTILAYER CHIRAL WAVEPLATES WITH MINIMAL LINEAR BIREFRINGENCE

# Femtosecond laser direct writing multilayer chiral waveplates with minimal linear birefringence

JIAFENG LU,[1,2] ENRIQUE GARCIA-CAUREL,[3] RAZVIGOR OSSIKOVSKI,[3] FRANCOIS COURVOISIER,[4] XIANGLONG ZENG,[2] BERTRAND POUMELLEC,[1] MATTHIEU LANCRY[1,*]

[1] *Institut de Chimie Moléculaire et des Matériaux d'Orsay, Université Paris Saclay, Orsay cedex 91405, France*
[2] *The Key Lab of Specialty Fiber Optics and Optical Access Network, Joint International Research Laboratory of Specialty Fiber Optics and Advanced Communication, Shanghai University, Shanghai 200444, China*
[3] *LPICM, CNRS, Ecole Polytechnique, Institut Polytechnique de Paris, Palaiseau 91128, France*
[4] *FEMTO-ST Institute, University Bourgogne Franche-Comté, CNRS, Besançon 25030, France*
[*] *Corresponding author: matthieu.lancry@universite-paris-saclay.fr*

Received XX Month XXXX; revised XX Month, XXXX; accepted XX Month XXXX; posted XX Month XXXX (Doc. ID XXXXX); published XX Month XXXX

**Chirality transfer from femtosecond laser direct writing in achiral transparent materials mainly originates from the interplay between anisotropic nanogratings and mechanical stress with non-parallel and non-perpendicular (oblique) neutral axes. Yet, the laser fabrication simultaneously induces non-negligible linear birefringence. For precise manipulation of circular polarization properties, as well as to unlock the full functionality, we report here a geometry-inspired multilayer method for direct writing of chiral waveplates with minimal linear birefringence. We perform a theoretical analysis of both circular and linear properties response for different multilayer configurations and achieve strong circular birefringence of up to -2.25 rad with an extinction ratio of circular birefringence to total linear birefringence of up to 5.5 dB at 550 nm. Our strategy enables the precise control of circular properties and provides a facile platform for chiral device exploration with almost no linear property existence.** 

***OCIS codes:*** *xxxxxxxxxxxx*

http://dx.doi.org/10.1364/OL.99.099999

Chiral effects originating from diverse phenomena in nature have shown their great importance both in fundamental science and in practical applications ranging from molecular chemistry to artificial metamaterials, such as optical recording [1], broadband circular polarizers [2] and quantum materials [3]. Chiral structures mix electric and magnetic contributions, originating in different optical responses to left- and right- handed circular polarized light. Thus, a chiral waveplate (like, e.g. water solution of sugar) enabling pure optical rotation without ellipticity is very useful. Compared to traditional optical rotators, such as half-waveplates that require very precise retardance and alignment and Faraday rotators that require complex devices, chiral waveplates exhibit compact sizes, are less sensitive to misalignment and are potentially achromatic [4].

Femtosecond (fs) laser direct writing (FLDW) is an alternative photonic device fabrication strategy, which, in recent years, has evolved from the proof-of-principle stage to a widely exploited procedure in optical manufacturing [5]. Due to its ultrahigh peak power and ultrashort pulse duration, a fs laser can locally deposit the energy in the irradiated region without any surrounding damage through nonlinear effects [6]. This subsequently results in diverse kinds of nanostructures. Among these, Type II structures (subwavelength nanogratings), consisting of an alternation of nanoporous layers, exhibit strong symmetry breaking [7–10]. In general, this gives rise to linear polarimetric properties, such as dichroism and birefringence [11]. Going a step further, the use of a fs laser to induce circular properties inside achiral materials opens up interesting perspectives for creating chirality in three-dimensional structures, which is the key step in fabricating chiral transparent waveplates [12]. Physically, the fs-laser-induced chirality was attributed to a volume torque resulting from a DC electric field and a stress field [12]. However, the changes in molecular configuration taking place in such an ultrashort light-matter interaction are difficult to observe. In a recent work, we proposed a new conceptual view according to which fs-induced circular properties are due to two main contributions: a form birefringence due to the nanogratings and a photoelastic birefringence originating from stress with oblique neutral axes [13].

A typical fs-laser-written chiral structure exhibits strong linear birefringence due to the anisotropic structure of nanogratings [14,15], restricting the performance of the chiral waveplate (because of linear birefringence transforming linearly polarized light into elliptically polarized one). Recently, Yoo et al. [16] reported that birefringent tapes stacked in multilayers with appropriate azimuth orientations (best results with 45° difference between the layers having been obtained) can create circular properties with suppressed linear properties. Following this conceptual view, here we go a step further in imprinting directly a

chiral waveplate structure with linear properties suppression by utilizing a multilayer stack configuration through FLDW.

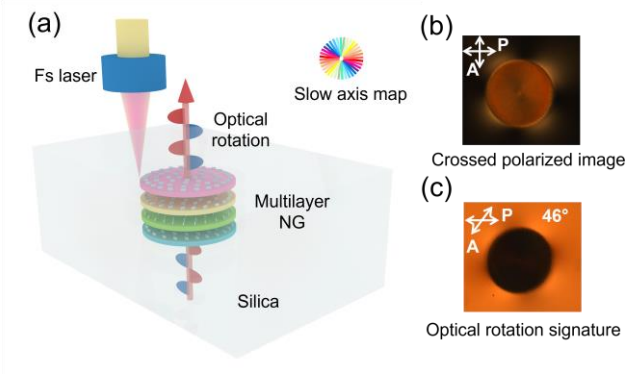


**Fig. 1**. (a) Scheme of the fs-laser-written structure consisting in layers of nanogratings with different slow axis orientations that lead to large optical rotation. The inset shows the map of the slow axis orientation, different colors corresponding to different slow axis orientations. (b) Cross-polarized microscope image of a four-layer sample written at 1030 nm, 800 fs, 0.16 NA, 100 kHz, 0.8 μJ, 1 mm/s, $\alpha = 45°$. (c) Optical rotation signature obtained with the analyzer in extinction configuration. This measurement confirms that the polarization remains linear, with an azimuth rotated by 46° with respect to the incident polarization.

Fs-laser-enabled writing of oriented multilayer assemblies is based on the neutral axis (typ. slow/fast axis in uniaxial materials) control of imprinted nanogratings by exploiting appropriate laser parameters such as laser polarization, as illustrated in **Fig. 1(a)**. In this paper, we adopt a four-layer configuration as an easy-to-obtain yet a practically useful design. Actually, four layers with rotated slow axis orientation angles (azimuths) create a staircase-like configuration resulting in strong chiral effects. Here, the increment angle α is defined as the angle between the slow axis directions of two adjacent layers. For simplicity, identical retardation for all layers is assumed and the increment angle α is kept constant in one single configuration.

The fs-laser system (Amplitude Systèmes, Pessac, France) delivers a laser beam at the wavelength $\lambda = 1030\ nm$ with an 800-fs duration time. A 100-kHz repetition rate with pulse energy in the 0.6-2.0 μJ range was used for the fabrication of Type II nanogratings. A low numerical aperture (0.16 NA) aspheric lens was used to minimize spherical aberration. We fabricated several mm-size disks using a spiral writing trajectory with an increment of 1 μm in order to ensure homogeneity and suppress diffraction. More information can be found in [13]. The samples were fabricated through irradiation of a 1-mm thick silica glass wafer (Suprasil CG, Heraeus, Hanau, Germany) by focusing the laser beam 400 μm below the surface. (The latter value corresponds to the deepest layer when in a multilayer configuration.) Based on preliminary calibrations, the laser parameters used were set at appropriate pulse energies and scanning speeds to ensure the fabrication of well-controlled Type II nanogratings.

We start with the increment orientation angle $\alpha = 45°$ inspired by the reported work from Yoo et al. [16]. **Figures 1(b)** and **1(c)** show the cross-polarized microscope image and the optical rotation signature (obtained with the analyzer in extinction configuration) of a four-layer sample, exhibiting a large optical rotation of up to 46°. The optical microscope images were recorded with an Olympus BX51 polarizing optical microscope equipped with a "de Sénarmont" compensator. This configuration not only enables the optical rotation measurement with a high precision 180-degree-rotation analyzing polarizer but also enables a linear retardance measurement with an accuracy of few nanometers at 550 nm by employing a highly precise quarter-waveplate.

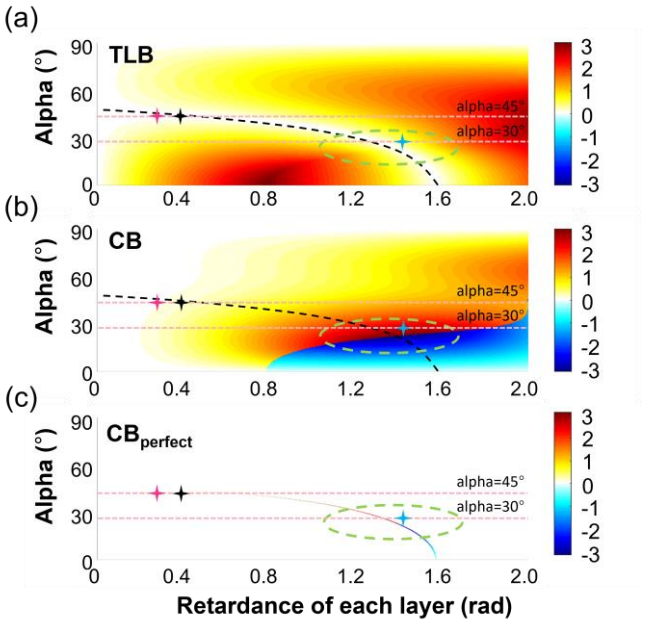


**Fig. 2**. Modeling results of four-layer staircase-like structures at different increment angles $\alpha$ and retardances. Top figure: TLB (total linear birefringence); Center figure: CB (circular birefringence); Bottom figure: $CB_{perfect}$ (CB values from the black dashed line). Black dashed line: zero-TLB curve; Red star: structure from Yoo et al. [16]; Black star: sample written by 0.8 μJ, 1 mm/s, $\alpha = 45°$; Blue star: sample written by 1.5 μJ, 1 mm/s, $\alpha = 30°$; Green dashed line region: chiral waveplates with strong CB and significantly small TLB.

The optical rotation signature originates not only from the chiroptic properties of each individual layer but also from the azimuth misalignment between layers. The thicker each layer, the higher the retardance (optical phase difference). The thickness of a single layer was measured to be around 40 μm and the distance between two adjacent layers was set to 100 μm, effectively allowing for stress uncoupling between layers. We have theoretically modeled the chiroptic properties of a four-layer configuration nanogratings-based waveplate using Mueller matrix formalism. Theoretically, the optical response of an individual nanogratings layer is that of a linear retarder with a retardation $R$ and a slow axis oriented at the angle $\alpha$. Hence, the Mueller matrix of each layer can be expressed as: $M_{in}(R, \alpha) = MR(-\alpha) \cdot MLR(R) \cdot MR(\alpha)$,

$$MLR(R) = \begin{bmatrix} 1 & 0 & 0 & 0 \\ 0 & 1 & 0 & 0 \\ 0 & 0 & cos\,(R) & sin\,(R) \\ 0 & 0 & -sin\,(R) & cos\,(R) \end{bmatrix}$$

$$where \qquad MR(\alpha) = \begin{bmatrix} 1 & 0 & 0 & 0 \\ 0 & cos\,(2\alpha) & sin\,(2\alpha) & 0 \\ 0 & -sin\,(2\alpha) & cos\,(2\alpha) & 0 \\ 0 & 0 & 0 & 1 \end{bmatrix} \qquad (1)$$

We have set the same interlayer rotation angle. The final Mueller matrix of the chiral waveplate is given by:

$$M = M_{in4th}(R, 3\alpha) \cdot M_{in3rd}(R, 2\alpha) \cdot M_{in2nd}(R, \alpha) \cdot M_{in1st}(R, 0°) \qquad (2)$$

The quantitative analysis of both linear and circular properties of the chiral waveplate is subsequently performed by applying the differential decomposition method [17,18]. The decomposed differential matrix is given by:

$$M_{dec} = \begin{bmatrix} 0 & LD & LD' & CD \\ LD & 0 & CB & -LB' \\ LD' & -CB & 0 & LB \\ CD & LB' & -LB & 0 \end{bmatrix} \qquad (3)$$

Thus, we obtain the full set of optical properties: circular birefringence (CB), circular dichroism (CD), *x-y* axis linear birefringence (LB), 45°-axis linear birefringence (LB'), *x-y* axis linear dichroism (LD), and 45°-axis linear dichroism (LD'). The total linear birefringence (TLB) is determined from $TLB = \sqrt{LB^2 + LB'^2}$.

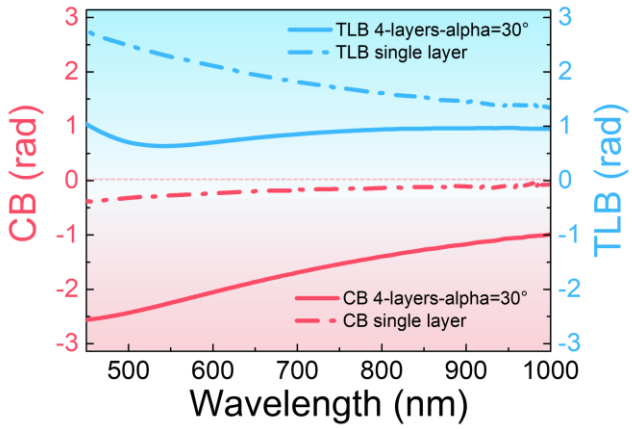


**Fig. 3**. CB and TLB wavelength dependence of the four-layer structure (solid lines) written at 1030 nm, 800 fs, 0.16 NA, 100 kHz, 1.5 µJ, 1 mm/s with an increment orientation angle $\alpha$ = 30°. Single-layer structure responses (dashed lines) with same laser parameters are reported for comparison.

**Figure. 2** shows the modeling results of four-layer structures. Calculated TLB (top), CB (center) and $CB_{perfect}$ (bottom), i.e., CB values from the zero-TLB curve (black dashed line), as functions of $R$ and $\alpha$ are shown. TLB is zero for certain pairs of $R$ and $\alpha$ values (black dashed line). The model also shows that CB reaches the maximum value, close to $\pi$, with still low TLB within the region bounded by the green dashed line. The latter region represents the most interesting configurations for practical applications.

To further explore the optical response of such chiral structures, we characterized them by spectroscopic Mueller ellipsometry and performed optical rotation measurements by cross-polarized microscopy. The normalized spectral Mueller matrix was first measured with a spectroscopic Mueller ellipsometer (Smart SE, JY HORIBA) and then decomposed with the differential decomposition method providing the matrix from **Eq. (3)**.

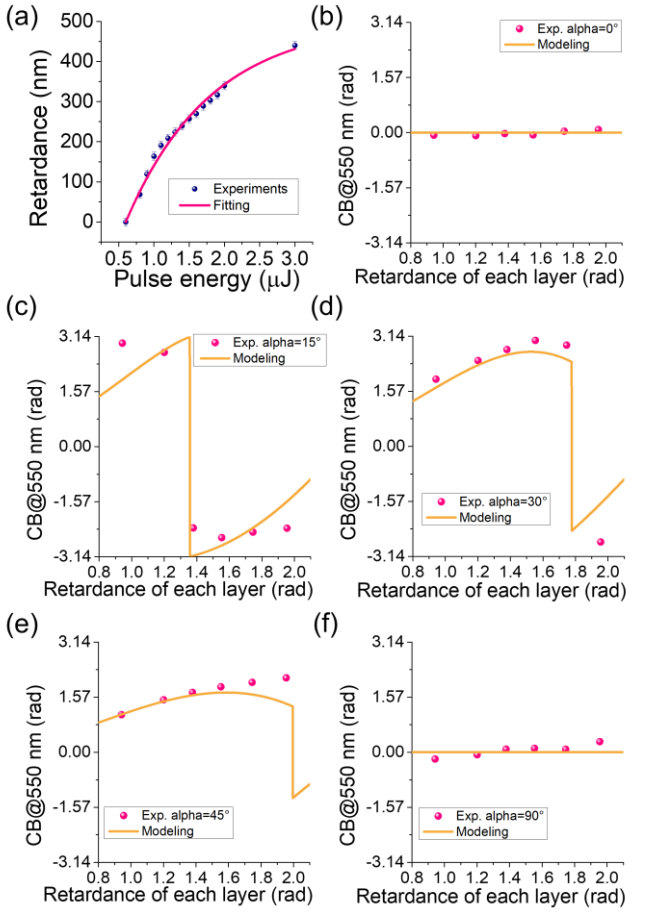


**Fig. 4**. (a) Experimental calibration results of retardance versus laser pulse energy. Experimental (points) and modeling (solid lines) results of four-layer structures with different orientation angle values versus retardance: $\alpha$ = 0°, 15°, 30°, 45°, 90° for (b)-(f), respectively.

The experimental CB and TLB spectroscopic dependence of the four-layer structure, as well as of a single layer structure given for comparison, are reported in **Fig. 3**. In order to reduce the impact of the mechanical stress resulting from the fs-laser-induced net volume expansion, the samples were annealed at 1125 °C for 30 minutes, a method proven to effectively relax the stress-induced birefringence [13]. The studied structure can thus be seen as a four-layers stack written at 1.5 µJ, 1 mm/s with an orientation difference angle α equal to 30°. Intuitively, such a staircase-like pile of layers acts somewhat similarly to a helix and exhibits remarkable CB values of up to -2.25 rad at 550 nm while the TLB value is only 0.64 rad. In contrast, a normal single layer structure written with the same parameters exhibits a very small CB of -0.27 rad but a high TLB value of 2.29 rad, as shown in **Fig. 3**. Our experimental approach thus demonstrates the ability of suppressing the TLB value while achieving high CB in a multilayer chiral waveplate. To quantify the performance of the chiral waveplate, we define an extinction ratio of CB to TLB as follows:

$$ER = 10 * Log(|CB|/|TLB|) \qquad (4)$$

One obtains an ER of 5.5 dB at 550 nm for the chiral waveplate

marked with the blue star located close to the center in the green dash line region in **Fig. 2**. One can still slightly tune the writing parameters and optimize the assembly of multilayers to obtain an even higher ER value by reaching the center of the target region.

Regarding practical applications, one should consider the tailoring of chiral optical properties through simple writing parameters manipulation. Here, we utilize pulse energy as a parameter to tailor the optical properties profile of the multilayer structures. **Figure 4(a)** shows the single layer calibration result of the retardance (expressed in nanometers and related to TLB through $R/\lambda = TLB/\pi$) as a function of the laser pulse energy. We also explore the effect of the increment angle α between adjacent layers. **Figures 4(b-f)** show experimental data combined with modeling results of four-layer structures with different $\alpha$ versus the imprinted retardance. There are a few degrees (7°−8°) of deviation between the nominal and modeled values of $\alpha$, tentatively attributed to a bias in the orientation of the slow axis of the nanogratings, which could be either due to the pulse front tilt (PFT) effect and/or the influence of the stress field on the nanolayers orientation [19]. Temporal and spatial chirps (caused by a slight misalignment of the laser compressor) can lead to PFT effect as investigated by Dai et al. [19]. After accounting for the deviation, we observe a quite good agreement between the experiment and the model for the CB evolution with retardance. Note that if one reduces the increment, the cumulative stress in the transition region cannot be ignored and will affect the chiroptic properties. Besides, if the increment is further reduced so that an overlap of adjacent layers, or even continuous writing, is obtained, the presence of transition regions should be considered and the model should be refined. However, after having modeled different kinds of transition regions, we found that the staircase model of "independent" layers without transition regions described best our experimental results.

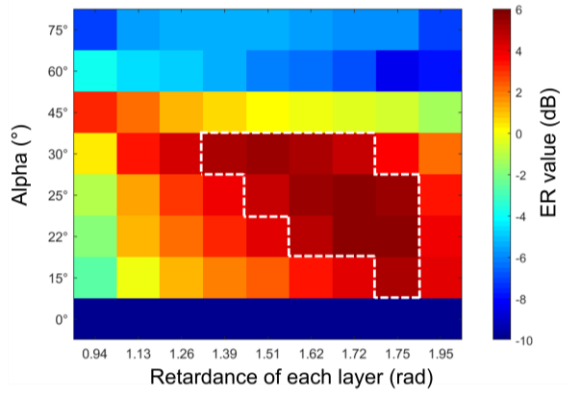


**Fig. 5**. (a) Experimental ER value map of four-layer structures for different orientation angle and retardance values. White dashed line region: the most interesting structures that exhibit ER values higher than 4.5 dB.

Next, we summarize the ER value map of the four-layer structures with different alpha and retardance values. It can be observed in **Fig. 5** that "$\alpha = 0°$" structures exhibit very small ER values (i.e., very small CB but large TLB) whatever the retardance value of the layers. Large ER values (higher than 4.5 dB as delimited by the white dash line) are found in structures with $\alpha$ ranging from 15° to 30° and an easy-to-obtain range of retardances. Thus, complete tailoring of both circular and linear properties can be achieved through an appropriate choice of laser parameters. From a practical viewpoint, one has to take also into account the optical loss of the waveplate (due to absorption and scattering). Our structures exhibited a typical 74% transmission at 550 nm.

In summary, we propose a multilayer strategy for the fabrication of chiral waveplates with suppressed linear birefringence. Our theoretical model indicates the possibility of achieving large CB values accompanied by close-to-zero TLB ones. Experimentally, tailoring circular and linear properties is achieved by tuning the laser parameters (such as, for instance, the laser pulse energy). This work is believed to contribute to the study of fundamental light-matter interaction, as well as to provide new perspectives in laser manufacturing, especially in polarization control devices such as optical rotators and passive optical isolators.

**Disclosures.** The authors declare no conflicts of interest.

**Data availability.** Data is available upon reasonable requirements.

**Funding.** Agence Nationale pour la Recherche, FLAG-IR project (ANR-18-CE08-0004-01); Jiafeng Lu acknowledges the China Scholarship Council (CSC) for the funding No. 202006890077.

## References

1. P. Zijlstra, J. W. M. Chon, and M. Gu, Nature **459**, 410 (2009).
2. J. K. Gansel, M. Thiel, M. S. Rill, M. Decker, K. Bade, V. Saile, G. Von Freymann, S. Linden, and M. Wegener, Science **325**, 1513 (2009).
3. H. Hübener, U. De Giovannini, C. Schäfer, J. Andberger, M. Ruggenthaler, J. Faist, and A. Rubio, Nat. Mater. **20**, 438 (2021).
4. R. Desmarchelier, M. Lancry, M. Gecevicius, M. Beresna, P. G. Kazansky, and B. Poumellec, Appl. Phys. Lett. **107**, 181111 (2015).
5. X. Wang, H. Yu, P. Li, Y. Zhang, Y. Wen, Y. Qiu, Z. Liu, Y. P. Li, and L. Liu, Opt. Laser Technol. **135**, 106687 (2021).
6. K. Sugioka and Y. Cheng, Light Sci. Appl. **3**, e149 (2014).
7. Y. Shimotsuma, P. G. Kazansky, J. Qiu, and K. Hirao, Phys. Rev. Lett. **91**, 247405 (2003).
8. M. Lancry, B. Poumellec, J. Canning, K. Cook, J. C. Poulin, and F. Brisset, Laser Photonics Rev. **7**, 953 (2013).
9. J. Lu, Y. Dai, Q. Li, Y. Zhang, C. Wang, F. Pang, T. Wang, and X. Zeng, Nanoscale **11**, 908 (2019).
10. Y. Shimotsuma, M. Sakakura, P. G. Kazansky, M. Beresna, J. Qiu, K. Miura, and K. Hirao, Adv. Mater. **22**, 4039 (2010).
11. Y. Shimotsuma, K. Miura, and H. Kazuyuki, Int. J. Appl. Glas. Sci. **4**, 182 (2013).
12. B. Poumellec, M. Lancry, R. Desmarchelier, E. Hervé, and B. Bourguignon, Light Sci. Appl. **5**, e16178 (2016).
13. J. Lu, J. Tian, B. Poumellec, E. Garcia-caurel, R. Ossikovski, X. Zeng, and M. Lancry, Light Sci. Appl. accepted, (2022).
14. J. Tian, R. Li, S. H. Yoo, B. Poumellec, E. Garcia-Caurel, R. Ossikovski, M. Stchakovsky, C. Eypert, J. Canning, and M. Lancry, OSA Contin. **2**, 1233 (2019).
15. R. Desmarchelier, M. Lancry, J. Tian, and B. Poumellec, Appl. Phys. Lett. **110**, 021112 (2017).
16. S. H. Yoo, R. Ossikovski, and E. Garcia-Caurel, Appl. Surf. Sci. **421**, 870 (2017).
17. R. Ossikovski, Opt. Lett. **36**, 2330 (2011).
18. R. Ossikovski and O. Arteaga, Opt. Lett. **39**, 4470 (2014).
19. Y. Dai, J. Ye, M. Gong, X. Ye, X. Yan, G. Ma, and J. Qiu, Opt. Express **22**, 28500 (2014).

## **References** (full information)


1. P. Zijlstra, J. W. M. Chon, and M. Gu, "Five-dimensional optical recording mediated by surface plasmons in gold nanorods," Nature 459(7245), 410–413 (2009).

2. J. K. Gansel, M. Thiel, M. S. Rill, M. Decker, K. Bade, V. Saile, G. Von Freymann, S. Linden, and M. Wegener, "Gold helix photonic metamaterial as broadband circular polarizer," Science 325(5947), 1513–1515 (2009).

3. H. Hübener, U. De Giovannini, C. Schäfer, J. Andberger, M. Ruggenthaler, J. Faist, and A. Rubio, "Engineering quantum materials with chiral optical cavities," Nat. Mater. 20(4), 438–442 (2021).

4. R. Desmarchelier, M. Lancry, M. Gecevicius, M. Beresna, P. G. Kazansky, and B. Poumellec, "Achromatic polarization rotator imprinted by ultrafast laser nanostructuring in glass," Appl. Phys. Lett. 107(18), 181111 (2015).

5. X. Wang, H. Yu, P. Li, Y. Zhang, Y. Wen, Y. Qiu, Z. Liu, Y. P. Li, and L. Liu, "Femtosecond laser-based processing methods and their applications in optical device manufacturing: A review," Opt. Laser Technol. 135(November 2020), 106687 (2021).

6. K. Sugioka and Y. Cheng, "Ultrafast lasers-reliable tools for advanced materials processing," Light Sci. Appl. 3, e149 (2014).

7. Y. Shimotsuma, P. G. Kazansky, J. Qiu, and K. Hirao, "Self-organized nanogratings in glass irradiated by ultrashort light pulses," Phys. Rev. Lett. 91(24), 247405 (2003).

8. M. Lancry, B. Poumellec, J. Canning, K. Cook, J. C. Poulin, and F. Brisset, "Ultrafast nanoporous silica formation driven by femtosecond laser irradiation," Laser Photonics Rev. 7(6), 953–962 (2013).

9. J. Lu, Y. Dai, Q. Li, Y. Zhang, C. Wang, F. Pang, T. Wang, and X. Zeng, "Fiber nanogratings induced by femtosecond pulse laser direct writing for in-line polarizer," Nanoscale 11(3), 908–914 (2019).

10. Y. Shimotsuma, M. Sakakura, P. G. Kazansky, M. Beresna, J. Qiu, K. Miura, and K. Hirao, "Ultrafast manipulation of self-assembled form birefringence in glass," Adv. Mater. 22(36), 4039–4043 (2010).

11. Y. Shimotsuma, K. Miura, and H. Kazuyuki, "Nanomodification of glass using fs laser," Int. J. Appl. Glas. Sci. 4(3), 182–191 (2013).

12. B. Poumellec, M. Lancry, R. Desmarchelier, E. Hervé, and B. Bourguignon, "Parity violation in chiral structure creation under femtosecond laser irradiation in silica glass?," Light Sci. Appl. 5(11), e16178 (2016).

13. J. Lu, J. Tian, B. Poumellec, E. Garcia-caurel, R. Ossikovski, X. Zeng, and M. Lancry, "Tailoring chiral optical properties by femtosecond laser direct writing in silica," Light Sci. Appl. accepted, (2022).

14. J. Tian, R. Li, S. H. Yoo, B. Poumellec, E. Garcia-Caurel, R. Ossikovski, M. Stchakovsky, C. Eypert, J. Canning, and M. Lancry, "Spectral dependence of femtosecond laser induced circular optical properties in silica," OSA Contin. 2(4), 1233 (2019).

15. R. Desmarchelier, M. Lancry, J. Tian, and B. Poumellec, "Chiroptical properties photo-induced by femtosecond laser irradiation in silica glass," Appl. Phys. Lett. 110(2), 021112 (2017).

16. S. H. Yoo, R. Ossikovski, and E. Garcia-Caurel, "Experimental study of thickness dependence of polarization and depolarization properties of anisotropic turbid media using Mueller matrix polarimetry and differential decomposition," Appl. Surf. Sci. 421, 870–877 (2017).

17. R. Ossikovski, "Differential matrix formalism for depolarizing anisotropic media," Opt. Lett. 36(12), 2330 (2011).

18. R. Ossikovski and O. Arteaga, "Statistical meaning of the differential Mueller matrix of depolarizing homogeneous media," Opt. Lett. 39(15), 4470 (2014).

19. Y. Dai, J. Ye, M. Gong, X. Ye, X. Yan, G. Ma, and J. Qiu, "Forced rotation of nanograting in glass by pulse-front tilted femtosecond laser direct writing," Opt. Express 22(23), 28500 (2014).

## VI.4 3D STRUCTURED BESSEL BEAM POLARIZATION AND ITS APPLICATION TO IMPRINT CHIRAL OPTICAL PROPERTIES IN SILICA

# 3D structured Bessel beam polarization and its application to imprint chiral optical properties in silica

Cite as: APL Photon. 8, 060801 (2023); doi: 10.1063/5.0140843
Submitted: 31 December 2022 • Accepted: 17 May 2023 •
Published Online: 2 June 2023



Jiafeng Lu,[1,2] Mostafa Hassan,[3] François Courvoisier,[3] Enrique Garcia-Caurel,[4] François Brisset,[1] Razvigor Ossikovski,[4] Xianglong Zeng,[2] Bertrand Poumellec,[1] and Matthieu Lancry[1,a)]

## AFFILIATIONS

[1] Institut de Chimie Moléculaire et des Matériaux d'Orsay, Université Paris Saclay, Orsay 91405, France
[2] Key Laboratory of Specialty Fiber Optics and Optical Access Networks, Joint International Research Laboratory of Specialty Fiber Optics and Advanced Communication, Shanghai Institute for Advanced Communication and Data Science, Shanghai University, Shanghai 200444, China
[3] FEMTO-ST Institute, CNRS, University of Franche-Comté, Besançon 25030, France
[4] LPICM, CNRS, Ecole Polytechnique, Institut Polytechnique de Paris, Palaiseau 91128, France

**Note:** This paper is part of the APL Photonics Special Topic on Ultrafast Laser Fabrication Enabled Photonics and Devices.
[a)]**Author to whom correspondence should be addressed:** matthieu.lancry@universite-paris-saclay.fr

## ABSTRACT

Polarization plays a crucial role in light–matter interactions; hence its overall manipulation is an essential key to unlock the versatility of light manufacturing, especially in femtosecond laser direct writing. Existing polarization-shaping techniques, however, only focus on their manipulation in the transverse plane of light beams, i.e., two-dimensional control. In this paper, we propose a novel passive strategy that exploits a class of femtosecond laser written space varying birefringent elements to shape the polarization state along the optical path. As a demonstration, we generate a three-dimensional structured Bessel beam whose linear polarization state slowly evolves along the focus (typ. 90° within 60λ). Such a "helically polarized" Bessel beam allows imprinting "twisted nanogratings" in $SiO_2$ glass which result in an extrinsic optical chirality at a micrometric scale and own a high optical rotation. Our work provides new perspectives for three-dimensional polarization manipulation and insights into applications in structured light, light–matter interaction, and chiral device fabrication.





## I. INTRODUCTION

Polarization, as a fundamental property of light, lies at the core of many important light-driven applications in various domains, such as light–matter interaction,[1] optical display,[2,3] light sensing,[4] and data storage.[5] In light science, polarization refers to the vibration mode of the electric field vector of light and, thus, corresponds to the spin angular momentum of photons. Hence, polarization manipulation can help control light–matter interactions in a desirable manner to unlock the versatile functions of light-driven technologies, especially in ultrafast laser manufacturing.

Light–matter interaction at the femtosecond (fs) scale consists in their absorption through nonlinear photoionization mechanism, which enables precise energy deposition in any volume of transparent materials without damage to the surrounding.[6] Such a mechanism results in diverse modifications inside the material that are dependent on the laser parameters, such as refractive index three-dimensional (3D) profiling,[7] anisotropic subwavelength nanogratings,[8] and void formation.[9] Owing to their strong anisotropic optical properties and also outstanding thermal properties, nanogratings have attracted significant interest in birefringent element fabrication,[10,11] microfluidic channels,[12] and high temperature sensing.[13,14] Considerable research efforts have proven that, ideally (neglecting tilt effects, for example, the pulse front tilt, PFT), self-organization of nanogratings coincides with fs laser polarization.[8] This may be attributed to a multiple scattered wave

interference mechanism[15,16] and, on the other hand, illustrates that fs laser polarization can dominantly structure nanogratings' orientation in a desirable way. Hence, polarization is a crucial parameter in determining imprinted nanogratings' distribution, which has been adopted as one dimension of the 5D data storage.[17] Within this field, in the work of Sakakura *et al.*, a new type of fs laser induced modification has been recently reported and it consists of random nanopores elongated perpendicular to the laser polarization: "Type X" modification[18] corresponding to the early birth of nanogratings. From an application point of view, these nanostructures exhibit advantages such as ultralow loss with controllable form birefringence enabled by laser polarization.

Polarization is not only important in laser materials processing but also essential for probing and imprinting chiral structures.[19,20] Basically, an object that exhibits chirality possesses the geometric property of being incapable of coinciding with its mirror image by translation and rotation.[21] This feature predominantly results in different chiroptical responses to left- and right-handed circularly polarized lights, which lays the foundation of diverse chiroptic technologies ranging from analytical chemistry to chiral switches in polarization optics.[22–24] Two decades ago, chiral gratings with double helix symmetry were proved to possess polarization-selective properties in the groundbreaking work of Kopp *et al.*[25] Since then, chiral (or helical) long period fiber gratings (LPFGs) and fiber Bragg gratings (FBGs), fabricated on a twisted optical fiber passed through a miniature heat zone or by a helical refractive index modulation in the laser writing process, have gained more attention in torsion and torque sensing, orbital angular momentum mode converters, and circular polarizers.[26–31] The pioneered research that fs lasers can directly induce chiral optical properties inside achiral transparent materials enriches the fundamental mechanisms of light–matter interaction.[19] However, for now, the tailoring of fs laser generated chirality stays on the 2D plane (single layer with small thickness), which restricts the level of chiroptic effects that may be produced. 3D symmetry breaking has been proven to prominently raise chiral optical properties compared to 2D asymmetry.[32] However, most of the existing polarization manipulation techniques consist in 2D transformations through conventional birefringent optics (like waveplates),[33] digital holography (like spatial light modulators, SLMs),[34] or geometric phase optics.[35] These strategies share a common limitation: The polarization behavior and its spatial structuration are considered only in the transverse plane, which makes it difficult

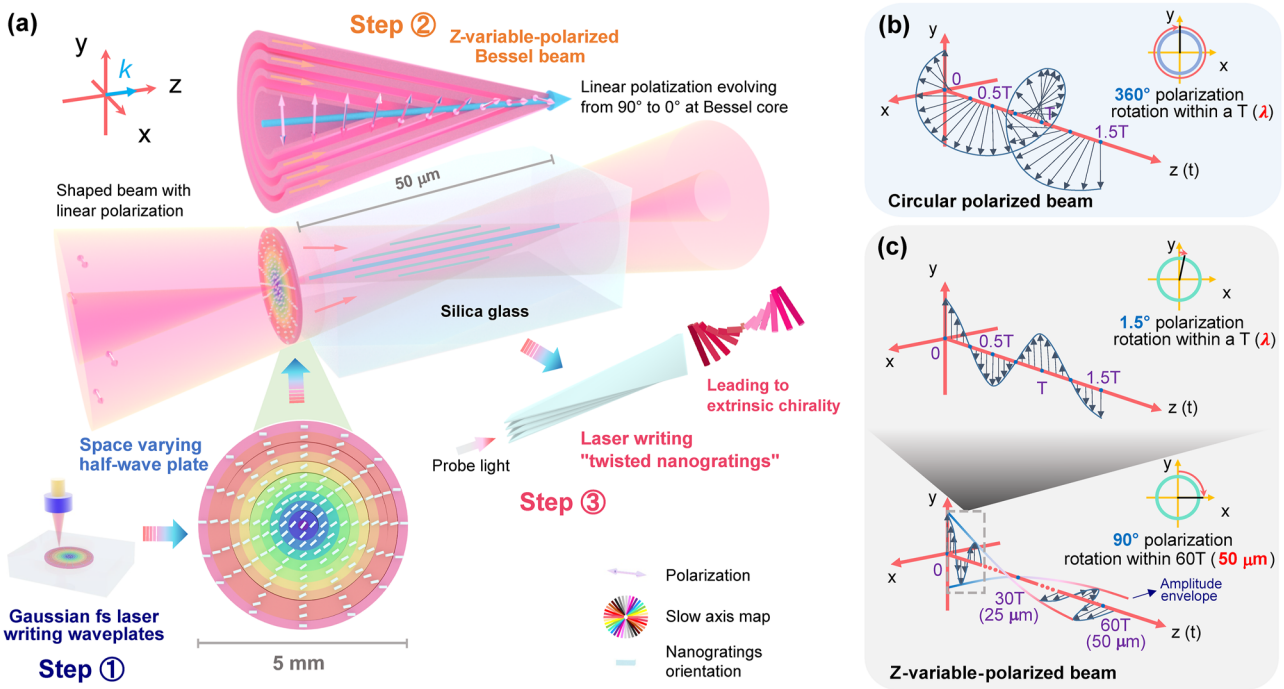


**FIG. 1.** Schematic of the concept of 3D polarization structuring of a Bessel beam via a space varying birefringent element and its application to imprint "twisted nanogratings" for extrinsic chirality. (a) Schematic for generating a *z*-variable-polarized fs Bessel beam by employing a space varying half-wave plate. The homemade wave plate is written by a Gaussian fs laser and then inserted into the Bessel focusing path to convert a linearly polarized Bessel beam into a "*z*-variable-polarized" Bessel beam. That is, it is helically polarized in the central lobe of the Bessel beam: The polarization state is linearly polarized with an orientation that evolves from 90° up to 0° within the 50 $\mu$m focus (along the optical path). Space varying half-wave plate is written at 1030 nm, 800 fs, 100 kHz, 0.16 NA, 1 mm/s, 2.5 $\mu$J. The birefringence slow axis azimuth was varied from 0° at the outside "ring" region to 45° at the central "ring" region. Eventually, such a z-variable-polarized Bessel fs beam is used to imprint "twisted nanogratings" leading to extrinsic optical chirality. "*k*" is the direction of the light wavevector. (b) Schematic of the propagation of a circularly polarized beam shown for the sake of comparison. "*T*" refers to the period of light wave; "$\lambda$" refers to the wavelength of light, i.e., 800 nm for the Bessel fs laser. Here, considering light propagating in free space (speed approximates to velocity of light, *c*), the propagation distance of a single period *T* is equal to $\lambda$. (c) Schematic of the propagation of *z*-variable-polarized beam within a single light wave period (above) and along a 50 $\mu$m long focus (below).

to imprint 3D symmetry breaking and the related chiral optical properties.

In this paper, we present a unified strategy that exploits homemade space varying birefringent optical elements to structure a fs Bessel beam with a polarization function that evolves along its focus. This is a passive method for 3D polarization structuration resulting in a $z$-variable linearly polarized fs Bessel beam. Specifically, we experimentally fabricated a space varying half-wave plate by Gaussian fs laser direct writing and thus created a linearly polarized Bessel beam whose orientation evolves along the optical propagating direction. Such a versatile longitudinal polarization shaping strategy exhibits a strong ability for symmetry breaking along the optical path and, thus, can create strong extrinsic chirality inside transparent materials (here in silica) upon single scanning as depicted in Fig. 1(a). This is just an easy-to-obtain but instructive example of such an advanced direct writing strategy. Indeed, one can even shape the polarization in 3D for any polarization state (linear, circular, or elliptical) in different positions by adjusting the design of the space varying birefringent element. To our knowledge, this is the first report using a $z$-variable-polarized laser beam for laser materials processing. One can envision this work not only to fabricate chiral optical elements with high efficiency but also to inspire new groundbreaking perspectives in 3D light–matter interaction, polarization switching, and light control.

## II. RESULTS

### A. Mathematical description of $z$-variable-polarized Bessel beam and definitions of anisotropic optical properties

Bessel beams that possess non-diffracting nature over long distance[36] can be seen as a coherent superposition of a set of infinite plane waves with their wavevector along the generatrix of a cone with half cone angle θ. The infinite Bessel beam is a propagation-invariant solution of the Helmholtz equation calculated in the work of Durnin *et al.*[37] Because of the conical flow of light in a Bessel beam, the polarization state of the central lobe on the optical axis at a distance $z$ can be controlled from the plane $z = 0$ by the polarization state of the geometrical rays emerging from a circle of radius $r = z \cdot \tan(\theta)$ that will focus in $(r = 0, z)$ as shown in Fig. 1(a).

In our case, we choose to produce linear polarization on the axis with a rotating orientation with propagation distance. In our approach, it can be created with an input polarization distribution where the orientation of the polarization varies with the radius at the $z = 0$ plane. We note that the polarization state in the other lobes of the Bessel beam, outside the central core, is more complex because it is created by the interference of waves with different linear polarization orientations.

The $x$ and $y$ components of the electric field vector on the optical axis can be expressed as

$$\boldsymbol{E}(r = 0, z) = E_0 \cdot \begin{bmatrix} \cos(\alpha(z)) \\ \sin(\alpha(z)) \end{bmatrix} \cdot e^{i(k_z \cdot z - \omega t)}, \quad (1)$$

where $E_0$ and $k_z$ represent the on-axis Bessel beam amplitude and the longitudinal component of the wavevector, respectively. The linear polarization orientation is $\alpha(z) = \frac{\pi}{2} - \rho \cdot z$, where $\rho$ is the rotation speed parameter in rad/m. Therefore, the polarization direction evolves very slowly from 90° at the beginning of the focus ($z = 0$ μm) to 0° at the end of the focus ($z = 50$ μm), so $\rho = \frac{\pi/2\ (\text{rad})}{50\ (\mu\text{m})} = \pi \times 10^4$ rad/m in our experiment. We have tentatively chosen a linear variation of the angle $\alpha(z)$ in our work; however, we also remark that it can be arbitrarily chosen.

The polarization state we create remains linearly polarized, i.e., the field oscillates along a controlled direction and slowly evolves as depicted in Fig. 1(c). Comparing to Fig. 1(b), this contrasts with circular polarization for which the polarization vector rotates during the same period T and cannot induce such "twisted nanogratings." It is somehow expected because at every point, the circularly polarized beam makes a full circle: There is zero preferential direction, as shown in Fig. 1(b). However, note that an elliptically polarized beam can imprint a strong linear birefringence due to anisotropic nanopore formation.[38]

Now, considering our $z$-variable-polarized Bessel fs beam, this kind of "helical polarization distribution" can be utilized to write some chiral nanostructures (such as "twisted nanograting" structures) resulting in significant optical chirality, as illustrated in Fig. 2(a) and studied in "Sec. II D."

In addition, for better describing the subsequent results section that contains many polarimetric properties, the definitions of both linear and circular optical properties are listed in Table I. Moreover, it is more convenient in experiments to consider real polarization effects caused by these anisotropic optical properties to a light beam, which are also included in the table together with their units.

### B. Gaussian fs laser writing space varying birefringent elements

In order to impart 3D polarization manipulation, the key point is to use a space varying birefringent element to shape, point-by-point, the state of polarization of the incident light. This 2D structured light beam with transverse polarization shaping is then converted into polarization variation along the optical path by using Bessel focusing as depicted in Fig. 2(b) resulting in on-axis shaping, i.e., "along a line."

Experimentally, this space varying birefringent element is fabricated by Gaussian fs laser direct writing, as shown in Fig. 1(a). The Gaussian fs laser beam is delivered from a system (Amplitude Systèmes, Pessac, France) operating at $\lambda = 1030$ nm, 800 fs pulse duration, 100 kHz repetition rate and then is focused 1.5 mm below the surface of a 3 mm-thick silica glass wafer (Suprasil CG, Heraeus, Hanau, Germany) by an aspherical lens with 0.16 numerical aperture (NA). Specifically, since the retardance of such a birefringent element is wavelength dependent,[10,39] we designed and fabricated a space varying half-wave plate obtaining a $\lambda/2$ retardance for the targeted wavelength, i.e., a fs Bessel beam at 800 nm. Therefore, the laser parameters were chosen to fall within the nanogratings' regime, resulting in controllable form birefringence. That is, the homogeneous space varying half-wave plate with a diameter of 5 mm is written at 1 mm/s, 2.5 μJ/pulse with spiral trajectory.

Here, we divided the space varying half-wave plate into ten concentric "ring" regions, leading to a simple fabrication process. This is enough to approximate continuous shaping for further 3D polarization manipulation. The linear polarization orientation of the Gaussian fs laser is set differently in each "ring" to imprint form

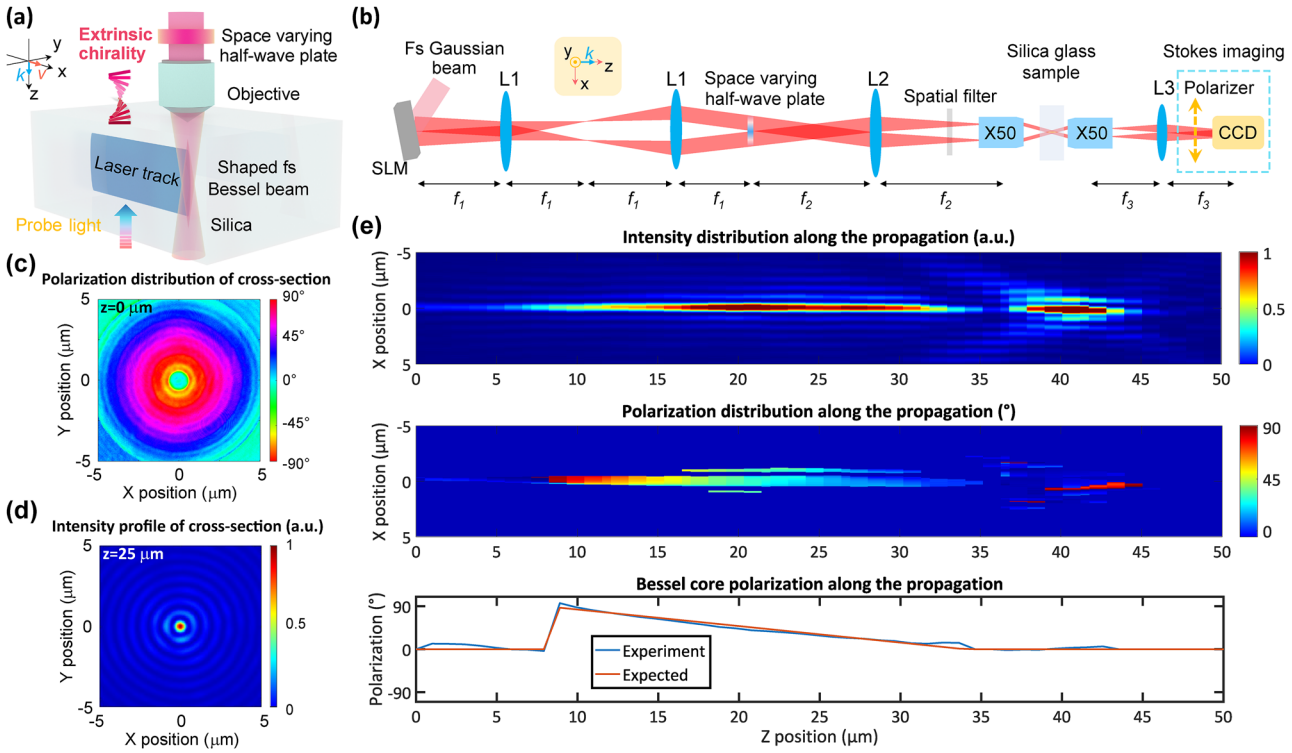


**FIG. 2.** Generation of the *z*-variable-polarized fs Bessel beam using a space varying half-wave plate. (a) Schematics of *z*-variable-polarized fs Bessel beam writing nanogratings in silica glass. *k*: direction of the light wavevector; *v*: fs laser scanning direction. (b) Schematics of light propagation with *z*-variable polarization control (rotation). SLM: spatial light modulator; L1, 2, 3: focusing lenses; $f_{1,2,3}$: focal distance of the corresponding lens; ×50: objective of 50 times; CCD: charge coupled device. The dashed blue rectangle region refers to the Stokes imaging polarimeter. *k*: direction of the light wavevector. (c) Polarization distribution (color map) of cross section of the Gaussian beam (obtained by closing the conical phase on the SLM and measured at $z = 0$ $\mu$m). (d) Intensity profile of cross section of the generated *z*-variable-polarized fs Bessel beam (recorded at $z = 25$ $\mu$m). (e) Characterization of the generated *z*-variable-polarized fs Bessel beam along the propagation: intensity distribution (top panel), polarization distribution color map (middle panel), and quantitative Bessel core polarization distribution curve (bottom panel).

birefringence with a slow axis azimuth that evolves from 0° at the outside "ring" to 45° at the central "ring." This writing process is depicted by both slow axis color map and nanogratings' orientation illustrated in Fig. 1(a).

Then, when using this homemade half-wave plate with slow axis azimuth "rings" distribution from 0° to 45°, we obtain a linear polarization distribution of the output beam ranging from 0°on the outside to 90° inside, as shown in Fig. 2(c). This polarization distribution of the Gaussian beam cross section is measured (using a Stokes imaging polarimeter) before geometric building, just converted by the space varying half-wave plate. Clearly, one can observe a well-structured radial evolution of the linear polarization orientation across the laser beam profile, except for the center. In the current design, it was indeed not possible to imprint birefringence at the chosen speed at 1 mm/s within a central part of about 100 $\mu$m diameter because this leads to extremely large acceleration for our 2D *xy*-scanning platform. However, this technical problem can be easily overcome by using a higher translation speed 2D scanning platform, by a scanning mirror technique, or by filling the central part simply using a line-by-line scanning geometry instead of a spiral trajectory.

### C. Polarization manipulation along the optical path of a fs Bessel beam

Our objective is to realize a *z*-variable-polarized fs Bessel beam that exhibits an evolving but still linear polarization state at different longitudinal *z* axis positions and then to apply it, for the first time, to structure a chosen optical material. To validate such a "helical polarization distribution" along the focus, we first convert a horizontally linearly polarized (0°) Gaussian fs laser beam (from an amplified Ti:Sa laser operating at $\lambda = 800$ nm, 120 fs pulse duration and 1 kHz repetition rate) to a Bessel beam. This was performed by applying, using a spatial light modulator, a conical phase onto the input Gaussian beam: $\Phi(r) = -2\pi r \sin(\theta)/\lambda$, which was imaged 1:1 by a first telescope consisting of two identical lenses (L1) positioned as a classical 4*f*-configuration, as shown in Fig. 2(b).

Then, our space varying half-wave plate was placed precisely at the relay image of the spatial light modulator to shape the 2D polarization. The polarization shaped beam was demagnified by a combination of a 750 mm lens (L2) and a ×50 microscope objective, forming a telescope with lateral magnification ×1/278. Here, a spatial filter ensures that only the zero-order Bessel beam is

**TABLE I.** Linear and circular optical properties: $n_{[]}$, refractive index; $\kappa_{[]}$, absorption index; $d$, thickness of anisotropic layer; $\lambda$, probe light wavelength. "$x$," $x$ axis; "$y$," $y$ axis; "$e$," extraordinary light; "$o$," ordinary light; "−," left-handed; "+," right-handed. The table is reproduced with the permission from the authors of Ref. 20.

| Property | Definition | Commonly described in polarimetry |
|---|---|---|
| LB (linear birefringence) | $\Delta n_L = (n_x - n_y)$ | $LB = \frac{2\pi}{\lambda}(n_x - n_y)\cdot d$ |
| LB′ (45°-linear birefringence) | $\Delta n_{L'} = (n_{45^\circ} - n_{-45^\circ})$ | $LB' = \frac{2\pi}{\lambda}(n_{45^\circ} - n_{-45^\circ})\cdot d$ |
| TLB (total linear birefringence) | $\Delta n_{TLB} = (n_e - n_o)$ <for a uniaxial material> | $TLB = \sqrt{LB^2 + LB'^2}$ |
| LD (linear dichroism) | $\Delta\kappa_L = (\kappa_x - \kappa_y)$ | $LD = \frac{2\pi}{\lambda}(\kappa_x - \kappa_y)\cdot d$ |
| LD′ (45°-linear dichroism) | $\Delta\kappa_{L'} = (\kappa_{45^\circ} - \kappa_{-45^\circ})$ | $LD' = \frac{2\pi}{\lambda}(\kappa_{45^\circ} - \kappa_{-45^\circ})\cdot d$ |
| TLD (total linear dichroism) | $\Delta\kappa_{TLD} = (\kappa_{high} - \kappa_{low})$ | $TLD = \sqrt{LD^2 + LD'^2}$ |
| CB (circular birefringence) | $\Delta n_C = (n_- - n_+)$ | $CB = \frac{2\pi}{\lambda}(n_- - n_+)\cdot d$ |
| Optical rotation | ⋯ | $\theta_r = \frac{\pi}{\lambda}(n_- - n_+)\cdot d\cdot\frac{180^\circ}{\pi}$ |
| CD (circular dichroism) | $\Delta\kappa_C = (\kappa_- - \kappa_+)$ | $CD = \frac{2\pi}{\lambda}(\kappa_- - \kappa_+)\cdot d$ |

transmitted to the following focusing stage. Owing to the long focal region (~50 $\mu$m) of the Bessel beam, the polarization distribution in the transverse plane can be transformed so as to vary along the $z$ axis, as shown conceptually in the polarization evolution schematics reported in Fig. 1(a). The produced $z$-variable-polarized Bessel beam has a cone half angle $\theta = 12.5^\circ$ (central core of 0.7 $\mu$m FWHM). In these conditions due to the use of Bessel beam, we can shape the polarization state on the axis itself, i.e., along a line.

Eventually, a second ×50 objective and a lens L3 are used to enable imaging in a charge coupled device (CCD) camera. The cross section intensity profile image of the middle of the structured light beam ($z$ = 25 $\mu$m) is recorded in Fig. 2(d), which confirms the spatial profile of a Bessel beam. The intensity distribution and the polarization state distribution along the propagation of the shaped Bessel beam are also characterized experimentally, as shown in Fig. 2(e). Since the Bessel beam has a focal region about 50 $\mu$m, we move the CCD camera to obtain the intensity profile of the $z$-variable-polarized Bessel beam at each $z$ axis position. In addition, the polarization distribution along the direction of propagation is measured similarly moving the camera but combined with a rotating polarizer to build a Stokes imaging polarimeter.[40]

It is to be mentioned that one can adjust the focusing conditions, for example, the diameter of the incident fs Gaussian beam, the apex angle of the axicon through the spatial light modulator and telescope demagnification, so as to obtain either a longer or shorter focal region of the $z$-variable-polarized Bessel beam. Then, both the polarization spatial distribution (middle panel) and the quantitative curve (polarization of the Bessel central core, bottom panel) are found to show good "helical polarization distribution" after $z$ = 9 $\mu$m, i.e., the polarization evolves from 90° at the beginning to 0° at the end of the fs Bessel beam.

### D. Longitudinal rotation of nanogratings fabricated by the *z*-variable-polarized fs Bessel beam

Since the nanogratings' orientation is well controlled by fs laser polarization (ideally perpendicular, considering no PFT and normal incidence), to gain insight into their manipulation during a single laser scan, we used the $z$-variable-polarized fs Bessel beam to tentatively imprint "twisted nanogratings."

Experimentally, the laser track is written by scanning the $z$-variable-polarized fs Bessel beam along $x$ axis inside the silica glass, as depicted in Fig. 2(a). Then, the written line is cut perpendicular to the $x$ axis to get the cross section of the laser track in the $y$–$z$ plane. Thus, we can see the overall nanogratings' orientation along $z$ axis for a single laser track, as shown in "Step ③" of Fig. 1(a). This schematic image shows the cross section view of the fs laser written track where the nanogratings' orientation is rotating. Note that this kind of "twisted nanograting" is obtained through a single pass writing using the "helical Bessel beam" with laser parameters set at 800 nm, 120 fs, 1 kHz, 0.8 NA, 10 $\mu$m/s, 0.6 $\mu$J and focused 250 $\mu$m below the surface of a 400 $\mu$m-thick silica slide (Suprasil CG, Heraeus, Hanau, Germany). Then, the laser track is captured by scanning electron microscope (SEM, ZEISS SUPRA 55 VP, 1 kV accelerating voltage) using secondary electrons imaging. Figure 3(a) depicts the global cross-sectional view of the photoinduced track. Obviously, the SEM images show rotation morphology from head to tail along the laser track due to the linear polarization evolving along the fs Bessel beam. Zoomed-in images of the head, middle, and tail regions of the same laser track are shown in Figs. 3(b$_1$)–3(b3), respectively. Note that because the polarization rotation plane is perpendicular to the SEM observation cross section (making it difficult to describe the polarization rotation in a 2D drawing), the axial labels on the right of each detailed SEM image are slightly tilted as to depict the different polarization directions at different positions from a 3D viewpoint. Here, in order to describe the SEM images related to the nanogratings distribution, we define the polarization configuration as "scanning direction + polarization direction" since the laser polarization is different at different $z$ positions of the $z$-variable-polarized fs Bessel beam.

One can observe clear nanopores at the head of the laser track due to an "Xx" polarization configuration and well-oriented nanolayers at the tail of the laser track due to an "Xy" polarization configuration. In the middle of the laser track, one can see the

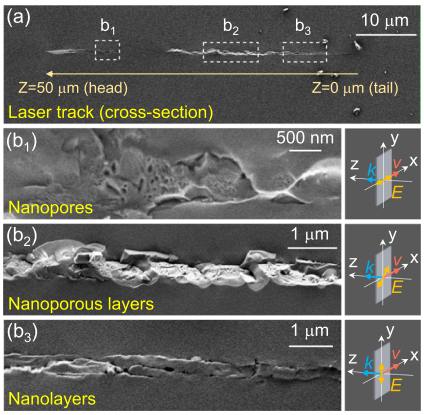


**FIG. 3.** SEM cross section images of *z*-variable-polarized fs Bessel beam written nanogratings in $SiO_2$ with the parameters set at 800 nm, 120 fs, 1 kHz, 0.8 NA, 10 $\mu$m/s, 0.6 $\mu$J. (a) An overall view of the cleaved laser track. Detailed pictures of the head ($b_1$), the middle ($b_2$), and the tail ($b_3$) of the laser track. The axial labels are presented at the right part corresponding to each detailed SEM image. *k*: direction of the light wavevector; *v*: fs laser scanning direction; *E*: electric field direction of the fs Bessel beam (polarization direction).

nanoporous layers due to a "X + 45°" configuration since the layers are tilted out of the plane. The depicted nanopores located in the nanolayer are mainly attributed to the decomposition of silica from $SiO_2$ to $SiO_{2(1-x)} + x \cdot O_2$. This subsequently results in expulsion of ionized oxygen atoms to the surrounding lattice assisted by a tensile stress, which has been recently revisited as a tensile stress assisted nano-cavitation process leading to the formation of a "self-assembly" of anisotropic nanopores.[41,42]

The experimental results show a kind of "twisted nanogratings" distribution. It is thus a fact that the *z*-variable-polarized fs Bessel beam possesses different linear polarization orientations at different *z* positions, leading to different arrangements of the nanogratings (from head to tail). Hence, it can be expected that an arbitrary, longitudinal orientation distribution of nanogratings can be enabled by designed polarization conversions of the laser beam through space varying birefringent elements, combined with Bessel focusing.

### E. *z*-variable-polarized fs Bessel beam written chirality

As a result of the varying orientation (here, a 3D rotation) of the nanogratings generated by the *z*-variable-polarized fs Bessel beam, strong symmetry breaking is obtained, leading to chiral optical properties. To highlight the achieved optical performance, a 45° linearly polarized fs Bessel beam was used for comparison. The latter choice is justified because 45° linearly polarized fs laser beams have been proven to imprint highest chiral optical properties among all linearly polarized fs laser beams.[19,20]

First, the retardance induced by both the 45° linearly polarized fs Bessel beam and the *z*-variable-polarized fs Bessel beam was characterized by a polarizing microscope (Olympus BX51, Tokyo, Japan) equipped with a "de Sénarmont" compensator. The "de Sénarmont" arrangement uses a highly precise quarter-wave plate and a 180°-rotation analyzing polarizer to perform retardance measurements with a typical error range within ±10 nm at the wavelength of 550 nm. Here, the retardance is the optical phase difference related to total linear birefringence (TLB); the relationship between these two quantities is given by $TLB/\pi = retardance/\lambda$.

Figure 4(a) reports the retardance results of samples irradiated by both 45° linearly polarized fs Bessel beam and *z*-variable-polarized fs Bessel beam at different pulse energies. Clearly, the retardance induced by the *z*-variable-polarized fs Bessel beam is less (by one half roughly) than that induced by the 45° linearly polarized fs Bessel beam. It is mainly attributed to the (partial) suppression of linear birefringence due to different slow axes at different *z* positions as investigated in our previous work.[33] In addition, the insets show the corresponding crossed-polarizer microscopic images of the irradiated samples at a pulse energy of 1.1 $\mu$J as an illustration. The colors of different samples are due to different retardance amplitudes in agreement with Michel–Levy color chart, which also confirms a lower retardance when using the *z*-variable-polarized fs Bessel beam instead of the 45° linearly polarized fs Bessel beam. Furthermore, since an object that possesses chiral optical properties can rotate the polarization plane of a linearly polarized probe light (a so-called optical rotation), one can measure this optical rotation (with an error of ±1°) to unveil the chiral optical properties in a simple way as shown in Fig. 4(b). The results clearly indicate higher (twice as high, roughly) optical rotation values for the *z*-variable-polarized fs Bessel beam written samples compared to the 45° linearly polarized fs Bessel beam written samples.

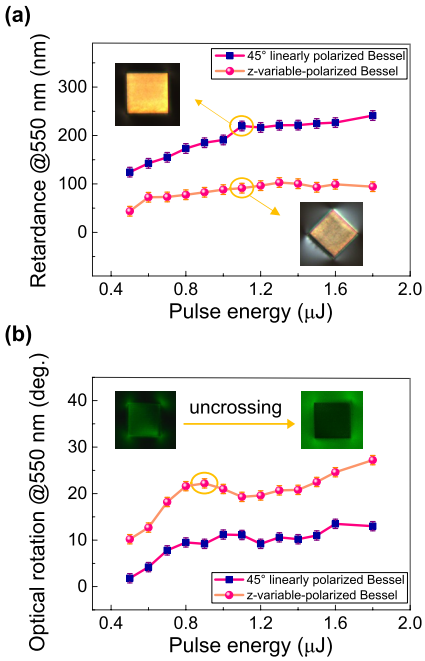


**FIG. 4.** Optical characterizations enabled by crossed-polarizer microscopy. $SiO_2$ samples are written at 800 nm, 120 fs, 1 kHz, 0.8 NA, 10 $\mu$m/s. (a) Retardance measurements at different laser pulse energies written by both the 45° linearly polarized fs Bessel beam and the *z*-variable-polarized fs Bessel beam. (b) Optical rotation measurements with different laser pulse energies written by both the 45° linearly polarized fs Bessel beam and the *z*-variable-polarized fs Bessel beam. Measurements are done at 550 nm.

As confirmed experimentally, the *z*-variable-polarized fs Bessel beam can modify the nanogratings' orientation along the optical path, thus forming a chiral structure on the micrometric scale. This appealing feature allows the fabrication of chiral wave plates (wave plates that exploit chiral optical properties to control the light propagation, especially for polarization manipulation) with high circular birefringence and a rather small (ideally none) linear birefringence.

To quantitatively characterize the performances of imprinting extrinsic chirality in $SiO_2$ using this *z*-variable-polarized fs Bessel beam, a spectroscopic Mueller polarimeter (based on a modified Smart SE ellipsometer, JY HORIBA) was used to obtain the Mueller matrix of each sample. The obtained Mueller matrix was subsequently decomposed by differential decomposition, thus providing the differential matrix of the irradiated sample,[43,44] which allows easy determination of all the anisotropic optical properties of the sample as follows:

$$M_{diff} = \begin{bmatrix} 0 & LD & LD' & CD \\ LD & 0 & CB & -LB' \\ LD' & -CB & 0 & LB \\ CD & LB' & -LB & 0 \end{bmatrix}. \quad (2)$$

As a result, the values (expressed in radians) of both the linear properties and the circular properties are obtained simultaneously. The TLB value can be calculated by $TLB = \sqrt{LB^2 + LB'^2}$, as shown in Table I.

Experimentally, homogeneous square-shaped samples with a size of 0.2 × 0.2 $mm^2$ were written using *z*-variable-polarized fs Bessel beam, 45° linearly polarized fs Bessel beam, and 0° linearly polarized fs Gaussian beam (for comparison). Each square is made of a set of lines with a pitch of 1 $\mu$m and the line scanning direction is always along "+X" direction to avoid any nonreciprocal or "quill" writing.[45,46] Then, the samples were measured with a spectroscopic Mueller polarimeter in transmission mode. Figure 5 displays the spectroscopic results for both TLB (solid lines) and circular birefringence (CB) (dashed lines) of a *z*-variable-polarized fs Bessel beam (red), a 45° linearly polarized fs Bessel beam (blue), and a 0° linearly polarized fs Gaussian beam (gray).

A large difference in both TLB and CB values can be observed between the different fs laser beam configurations. Clearly, the *z*-variable-polarized fs Bessel beam simultaneously induces large CB yet small TLB over the entire measuring wavelength range from 450 to 1000 nm. By the way, both anisotropic optical properties exhibit large values at small wavelengths and decrease with increasing wavelength due to their 1/λ inherent behavior according to the descriptions depicted in Table I.

To further explore the optical response and to tailor the optical properties of the *z*-variable-polarized fs Bessel beam written extrinsic chirality in silica glass, a set of pulse energies (all the other laser parameters being fixed) was adopted for investigating both TLB and CB properties, as shown in Fig. 6. Thus, for the *z*-variable-polarized fs Bessel beam written samples, the CB value reaches −0.2 rad (which, in absolute value, is three times as much

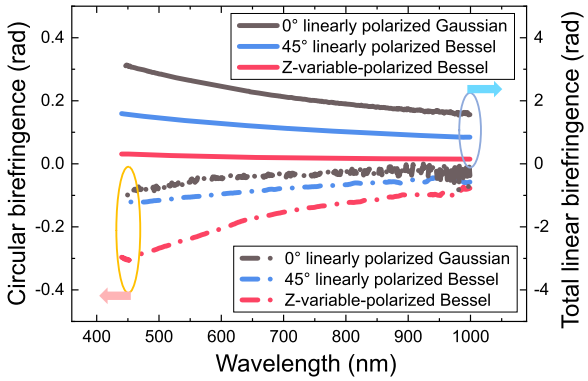


**FIG. 5.** Spectroscopic Mueller polarimetry results for circular birefringence (dashed lines) and total linear birefringence (solid lines) of $SiO_2$ samples written by a 0° linearly polarized fs Gaussian beam (gray), a 45° linearly polarized fs Bessel beam (blue), and a *z*-variable-polarized fs Bessel beam (red). Laser parameters are 800 nm, 120 fs, 1 kHz, 0.8 NA, 10 $\mu$m/s, 0.7 $\mu$J.

as the CB created by the 45° linearly polarized fs Bessel beam) over the laser pulse energy range of 0.7–1.0 $\mu$J. If one considers the induced TLB as well, 0.7 $\mu$J is definitely the optimal laser energy parameter since it exhibits a TLB value of only 0.2 rad, which is four times as less as the TLB induced by the 45° linearly polarized fs Bessel beam. In similar conditions, a 0° linearly polarized fs Bessel (or Gaussian) beam writing would generate negligible circular properties.[20]

These results explicitly provide a new pathway to fabricate chiral wave plates with high CB and almost suppressed TLB. This is a novel and more integrated approach, which differs from our previous strategy of utilizing multilayer configurations.[33]

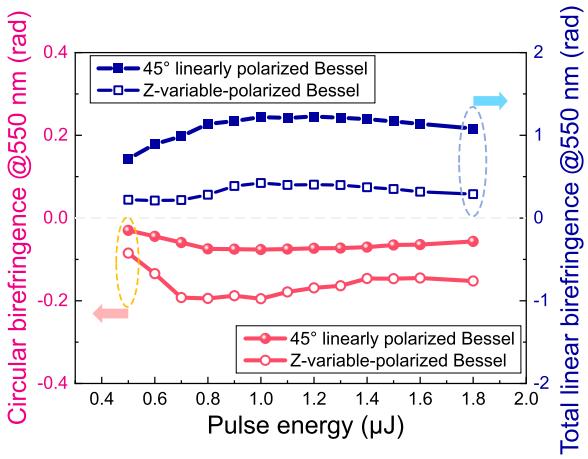


**FIG. 6.** Mueller polarimetry results of circular birefringence (red) and total linear birefringence (blue) of the $SiO_2$ samples written at different laser pulse energies by both 45° linearly polarized fs Bessel beam (full symbols) and *z*-variable-polarized fs Bessel beam (hollow symbols). Measurements are done at 550 nm. $SiO_2$ samples are written at 800 nm, 120 fs, 1 kHz, 0.8 NA, 10 $\mu$m/s.

## III. DISCUSSION AND CONCLUSION

### A. Controlling the nanogratings' orientation by fs laser polarization

Since the first morphology observations performed in the work of Shimotsuma *et al.* in 2003,[8] fs laser written nanogratings have attracted tremendous attention in the field of ultrafast light–matter interaction. However, until now, the mechanism of nanogratings formation has remained unclear. Several compelling assumptions have emerged in explaining the fundamentals of nanogratings formation process. For instance, it was proposed in the work of Shimotsuma *et al.*[8] that interference between the light field and a bulk plasma wave may account for nanogratings formation, especially in explaining their periodicity, whereas other groups proposed a scattered waves interference model.[15,16] Recently, our group has revealed the occurrence of elongated nanopores, thus leading to the formation of nanolayers. Ultrafast silica decomposition through nanocavitation was proposed as a tentative explanation.[41] Although direct evidence for the ultrafast process is difficult to obtain because of the limited frame rate and time resolution of camera, the imprinted orientation of nanogratings distribution has been proved to be almost perpendicular to laser polarization.[8] In addition, it has been discussed that PFT can lead to a small tilt in the nanogratings' orientation due to spatiotemporal chirp and angular dispersion. When light propagates to the focal plane, PFT-related effects grow exponentially and can induce a few degrees of tilt at 100 fs/mm to the nanogratings.[47] Nevertheless, this tilt in question represents only a small deviation from the nanogratings' orientation.

### B. Origin of the written chirality

The chirality originates from molecular chiral arrangement at the nanoscale, that is, intrinsic chirality contributes to optical activity and, thus, to the manifestation of chiral optical properties. However, the chiral optical properties can also arise due to the so-called extrinsic chirality, which is related to a chiral object constructed in an experimental arrangement not coincident with its mirror image.[48] Hence, recently we have advanced a novel conceptual view according to which the fs laser written extrinsic chirality arises from two contributions: a form-related birefringence and a stress-related birefringence with non-parallel and non-perpendicular neutral axes. We therefore deal with extrinsic chirality arising from the experimental arrangement of linear optical properties.[20] Compared to intrinsic chirality, extrinsic chirality can exhibit larger optical rotation due to strong symmetry breaking at a larger, typically micrometric scale. In this paper, the *z*-variable-polarized fs Bessel beam-driven orientation rotated nanogratings structure is a form of experimental chiral arrangement corresponding to extrinsic chirality and is potentially useful in the fabrication of chiral devices with large and controllable optical rotation.

### C. *z*-variable-polarized fs Bessel beam writing vs multilayer strategy

In regard to extrinsic chirality implantation, the multilayer strategy has proven to be a realizable approach for generating high CB with minimal TLB due to (partial) suppression of linear birefringence through the alignment of fast/slow axes of different layers.[20,33] However, such a multilayer strategy features limitations, such as low fabrication speed and requirement for precise alignment between layers. Geometrically, the multilayer strategy amounts to fabricating a staircase-like chiral arrangement without transition region between layers. Conversely, the *z*-variable-polarized fs Bessel beam writing approach can help accomplish the following: (1) It can facilitate the writing task in a single scan—which leads to high efficiency—and, thus, unlock the versatility of fabricating chiral devices in a fast manner; (2) more importantly, *z*-variable-polarized fs Bessel beam irradiation enables a quasi-gradual evolution of polarization, that is, a smoother variation of the nanogratings' orientation compared to the staircase-like structure written by using the multilayer strategy. Note that by further engineering the space varying birefringent elements, one can tailor a continuous chiral arrangement by choosing the pitch and the length of the "twisted silica glass." However, the absolute CB value appears to be not so large if compared, for example, to our best multilayer structure results (CB = −2.25 rad with a total thickness of 340 $\mu$m, measured at 550 nm).[33] Therefore, for a multilayer strategy, the CB per unit length is calculated to be −6.6 rad/mm whereas for a *z*-variable-polarized fs Bessel beam writing, it is around −5.0 rad/mm (i.e., −0.2 rad with a thickness of 40 $\mu$m). This preliminary result is attributed to the relatively short extent of the Bessel beam used in this study, which could be enlarged by, for example, using a smaller demagnification factor of the imaging telescope. Nevertheless, if compared to 45° linearly polarized fs Bessel beam writing under identical conditions, our results clearly prove the potential of implanting high CB by using such a controllable "helical polarization distribution."

In view of practical applications, one needs to consider the limitations of this strategy as well: (1) To date, the fs laser written space varying birefringent elements have been based on self-organized nanogratings whose nanoporous structures can lead to strong scattering losses. The spectral signature possesses a $1/\lambda^4$ dependence and corresponds to a strong anisotropic loss in the ultraviolet–visible range,[49] which exemplified to be a 74% transmittance measured at 550 nm. However, this restriction is expected to be partly solved by employing a "Type X" modification with its ultralow loss.[18] (2) It is difficult to use our shaping strategy in the mid-infrared range, which needs further work to imprint higher birefringence, such as in ZnO-Barium Gallo-Germanate glasses.[50] (3) The spatial resolution of the fs written space varying wave plate is on the order of micrometer size, which might restrict their potential of applications in sub-micrometer and nanometer scale integrated systems.

### D. Conclusion and potential applications

In summary, in view of the current state of light control, we proposed a novel concept to extend polarization manipulation along the optical path, which provides new perspectives in polarization transformation and, therefore, enriches the state of the art of light manipulation. A stable "helical polarization distribution" fs Bessel beam was generated for the first time by using a fs written space varying half-wave plate. In addition, for the first time, according to our knowledge, such a *z*-variable-polarized laser beam was implemented for laser materials processing in silica glass. This enables the experimental achievement of twice as large circular birefringence with, simultaneously, four times smaller linear birefringence, compared to a 45° linearly polarized fs Bessel beam or Gaussian beam.

Several applications would benefit from this 3D polarization structuring strategy: (1) This technique can be directly used for chiral wave plates fabrication in linear polarization rotators with high optical rotation and ultimately no linear birefringence. Our proposed optical rotators own advantages of alignment-free compared to conventional half-wave plate and potential achromatic properties. (2) Since polarization is an essential parameter in 5D data storage,[5] our strategy of 3D control of polarization may be useful for increasing the writing and reading speed. Optical chirality could even be a new dimension for increasing the capacity of information storage. (3) This 3D polarization structuring approach will be beneficial for obtaining a fundamental understanding of light–matter interaction and will allow ultrafast light manipulation with additional degrees of freedom. For example, this could provide a platform for laser-based production of cholesteric liquid crystal analogous optical devices using tiny lengths of inorganic glass, i.e., "twisted silica glass." In general, it will not only facilitate the implementation of polarization optics through the mediation of space varying optical devices but also underpin numerous potential chiroptic applications, such as passive isolators, quantum emitters, optical tweezers, achromatic devices, and beyond.

## ACKNOWLEDGMENTS

This work was supported by Agence Nationale pour la Recherche, FLAG-IR project (Grant No. ANR-18-CE08-0004-01) and European Research Council (ERC) Grant No. 682032-PULSAR; Jiafeng Lu thanks the China Scholarship Council (CSC) for the funding Grant No. 202006890077.

## AUTHOR DECLARATIONS

### Conflict of Interest

The authors have no conflicts to disclose.

### Author Contributions

M.L. supervised the project. J.L., F.C., and M.L. wrote the manuscript. J.L. carried out the design and fabrication of the space varying birefringent elements. M.H. and F.C. carried out the Bessel beam generation and laser writing. J.L. carried out the sample treatment and optical properties characterization. J.L. and E.G.-C. performed the Mueller polarimetry measurements. J.L., F.B., and M.L. performed the SEM measurements. J.L., M.H., F.C., and M.L. processed and analyzed the data. J.L., M.L., F.C., E.G.-C., R.O., B.P., and X.Z. discussed the experimental results. All authors commented and discussed this work.

**Jiafeng Lu**: Data curation (equal); Formal analysis (equal); Funding acquisition (equal); Investigation (equal); Methodology (equal); Software (equal); Validation (equal); Visualization (equal); Writing – original draft (equal); Writing – review & editing (equal). **Mostafa Hassan**: Data curation (equal); Formal analysis (equal); Investigation (lead); Methodology (equal); Validation (equal); Visualization (supporting). **François Courvoisier**: Conceptualization (equal); Data curation (equal); Formal analysis (equal); Funding acquisition (equal); Investigation (equal); Project administration (equal); Resources (equal); Supervision (equal); Writing – original draft (equal); Writing – review & editing (lead). **Enrique Garcia-Caurel**: Data curation (equal); Formal analysis (equal); Investigation (supporting); Methodology (supporting); Writing – review & editing (equal). **François Brisset**: Data curation (equal); Investigation (equal). **Razvigor Ossikovski**: Data curation (supporting); Formal analysis (supporting); Methodology (supporting); Writing – review & editing (lead). **Xianglong Zeng**: Supervision (equal). **Bertrand Poumellec**: Conceptualization (equal). **Matthieu Lancry**: Conceptualization (lead); Data curation (equal); Formal analysis (lead); Funding acquisition (lead); Project administration (lead); Resources (lead); Supervision (lead); Validation (equal); Writing – original draft (equal); Writing – review & editing (equal).

## DATA AVAILABILITY

The data that support the findings of this study are available from the corresponding author upon reasonable request.

## REFERENCES

[1] K. Sugioka and Y. Cheng, "Ultrafast lasers-reliable tools for advanced materials processing," Light: Sci. Appl. **3**(1), e149 (2014).
[2] D. Wen, J. J. Cadusch, J. Meng, and K. B. Crozier, "Vectorial holograms with spatially continuous polarization distributions," Nano Lett. **21**(4), 1735–1741 (2021).
[3] C. Xie, R. Meyer, L. Froehly, R. Giust, and F. Courvoisier, "In-situ diagnostic of femtosecond laser probe pulses for high resolution ultrafast imaging," Light: Sci. Appl. **10**(1), 126 (2021).
[4] A. Yan, S. Huang, S. Li, R. Chen, P. Ohodnicki, M. Buric, S. Lee, M.-J. Li, and K. P. Chen, "Distributed optical fiber sensors with ultrafast laser enhanced Rayleigh backscattering profiles for real-time monitoring of solid oxide fuel cell operations," Sci. Rep. **7**(1), 9360 (2017).
[5] H. Wang, Y. Lei, L. Wang, M. Sakakura, Y. Yu, G. Shayeganrad, and P. G. Kazansky, "100-layer error-free 5D optical data storage by ultrafast laser nanostructuring in glass," Laser Photonics Rev. **16**(4), 2100563 (2022).
[6] M. Beresna, M. Gecevičius, and P. G. Kazansky, "Ultrafast laser direct writing and nanostructuring in transparent materials," Adv. Opt. Photonics **6**(3), 293–339 (2014).
[7] K. M. Davis, K. Miura, N. Sugimoto, and K. Hirao, "Writing waveguides in glass with a femtosecond laser," Opt. Lett. **21**(21), 1729–1731 (1996).
[8] Y. Shimotsuma, P. G. Kazansky, J. Qiu, and K. Hirao, "Self-organized nanogratings in glass irradiated by ultrashort light pulses," Phys. Rev. Lett. **91**(24), 247405 (2003).
[9] X. Wang, F. Chen, Q. Yang, H. Liu, H. Bian, J. Si, and X. Hou, "Fabrication of quasi-periodic micro-voids in fused silica by single femtosecond laser pulse," Appl. Phys. A **102**(1), 39–44 (2011).
[10] M. Lancry, R. Desmarchelier, K. Cook, B. Poumellec, and J. Canning, "Compact birefringent waveplates photo-induced in silica by femtosecond laser," Micromachines **5**(4), 825–838 (2014).
[11] J. Lu, Y. Dai, Q. Li, Y. Zhang, C. Wang, F. Pang, T. Wang, and X. Zeng, "Fiber nanogratings induced by femtosecond pulse laser direct writing for in-line polarizer," Nanoscale **11**(3), 908–914 (2019).
[12] C. Hnatovsky, R. S. Taylor, E. Simova, P. P. Rajeev, D. M. Rayner, V. R. Bhardwaj, and P. B. Corkum, "Fabrication of microchannels in glass using focused femtosecond laser radiation and selective chemical etching," Appl. Phys. A **84**(1–2), 47–61 (2006).
[13] S. Mihailov, D. Grobnic, C. Hnatovsky, R. Walker, P. Lu, D. Coulas, and H. Ding, "Extreme environment sensing using femtosecond laser-inscribed fiber Bragg gratings," Sensors **17**(12), 2909 (2017).

[14]Y. Wang, M. Cavillon, J. Ballato, T. Hawkins, T. Elsmann, M. Rothhardt, R. Desmarchelier, G. Laffont, B. Poumellec, and M. Lancry, "3D laser engineering of molten core optical fibers: Toward a new generation of harsh environment sensing devices," Adv. Opt. Mater. **10**(18), 2200379 (2022).
[15]R. Buschlinger, S. Nolte, and U. Peschel, "Self-organized pattern formation in laser-induced multiphoton ionization," Phys. Rev. B **89**(18), 184306 (2014).
[16]A. Rudenko, J. P. Colombier, T. E. Itina, and R. Stoian, "Genesis of nanogratings in silica bulk via multipulse interplay of ultrafast photo-excitation and hydrodynamics," Adv. Opt. Mater. **9**(20), 2100973 (2021).
[17]J. Zhang, M. Gecevičius, M. Beresna, and P. G. Kazansky, "Seemingly unlimited lifetime data storage in nanostructured glass," Phys. Rev. Lett. **112**(3), 033901 (2014).
[18]M. Sakakura, Y. Lei, L. Wang, Y.-H. Yu, and P. G. Kazansky, "Ultralow-loss geometric phase and polarization shaping by ultrafast laser writing in silica glass," Light: Sci. Appl. **9**(1), 15 (2020).
[19]B. Poumellec, M. Lancry, R. Desmarchelier, E. Hervé, and B. Bourguignon, "Parity violation in chiral structure creation under femtosecond laser irradiation in silica glass?," Light: Sci. Appl. **5**(11), e16178 (2016).
[20]J. Lu, J. Tian, B. Poumellec, E. Garcia-caurel, R. Ossikovski, X. Zeng, and M. Lancry, "Tailoring chiral optical properties by femtosecond laser direct writing in silica," Light: Sci. Appl. **12**(1), 46 (2023).
[21]Y. Kim, B. Yeom, O. Arteaga, S. Jo Yoo, S.-G. Lee, J.-G. Kim, and N. A. Kotov, "Reconfigurable chiroptical nanocomposites with chirality transfer from the macro- to the nanoscale," Nat. Mater. **15**(4), 461–468 (2016).
[22]M. B. Steffensen, D. Rotem, and H. Bayley, "Single-molecule analysis of chirality in a multicomponent reaction network," Nat. Chem. **6**(7), 603–607 (2014).
[23]Y. Wang and Q. Li, "Light-driven chiral molecular switches or motors in liquid crystals," Adv. Mater. **24**(15), 1926–1945 (2012).
[24]J. K. Gansel, M. Thiel, M. S. Rill, M. Decker, K. Bade, V. Saile, G. Von Freymann, S. Linden, and M. Wegener, "Gold helix photonic metamaterial as broadband circular polarizer," Science **325**(5947), 1513–1515 (2009).
[25]V. I. Kopp, V. M. Churikov, J. Singer, N. Chao, D. Neugroschl, and A. Z. Genack, "Chiral fiber gratings," Science **305**(5680), 74–75 (2004).
[26]V. I. Kopp and A. Z. Genack, "Chiral fibres: Adding twist," Nat. Photonics **5**(8), 470–472 (2011).
[27]C. Liao, K. Yang, J. Wang, Z. Bai, Z. Gan, and Y. Wang, "Helical microfiber Bragg grating printed by femtosecond laser for refractive index sensing," IEEE Photonics Technol. Lett. **31**(12), 971–974 (2019).
[28]S. Oh, K. R. Lee, U.-C. Paek, and Y. Chung, "Fabrication of helical long-period fiber gratings by use of a $CO_2$ laser," Opt. Lett. **29**(13), 1464–1466 (2004).
[29]C. Ma, J. Wang, and L. Yuan, "Review of helical long-period fiber gratings," Photonics **8**(6), 193 (2021).
[30]X. Zhang, A. Wang, R. Chen, Y. Zhou, H. Ming, and Q. Zhan, "Generation and conversion of higher order optical vortices in optical fiber with helical fiber Bragg gratings," J. Lightwave Technol. **34**(10), 2413–2418 (2016).
[31]J. Canning, Y. Wang, M. Lancry, Y. Luo, and G.-D. Peng, "Helical distributed feedback fiber Bragg gratings and rocking filters in a 3D printed preform-drawn fiber," Opt. Lett. **45**(19), 5444 (2020).
[32]O. Arteaga, J. Sancho-Parramon, S. Nichols, B. M. Maoz, A. Canillas, S. Bosch, G. Markovich, and B. Kahr, "Relation between 2D/3D chirality and the appearance of chiroptical effects in real nanostructures," Opt. Express **24**(3), 2242–2252 (2016).
[33]J. Lu, E. Garcia-Caurel, R. Ossikovski, F. Courvoisier, X. Zeng, B. Poumellec, and M. Lancry, "Femtosecond laser direct writing multilayer chiral waveplates with minimal linear birefringence," Opt. Lett. **48**(2), 271–274 (2023).
[34]S. Hasegawa, K. Shiono, and Y. Hayasaki, "Femtosecond laser processing with a holographic line-shaped beam," Opt. Express **23**(18), 23185–23194 (2015).
[35]C. P. Jisha, S. Nolte, and A. Alberucci, "Geometric phase in optics: From wavefront manipulation to waveguiding," Laser Photonics Rev. **15**(10), 2100003 (2021).
[36]M. K. Bhuyan, F. Courvoisier, P. A. Lacourt, M. Jacquot, R. Salut, L. Furfaro, and J. M. Dudley, "High aspect ratio nanochannel machining using single shot femtosecond Bessel beams," Appl. Phys. Lett. **97**(8), 081102 (2010).
[37]J. Durnin, J. J. Miceli, and J. H. Eberly, "Diffraction-free beams," Phys. Rev. Lett. **58**(15), 1499–1501 (1987).
[38]Y. Lei, G. Shayeganrad, H. Wang, M. Sakakura, Y. Yu, L. Wang, D. Kliukin, L. Skuja, Y. Svirko, and P. G. Kazansky, "Efficient ultrafast laser writing with elliptical polarization," Light: Sci. Appl. **12**(1), 74 (2023).
[39]M. Beresna, M. Gecevičius, P. G. Kazansky, and T. Gertus, "Radially polarized optical vortex converter created by femtosecond laser nanostructuring of glass," Appl. Phys. Lett. **98**(20), 201101 (2011).
[40]G. Milione, A. Dudley, T. A. Nguyen, O. Chakraborty, E. Karimi, A. Forbes, and R. R. Alfano, "Experimental measurement of the self-healing of the spatially inhomogeneous states of polarization of radially and azimuthally polarized vector Bessel beams," arXiv:1412.2722 (2014).
[41]M. Lancry, B. Poumellec, J. Canning, K. Cook, J.-C. Poulin, and F. Brisset, "Ultrafast nanoporous silica formation driven by femtosecond laser irradiation," Laser Photonics Rev. **7**(6), 953–962 (2013).
[42]M. Lancry, J. Canning, K. Cook, M. Heili, D. R. Neuville, and B. Poumellec, "Nanoscale femtosecond laser milling and control of nanoporosity in the normal and anomalous regimes of $GeO_2$-$SiO_2$ glasses," Opt. Mater. Express **6**(2), 321–330 (2016).
[43]R. Ossikovski, "Differential matrix formalism for depolarizing anisotropic media," Opt. Lett. **36**(12), 2330–2332 (2011).
[44]R. Ossikovski and O. Arteaga, "Statistical meaning of the differential Mueller matrix of depolarizing homogeneous media," Opt. Lett. **39**(15), 4470–4473 (2014).
[45]B. Poumellec, M. Lancry, R. Desmarchelier, E. Hervé, F. Brisset, and J. C. Poulin, "Asymmetric Orientational Writing in glass with femtosecond laser irradiation," Opt. Mater. Express **3**(10), 1586–1599 (2013).
[46]P. G. Kazansky, W. Yang, E. Bricchi, J. Bovatsek, A. Arai, Y. Shimotsuma, K. Miura, and K. Hirao, "'Quill' writing with ultrashort light pulses in transparent materials," Appl. Phys. Lett. **90**(15), 151120 (2007).
[47]Y. Dai, J. Ye, M. Gong, X. Ye, X. Yan, G. Ma, and J. Qiu, "Forced rotation of nanograting in glass by pulse-front tilted femtosecond laser direct writing," Opt. Express **22**(23), 28500–28505 (2014).
[48]E. Plum, "Extrinsic chirality: Tunable optically active reflectors and perfect absorbers," Appl. Phys. Lett. **108**(24), 241905 (2016).
[49]M. Beresna, M. Gecevičius, M. Lancry, B. Poumellec, and P. G. Kazansky, "Broadband anisotropy of femtosecond laser induced nanogratings in fused silica," Appl. Phys. Lett. **103**(13), 131903 (2013).
[50]H. Yao, R. Zaiter, M. Cavillon, P. Delullier, B. Lu, T. Cardinal, Y. Dai, B. Poumellec, and M. Lancry, "Formation of nanogratings driven by ultrafast laser irradiation in mid-IR heavy oxide glasses," Ceram. Int. **48**(21), 31363–31369 (2022).

## VI.5 **CONCLUSION**

In this Chapter, we present our important work on both revealing the origin of light induced chirality in silica and tailoring the related chiral optical properties by a multilayer strategy and a fs 3D structured light beam approach.

Below are some highlighted results summarized from this Chapter:

1. The origin of the light induced chirality in fs laser direct writing in silica glasses is revealed to be an extrinsic chirality that is formed by a chiral arrangement of two linear optical property contributions, i.e., a form birefringence and a stress related birefringence with non-parallel and non-perpendicular neutral axes.
2. The slow axis orientation of stress related birefringence is only dependent on the laser scanning geometry but with no relationship of laser polarization orientation.
3. Multilayer configuration can generate very strong chiral optical properties (typ., $+/-\pi$ rad of circular birefringence). For example, an on-demand optical rotation between [-90°, 90°] within a thickness of the chiral waveplate smaller than 200 μm is obtained.
4. Suppression of linear optical properties (e.g., linear birefringence) is available with an appropriate design of the multilayer configuration in fs laser direct writing chiral waveplates, for example, a four-layers structure with a 45° slow axis rotation between two adjacent layers. The current results show a strong circular birefringence of -2.25 rad with a simultaneous extinction ratio up to 5.5 dB at 550 nm. It can be further improved (likely up to 30 dB as a perspective) by exploiting an appropriate design and control of nanograting orientation.
5. A chiral Bessel fs beam with a linear polarization evolving along the focus (namely a rotation of 90° within $60\lambda$) is generated for the first time. It is created by a space variant birefringent waveplate (for creating a space variant polarization distribution at first) incorporating with an axicon focusing (to converting the 2D space variant polarization distribution to be along the focus, i.e., z axis).
6. Such a chiral Bessel fs beam can induce a "twisted nanograting"

structure where the "planar" layers containing nanopores are found in the head of the laser tracks, the nanolayers are distributed in the tail and slanted nanoporous layers in the middle.

7. These "twisted nanogratings" own larger circular birefringence (twice) and smaller linear birefringence (four times) when compared to a 45° linearly polarized Bessel fs beam.

In conclusion, all these pioneered findings draw a nascent landscape of the light induced chirality by fs laser direct writing in silica glasses. It indeed grows our understanding of light-matter interaction mechanisms on a relatively deeper aspect, which enriches the physical fundamentals and leads to great potentials of novel light-fabricated devices enabled by the induced chiral optical properties.

# GENERAL CONCLUSION

Chirality is an important property both in light and matter. With its origin of symmetry breaking, chirality can be transferred from matter to light as well as from light to matter via appropriate interactions. On the road of exploring the complex physical fundamentals in light-matter interactions with chirality, it provides a new platform on manipulating both light fields and material modifications with a higher degree of freedom. These manipulations lie on the heart of connections of light field parameters (such as intensity, polarization, phase etc.), topological geometry of the material structures and the interaction manners.

Vortex light generation and tunability is the main topic in chiral optical field manipulation since it owns unique properties of donut intensity profile, helical phase and carrying OAMs. These outstanding properties provide many possibilities for the applications ranging from physical fundamentals, nonlinear optics to diverse applications. For example, the OAMs carried by optical vortex beams provides a new degree of freedom in the optical communication system to meet high capacity [215]. Additionally, Gaussian vortex beams possess donut shape of the intensity profile, which is highly suitable for the depletion source in the stimulated emission depletion microscopy (STED) to achieve an ultrahigh resolution in the micro imaging system [191]. Besides, vortex light is drawing great interest in optical tweezers because the helical phase provides a larger opto-mechanical force to catch, move and even twist the nanoparticles to achieve complex micro activities.

Conventionally, most manipulation of vortex light fields stays in a statistic way. Namely, the generation and tunability of the vortex light is based on a specific component with determined permanent structures such as spiral phase plates, Q-plates, micro ring resonators, meta-surface structures in free space and long period fiber gratings, mode selective couplers in fiber optics. Despite of their accurate generation of vortex lights with a certain matching relation, they share a common restriction of dynamic flexibility. Spatial light

modulators may somewhat be a solution in this case, but it can only provide a quite low switching rate of about 60 Hz due to the inherent property of liquid crystal materials. Thus, acousto-optic interaction emerges to be the most effective way to break the limit and to pave the way of dynamic switching of vortex light manipulation, which could extend the application potentials of vortex light and meet higher requirements of flexibility.

Prior to this work, acousto-optic interactions are mostly utilized to obtain wavelength tunability by shifting the applied frequency of the PZT. With resonances at different wavelengths, the higher order modes and OAM lights can be generated at different wavelengths. Benefit from the dynamic tunability of the acousto-optic interactions in fibers, heterodyne detections, higher order modes fiber lasers, Brillouin fiber lasers are possible. To date, the dynamic fiber gratings enabled by acousto-optic interactions involve that how to achieve the resonant responses from low efficient resonances to deep resonant peaks, from narrow resonance bandwidths (typically <10 nm) to broadband resonances (several 10s nm) for satisfying broadband vortex light generation in ultrafast lasers. However, one critical property is still missing in the research community: the integration of dynamic switching of chirality of the vortex light, i.e., the topological charge numbers especially the sign. This key point will be a breakthrough because new degree of dynamic manipulation is proposed in the vortex light control and can meet new possibilities in the applications. For example, the new dynamic switching of the topological charge numbers enables a fast switching between left-handed OAM and right-handed OAM to give the dynamic activity of rotating nanoparticles with two directions in optical tweezers or a modulation coding of signals in the optical communication. Furthermore, highly flexible manipulations of chiral light fields also imply new potentials in structured light micro-nano manufacturing.

For the case of light induced chirality in matters, the simplest way is to fabricate helical structures in the material with both additive manufacturing and subtractive manufacturing strategies. However, this method owns complex writing processes and suffers with a low efficiency. Fs laser direct writing emerges to be a reliable strategy as a simple and effective way of imprinting chiral optical properties inside

transparent materials. It starts from nonlinear absorptions (e.g., multiphoton absorption) for creating diverse permanent structural modifications to the solid, typically silicate materials. The process and the caused optical properties are strongly related to the laser writing configurations and parameters can be precisely controlled. These permanent modifications such as refractive index modifications, porous nanograting structures with strong birefringence and voids. Indeed, the FLDW strategy with flexible parameters tunability (including laser polarization, duration, pulse energy, repetition rate, scanning speed, NA of focusing lens, etc.) defines a novel platform for new potentials in photonic applications ranging from 5D data storage, micro fluid channels, polarizing devices, 3D photonic waveguide and material marking and cleaving.

Refining light manufacturing in integrated devices appears great interests since the FLDW is capable of strong linear birefringence up to $10^{-2}$ in a large range of transparent glass materials. Besides, this modification is related to the localized volume change through strong nonlinear effects, which allows a very precise 3D fabrication capability. Manipulating these types of modifications would improve the current fs laser applications. Furthermore, from an industrial aspect, the demand for sophisticated optical integration increases due to the growing of exchanged data and information in the society. This yields the demand of information devices with "smartness" to improve the performance, which subsequently requires a complex laser fabrication. Thus, this stimulates the optical integration of diverse optical functional components in the integrated circuits that light can do.

For improving the performance of the functional devices, one critical point is the integration of circular optical properties. Prior to this thesis work, our group previously performed an experimental proof that a fs laser can somewhat shear the matter as a scissor can do. It is based on a phase shift interferometer technique. This ability gives a chiral strain when the light propagation is considered. This is fundamentally novel, but a shear cannot directly give a birth of circular optical properties by itself. Circularly polarized light is capable of highly ordered "chiral like" structures, but unfortunately it can neither give rise to the circular optical properties, as reported by

Taylor et al. Recently, in the PhD thesis of Tian in our group, the creation of circular optical properties in achiral materials (silica glass) by an achiral fs laser beam (considering an orthogonal incidence) is demonstrated. It has been proved that a ±45° orientated linearly polarized fs light can produce the maximum of circular optical properties (e.g., a circular birefringence of ~0.4 rad with a thickness of about 40 μm). The community then debates thoroughly with this result with the experimental conditions obtained as well as the origin of this phenomenon. However, it is still novel related to the fact that the created circular optical properties can be well controlled in an achiral solid. The remaining questions correlate to the reveling of inner mechanism of the chirality origin and the corresponded tailoring of all the anisotropic optical properties via an ideally low-cost and environmental-friendly strategy.

In this PhD thesis, dynamic manipulations of vortex beams are demonstrated in few-mode fibers via acousto-optic interactions. Based on this dynamic switching capability, dynamic perturbation can be introduced in the ultrafast mode-locked fiber lasers and the transient dynamic processes of different vortex modes switching enrich the fundamental laser physics. In addition, fs laser written chirality in silica fibers and silica glasses is investigated. Furthermore, the origin of the chirality is revealed and thus, the chiral optical properties are tailored by manipulating the laser writing configurations. All the work presented in this PhD thesis is about the interactions between light and matter with chirality and can be categorized as two main parts:

1. From matter to light for manipulating the chiral light fields (specifically for vortex light fields) via acousto-optic interactions.
2. From light to matter for imprinting and tailoring the chiral optical properties in silica materials via fs laser direct writing.

**Key results**

In **Chapter III**, we address an investigation of dynamic vortex mode switching via acousto-optic interactions in CW fiber lasers. Indeed, we revealed that the dual-peak resonance is related to a mode conversion from fundamental $LP_{01}$ mode to two orthogonal high

order modes, namely $LP_{11a}$ and $LP_{11b}$ modes. We then proposed a theory that the dual-resonance is attributed to a co-effect of acoustic birefringence and optical birefringence according to a geometric irregularity of the few-mode fiber. With different adhere angles between the fiber axis and the PZT vibration direction, the conversion efficiencies of the orthogonal modes (the depths of the two resonant peaks) can be controlled. Importantly, combined with the wavelength tunability, an alternation of two applied frequencies of the acoustic waves can achieve the mode switching between $LP_{11a}$ and $LP_{11b}$ modes at the same wavelength. **Furthermore, by employing the phase manipulation of the polarization controller, the mode switching between two orthogonal modes can be transferred to a mode switching between two vortex modes, i.e., a mode switching between +1-order OAM and -1-order OAM modes. This result is fundamentally new because it provides the new possibility of altering the chirality of the OAM beams between left-handedness and right-handedness. Besides, this fast switching of OAM modes with different topological charges owns a switching speed up to 4.3 kHz**, which satisfies the most requirements of dynamic switching in the applications.

Since the acousto-optic interactions in fibers provides a dynamic non-destroyed acoustically induced fiber grating, it is very suitable for the high-power fiber lasers. It is because the heat accumulation in the high-power fiber laser restricts the maximum power of the laser. But the acousto-optic interactions induce almost no heat accumulation in the mode conversion region when compared to conventional mode conversion devices, e.g., long period fiber gratings or mode selective couplers. **A stable output of switching between 5.85 W of $LP_{11}$ mode and 6.06 W of $LP_{01}$ mode is demonstrated. Although the investigation of this work does not achieve very high-power output, it is still a breakthrough because it implies that acousto-optic interactions in fibers could pave the way of non-heat-accumulated mode conversion with fast switching dynamic capability in high-power fiber lasers.** Besides, the acousto-optic device in this work exhibits a fast-switching speed of around 1 kHz. However, we only obtain a switching speed of about 250 Hz in the high-power fiber laser due to

a restriction of the build-up process of the laser. By the way, not only the switching speed but also the output power of the fiber laser can be optimized with appropriate configurations.

The **Chapter IV** illustrates the work of observing the vortex mode switching dynamics in a narrow-linewidth mode locked fiber laser. Ultrafast dynamic process is an interesting topic in the ultrafast laser community owning to development of time-stretched dispersive Fourier transform technique. However, the current studies are mostly related to build-up dynamics and soliton behaviors in different types of single transverse mode ultrafast fiber lasers. **Here, we demonstrated the vortex mode switching dynamics observation for the first time. The vortex mode switching dynamics includes four stages in the whole process, namely quiet-down process, relaxation oscillation phase, quasi-mode locking stage and the ultimate energy recovery prior to another vortex mode locking state.** Benefit from a few-mode fiber Bragg grating as a side mirror of the narrow-linewidth mode locked fiber laser, the OAM modes with different orders possess different reflection wavelengths (a difference of about 1.4 nm). This allows us to observe a real-time evolution of the wavelength shifting during the vortex mode switching dynamics, which is clearly observed via the time-stretched dispersive Fourier transform technique. **Besides, in the vortex mode switching dynamic process, we found an energy fluctuation between different orders of vortex modes, which is strong enough to form the irregular laser strikes. We suggest that the mode conversion and the mode competition are responsible for this energy fluctuation and thus determine the switching evolution dynamics.**

In the second section, we present an extended work related to the acousto-optic based attenuation strategy and a novel work of pulse width switching dynamics between femtosecond scale and picosecond scale. **It is a quite fresh result to the best of our knowledge since it is no more a static altering between different pulse widths but a dynamic manipulation with high flexibility instead.** Besides, this pulse width switchable mode locked fiber laser with acousto-optic attenuation has a novel mode locking evolution property at the modulation of the applied microwave signal. The

evolution includes not only the switching between narrowband mode locking and broadband mode locking but also a wavelength shifting with broadband mode locking states. **More importantly, the pulse width switching dynamics is also recorded by the time-stretched dispersive Fourier transform technique.** During the pulse width switching process, these exists a spectral intensity oscillation phenomenon that is mainly attributed to the structured soliton shaping by the nonlinear saturable absorption effects in the laser cavity.

In the first section of **Chapter V**, **fiber nanogratings are induced by fs laser direct writing in both single-mode fibers and few-mode fibers.** Clear SEM images are obtained confirming a well-established nanograting structures imprinted in fibers via precise polishing and hydrofluoric etching. From the experimental results, the Ge-doping plays a critical role in the formation of the fiber nanogratings. Fiber nanograting structures possess continuity and erasure rewriting properties, which are suitable for large-area fabrication and potentially data storage. With refractive index characteristics, a raw structure of the refractive index distribution is observed, which can be attributed to the alternative nanolayers structure of the fiber nanogratings. By the calibration of laser pulse energy, the linear birefringence induced in the nanograting regions can be manipulated. In addition, the retardation, and the depolarizing effect of the fiber nanograting structures are well investigated by a micro imaging Mueller polarimeter together with a product decomposition formalism. **Consequently, a broadband in-line polarizer is demonstrated by fs laser writing a fiber nanograting array around the fiber core.** Since the fiber nanograting structure has the linear dichroism property, the linearly polarized light with an orientation parallel to the slow axis of the fiber nanogratings can pass through it with low loss while the linearly polarized light with an orientation perpendicular to the slow axis of the fiber nanogratings suffers a large diattenuation effect. **The in-line polarizer based on fiber nanograting arrays own an extinction ratio of 5.43 dB at 1310 nm and 6.32 dB at 1550 nm.** The performance of the in-line polarizer can be optimized by smoothing the nanograting structures and a well-arranged array design. However, this approach for

realizing an in-line polarizer is technically new and show good implications to the research community.

In the second section, **space variant fiber nanograting structures are enabled by utilizing a computer-controlled half-wave plate to automatically vary the laser polarization orientation during the fs laser scanning process.** A full 3D manipulation of the space variant fiber nanograting structures is demonstrated. Specifically, the fiber nanograting rotations with the scanning direction both parallel and perpendicular to the fiber axis are investigated. With calibration of fs pulse energy and scanning speed, the retardance of the space variant fiber nanograting is well controlled. **More importantly, the circular optical property (e.g., circular birefringence) is characterized for the first time with a fiber nanograting structure via a Mueller imaging polarimeter with a logarithmic decomposition method.** Besides, **complex patterns consisting of space variant fiber nanogratings are enabled with a synchrotronic polarization control strategy.** This work paves the way for the integration of nanograting-based optical devices such as wave-plates, polarization rotator, isolators, and vector mode converters in "Lab-on-fiber" and "Lab-in-fiber" systems.

**Chapter VI** addresses important works for the fs laser direct writing chirality in silica glasses. The first section is about a revealing of the origin of the light induced chirality in inorganic glass materials. In the previous work from our group, a tentative interpretation of the fs laser writing chirality inside the silica glass could be a volume torque induced by a combined effect between the direct current field of the laser and the stress field. Specifically, the misalignment of the direct current electric field and the polarization field of the material creates the volume torque that gives rise to the symmetry breaking, which is responsible to the matter twist. However, it has no obvious evident to support this assumption. **In this section, we propose another point of perspective that the fs laser written chirality is an extrinsic chirality related to a chiral arrangement of several linearly polarimetric contributions with non-parallel and non-perpendicular neutral axes. Typically, in this case, they are form birefringence contribution and compressive stress-induced birefringence contribution oriented at different z positions with**

**non-parallel and non-perpendicular neutral axes.** This proposal is confirmed by the polarization dependence investigation of circular optical properties, form birefringence, and stress induced birefringence. LB is strongly dependent on the laser polarization but there are some deviations from an ideal sinusoidal shape. In contrary, the stress is not dependent on the laser polarization but related to the laser scanning geometry. **Then we propose a simple but powerful two-layer model to explain and exploit these two contributions enabled by a Mueller formalism.** The model agrees well with our experiments. Besides, a step isochronal thermal annealing of the two layers Type II based waveplate is demonstrated. From the annealing result, the circular birefringence declines a little when the stress is relaxed by annealing, which means that stress field owns a contribution but the dominate part is form birefringence. When the nanograting structure is gradually erased by annealing, the circular birefringence disappears accordingly. All the result indicates that the fs laser induced chirality is an optical chirality consisting of at least two linear contributions (e.g., form birefringence and stress related birefringence).

**The second section is dedicated to the multilayer strategy to fabricate chiral waveplates with very high circular optical properties and likely suppressed linear optical properties.** According to the two-layer model presented in the above section, the fs laser induced chirality can be tailored by manipulating the linear optical properties of each layer as well as their misalignment design (i.e., the chiral arrangement). Experimentally, we tentatively fabricate a four-layers based chiral waveplate due to its easy-obtain but useful helical design with a “rotated” slow axis evolution from bottom layer to upper layer. **To quantitatively characterize the result of the four-layer chiral waveplate, we use a Mueller formalism to simulate the anisotropic optical properties including linear optical properties and the circular ones. The theoretical result shows a region with several pairs of retardance in each layer and the angle between the slow axes of adjacent layers, which can achieve simultaneous strong circular birefringence but nearly zero linear birefringence.** This exhibits a high potential for chiral waveplate based devices since linear birefringence will change the

ellipticity of the polarization state of the incident light, which is not expected in a chiral waveplate. **Experimentally, we demonstrated the calibration of the four-layer chiral waveplate and obtained a circular birefringence of -2.25 rad with simultaneously an extinction ratio (the ratio of circular/linear birefringence) of up to 5.5 dB.** This result provides new possibilities for chiral waveplate fabrication with linear optical properties suppression but also for tailoring strong circular optical properties towards applications of polarization control devices such as optical rotators and isolators.

The final section depicts a work combining two main topics in this PhD thesis, namely manipulation of chiral light field and imprinting chiral optical properties by fs light direct writing. **Specifically, we propose and demonstrate a novel strategy to generate a chiral Bessel beam (i.e., a z-variable-polarized Bessel fs beam) with its linear polarization orientation rotating along the light propagation direction (i.e., z axis).** It is enabled by a fs laser direct written space varying birefringent element combined with an axicon focusing. This passive strategy converts the polarization distribution in the transverse plane (in two-dimension) to the longitudinal evolution that is evolved in three-dimension. Experimentally, we achieve a 90° rotation within the focus of the chiral Bessel beam of around 50 μm z distance. **This beam is considered as a "helical polarized beam" and is rotating slowly enough to create a "twisted" nanograting structure without any scanning.** The induced nanograting structure owns planar nanoporous layers in the head of the laser track and a well-orientated nanolayer structure in the tail of the laser track. The middle of the laser track reveals nanoporous "slanted nanolayers" due to a 45° polarization orientation of the z-variable-polarized light. **As a preliminary result, this "twisted" nanograting structure possesses a twice higher circular birefringence and a four times lower linear birefringence when compared to the nanograting structure written by a 45° linearly polarized fs Bessel beam.** This work leads to the novel idea from chiral light field manipulation to create high chiral optical properties implantation in transparent materials and open the door to twist the matters (glasses, organics, polymers) in a controllable manner.

# FUTURE WORK AND PROSPECTS

Even though we have contributed to a series of work related to chiral manipulation of optical field and its interaction with silica glass materials for imprinting chiral optical properties, there are still many works to pursue. In this thesis, despite many exciting key results are discovered, we can continue to conduct more in-depth explorations.

**Discovering more possibility of acousto-optic interactions**

We have tentatively demonstrated various investigations of acousto-optic interactions in fibers for dynamic spatial mode conversions under modulation of microwave radio-frequency signals. This provides a new degree of freedom in chiral optical vortex generation and manipulation. However, what is the future of acousto-optic interactions in fibers? How to discover new mechanisms as well as practical applications? Compared to conventional static spatial mode control strategies, acousto-optic interactions own advantages of fast switching and frequency shifting, which is demonstrated in this thesis. For continuity, several potential topics could be expected:

(1) Acousto-optic interactions enable dynamic evolution of spatial mode conversion in the fiber laser cavity. This positive manipulation allows external perturbations applied to the laser cavity which leads to a new platform for discovering a number of interesting transient processes in the ultrafast lasers. Thanks to the time-stretched dispersive Fourier transform technique, these dynamic behaviors taking place in the ultrafast laser cavity modulated by acousto-optic interactions can be observed as a real-time perspective. To date, researchers mainly focus on fundamental mode ultrafast lasers theoretically and experimentally. However, multiple spatial modes interactions in the mode locked fiber lasers exhibit more interesting phenomena. Acousto-optic interactions could be a very useful switch or "trigger" signal to modulate the transient spatial mode perturbation in ultrafast laser cavities. Therefore, inducing acousto-optic interactions into ultrafast lasers provides new scientific potentials in the future work.

(2) Vector beams, as optical fields with donut intensity profiles and unique polarization distribution, contribute great potentials in practical applications. Due to the dynamic manipulation capability of acousto-optic interactions, a high degree of freedom in vector modes tuning can extend the future work of acousto-optic interactions. For example, in a stimulated emission depletion microscopy, it requires a fundamental mode field as an excited source and a donut optical field as a depletion source. Since acousto-optic interactions in fibers are capable of dynamic mode switching between fundamental mode and vortex modes, it can provide new flexible functionality in the stimulated emission depletion system to serve the super-diffraction imaging. Besides, optical tweezer is another important direction of future work. Chiral vortex beams generation and manipulation are very useful in nanoparticle controlling including catching, moving and even rotating. Our result of dynamic chiral switching of vortex beams via acousto-optic interactions with different topological charge numbers provides the implication of high-dimensional behaviors of the particles. For instance, orchestrating a train of particle behaviors like a "particle dance" is possible.

(3) With a tunable mode conversion efficiency, acousto-optic interactions are capable of hybrid spatial mode sources, namely fundamental and higher-order modes co-existing via a partial mode conversion. This is quite useful in optical device characterizations, especially for few-mode components. For example, few-mode fiber Bragg grating has been widely used in higher-order mode fiber lasers or even vortex mode fiber lasers due to its high reflection efficiency of both fundamental and higher-order modes. In general, only reflected wavelengths of fundamental and higher-order modes are considered since they determine the oscillation wavelength of the fiber laser. However, the reflection efficiencies of each mode are also important for the equilibrium of energy and loss, which will decide the resonance of each mode in the laser cavity. Surprisingly, acousto-optic interactions with dynamic mode conversion efficiency tunability (further contributes to a proportion tunability of each mode) can fill the vacancy of an easy-obtain proportion-controllable hybrid mode source for the probing light. Thus, the reflection efficiencies

of each mode of the few-mode fiber Bragg grating can be easily obtained by adjusting the mode proportion distribution of the probing light via acousto-optic interactions and analyzing the reflection spectra.

(4) Acousto-optic interaction has been proved to be an excellent solution for spatial mode manipulation in high-power fiber lasers since its non-destroyed approach and dynamic tunability. In the future work, we can employ this acousto-optic device to achieve higher powers such as several hundreds of Watts or even thousands of Watts in the fiber lasers with controllable modes.

(5) Acousto-optic interactions employ microwave radio-frequency signals to manipulate the phonon-photon coupling in the fiber media. That is, the microwave signals propagate along the fiber with the modulation of the light wave. Thus, the carried information from the microwave signal would be somehow demodulated from the light wave. More importantly, operating microwave signals onto the PZT devices in a soliton laser cavity enables enhanced nonlinear interactions of microwave signals and soliton pulses, which could lead to a microwave spectrum purifying effect to achieve high-quality microwave signals for further diverse applications. Besides, the inner mechanism of the nonlinear interactions between microwave signals and soliton pulses also appears to tremendous research interests in the community.

(6) In this thesis, acousto-optic interactions in only single-mode fibers and few-mode fibers are demonstrated. However, these two kinds of fibers are quite same in principle (the few-mode fiber only changes the fiber core diameter). However, more kinds of special fibers can be utilized in acousto-optic interaction configurations to pursue more possibilities for novel functions. For example, further explorations can be acousto-optic interactions in multimode fibers, photonic crystal fibers, rare-earth-doped fibers (gain fibers), ring-core fibers, and double-cladding fibers.

**Challenges on acousto-optic interactions**

Despite of the unique advantages of acousto-optic interaction, it still possesses some challenges due to its inherent mechanism and

configuration.

(1) Acousto-optic interactions exploit acoustic vibrations along the fiber to construct the mode control inside the fiber. Despite it is an external modulation with a dynamic tunability, it introduces vibration perturbations on the fiber. Compared to general passive mode converters such as long-period fiber gratings and mode selective couplers, acousto-optic interactions are more complex in the practical use since the environmental vibrations (when their vibration frequencies are close to the applied microwave radio-frequency signals) may influence the acoustic modulation. Thus, the mode conversion efficiency would be affected.
(2) Acousto-optic interaction is an active approach of chiral vortex field manipulation, which requires an external unit of modulation (a microwave radio-frequency signal generator, a PZT transducer, and sometime a signal amplifier). This part will indeed increase the size of the acousto-optic device, which may restrict the integration in some applications.
(3) According to the theory of acousto-optic interactions in fibers, a highly efficient mode conversion requires an acousto-optic interaction region with a length of several centimeters, which is another limit of the size. If one wants to reduce the acousto-optic interaction length, or to approach a wider resonant wavelength range, a straightforward solution is to decline the fiber diameter in the acousto-optic interaction region by hydrofluoric etching. However, it may thus decrease the robustness of the acousto-optic device because the etched fiber will be fragile under strong acoustic vibrations.

**Explorations in interaction of matters with vectorial lights**

The experimental proof indicates that the laser polarization plays a crucial role in light-matter interactions. Thus, both the structural modifications and the imprinted optical properties are expected to be richer under vectorial light fabrication especially with tight focusing. One exciting aspect of the future work is operating temporal and spatial manipulation of intensity, polarization, and phase to efficiently control the nonlinear force targeting the imprinting of oriented objects through 3D manipulation of the

excited plasma. This allows exerting opto-mechanical actions potentially assisted by thermal effects in the matter to imprint the desired physicochemical properties. It is quite possible for short duration and large intensity while the electrons could be excited with delocalized states that are independent to the ionic motions.

From a practical point of view, the essential idea is to match the ultrafast light to a given task via a spatiotemporal shaping. In this thesis, we demonstrated for the first time the generation of z-variable-polarized Bessel beam that was subsequently used to create chiral structures, i.e., "twisted nanogratings". However, future works can be carried out by creating 3D structured polarization beams (e.g., C-points, V-points, L-lines, Möbius strips, links, knots, etc.) to achieve complex nanograting structures and high degree of symmetry breaking. Besides, exploring the light-matter interactions with lights that carry both SAMs and OAMs may be useful to answer the unrevealed questions that if SAMs and OAMs are equivalent with nonlinear light absorption and how the chirality of the light (SAMs and OAMs) can be effectively transferred to the matter. Besides, other vector beams such as cylindrical vector beams, Hermite-Gaussian beams, Laguerre-Gaussian beams, and especially Poincare beams can also be interesting topics for discovering intriguing effects in interactions of matter with special light fields.

**Towards chiral control at a molecular scale**

The experimental results presented herein exhibit the possibility of "twisting" a nanograting structure to be "helical" distributed. Towards an in-depth exploration of further study, a full chiral manipulation of matter at a nanoscale is expected. From a chemical point of view, the chirality originates from a chiral arrangement of molecules or network in the material. If a light can manipulate the chiral arrangement of the material at a molecular scale, we will abandon the classical point of view from elaboration chemistry that laser is only an energy deposit tool, towards to a new paradigm where light could shape the matter with a microscopic scale in expected manners. In order to highly twist the molecules, a strong helical light should be generated. OAM-SAM coupled beams or polarization shaped beams with high chirality may be plausible candidates for manipulating the

chirality of the matter such as changing the sign of chirality of the chiral quartz ponders or endowing intrinsic chirality to an achiral material.

**Discovering possibilities in other glass systems**

Crystallographic structures are controllable in a transparent material by playing the morphology of the electromagnetic field of the focused laser beam. The chirality in light could lead to the control of chiral crystal precipitation. For instance, an axisymmetric laser beam (with no chirality due to its axial symmetry) contributes to a racemic nanocrystal assembly while a non-axisymmetric laser beam (with chirality due to its symmetry breaking) contributes to enantiomeric excess. The latter demonstrates the chirality transfer from light to the matter via a light assisted nano crystallization process and leads to the related circular optical properties. Furthermore, the amplitude and the orientation of these induced circular optical properties are probably related to the vectorial properties of the light such as the polarization distribution, gradients of the intensity profile as well as phase.

**Towards helical optical properties**

We expect to point out that our results in this thesis are mainly focusing on the circular optical properties. However, there exists a novel chiral optical property, namely a helical optical property that correlates to different optical responses to positive order and negative order of OAM beams. This is fundamentally new because the helical optical properties indicate the chiral interactions of matters with vortex lights and bring new freedom in the design of light beams and optical properties. Monochromatic vortex light is capable of unambiguous distinguishments of the inherent chirality of the material structure. Single planar chiral structures can achieve giant helical dichroism of about 20%, as reported by Ni and Wu et al. [216]. This brings new idea in chiral optics and chiroptic detection. For instance, concerning the circular optical properties in a single planar chiral structure, helical optical properties yield giant signals for easy detection and identification. Furthermore, one can imagine that significant helical optical properties such as helical birefringence and

helical dichroism in a 3D chiral structure would provide new possibilities for manipulating vortex lights.

## PUBLICATIONS LIST

### Journal papers

1. **J. Lu**, L. Teng, Q. Zhai, C. Wang, M. Lancry, Y. Dai, and X. Zeng, "Space variant fiber nanogratings induced by femtosecond laser direct writing," ***Appl. Sur. Sci.*** 646, 158787 (2023) (IF: 6.7).
2. **J. Lu**, J. Tian, B. Poumellec, E. Garcia-caurel, R. Ossikovski, X. Zeng, and M. Lancry, "Tailoring chiral optical properties by femtosecond laser direct writing in silica," ***Light Sci. Appl.*** 12, 46 (2023) (IF: 19.4).
3. **J. Lu**, M Hassan, F. Courvoisier, E. Garcia-Caurel, F. Brisset, R. Ossikovski, X. Zeng, B. Poumellec, and M. Lancry, "3D structured Bessel beam polarization and its application to imprint chiral optical properties in silica," ***APL Photon.*** 8, 060801 (2023) (IF: 5.6).
4. **J. Lu**, E. Garcia-Caurel, R. Ossikovski, F. Courvoisier, X. Zeng, B. Poumellec, and M. Lancry, "Femtosecond laser direct writing multilayer chiral waveplates with minimal linear birefringence," ***Opt. Lett.*** 48, 271–274 (2023) (IF: 3.6).
5. M. Hou, M. Xu, J. Xu, **J. Lu**, Y. An, L. Huang, X. Zeng, F. Pang, J. Li, L. Yi, "Deep learning–based vortex decomposition and switching based on fiber vector eigenmodes," ***Nanophotonics*** 12(15), 3165–3177 (2023) (IF: 7.5).
6. X. Zhou, F. Shi, **J. Lu**, M. Xu, M. Hou, M. Bonn, X. Liu, and X. Zeng, "Generating Femtosecond Visible Doughnut Beams Based on Transverse-Mode Modulation," ***J. Light. Technol.*** 40, 6493–6500 (2022) (IF: 4.7).
7. M. Mobasher, M. Lancry, **J. Lu**, D. Neuville, L. Bellot Gurlet, and N. Ollier, "Thermal relaxation of silica phases densified under electron irradiation," ***J. Non. Cryst. Solids*** 597, 121917 (2022) (IF: 3.5).
8. **J. Lu**, F. Shi, J. Xu, L. Meng, L. Zhang, P. Cheng, X. Zhou, F. Pang, and X. Zeng, "Recent progress of dynamic mode manipulation via acousto-optic interactions in few-mode fiber lasers: Mechanism, device and applications," ***Nanophotonics*** 10, 983–1010 (2021) (IF: 7.5).
9. L. Wang, J. Xu, **J. Lu**, L. Teng, Z. Luo, F. Pang, and X. Zeng, "3 W

average-power high-order mode pulse in dissipative soliton resonance mode-locked fiber laser," ***Nanophotonics*** 10, 3527–3539 (2021) (IF: 7.5).
10. L. Teng, **J. Lu**, Y. He, L. Wang, and X. Zeng, "Vortex soliton oscillation in a mode-locked laser based on broadband long-period fiber grating," ***Opt. Lett.*** 46, 2710–2713 (2021) (IF: 3.6).
11. T. Wang, **J. Lu**, H. Yao, F. Shi, L. Meng, P. Cheng, and X. Zeng, "Recent progress in all-fiber ultrafast high-order mode lasers," ***J. Phys. Photonics*** 3, 012007 (2021) (IF: 3.8).
12. Y. Huang, S. Lv, L. Teng, L. Wang, **J. Lu**, J. Xu, and X. Zeng, "High-Order Mode Mode-Locked Fiber Laser Based on Few-Mode Saturable Absorber," ***IEEE Photonics J.*** 13, 1500909 (2021) (IF: 2.4).
13. J. Xu, L. Zhang, X. Liu, L. Zhang, **J. Lu**, L. Wang, and X. Zeng, "Dynamic vortex mode-switchable erbium-doped Brillouin laser pumped by high-order mode," ***Opt. Lett.*** 46, 468–471 (2021) (IF: 3.6).
14. **J. Lu**, F. Shi, L. Meng, L. Zhang, L. Teng, Z. Luo, P. Yan, F. Pang, and X. Zeng, "Real-time observation of vortex mode switching in a narrow-linewidth mode-locked fiber laser," ***Photonics Res.*** 8, 1203–1212 (2020) (IF: 7.6).
15. H. Wu, **J. Lu** (co-first author), L. Huang, X. Zeng, and P. Zhou, "All-Fiber Laser with Agile Mode-Switching Capability through Intra-Cavity Conversion," ***IEEE Photonics J.*** 12, 1500709 (2020) (IF: 2.4).
16. L. Meng, **J. Lu**, F. Shi, J. Xu, L. Zhang, H. Yao, and X. Zeng, "Multi-Orthogonal High-Order Mode Converter Based on Acoustically Induced Fiber Gratings," ***IEEE Photonics Technol. Lett.*** 32, 819–822 (2020) (IF: 2.6).
17. F. Shi, **J. Lu**, L. Meng, P. Cheng, X. Liu, F. Pang, and X. Zeng, "All-Fiber Method for Real-Time Transverse-Mode Switching of Ultrashort Pulse," ***IEEE Photonics Technol. Lett.*** 32, 97–100 (2020) (IF: 2.6).
18. L. Zhang, **J. Lu**, L. Meng, P. Cheng, W. Li, J. Sun, T. Wang, and X. Zeng, "A lower frequency shift based on mode conversion for optical heterodyne micro-vibration measurement," ***J. Light. Technol.*** 38, 6057–6062 (2020) (IF: 4.7).
19. **J. Lu**, Y. Dai, Q. Li, Y. Zhang, C. Wang, F. Pang, T. Wang, and X. Zeng, "Fiber nanogratings induced by femtosecond pulse laser direct writing for in-line polarizer," ***Nanoscale*** 11, 908–914 (2019)

(back cover letter, IF: 6.7).

20. T. Wang, **J. Lu**, Y. Huang, L. Meng, F. Shi, and X. Zeng, "Generation and Research Progress of All Fiber Ultrafast Vector Optical Field," ***Chinese Journal of Lasers*** 46(5), 0508010 (2019) (IF: 1.7).
21. **J. Lu**, L. Meng, F. Shi, X. Liu, Z. Luo, P. Yan, L. Huang, F. Pang, T. Wang, X. Zeng, and P. Zhou, "Dynamic mode-switchable optical vortex beams using acousto-optic mode converter," ***Opt. Lett.*** 43, 5841–5844 (2018) (IF: 3.6).

## International conferences

1. **J. Lu**, J. Tian, B. Poumellec, E. Garcia-Caurel, R. Ossikovski, M. Stchakovsky, and M. Lancry, "Shaping of femtosecond laser direct writing circular optical properties in silica by means of Mueller spectroscopic ellipsometry detection," *the 9th international conference on spectroscopic ellipsometry (**ICSE-9**)*, paper 6.3 (2022) (oral).
2. M. Hassan, **J. Lu**, B. Sapaly, M. Lancry, and F. Courvoisier, "Polarization shaping of a femtosecond Bessel beam to control birefringence writing in silica," in *Fiber Lasers and Glass Photonics: Materials through Applications III (**SPIE**)*, p. PC1214209 (2022).
3. X. Zhou, F. Shi, **J. Lu**, J. Zhu, X. Liu, and X. Zeng, "All-fiber femtosecond visible vortex beam based on Cherenkov radiation," in *Conference on Lasers and Electro-Optics (**CLEO**)*, paper JW1A.37 (2021).
4. L. Teng, F. Shi, **J. Lu**, J. Xu, and X. Zeng, "Intra-cavity HOM mode-locked laser based on broadband LPFG," in *Asia Communications and Photonics Conference/International Conference on Information Photonics and Optical Communications (**ACP/IPOC**)*, paper M4A.122 (2020).
5. L. Zhang, **J. Lu**, Q. Xu, J. Sun, and X. Zeng, "All-fiber frequency shifter via mode conversion for optical heterodyne micro-vibration measurement," in *Conference on Lasers and Electro-Optics (**CLEO**)*, paper JW2B.12 (2020).
6. **J. Lu**, L. Meng, F. Shi, and X. Zeng, "A mode locked fiber laser with switchable high-order modes using intracavity acousto-optic mode converter," in *Optical Fiber Communication Conference (**OFC**)*, paper W3C.3 (2019) (oral).

7. F. Shi, **J. Lu**, L. Meng, P. Cheng, and X. Zeng, "Delivering Transverse-mode Switching based on All-fiber Femtosecond Laser," in *Conference on Lasers and Electro-Optics Europe and European Quantum Electronics Conference (**CLEO-Europe**)*, paper cj_11_2 (2019).
8. L. Meng, **J. Lu**, L. Zhang, F. Shi, and X. Zeng, "Multi-orthogonal High-order Modes Converter," in *Conference on Lasers and Electro-Optics (**CLEO**)*, paper STh3L.4 (2019).
9. **J. Lu**, Q. Li, Y. Dai, Y. Zhang, C. Wang, F. Pang, T. Wang, and X. Zeng, "Self-organized nanogratings induced by femtosecond laser pulse direct writing in optical fibers," in *Conference on Lasers and Electro-Optics (**CLEO**)*, paper JTu3O.2 (2018) (oral).
10. L. Meng, **J. Lu**, F. Shi, F. Pang, and X. Zeng, "Orthogonal mode-switching fiber laser based on acoustically-induced fiber grating," in *Asia Communications and Photonics Conference (**ACP**)*, paper M1A.5 (2018).

## REFERENCES


1. Y. Shen, Q. Zhan, L. G. Wright, D. N. Christodoulides, F. W. Wise, A. E. Willner, Z. Zhao, K. Zou, C. Liao, C. Hernández-garcí, M. Murnane, M. A. Porras, A. Chong, C. Wan, K. Y. Bliokh, M. Yessenov, A. F. Abouraddy, L. J. Wong, M. Go, S. Kumar, C. Guo, S. Fan, N. Papasimakis, N. I. Zheludev, L. Chen, W. Zhu, A. Agrawal, S. W. Jolly, C. Dorrer, B. Alonso, I. Lopez-Quintas, M. López-ripa, Í. J. Sola, Y. Fang, Q. Gong, Y. Liu, J. Huang, H. Zhang, Z. Ruan, M. Mounaix, N. K. Fontaine, J. Carpenter, A. H. Dorrah, F. Capasso, and A. Forbes, "Roadmap on spatiotemporal light fields," J. Opt. **Early post**, DOI 10.1088/2040-8986/ace4dc (2022).
2. M. Rothschild, "A review of excimer laser projection lithography," J. Vac. Sci. Technol. B Microelectron. Nanom. Struct. **6**(1), 1–17 (1988).
3. A. Forbes, M. de Oliveira, and M. R. Dennis, "Structured light," Nat. Photonics **15**(4), 253–262 (2021).
4. L. Allen, M. W. Beijersbergen, R. J. C. Spreeuw, and J. P. Woerdman, "Orbital angular momentum of light and the transformation of Laguerre-Gaussian laser modes," Phys. Rev. A **45**(11), 8185–8189 (1992).
5. R. Stoian, M. K. Bhuyan, G. Zhang, G. Cheng, R. Meyer, and F. Courvoisier, "Ultrafast Bessel beams: Advanced tools for laser materials processing," Adv. Opt. Technol. **7**(3), 165–174 (2018).
6. A. H. Dorrah, M. Zamboni-Rached, and M. Mojahedi, "Engineering the Wavelength and Topological Charge of Non-Diffracting Beams Along Their Axis of Propagation," J. Opt. Soc. Am. B **36**(7), 1867–1872 (2019).
7. A. H. Dorrah, N. A. Rubin, A. Zaidi, M. Tamagnone, and F. Capasso, "Metasurface optics for on-demand polarization transformations along the optical path," Nat. Photonics **15**(4), 287–296 (2021).
8. Y. Aborahama, A. H. Dorrah, and M. Mojahedi, "Designing the phase and amplitude of scalar optical fields in three dimensions," Opt. Express **28**(17), 24721–24730 (2020).
9. A. Chong, C. Wan, J. Chen, and Q. Zhan, "Generation of

spatiotemporal optical vortices with controllable transverse orbital angular momentum," Nat. Photonics **14**(6), 350–354 (2020).
10. Y. Shimotsuma, P. G. Kazansky, J. Qiu, and K. Hirao, "Self-organized nanogratings in glass irradiated by ultrashort light pulses," Phys. Rev. Lett. **91**(24), 247405 (2003).
11. J. Canning, M. Lancry, K. Cook, A. Weickman, F. Brisset, and B. Poumellec, "Anatomy of a femtosecond laser processed silica waveguide [Invited]," Opt. Mater. Express **1**(5), 998–1008 (2011).
12. M. Lancry, B. Poumellec, J. Canning, K. Cook, J. C. Poulin, and F. Brisset, "Ultrafast nanoporous silica formation driven by femtosecond laser irradiation," Laser Photon. Rev. **7**(6), 953–962 (2013).
13. A. Rudenko, J. P. Colombier, and T. E. Itina, "Nanopore-mediated ultrashort laser-induced formation and erasure of volume nanogratings in glass," Phys. Chem. Chem. Phys. **20**(8), 5887–5899 (2018).
14. B. Poumellec, M. Lancry, R. Desmarchelier, E. Hervé, and B. Bourguignon, "Parity violation in chiral structure creation under femtosecond laser irradiation in silica glass?," Light Sci. Appl. **5**(11), e16178 (2016).
15. B. K. Kim, J. N. Blake, H. E. Engan, and H. J. Shaw, "All-fiber acousto-optic frequency shifter," Opt. Lett. **11**(6), 389–391 (1986).
16. L. Zhang, J. Lu, L. Meng, P. Cheng, W. Li, J. Sun, T. Wang, and X. Zeng, "A lower frequency shift based on mode conversion for optical heterodyne micro-vibration measurement," J. Light. Technol. **38**(21), 6057–6062 (2020).
17. W. Zhang, L. Huang, F. Gao, F. Bo, L. Xuan, G. Zhang, and J. Xu, "Tunable add/drop channel coupler based on an acousto-optic tunable filter and a tapered fiber," Opt. Lett. **37**(7), 1241 (2012).
18. D. Mao, X. Cui, X. Gan, M. Li, W. Zhang, H. Lu, and J. Zhao, "Passively Q-Switched and Mode-Locked Fiber Laser Based on an ReS2 Saturable Absorber," IEEE J. Sel. Top. Quantum Electron. **24**(3), (2018).
19. W. Zhang, L. Huang, F. Gao, F. Bo, G. Zhang, and J. Xu, "All-fiber tunable Mach-Zehnder interferometer based on an acousto-optic tunable filter cascaded with a tapered fiber," Opt.

Commun. **292**, 46–48 (2013).
20. W. Zhang, L. Huang, K. Wei, P. Li, B. Jiang, D. Mao, F. Gao, T. Mei, G. Zhang, and J. Zhao, "Cylindrical vector beam generation in fiber with mode selectivity and wavelength tunability over broadband by acoustic flexural wave," Opt. Express **24**(10), 10376–10384 (2016).
21. J. Lu, F. Shi, L. Meng, L. Zhang, L. Teng, Z. Luo, P. Yan, F. Pang, and X. Zeng, "Real-time observation of vortex mode switching in a narrow-linewidth mode-locked fiber laser," Photonics Res. **8**(7), 1203–1212 (2020).
22. J. Lu, Y. Dai, Q. Li, Y. Zhang, C. Wang, F. Pang, T. Wang, and X. Zeng, "Fiber nanogratings induced by femtosecond pulse laser direct writing for in-line polarizer," Nanoscale **11**(3), 908–914 (2019).
23. J. Lu, J. Tian, B. Poumellec, E. Garcia-caurel, R. Ossikovski, X. Zeng, and M. Lancry, "Tailoring chiral optical properties by femtosecond laser direct writing in silica," Light Sci. Appl. **12**(1), 46 (2023).
24. J. Lu, E. Garcia-Caurel, R. Ossikovski, F. Courvoisier, X. Zeng, B. Poumellec, and M. Lancry, "Femtosecond laser direct writing multilayer chiral waveplates with minimal linear birefringence," Opt. Lett. **48**(2), 271–274 (2023).
25. J. Lu, M. Hassan, F. Courvoisier, E. Garcia-Caurel, F. Brisset, R. Ossikovski, X. Zeng, B. Poumellec, and M. Lancry, "3D structured Bessel beam polarization and its application to imprint chiral optical properties in silica," APL Photonics **8**(6), 060801 (2023).
26. U. Keller, "Recent developments in compact ultrafast lasers," Nature **424**, 831–838 (2003).
27. G. A. Mourou, C. L. Labaune, M. Dunne, N. Naumova, and V. T. Tikhonchuk, "Relativistic laser-matter interaction: From attosecond pulse generation to fast ignition," Plasma Phys. Control. Fusion **49**(12), B667–B675 (2007).
28. D. Strickland and G. Mourou, "Compression of amplified chirped optical pulses," Opt. Commun. **56**(3), 219–221 (1985).
29. X. Shang, L. Guo, J. Gao, S. Jiang, X. Han, Q. Guo, X. Chen, D. Li, and H. Zhang, "170 mW-level mode-locked Er-doped fiber laser oscillator based on nonlinear polarization rotation," Appl.

Phys. B Lasers Opt. **125**(10), 193 (2019).
30. J.-H. Lin, C.-L. Chen, C.-W. Chan, W.-C. Chang, and Y.-H. Chen, "Investigation of noise-like pulses from a net normal Yb-doped fiber laser based on a nonlinear polarization rotation mechanism," Opt. Lett. **41**(22), 5310–5313 (2016).
31. Y. Yu, H. Teng, H. Wang, L. Wang, J. Zhu, S. Fang, G. Chang, J. Wang, and Z. Wei, "Highly-stable mode-locked PM Yb-fiber laser with 10 nJ in 93-fs at 6 MHz using NALM," Opt. Express **26**(8), 10428–10434 (2018).
32. W. G. Wanli Gao, G. L. Guanyu Liu, and Z. Z. Zhigang Zhang, "44.6 fs pulses from a 257 MHz Er:fiber laser mode-locked by biased NALM," Chinese Opt. Lett. **16**(11), 111401 (2018).
33. S. Smirnov, S. Kobtsev, A. Ivanenko, A. Kokhanovskiy, A. Kemmer, and M. Gervaziev, "Layout of NALM fiber laser with adjustable peak power of generated pulses," Opt. Lett. **42**(9), 1732–1735 (2017).
34. H. Ahmad, M. H. M. Ahmed, and M. Z. Samion, "Generation of mode-locked noise-like pulses in double-clad Tm-doped fibre laser with nonlinear optical loop mirror," J. Mod. Opt. **67**(2), 146–152 (2020).
35. Z. Xu, Z.-Y. Dou, J. Hou, and X.-J. Xu, "All-fiber wavelength-tunable Tm-doped fiber laser mode locked by SESAM with 120 nm tuning range," Appl. Opt. **56**(21), 5978–5981 (2017).
36. J. Liu, J. Xu, and P. Wang, "High Repetition-Rate Narrow Bandwidth SESAM Mode-locked Yb-doped Fiber Lasers," IEEE Photonics Technol. Lett. **24**(7), 539–541 (2012).
37. H. Jeong, S. Y. Choi, F. Rotermund, Y.-H. Cha, D.-Y. Jeong, and D.-I. Yeom, "All-fiber mode-locked laser oscillator with pulse energy of 34 nJ using a single-walled carbon nanotube saturable absorber," Opt. Express **22**(19), 22667–22672 (2014).
38. Z. Tian, K. Wu, L. Kong, N. Yang, Y. Wang, R. Chen, W. Hu, J. Xu, and Y. Tang, "Mode-locked thulium fiber laser with MoS2," Laser Phys. Lett. **12**(6), 065104 (2015).
39. R. Khazaeinezhad, S. H. Kassani, H. Jeong, D. Il Yeom, and K. Oh, "Femtosecond Soliton Pulse Generation Using Evanescent Field Interaction Through Tungsten Disulfide (WS2) Film," J. Light. Technol. **33**(17), 3550–3557 (2015).
40. J. Sotor, G. Sobon, and K. M. Abramski, "Sub-130 fs mode-

locked Er-doped fiber laser based on topological insulator," Opt. Express **22**(11), 13244–13249 (2014).
41. U. Keller, K. J. Weingarten, F. X. Kärtner, D. Kopf, B. Braun, I. D. Jung, R. Fluck, C. Hönninger, N. Matuschek, and J. Aus Der Au, "Semiconductor saturable absorber mirrors (SESAM's) for femtosecond to nanosecond pulse generation in solid-state lasers," IEEE J. Sel. Top. Quantum Electron. **2**(3), 435–451 (1996).
42. U. Siegner, R. Fluck, G. Zhang, and U. Keller, "Ultrafast high-intensity nonlinear absorption dynamics in low-temperature grown gallium arsenide," Appl. Phys. Lett. **69**(17), 2566–2568 (1996).
43. M. Guina, N. Xiang, A. Vainionpää, O. G. Okhotnikov, T. Sajavaara, and J. Keinonen, "Self-starting stretched-pulse fiber laser mode locked and stabilized with slow and fast semiconductor saturable absorbers," Opt. Lett. **26**(22), 1809–1811 (2001).
44. F. X. Kärtner, J. Aus Der Au, and U. Keller, "Mode-locking with slow and fast saturable absorbers - What's the difference?," IEEE J. Sel. Top. Quantum Electron. **4**(2), 159–168 (1998).
45. I. A. Litago, D. Leandro, M. Á. Quintela, R. A. Pérez-Herrera, M. López-Amo, and J. M. López-Higuera, "Tunable SESAM-Based Mode-Locked Soliton Fiber Laser in Linear Cavity by Axial-Strain Applied to an FBG," J. Light. Technol. **35**(23), 5003–5009 (2017).
46. H. Wang, H. Han, Y. Xie, Y. Yu, H. Teng, S. Fang, J. Zhu, and Z. Wei, "Stable SESAM-mode-locked Yb fiber laser in the similariton regime," in *OSA Laser Congress (ASSL,LAC)* (2017), p. JTh2A.37.
47. K. C. Phillips, H. H. Gandhi, E. Mazur, and S. K. Sundaram, "Ultrafast laser processing of materials: a review," Adv. Opt. Photonics **7**(4), 684–712 (2015).
48. K. O. Hill, Y. Fujii, D. C. Johnson, and B. S. Kawasaki, "Photosensitivity in optical fiber waveguides: Application to reflection filter fabrication," Appl. Phys. Lett. **32**(10), 647–649 (1978).
49. G. W. Arnold and W. D. Compton, "Radiation effects in silica at low temperatures," Phys. Rev. **116**(4), 802–811 (1959).
50. D. Barbier, M. Green, and S. J. Madden, "Waveguide Fabrication

for Integrated Optics by Electron Beam Irradiation of Silica," J. Light. Technol. **9**(6), 715–720 (1991).
51. R. R. A. Syms, T. J. Tate, and M. F. Grant, "Reduction of propagation loss in silica-on-silicon channel waveguides formed by electron beam irradiation," Electron. Lett. **30**(18), 1480–1481 (1994).
52. L. Lichtenstein, M. Heyde, and H. J. Freund, "Atomic arrangement in two-dimensional silica: From crystalline to vitreous structures," J. Phys. Chem. C **116**(38), 20426–20432 (2012).
53. B. E. Warren, "Summary of Work on Atomic Arrangement in Glass," J. Am. Ceram. Soc. **24**(8), 256–261 (1941).
54. M. Lancry, E. Régnier, and B. Poumellec, "Fictive temperature in silica-based glasses and its application to optical fiber manufacturing," Prog. Mater. Sci. **57**(1), 63–94 (2012).
55. M. M. Smedskjaer, Y. Yue, J. Deubener, and S. Mørup, "Impact of cationic diffusion on properties of iron- bearing glass fibres," Phys. Chem. Glas. J. Glas. Sci. Technol. Part B **51**(5), 271–280 (2010).
56. S. S. Mao, F. Quéré, S. Guizard, X. Mao, R. E. Russo, G. Petite, and P. Martin, "Dynamics of femtosecond laser interactions with dielectrics," Appl. Phys. A Mater. Sci. Process. **79**(7), 1695–1709 (2004).
57. C. B. Schaffer, J. F. García, and E. Mazur, "Bulk heating of transparent materials using a high-repetition-rate femtosecond laser," Appl. Phys. A Mater. Sci. Process. **76**(3), 351–354 (2003).
58. S. M. Eaton, H. Zhang, P. R. Herman, F. Yoshino, L. Shah, J. Bovatsek, and A. Y. Arai, "Heat accumulation effects in femtosecond laser-written waveguides with variable repetition rate," Opt. Express **13**(12), 4708–4716 (2005).
59. Y. Bellouard, A. Champion, B. McMillen, S. Mukherjee, R. R. Thomson, C. Pépin, P. Gillet, and Y. Cheng, "Stress-state manipulation in fused silica via femtosecond laser irradiation," Optica **3**(12), 1285–1293 (2016).
60. A. Champion, M. Beresna, P. Kazansky, and Y. Bellouard, "Stress distribution around femtosecond laser affected zones: Effect of nanogratings orientation," Opt. Express **21**(21), 24942–24951 (2013).

61. F. Dürr, H. G. Limberger, R. P. Salathé, F. Hindle, M. Douay, E. Fertein, and C. Przygodzki, "Tomographic measurement of femtosecond-laser induced stress changes in optical fibers," Appl. Phys. Lett. **84**(24), 4983–4985 (2004).
62. V. R. Bhardwaj, P. B. Corkum, D. M. Rayner, C. Hnatovsky, E. Simova, and R. S. Taylor, "Stress in femtosecond-laser-written waveguides in fused silica," Opt. Lett. **29**(12), 1312–1314 (2004).
63. B. Poumellec, L. Sudrie, M. Franco, B. Prade, and A. Mysyrowicz, "Femtosecond laser irradiation stress induced in pure silica," Opt. Express **11**(9), 1070–1079 (2003).
64. S. Guizard, P. Martin, G. Petite, P. D'Oliveira, and P. Meynadieri, "Time-resolved study of laser-induced colour centres in SiO2," J. Phys. Condens. Matter **8**(9), 1281–1290 (1996).
65. A. Rudenko, "Numerical study of ultrashort laser-induced periodic nanostructure formation in dielectric materials," Université de Lyon (2017).
66. M. Lancry, N. Groothoff, B. Poumellec, S. Guizard, N. Fedorov, and J. Canning, "Time-resolved plasma measurements in Ge-doped silica exposed to infrared femtosecond laser," Phys. Rev. B - Condens. Matter Mater. Phys. **84**(24), 245103 (2011).
67. A. Mouskeftaras, S. Guizard, N. Fedorov, and S. Klimentov, "Mechanisms of femtosecond laser ablation of dielectrics revealed by double pump-probe experiment," Appl. Phys. A Mater. Sci. Process. **110**(3), 709–715 (2013).
68. T. E. Itina and N. Shcheblanov, "Electronic excitation in femtosecond laser interactions with wide-band-gap materials," Appl. Phys. A Mater. Sci. Process. **98**(4), 769–775 (2010).
69. C. B. Schaffer, A. Brodeur, and E. Mazur, "Laser-induced breakdown and damage in bulk transparent materials induced by tightly focused femtosecond laser pulses," Meas. Sci. Technol. **12**(11), 1784–1794 (2001).
70. J. Tian, "Femtosecond laser direct writing of circular optical properties in silica glass," Université Paris-Saclay (2020).
71. K. S. Song and R. T. Williams, "Temperature-dependent self-trapped exciton relaxation in alkali halides: Molecular dynamics study," Phys. Status Solidi Basic Res. **243**(14), 3782–3794 (2006).
72. B. Poumellec, M. Lancry, A. Chahid-Erraji, and P. G. Kazansky, "Modification thresholds in femtosecond laser processing of

pure silica: review of dependencies on laser parameters [Invited]," Opt. Mater. Express **1**(4), 766–782 (2011).
73. M. Royon, E. Marin, S. Girard, A. Boukenter, Y. Ouerdane, and R. Stoian, "X-ray preconditioning for enhancing refractive index contrast in femtosecond laser photoinscription of embedded waveguides in pure silica," Opt. Mater. Express **9**(1), 65–74 (2019).
74. M. Lancry and B. Poumellec, "UV laser processing and multiphoton absorption processes in optical telecommunication fiber materials," Phys. Rep. **523**(4), 207–229 (2013).
75. E. Bricchi and P. G. Kazansky, "Extraordinary stability of anisotropic femtosecond direct-written structures embedded in silica glass," Appl. Phys. Lett. **88**(11), 111119 (2006).
76. D. Grobnic, C. W. Smelser, S. J. Mihailov, and R. B. Walker, "Long-term thermal stability tests at 1000 °C of silica fibre Bragg gratings made with ultrafast laser radiation," Meas. Sci. Technol. **17**(5), 1009–1013 (2006).
77. L. Sudrie, M. Franco, B. Prade, and A. Mysyrowicz, "Writing of permanent birefringent microlayers in bulk fused silica with femtosecond laser pulses," Opt. Commun. **171**(4), 279–284 (1999).
78. E. Bricchi, B. G. Klappauf, and P. G. Kazansky, "Form birefringence and negative index change created by femtosecond direct writing in transparent materials," Opt. Lett. **29**(1), 119–121 (2004).
79. E. N. Glezer, M. Milosavljevic, L. Huang, R. L. Finlay, T. H. Her, J. P. Callan, and E. Mazur, "3-D optical storage and engraving inside transparent materials," in *Springer Series in Chemical Physics* (1996), **62**, pp. 157–158.
80. J. W. Chan, T. R. Huser, S. H. Risbud, and D. M. Krol, "Modification of the fused silica glass network associated with waveguide fabrication using femtosecond laser pulses," Appl. Phys. A Mater. Sci. Process. **76**(3), 367–372 (2003).
81. R. Brückner, "Properties and structure of vitreous silica. I," J. Non. Cryst. Solids **5**(2), 123–175 (1970).
82. K. Hirao and K. Miura, "Writing waveguides and gratings in silica and related materials by a femtosecond laser," J. Non.

Cryst. Solids **239**(1–3), 91–95 (1998).
83. A. Saliminia, R. Vallée, and S. L. Chin, "Waveguide writing in silica glass with femtosecond pulses from an optical parametric amplifier at 1.5 μm," Opt. Commun. **256**(4–6), 422–427 (2005).
84. M. Lancry, B. Poumellec, A. Chahid-Erraji, M. Beresna, and P. G. Kazansky, "Dependence of the femtosecond laser refractive index change thresholds on the chemical composition of doped-silica glasses," Opt. Express **1**(4), 711–723 (2011).
85. L. Bressel, D. de Ligny, C. Sonneville, V. Martinez, V. Mizeikis, R. Buividas, and S. Juodkazis, "Femtosecond laser induced density changes in GeO_2 and SiO_2 glasses: Fictive temperature effect [Invited]," Opt. Mater. Express **1**(4), 605–613 (2011).
86. J. W. Chan, T. Huser, S. Risbud, and D. M. Krol, "Structural changes in fused silica after exposure to focused femtosecond laser pulses," Opt. Lett. **26**(21), 1726–1728 (2001).
87. K. Miura, J. Qiu, H. Inouye, T. Mitsuyu, and K. Hirao, "Photowritten optical waveguides in various glasses with ultrashort pulse laser," Appl. Phys. Lett. **71**(23), 3329–3331 (1997).
88. A. M. Streltsov and N. F. Borrelli, "Study of femtosecond-laser-written waveguides in glasses," J. Opt. Soc. Am. B **19**(10), 2496–2504 (2002).
89. K. M. Davis, K. Miura, N. Sugimoto, and K. Hirao, "Writing waveguides in glass with a femtosecond laser," Opt. Lett. **21**(21), 1729–1731 (1996).
90. O. M. Efimov, L. B. Glebov, K. A. Richardson, E. Van Stryland, T. Cardinal, S. H. Park, M. Couzi, and J. L. Brunéel, "Waveguide writing in chalcogenide glasses by a train of femtosecond laser pulses," Opt. Mater. (Amst). **17**(3), 379–386 (2001).
91. G. Petite, P. Daguzan, S. Guizard, and P. Martin, "Ultrafast processes in laser irradiated wide bandgap insulators," Appl. Surf. Sci. **109**(110), 36–42 (1997).
92. V. Twersky, "Form and intrinsic birefringence," J. Opt. Soc. Am. **65**(3), 239–245 (1975).
93. R. Desmarchelier, B. Poumellec, F. Brisset, S. Mazerat, and M. Lancry, "In the heart of femtosecond laser induced nanogratings: From porous nanoplanes to form birefringence," World J. Nano Sci. Eng. **05**(04), 115–125 (2015).

94. F. Zimmermann, M. Lancry, A. Plech, S. Richter, B. Hari Babu, B. Poumellec, A. Tünnermann, and S. Nolte, "Femtosecond laser written nanostructures in Ge-doped glasses," Opt. Lett. **41**(6), 1161–1164 (2016).
95. M. Lancry, J. Canning, K. Cook, M. Heili, D. R. Neuville, and B. Poumellec, "Nanoscale femtosecond laser milling and control of nanoporosity in the normal and anomalous regimes of GeO2-SiO2 glasses," Opt. Mater. Express **6**(2), 321–330 (2016).
96. P. Vlugter and Y. Bellouard, "Elastic properties of self-organized nanogratings produced by femtosecond laser exposure of fused silica," Phys. Rev. Mater. **4**(2), 023607 (2020).
97. Y. Bellouard, T. Colomb, C. Depeursinge, M. Dugan, A. A. Said, and P. Bado, "Nanoindentation and birefringence measurements on fused silica specimen exposed to low-energy femtosecond pulses," Opt. Express **14**(18), 8360–8366 (2006).
98. Y. Wang, "A contribution to high temperature applications using femtosecond laser direct writing in silica-based glasses and optical fibers," Université Paris-Saclay (2021).
99. A. Champion and Y. Bellouard, "Direct volume variation measurements in fused silica specimens exposed to femtosecond laser," Opt. Mater. Express **2**(6), 789–798 (2012).
100. L. Yuan, B. Cheng, J. Huang, J. Liu, H. Wang, X. Lan, and H. Xiao, "Stress-induced birefringence and fabrication of in-fiber polarization devices by controlled femtosecond laser irradiations," Opt. Express **24**(2), 1062–1071 (2016).
101. L. A. Fernandes, J. R. Grenier, P. R. Herman, J. S. Aitchison, and P. V. S. Marques, "Stress induced birefringence tuning in femtosecond laser fabricated waveguides in fused silica," Opt. Express **20**(22), 24103–24114 (2012).
102. L. A. Fernandes, J. R. Grenier, P. V. S. Marques, J. Stewart Aitchison, and P. R. Herman, "Strong birefringence tuning of optical waveguides with femtosecond laser irradiation of bulk fused silica and single mode fibers," J. Light. Technol. **31**(22), 3563–3569 (2013).
103. R. L. Fleischer, P. B. Price, and R. M. Walker, "Solid-state track detectors: Applications to nuclear science and geophysics," Annu. Rev. Nucl. Sci. **15**(1), 1–28 (1965).
104. C. B. Schaffer, A. Brodeur, N. Nishimura, and E. Mazur, "Laser-

induced microexplosions in transparent materials: microstructuring with nanojoules," in *Commercial and Biomedical Applications of Ultrafast Lasers* (1999), **3616**, pp. 143–147.
105. M. Sakakura, Y. Lei, L. Wang, Y. H. Yu, and P. G. Kazansky, "Ultralow-loss geometric phase and polarization shaping by ultrafast laser writing in silica glass," Light Sci. Appl. **9**(1), 15 (2020).
106. H. Wang, Y. Lei, L. Wang, M. Sakakura, Y. Yu, G. Shayeganrad, and P. G. Kazansky, "100-layer error-free 5D optical data storage by ultrafast laser nanostructuring in glass," Laser Photon. Rev. **16**(4), 2100563 (2022).
107. V. R. Bhardwaj, E. Simova, P. P. Rajeev, C. Hnatovsky, R. S. Taylor, D. M. Rayner, and P. B. Corkum, "Optically produced arrays of planar nanostructures inside fused silica," Phys. Rev. Lett. **96**(5), 057404 (2006).
108. H. S. Carslaw and J. C. Jaeger, "Conduction of heat in solids," Clarendon Press (1992).
109. F. Zimmermann, M. Lancry, A. Plech, S. Richter, T. Ullsperger, B. Poumellec, A. Tünnermann, and S. Nolte, "Ultrashort pulse laser processing of silica at high repetition rates-from network change to residual strain," Int. J. Appl. Glas. Sci. **8**(2), 233–238 (2017).
110. C. R. Lee, S. H. Lin, H. S. Ku, J. H. Liu, P. C. Yang, C. Y. Huang, H. C. Yeh, and T. D. Ji, "Optically band-tunable color cone lasing emission in a dye-doped cholesteric liquid crystal with a photoisomerizable chiral dopant," Appl. Phys. Lett. **96**(11), 1–4 (2010).
111. H. Caner, E. Groner, L. Levy, and I. Agranat, "Trends in the development of chiral drugs," Drug Discov. Today **9**(3), 105–110 (2004).
112. A. J. Miles and B. A. Wallace, "Synchrotron radiation circular dichroism spectroscopy of proteins and applications in structural and functional genomics," Chem. Soc. Rev. **35**(1), 39–51 (2006).
113. M. B. Steffensen, D. Rotem, and H. Bayley, "Single-molecule analysis of chirality in a multicomponent reaction network," Nat. Chem. **6**(7), 603–607 (2014).

114. Y. Wang and Q. Li, "Light-driven chiral molecular switches or motors in liquid crystals," Adv. Mater. **24**(15), 1926–1945 (2012).
115. J. K. Gansel, M. Thiel, M. S. Rill, M. Decker, K. Bade, V. Saile, G. Von Freymann, S. Linden, and M. Wegener, "Gold helix photonic metamaterial as broadband circular polarizer," Science (80-. ). **325**(5947), 1513–1515 (2009).
116. P. Zijlstra, J. W. M. Chon, and M. Gu, "Five-dimensional optical recording mediated by surface plasmons in gold nanorods," Nature **459**(7245), 410–413 (2009).
117. H. Hübener, U. De Giovannini, C. Schäfer, J. Andberger, M. Ruggenthaler, J. Faist, and A. Rubio, "Engineering quantum materials with chiral optical cavities," Nat. Mater. **20**(4), 438–442 (2021).
118. D. G. Dimitriu and D. O. Dorohoi, "New method to determine the optical rotatory dispersion of inorganic crystals applied to some samples of Carpathian Quartz," Spectrochim. Acta - Part A Mol. Biomol. Spectrosc. **131**, 674–677 (2014).
119. S. H. Yoo, R. Ossikovski, and E. Garcia-Caurel, "Experimental study of thickness dependence of polarization and depolarization properties of anisotropic turbid media using Mueller matrix polarimetry and differential decomposition," Appl. Surf. Sci. **421**, 870–877 (2017).
120. O. Arteaga, "A note on optical activity and extrinsic chirality," (2015).
121. J. H. Poynting, "The wave motion of a revolving shaft, and a suggestion as to the angular momentum in a beam of circularly polarised light," Proc. R. Soc. A **82**, 560–567 (1909).
122. K. J. Moh, X. C. Yuan, D. Y. Tang, W. C. Cheong, L. S. Zhang, D. K. Y. Low, X. Peng, H. B. Niu, and Z. Y. Lin, "Generation of femtosecond optical vortices using a single refractive optical element," Appl. Phys. Lett. **88**(9), 1–4 (2006).
123. A. M. Yao and M. J. Padgett, "Orbital angular momentum: origins, behavior and applications," Adv. Opt. Photonics **3**(2), 161–204 (2011).
124. V. Y. Bazhenov, M. S. Soskin, and M. V Vasnetsov, "Screw dislocations in light wavefronts," J. Mod. Opt. **39**(5), 985–990 (1992).
125. N. R. Heckenberg, R. McDuff, C. P. Smith, and A. G. White,

"Generation of optical phase singularities by computer-generated holograms," Opt. Lett. **17**(3), 221–223 (1992).
126. J. Ouyang, W. Perrie, O. J. Allegre, T. Heil, Y. Jin, E. Fearon, D. Eckford, S. P. Edwardson, and G. Dearden, "Tailored optical vector fields for ultrashort-pulse laser induced complex surface plasmon structuring," Opt. Express **23**(10), 12562–12572 (2015).
127. M. Beresna, M. Gecevičius, P. G. Kazansky, and T. Gertus, "Radially polarized optical vortex converter created by femtosecond laser nanostructuring of glass," Appl. Phys. Lett. **98**(20), 201101 (2011).
128. L. Marrucci, C. Manzo, and D. Paparo, "Optical spin-to-orbital angular momentum conversion in inhomogeneous anisotropic media," Phys. Rev. Lett. **96**(16), 1–4 (2006).
129. X. Cai, J. Wang, M. J. Strain, and J. Zhu, "Integrated compact optical vortex beam emitters," Science (80-. ). **338**(6105), 363–366 (2012).
130. M. J. Strain, X. Cai, J. Wang, J. Zhu, D. B. Phillips, L. Chen, M. Lopez-garcia, J. L. O. Brien, M. G. Thompson, M. Sorel, and S. Yu, "Fast electrical switching of orbital angular momentum modes using ultra-compact integrated vortex emitters," Nat. Commun. **5**(1), 4856 (2014).
131. Z. Zhang, J. Sun, and W. Walasik, "Orbital angular momentum microlaser," Science (80-. ). **353**(6298), 464–466 (2016).
132. Z. Qiao, Z. Yuan, S. Zhu, C. Gong, Y. Liao, X. Gong, M. Kim, D. Zhang, and Y.-C. Chen, "High orbital angular momentum lasing with tunable degree of chirality in a symmetry-broken microcavity," Optica **10**(7), 846–853 (2023).
133. S. Sun, Q. He, J. Hao, S. Xiao, and L. Zhou, "Electromagnetic metasurfaces: Physics and applications," Adv. Opt. Photonics **11**(2), 380–479 (2019).
134. N. Yu, P. Genevet, M. A. Kats, F. Aieta, J. P. Tetienne, F. Capasso, and Z. Gaburro, "Light propagation with phase discontinuities: Generalized laws of reflection and refraction," Science (80-. ). **334**(6054), 333–337 (2011).
135. E. Karimi, S. A. Schulz, I. De Leon, H. Qassim, J. Upham, and R. W. Boyd, "Generating optical orbital angular momentum at visible wavelengths using a plasmonic metasurface," Light Sci. Appl. **3**(5), e167 (2014).

136. T. Wang, J. Lu, H. Yao, F. Shi, L. Meng, P. Cheng, and X. Zeng, "Recent progress in all-fiber ultrafast high-order mode lasers," J. Phys. Photonics **3**(1), 012007 (2021).
137. X. Jin, F. Pang, Y. Zhang, S. Huang, Y. Li, J. Wen, Z. Chen, M. Wang, and T. Wang, "Generation of the first-order OAM modes in single-ring fibers by offset splicing technology," IEEE Photonics Technol. Lett. **28**(14), 1581–1584 (2016).
138. T. Wang, F. Wang, F. Shi, F. Pang, S. Huang, T. Wang, and X. Zeng, "Generation of femtosecond optical vortex beams in all-fiber mode-locked fiber laser using mode selective coupler," J. Light. Technol. **35**(11), 2161–2166 (2017).
139. Y. Zhao, Y. Liu, L. Zhang, C. Zhang, J. Wen, and T. Wang, "Mode converter based on the long-period fiber gratings written in the two-mode fiber," Opt. Express **24**(6), 6186–6195 (2016).
140. J. Dong and K. S. Chiang, "Mode-locked fiber laser with transverse-mode selection based on a two-mode FBG," IEEE Photonics Technol. Lett. **26**(17), 1766–1769 (2014).
141. B. Sun, A. Wang, C. Gu, G. Chen, L. Xu, D. Chung, and Q. Zhan, "Mode-locked all-fiber laser producing radially polarized rectangular pulses," Opt. Lett. **40**(8), 1691–1694 (2015).
142. L. Wang, P. Vaity, B. Ung, Y. Messaddeq, L. A. Rusch, and S. Larochelle, "Characterization of OAM fibers using fiber Bragg gratings," Opt. Express **22**(13), 15653–15661 (2014).
143. P. Z. Dashti, F. Alhassen, and H. P. Lee, "Observation of orbital angular momentum transfer between acoustic and optical vortices in optical fiber," Phys. Rev. Lett. **96**(4), 043604 (2006).
144. B. Frank, X. Yin, M. Scha, J. Zhao, S. M. Hein, P. V Braun, and H. Giessen, "Large-area 3D chiral plasmonic structures," ACS Nano **7**(7), 6321–6329 (2013).
145. K. Toyoda, K. Miyamoto, N. Aoki, R. Morita, and T. Omatsu, "Using optical vortex to control the chirality of twisted metal nanostructures," Nano Lett. **12**(7), 3645–3649 (2012).
146. A. Ambrosio, L. Marrucci, F. Borbone, A. Roviello, and P. Maddalena, "Light-induced spiral mass transport in azo-polymer films under vortex-beam illumination," Nat. Commun. **3**(1), 989 (2012).
147. A. Ambrosio, P. Maddalena, L. Marrucci, C. Universitario, S. Angelo, F. Ii, C. Universitario, S. Angelo, and D. Fisica,

"Molecular model for light-driven spiral mass transport in azopolymer films," Phys. Rev. Lett. **110**(14), 146102 (2013).
148. M. Sakamoto, N. Uemura, R. Saito, H. Shimobayashi, Y. Yoshida, T. Mino, and T. Omatsu, "Chirogenesis and amplification of molecular chirality using optical vortices," Angew. Chemie - Int. Ed. **60**(23), 12819–12823 (2021).
149. J. Ni, C. Wang, C. Zhang, Y. Hu, L. Yang, Z. Lao, B. Xu, J. Li, D. Wu, and J. Chu, "Three-dimensional chiral microstructures fabricated by structured optical vortices in isotropic material," Light Sci. Appl. **6**(7), e17011 (2017).
150. D. Wu, J. Xu, L. Niu, S. Wu, K. Midorikawa, and K. Sugioka, "In-channel integration of designable microoptical devices using flat scaffold-supported femtosecond-laser microfabrication for coupling-free optofluidic cell counting," Light Sci. Appl. **4**(1), e228 (2015).
151. M. Deubel, G. V. O. N. Freymann, M. Wegener, S. Pereira, K. Busch, and C. M. Soukoulis, "Direct laser writing of three-dimensional photonic-crystal templates for telecommunications," Nat. Mater. **3**(7), 444–447 (2004).
152. H. Lin and M. Gu, "Creation of diffraction-limited non-Airy multifocal arrays using a spatially shifted vortex beam," Appl. Phys. Lett. **102**(8), 084103 (2013).
153. B. Poumellec, M. Lancry, R. Desmarchelier, E. Hervé, F. Brisset, and J. C. Poulin, "Asymmetric orientational writing in glass with femtosecond laser irradiation," Opt. Mater. Express **3**(10), 1586–1599 (2013).
154. P. G. Kazansky, W. Yang, E. Bricchi, J. Bovatsek, A. Arai, Y. Shimotsuma, K. Miura, and K. Hirao, ""Quill" writing with ultrashort light pulses in transparent materials," Appl. Phys. Lett. **90**(15), 12–15 (2007).
155. B. Poumellec, M. Lancry, J.-C. Poulin, and S. Ani-Joseph, "Non reciprocal writing and chirality in femtosecond laser irradiated silica," Opt. Express **16**(22), 18354–18361 (2008).
156. M. Lancry, B. Poumellec, R. Desmarchelier, and B. Bourguignon, "Oriented creation of anisotropic defects by IR femtosecond laser scanning in silica," Opt. Mater. Express **2**(12), 1809–1821 (2012).
157. N. Nakamura and H. Nagahama, "Curie symmetry principle:

Does it constrain the analysis of structural geology," Forma **15**, 87–94 (2000).
158. U. Österberg and W. Margulis, "Dye laser pumped by Nd:YAG laser pulses frequency doubled in a glass optical fiber," Opt. Lett. **11**(8), 516–518 (1986).
159. W. L. Noorduin, A. A. C. Bode, M. Van Der Meijden, H. Meekes, A. F. Van Etteger, W. J. P. Van Enckevort, P. C. M. Christianen, B. Kaptein, R. M. Kellogg, T. Rasing, and E. Vlieg, "Complete chiral symmetry breaking of an amino acid derivative directed by circularly polarized light," Nat. Chem. **1**(9), 729–732 (2009).
160. R. S. Taylor, E. Simova, and C. Hnatovsky, "Creation of chiral structures inside fused silica glass," Opt. Lett. **33**(12), 1312–1314 (2008).
161. J. Lu, F. Shi, J. Xu, L. Meng, L. Zhang, P. Cheng, X. Zhou, F. Pang, and X. Zeng, "Recent progress of dynamic mode manipulation via acousto-optic interactions in few-mode fiber lasers: Mechanism, device and applications," Nanophotonics **10**(3), 983–1010 (2021).
162. W. Zhang, F. Gao, F. Bo, Q. Wu, G. Zhang, and J. Xu, "All-fiber acousto-optic tunable notch filter with a fiber winding driven by a cuneal acoustic transducer," Opt. Lett. **36**(2), 271–273 (2011).
163. W. F. Liu, P. S. J. Russell, and L. Dong, "Acousto-optic superlattice modulator using a fiber Bragg grating," Opt. Lett. **22**(19), 1515–1517 (1997).
164. W. F. Liu, P. S. J. Russell, and L. Dong, "100% efficient narrow-band acoustooptic tunable reflector using fiber Bragg grating," J. Light. Technol. **16**(11), 2006–2009 (2006).
165. P. S. J. Russell and W. Liu, "Acousto-optic superlattice modulation in fiber Bragg gratings," J. Opt. Soc. Am. A **17**(8), 1421–1429 (2000).
166. M. Delgado-Pinar, D. Zalvidea, A. Díez, P. Pérez-Millán, and M. V Andrés, "Q-switching of an all-fiber laser by acousto-optic modulation of a fiber Bragg grating," Opt. Express **14**(3), 1106–1112 (2006).
167. H. M. Chan, R. Huang, F. Alhassen, O. Finch, I. V. Tomov, C. S. Park, and H. P. Lee, "A compact all-fiber LPG-AOTF frequency shifter on single-mode fiber and its application to vibration

measurement," IEEE Photonics Technol. Lett. **20**(18), 1572–1574 (2008).
168. K. J. Lee, H. C. Park, H. S. Park, and B. Y. Kim, "Highly efficient all-fiber tunable polarization filter using torsional acoustic wave," Opt. Express **15**(19), 12362–12367 (2007).
169. S. Do Lim, H. C. Park, and B. Y. Kim, "Twist effect on spectral properties of two-mode fiber acousto-optic filters," Opt. Express **16**(17), 13042–13051 (2008).
170. K. J. Lee, I.-K. Hwang, H. C. Park, and B. Y. Kim, "Polarization-independent all-fiber acousto-optic tunable filter using torsional acoustic wave," IEEE Photonics Technol. Lett. **22**(8), 523–525 (2010).
171. J. Ko, K. J. Lee, and B. Y. Kim, "Spectral shaping of an all-fiber torsional acousto-optic tunable filter," Appl. Opt. **53**(36), 8499–8506 (2014).
172. D.-R. Song, K. J. Lee, and B. Y. Kim, "Band-rejection filtering based on lossy torsional acousto-optic coupling in a single polarization fiber," Opt. Express **22**(20), 24034–24043 (2014).
173. I. K. Hwang, S. H. Yun, and B. Y. Kim, "All-fiber tunable comb filter with nonreciprocal transmission," IEEE Photonics Technol. Lett. **10**(10), 1437–1439 (1998).
174. R. Feced, C. Alegria, M. N. Zervas, and R. I. Laming, "Acoustooptic attenuation filters based on tapered optical fibers," IEEE J. Sel. Top. Quantum Electron. **5**(5), 1278–1288 (1999).
175. W. Zhang, L. Huang, F. Gao, F. Bo, G. Zhang, and J. Xu, "Tunable broadband light coupler based on two parallel all-fiber acousto-optic tunable filters," Opt. Express **21**(14), 16621–16628 (2013).
176. G. Ramírez-Meléndez, M. Bello-Jiménez, O. Pottiez, and M. V. Andrés, "Improved all-fiber acousto-optic tunable bandpass filter," IEEE Photonics Technol. Lett. **29**(12), 1015–1018 (2017).
177. W.-F. Liu, I.-M. Liu, L.-W. Chung, D.-W. Huang, and C. C. Yang, "Acoustic-induced switching of the reflection wavelength in a fiber Bragg grating," Opt. Lett. **25**(18), 1319–1321 (2000).
178. W. Zhang, W. Gao, L. Huang, D. Mao, B. Jiang, F. Gao, D. Yang, G. Zhang, J. Xu, and J. Zhao, "Optical heterodyne micro-vibration measurement based on all-fiber acousto-optic

frequency shifter," Opt. Express **23**(13), 17576–17583 (2015).
179. M. W. Haakestad and H. E. Engan, "Acoustooptic characterization of a birefringent two-mode photonic crystal fiber," Opt. Express **14**(16), 7319–7328 (2006).
180. L. Huang, P. Chang, X. Song, W. Peng, W. Zhang, F. Gao, F. Bo, G. Zhang, and J. Xu, "Tunable in-fiber Mach-Zehnder interferometer driven by unique acoustic transducer and its application in tunable multi-wavelength laser," Opt. Express **24**(3), 2406–2412 (2016).
181. D. Zalvidea, N. A. Russo, R. Duchowicz, M. Delgado-Pinar, A. Díez, J. L. Cruz, and M. V Andrés, "High-repetition rate acoustic-induced Q-switched all-fiber laser," Opt. Commun. **244**(1–6), 315–319 (2005).
182. M. Bello-Jiménez, C. Cuadrado-Laborde, A. Diez, J. L. Cruz, M. V. Andrés, and A. Rodríguez-Cobos, "Mode-locked all-fiber ring laser based on broad bandwidth in-fiber acousto-optic modulator," Appl. Phys. B Lasers Opt. **110**(1), 73–80 (2013).
183. Y. Li, L. Huang, H. Han, L. Gao, Y. Cao, Y. Gong, W. Zhang, F. Gao, I. P. Ikechukwu, and T. Zhu, "Acousto-optic tunable ultrafast laser with vector-mode-coupling-induced polarization conversion," Photonics Res. **7**(7), 798–805 (2019).
184. K. Wei, W. Zhang, L. Huang, D. Mao, F. Gao, T. Mei, and J. Zhao, "Generation of cylindrical vector beams and optical vortex by two acoustically induced fiber gratings with orthogonal vibration directions," Opt. Express **25**(3), 2733–2741 (2017).
185. L. Carrion-Higueras, E. P. Alcusa-Saez, A. Diez, and M. V. Andres, "All-fiber laser with intracavity acousto-optic dynamic mode converter for efficient generation of radially polarized cylindrical vector beams," IEEE Photonics J. **9**(1), 1500507 (2017).
186. H. S. Kim, S. H. Yun, I. K. Hwang, and B. Y. Kim, "All-fiber acousto-optic tunable notch filter with electronically controllable spectral profile," Opt. Lett. **22**(19), 1476–1478 (1997).
187. A. Diez, G. Kakarantzas, T. A. Birks, and P. S. J. Russell, "Acoustic stop-bands in periodically microtapered optical fibers," Appl. Phys. Lett. **76**(23), 3481–3483 (2000).
188. H. Zhang, S. Kang, B. Liu, H. Dong, and Y. Miao, "All-fiber acousto-optic tunable bandpass filter based on a lateral offset

fiber splicing structure," IEEE Photonics J. **7**(1), 2700312 (2015).
189. W. Zhang, K. Wei, L. Huang, D. Mao, B. Jiang, F. Gao, G. Zhang, T. Mei, and J. Zhao, "Optical vortex generation with wavelength tunability based on an acoustically-induced fiber grating," Opt. Express **24**(17), 19278–19285 (2016).
190. M. Yavorsky, D. V Vikulin, E. V Barshak, B. P. Lapin, and C. N. Alexeyev, "Revised model of acousto-optic interaction in optical fibers endowed with a flexural wave," Opt. Lett. **44**(3), 598–601 (2019).
191. L. Yan, P. Gregg, E. Karimi, A. Rubano, L. Marrucci, R. W. Boyd, and S. Ramachandran, "Q-plate enabled spectrally diverse orbital-angular- momentum conversion for stimulated emission depletion microscopy," Optica **2**(10), 900–903 (2015).
192. K. Goda, K. K. Tsia, and B. Jalali, "Serial time-encoded amplified imaging for real-time observation of fast dynamic phenomena," Nature **458**(7242), 1145–1149 (2009).
193. T. Jannson, "Real-time Fourier transformation in dispersive optical fibers," Opt. Lett. **8**(4), 232–234 (1983).
194. D. R. Solli, C. Ropers, P. Koonath, and B. Jalali, "Optical rogue waves," Nature **450**(7172), 1054–1057 (2007).
195. X. Liu and Y. Cui, "Revealing the behavior of soliton buildup in a mode-locked laser," Adv. Photonics **1**(1), 016003 (2019).
196. J. Peng and H. Zeng, "Build-up of dissipative optical soliton molecules via diverse soliton interactions," Laser Photon. Rev. **12**(8), 1800009 (2018).
197. P. Ryczkowski, M. Närhi, C. Billet, J. M. Merolla, G. Genty, and J. M. Dudley, "Real-time full-field characterization of transient dissipative soliton dynamics in a mode-locked laser," Nat. Photonics **12**(4), 221–227 (2018).
198. A. F. J. Runge, N. G. R. Broderick, and M. Erkintalo, "Observation of soliton explosions in a passively mode-locked fiber laser," Optica **2**(1), 36–39 (2015).
199. Y. Luo, R. Xia, P. P. Shum, W. Ni, Y. Liu, H. Q. Lam, Q. Sun, X. Tang, and L. Zhao, "Real-time dynamics of soliton triplets in fiber lasers," Photonics Res. **8**(6), 884–891 (2020).
200. I. Kudelin, S. Sugavanam, and M. Chernysheva, "Build-up dynamics in bidirectional soliton fiber lasers," Photonics Res. **8**(6), 776–780 (2020).

201. G. Herink, B. Jalali, C. Ropers, and D. R. Solli, "Resolving the build-up of femtosecond mode-locking with single-shot spectroscopy at 90 MHz frame rate," Nat. Photonics **10**(5), 321–326 (2016).
202. G. D. Marshall, M. Ams, and M. J. Withford, "Direct laser written waveguide-Bragg gratings in bulk fused silica," Opt. Lett. **31**(18), 2690–2691 (2006).
203. H. Zhang, S. M. Eaton, J. Li, A. H. Nejadmalayeri, and P. R. Herman, "Type II high-strength Bragg grating waveguides photowritten with ultrashort laser pulses," Opt. Express **15**(7), 4182–4191 (2007).
204. H. Zhang, S. M. Eaton, and P. R. Herman, "Single-step writing of Bragg grating waveguides in fused silica with an externally modulated femtosecond fiber laser," Opt. Lett. **32**(17), 2559–2561 (2007).
205. S.-Y. Lu and R. A. Chipman, "Interpretation of Mueller matrices based on polar decomposition," J. Opt. Soc. Am. A **13**(5), 1106–1113 (1996).
206. J. Morio and F. Goudail, "Influence of the order of diattenuator, retarder, and polarizer in polar decomposition of Mueller matrices," Opt. Lett. **29**(19), 2234–2236 (2004).
207. R. Ossikovski, "Differential matrix formalism for depolarizing anisotropic media," Opt. Lett. **36**(12), 2330–2332 (2011).
208. O. Arteaga, "Historical revision of the differential Stokes-Mueller formalism: discussion," J. Opt. Soc. Am. A **34**(3), 410–414 (2017).
209. J. C. Kemp, G. D. Henson, C. T. Steiner, I. S. Beardsley, and E. R. Powell, "The optical polarization of the Sun measured at a sensitivity of parts in ten million," Nature **326**(6110), 270–273 (1987).
210. A. De Martino, E. Garcia-Caurel, B. Laude, and B. Drévillon, "General methods for optimized design and calibration of Mueller polarimeters," Thin Solid Films **455**–**456**, 112–119 (2004).
211. E. Compain, S. Poirier, and B. Drevillon, "General and self-consistent method for the calibration of polarization modulators, polarimeters, and Mueller-matrix ellipsometers," Appl. Opt. **38**(16), 3490–3502 (1999).

212. F. Shi, H. Yao, Y. Huang, W. Li, T. Wang, and X. Zeng, "Wavelength-switchable all-fiber laser-emitting radially polarized beams," Appl. Opt. **59**(4), 1206–1211 (2020).
213. J. Lu, L. Meng, F. Shi, X. Liu, Z. Luo, P. Yan, L. Huang, F. Pang, T. Wang, X. Zeng, and P. Zhou, "Dynamic mode-switchable optical vortex beams using acousto-optic mode converter," Opt. Lett. **43**(23), 5841–5844 (2018).
214. H. J. Chen, M. Liu, J. Yao, S. Hu, J. B. He, A. P. Luo, Z. C. Luo, and W. C. Xu, "Soliton Booting Dynamics in an Ultrafast Anomalous Dispersion Fiber Laser," IEEE Photonics J. **10**(2), 1501809 (2018).
215. J. Wang, J. Y. Yang, I. M. Fazal, N. Ahmed, Y. Yan, H. Huang, Y. Ren, Y. Yue, S. Dolinar, M. Tur, and A. E. Willner, "Terabit free-space data transmission employing orbital angular momentum multiplexing," Nat. Photonics **6**(7), 488–496 (2012).
216. J. Li, D. Wu, C. W. Qiu, J. Ni, S. Liu, G. Hu, Y. Hu, Z. Lao, Q. Zhang, S. Dong, and J. Chu, "Giant helical dichroism of single chiral nanostructures with photonic orbital angular momentum," ACS Nano **15**(2), 2893–2900 (2021).

# RESUME ETENDU EN FRANÇAIS

La chiralité, ou l'incapacité à coïncider l'objet et son image par translation et rotation, existe largement dans la nature, comme les molécules d'ADN duplex qui contiennent des informations génétiques, les acides aminés ou les galaxies spirales dans l'univers. L'essence de la chiralité est la rupture de symétrie, qui présente des réponses différentes lors de l'interaction avec d'autres objets chiraux.

La lumière peut aussi être chirale. Par exemple, les faisceaux lumineux à polarisation circulaire gauche/droite et les faisceaux de vortex porteurs de moments angulaires orbitaux sont des énantiomères chiraux. Par conséquent, les champs lumineux chiraux sont souvent utilisés pour la détection de substances chirales, comme la technique de spectroscopie basée sur le dichroïsme circulaire. En raison des caractéristiques des distributions topologiques spatiales, la génération, la manipulation et l'application de champs de lumière vortex chiraux sont des sujets essentiels en optique et en nanophotonique.

L'une des principales clés pour répondre à ces problèmes est corrélé à la manipulation des champs de lumière chiraux tels que des vortex variant de l'espace. Comme phonons et photons peuvent interagir et se propager le long de la fibre, le contrôle d'un signal acoustique permet de manipuler de manière non destructive l'onde lumineuse voyageant à l'intérieur de la fibre. En comparaison à la génération statique de champs de lumière vortex, la manipulation du champ optique variant spatio-temporellement via des interactions acousto-optiques « redynamise » le vortex avec des possibilités de commutation rapide et d'accordabilité.

L'interaction chirale entre la lumière et la matière enrichit non seulement les fondamentaux, mais favorise également le développement de matériaux photoniques aux propriétés chirales. La chiralité peut ainsi être transférée entre la lumière et la matière, c.-à-d., la matière peut induire et manipuler la chiralité du champ

lumineux, tandis que le champ lumineux peut également induire et manipuler la chiralité de la matière. L'exploration du mécanisme d'interaction chirale entre la lumière et la matière amène une pierre à l'édifice et favorise par ce biais notre compréhension de l'origine de la chiralité de la vie. De plus, il nous aidera à clarifier le mécanisme de manipulation des matériaux fonctionnels chiraux ainsi que les propriétés optiques chirales sous-jacentes.

En partant des principes de manipulation des champs lumineux chiraux, cette thèse étudie la génération de champs lumineux structurés chiraux et cela au travers des interactions acousto-optiques et du contrôle de la polarisation ainsi que de sa distribution en 3D.

Par exemple, nous démontrons une commutation vortex entre différentes charges topologiques de "+1" et "-1" avec une vitesse de commutation pouvant atteindre 4 kHz. En outre, ce convertisseur de mode acousto-optique est un nouveau déclencheur permettant de contrôler non seulement les états de blocage de mode avec différents modes spatiaux, mais aussi la largeur d'impulsion dans un laser à fibre à blocage de mode. Grâce à la technique de la transformée de Fourier dispersive, la dynamique de commutation dans un laser à fibre est modélisée et observée. Par exemple, un procédé de commutation dynamique entre des états de blocage en mode vortex de 1 ordre et des états de blocage en mode vortex de 0 ordre comprend un étage « silencieux », une phase d'oscillation de relaxation, un état de blocage et un procédé de récupération d'énergie.

D'autre part, nous étudions la chiralité induite par la lumière à l'intérieur de matériaux tels que les fibres de silice et les verres de silice. Plus précisément, nous avons étudié le contrôle morphologique et l'implantation des propriétés optiques des nanoréseaux photoinduits dans des fibres par laser fs. En outre, nous utilisons la propriété de dichroïsme linéaire des nanoréseaux afin de fabriquer des polariseurs en ligne à large bande spectrale. De plus,

des nanoréseaux variants en 3D sont démontrés au moyen du contrôle synchrone de la polarisation pendant le processus d'écriture.

En outre, nous montrons que le mécanisme de la chiralité induite par laser femtoseconde dans les verres est bien une chiralité optique (mais une chiralité extrinsèque), qui est due à un effet joint de la biréfringence de forme et de la biréfringence induite par contrainte avec des axes neutres non parallèles et non perpendiculaires. En tirant profit d'un modèle à deux couches linéaires, de fortes propriétés optiques circulaires ont été réalisées dans la silice par une stratégie multicouche ou encore avec un faisceau Bessel chiral dont l'orientation de polarisation linéaire tourne le long de la propagation. En outre, des assemblages de nanoréseaux sont étudiés pour former des polariseurs intégrés dans une fibre optique et des dispositifs optiques potentiellement chiraux.

Ainsi l'étude de la manipulation du champ lumineux chiral et de son interaction avec les matériaux joue un rôle important dans les domaines du tri des particules, de la communication optique à grande capacité, des puces photoniques, de l'imagerie à super-résolution et du traitement micro-nano laser ultra-rapide.